Experimental and Theoretical Studies in Non-Linear Optical Applications

Fiber Oscillators, Regenerative Amplifiers, Simulations on White-Light Generation

Haider Zia

Fachbereich Physik

Universität Hamburg

This dissertation is submitted to the University of Hamburg for the degree of *Doctor rerum naturalium*

Fakultät für Mathematik,
Informatik und
Naturwissenschaften

July 2015

Dissertation review committee:

Prof. Dr. Dwayne Miller

Prof. Dr. Franz Kärtner

Date of oral disputaton: 23.11.2015

Oral disputaton committee:

Prof. Dr. Michael A. Rübhausen (chair)

Prof. Dr. Dwayne Miller

Prof. Dr. Nils Huse

Korrigierte Fassung (Corrected Version)

Eidesstattliche Versicherung/Declaration on Oath

Hiermit erkläre ich an Eides statt, dass ich die vorliegende Dissertationsschrift selbst verfasst und keine anderen als die angegebenen Quellen und Hilfsmittel benutzt habe.

I hereby declare that except where specific reference and acknowledgement is given to the work of others, all contents of this dissertation are original and have not been submitted in whole or in part for consideration for any other degree or qualification in this, or any other university. This dissertation is my work and contains nothing which is the outcome of work done in collaboration with others, except as specified in the text and acknowledgements.

Haider Zia

August 2015

Kurzzusammenfassung/Abstract

Kompakte und stabile ultraschnelle Laserquellen für Elektronenbeugungsexperimente sind der erste Schritt um den *molecular movie*, das Wunschexperiment der Moleküldynamik schlechthin, zu erreichen. Diese Arbeit konzentriert sich auf die Entwicklung neuartiger, robuster Laserquellen mit frei skalierbarer Wiederholungsrate, Pulsenergie und – dauer, sowie Stabilität. Solche Quellen sind wichtig um hochwertige Elektronenbeugungsbilder zu erzeugen, wobei die Intensität ausreichend sein muss um durch Invertierung den Ortsraum zeitabhängig darstellen zu können. Das zweite Kapitel beschreibt die Konstruktion eines neuartigen pulsstreckenden Hochleistungsfaseroszillators mit einer Ausgangsleistung von 300 mW bei 31 MHz, dessen Pulse bis unterhalb 90 fs komprimiert werden können. Im dritten Kapitel wird die Konstruktion eines regenerativen Festkörperverstärkers beschrieben, der für Pulsenergien über 1 mJ entwickelt wurde, wobei bereits 0.4 mJ erreicht werden konnten. Neuartige Simulationstechniken wurden untersucht, um die Konstruktion des Verstärkers zu unterstützen. In Kapitel 4 wird eine neue, schnelle und mächtige Theorie hergeleitet, die auf mehrdimensionale zeitabhängige nichtlineare Schrödingergleichungen in einer verallgemeinerten Form angewandt wird. Die neue Methode kann komplizierte Terme innerhalb dieser Gleichungen modellieren, wobei sie andere Methoden in ihrer Leistungsfähigkeit bezüglich numerischen Fehlern und Geschwindigkeit übertrifft. Diese Vorteile werden durch die Anwendung von Fourier Methoden erreicht. Damit wurde ein Hilfsmittel für die Simulation von Weißlichterzeugung mit Hilfe dieser Numerik erstellt. Die Simulation stimmt außerordentlich gut mit publizierten experimentellen Daten überein, und ist eine Verbesserung im Vergleich zur herkömmlichen Methoden. Die Verwendung des Hilfsmittels ermöglicht genaue Berechnungen von Kontinuums- oder Weißlichterzeugung, wie sie für verschiedene experimentelle Protokolle benötigt wird und als Einspeisung für die Erzeugung von breitbandigem kohärentem Licht dient.

Diese Arbeit löst das Problem, innerhalb eines vorgegebenen Wellenlängenbereichs die Erzeugung von Kontinuumslicht vorhersagbar zu konzipieren. Diese Information wird im Gesamtzusammenhang der Laserentwicklung für die kohärente Kontrolle von Molekülen im Infrarotbereich benötigt, um neue lichtinduzierte Quellen für molekulare Dynamik zur Verfügung zu stellen. Diese werden essentiell sein, um chemische Reaktionsdynamik zu erforschen.

Compact and stable ultrafast laser sources for electron diffraction experiments are the first step in accomplishing the dream experiment of producing a molecular movie. This thesis work focuses on developing new robust laser sources to enable arbitrary scaling in laser repetition rate, pulse energy, duration and stability as needed to provide sufficient integrated detected electrons for high quality diffraction patterns that can be inverted to real space movies. In chapter 2, the construction of a novel stable and high power stretched pulse fiber oscillator outputting 300mW at 31 MHz and compressible pulses to below 90fs will be described. Chapter 3 will describe the construction of a solid-state regenerative amplifier that was developed to achieve pulse energies above 1mJ with 0.40 mJ already achieved at 1 kHz. Novel simulation techniques were explored that aided the construction of the amplifier. Chapter 4 derives a new, fast and powerful numerical theory that is implemented for generalized non-linear Schrodinger equations in all spatial dimensions and time. This new method can model complicated terms in these equations that outperforms other numerical methods with respect to minimizing numerical error and increased speed. These advantages are due to this method's Fourier nature. A simulation tool was created, employing this numerical technique to simulate white-light generation in bulk media. The simulation matches extremely well with published experimental data, and is superior to the original simulation method used to match the experiment. The use of this tool enables accurate calculations of continuum or white light generation as needed for different experimental protocols and serves as the primary input to generate wide bandwidth coherent light.

This work has solved the problem of predictably designing continuum generation within targeted wavelength ranges. This information is needed as part of an overall scheme in laser source development to coherently control molecules in the IR region to provide a new photo trigger source for molecular reaction dynamics that will be essential to explore chemical reaction dynamics in general.

List of Selected Publications

1. Chen, Hung-Wen, Zia, Haider, et al. "Yb-fiber oscillator based, few-cycle ultrafast source at 850nm." *Lasers and Electro-Optics Pacific Rim (CLEO-PR), 2013 Conference on*. IEEE, 2013.

2. Chen, Hung-Wen, Zia, Haider et al. "3 GHz, Yb-fiber laser-based, few-cycle ultrafast source at the Ti: sapphire laser wavelength." *Optics letters* 38.22 (2013): 4927-4930.

3. Casandruc, Albert, et al. "A novel fiber tip based electron source." *Vacuum Nanoelectronics Conference (IVNC), 2014 27th International*. IEEE, 2014.

4. Casandruc, Albert, et al. "Fiber tip-based electron source." *Journal of Vacuum Science & Technology B* 33.3 (2015): 03C101.

5. Zia, Haider, et al. "Full (3+ 1) D Split-Step Technique for Spatial Mode Analysis of White Light Generation in Bulk Kerr-Media." *CLEO: QELS_Fundamental Science*. Optical Society of America, 2015.

6. Zia, Haider, et al. "Updated Strang Symmetrized Fourier Method to Solve a Larger Class of Generalized Non-linear Equations". *TBP*.

7. Zia, Haider, et al. "Novel Full (3+1)D Split-Step Fourier Method Used to Simulate White Light Generation in Bulk Kerr-Media". *TBP*.

8. Zia, Haider, et al. "White-Light Beam Shaping Simulations for Seeding in Downstream Optical Elements". *TBP*.

Contents

Acknowledgements

I would like to thank Dwayne Miller, my supervising professor for the many discussions, ideas and lessons that I have learned from him. His insights and the free flow of ideas that could be discussed helped in my inspiration and developed my understanding and love for science. I would also like to thank Franz Kaertner who supervised me during my time as a visiting student in his group at MIT. I found his openness and acceptance a very great help during my stay.

I would also like to thank Noah Chang and Hung-Wen Chen for the help in the construction of the fiber laser, their ideas and for the friendship that has developed over the many years. I will miss the many scientific discussions we had during my stay at MIT and at CFEL. They will always be gurus for me in the domain of fiber lasers and general optics

Others that have helped me over my various projects and deserve a personal thank you are: Rolf Loch who helped me build up the regenerative amplifier, Gunther Kassier, Robert Buecker, and Albert Casandruc who I collaborated on with photoemission experiments. I would also like to thank Regis Gengler and Daniel Badali who I originally worked with when I first started my doctorate studies.

Axel Ruehl and Ara Choudhuri recruited me to the problem of simulating white-light generation and showed me the relevant equation that needed to be simulated. It was from that discussion that I started my journey that culminated in chapter 4 of this thesis. As well, Ara set up a skeleton structure of the Matlab script of my numerical technique that was further developed into working code by me. I keep her subroutine titles and program organization as a nice reminder of a lovely and entertaining friend who shared my office over these years.

Peter Kroetz introduced me to the question of using the Franz-Nodvik algorithm for pumping simulations instead of pulse amplification simulations. Directly because of this discussion, I found a way to update the Franz-Nodvick algorithm to cover this case as well.

I would also like to thank in no particular order, Liu Wei, Anne-Laure Calendron (who helped in the pre-stages of the amplifier design), Huseyin Cankaya, Damien Schimpf, Djordje Gitaric, Josef Gonschior and Stephanie Manz.

Finally I would like to extend my deepest thanks and gratitude towards my parents Aftab, Amira and my sister Dunya for their love and support throughout the years and for fostering my scientific interest in the world. I thank Caroline as well for her understanding and support especially during the writing of my thesis.

List of Figures:

Chapter 2

Chapter 3

Chapter 4

List of Tables

Chapter 2

Chapter 3

Chapter 4

Chapter 1: Introduction

This thesis work is dedicated to the development of novel laser sources to cover all required excitation conditions of matter as needed for femtosecond electron diffraction experiments geared towards capturing atomic motions in real time. To this objective, there are both laser excitation conditions, arising from the photochemistry needed to trigger the atomic motions of interest and laser conditions needed to obtain suitable electron sources with sufficient brightness to view these atomic motions. This thesis work focuses on providing a robust flexible laser platform to provide the trigger sequences for the so-called molecular movies.

As further background to the significance of this objective, it needs to be appreciated that the direct observation of atomic motions during a chemical reaction is a dream experiment for physicists and chemists[1]. Significant progress has been made by time resolved electron diffraction experiments[1-7]. The experiment at its core, analyzes the scattered pattern of electrons being launched at a sample undergoing a chemical change. From the changes of the scattered pattern, timescales of structural changes in the material can be deduced. In order to accomplish such an experiment, electron pulses are created from a pulsed laser source interacting with a photocathode[1,7]. Electrons are emitted if the incoming photons have energies above the work function of the metal. These electron bunches then propagate towards the sample. By delaying the arrival time of this electron bunch one can deduce the differences in the average atomic structure of the material over the electron pulse duration (fs) at different time points. This is equivalent to the delay imposed by looking at the corresponding differences in the diffraction pattern[7]. The electron bunch duration must be substantially shorter than the timescale of the chemical reaction so distinct time points in the delay period can be recorded. Under appropriate conditions in electron extraction and propagation to the sample, the bunch duration can be made to approximate the duration of the laser pulse exciting the electrons from the photocathode. To properly resolve interesting chemical dynamics, the electron pulses should be substantially less than the chemical reaction timescale being on the order of 100 fs to 1 ps [2]. The laser excitation pulse must be tuned to specifically trigger the processes of interest and also must be shorter than the time scales of interest.

The molecule must undergo a chemical reaction at the appropriate time starting at the arrival of the first electron bunch at the sample. Otherwise, the delay interval may miss the chemical reaction entirely[7]. If a sample can be optically pumped, the sample is activated by a photo-transition by intensity from the same laser pulse used for the electron pulse generation, following nonlinear conversion to the appropriate excitation wavelength[7]. Thus, time zero of the chemical reaction in relation to the first electron bunch in the series can be determined with effectively zero time jitter in establishing the ensuing molecular dynamics. This experiment is accordingly named a pump-probe experiment (electron probe and optical sample pump).

As one can see, the burden on the laser source in temporally resolved electron diffraction experiments is of utmost importance. In order to develop new electron diffraction sources and experiments, the laser system must be optimized for this particular class of experiments. Solid-state femtosecond laser sources such as the Ti:Sapphire laser have been used in previous experiments. However, the stability of such oscillators, the performance of the oscillator over time and the temporal and spatial quality of the outgoing laser radiation poses several disadvantages compared to new laser oscillator technologies such as fiber oscillators.

The main topic of this thesis will be to develop new laser sources that are tailor made for electron diffraction experiments. These sources include systems that were built up (Chapter 1 and Chapter 2)

that have never before been used in electron diffraction experiments and new theoretical models and numerical tools that were derived to explore solutions of the optical sources that overcome previous constraints in excitation wavelengths in previous pump-probe experiments.

In Chapter 2, a novel stretched pulse non-linear polarization mode-locked fiber laser was designed and shown to be a viable source for electron diffraction experiments. The importance in the design of this fiber oscillator for electron diffraction experiments is to minimize the phase and amplitude noise present in the optical waveform so that it can be a stable source for generating electron pulses through photo-emission at a cathode, as well as pumping the sample. Any amplitude or repetition rate (rep. rate) deviations existent in the optical pulse train will be directly mapped onto the electron bunch; any spatial distortions in the optical pulse will map onto spatial distortions in the electron bunch and can influence electron bunch properties such as emittance, bunch charge, etc [1,4,7]. A stable system must minimize the contributions of mechanical noise present in non-optics labs since this laser must operate under such conditions in the presence of vacuum pumps and related mechanical movements involved in sample exchange. Finally, the footprint of the oscillator should be minimized as it will be in a lab primarily focused on electron diffraction experiments and thus, space for optics will be scarce. Since fiber can be rolled up or bent into space minimizing configurations fiber oscillators are ideal for seeking a low footprint option. Additional arguments for why fiber oscillators are more stable and results are found in Chapter 1.

Chapter 3, focuses on the system that was built to amplify stable oscillator pulses to energies in the range of half a milijoule. The initial pulse energy from the oscillator and fiber pre-amplifier stages is insufficient for downstream generation of the needed laser excitation wavelengths via nonlinear conversion. There are minimum requirements for the electron injection process. For typical experiments, the number of electrons needed to resolve diffraction peaks and to be adequately over the noise floor of the multi-channel phosphor (MCP) detectors must be on the order of 10^5 to 10^6 electrons/bunch[4]. Also, the quantum efficiency, meaning the number of photons needed to generate one electron from the photo-emitter needs to be considered and can translate to a high loss factor[8]. A typical 2nd harmonic generation scheme in BBO carries an efficiency on the order of ~20-30%. Thus, two cascaded 2nd harmonic generation schemes from 1.03 μm in BBO crystals carries an overall efficiency roughly on the order of ~4%*. To also account for losses and different experimental schemes, a >300 μJ 1.03 μm source is required while 1mJ is preferred. Camera shutter speeds used in these electron diffraction experiments usually perform well with exposure times on the order of 10ms. Therefore, an overall repetition rate in the kHz range or less is adequate for the experiment.

A solid state regenerative amplifier was built and described in this chapter. The novel combination of a fiber oscillator for pulse stability right from the source and a solid-state amplifier is ideal for electron diffraction experiments, the reasons of which will also be described in the chapter. The novelty in this chapter includes the simulation techniques used in the construction of the regenerative amplifier and the design.

Chapter 4, changes track from the first two chapters. Instead of the building of a source, a new type of tool was created to aid in the design of laser sources for electron diffraction experiments. While, discussion in chapter 1 and 2 has centered on the laser sources needed to pump out electrons from the photocathode, the photo-transition dynamics of the sample have been ignored. To channel energy in a coherent way as to guide a chemical reaction along a pathway is a scientific dream that goes hand in hand with the first one described here[9-16]. For example, the prospect of specifically exciting certain vibrational modes to drive chemical reactions is one important application[17].

However, in order to do this, a wide wavelength bandwidth of light must be generated and must be coherently locked to each other (for example, see 13,14) . That is, each pulse of light centered at different wavelengths must interact with the sample at set relative time intervals. To generate such a coherent wide bandwidth, optical methods using so-called white-light generation in bulk must be explored. However, to fine tune the white-light generation, extensive simulations and theoretical modelling must be carried out. Chapter 4, derives a novel methodology to accurately simulate white-light generation in bulk, over all spatial dimensions and time, with various linear and non-linear terms and the presence of plasma generated from the optical radiation. The general methodology to treat these highly nonlinear multidimensional problems is novel and is derived for the first time in this thesis. It is shown in Chapter 4 that results of the simulation matches almost exactly with experimental data.

In addition to the above focused laser development work, there were experiments conducted that explicitly used the laser sources described herein. These experiments are outside the scope of the thesis but are important developments in their own right. For completeness regarding describing my PhD research activities, these include:

1. The fiber source that was developed was used in an electron diffraction experiment using fiber terminated with a photocathode. Light was propagated in the fiber structure after the oscillator and was channeled to a photocathode. As well, the fiber was pulled to a 200nm tip (NSOM fiber). The experiment yielded thermal electron emission from this novel fiber tip source. More details can be found in [18].
2. Also, the fiber source was used in generating Cherenkov radiation in photonic crystal fiber to generate an octave spanning supercontinuum. The supercontinuum pulse was then compressed to sub 11fs. A short summary and reference can be found in chapter 2.

The above applications highlight the utility of the laser development work conducted during the course of this thesis work.

*Value that is experimentally obtained for an aligned setup.

Chapter 1 Bibliography

1 Miller, RJ Dwayne. "Mapping atomic motions with ultra-bright electrons: The chemists' Gedanken experiment enters the lab frame." *Annual review of physical chemistry* 65 (2014): 583-604.

2 Sciaini, Germán, et al. "Electronic acceleration of atomic motions and disordering in bismuth." *Nature* 458.7234 (2009): 56-59.

3 Harb, Maher, et al. "Electronically driven structure changes of Si captured by femtosecond electron diffraction." *Physical review letters* 100.15 (2008): 155504.

4 Siwick, Bradley J., et al. "Ultrafast electron optics: Propagation dynamics of femtosecond electron packets." *Journal of Applied Physics* 92.3 (2002): 1643-1648.

5 Siwick, Bradley J., et al. "An atomic-level view of melting using femtosecond electron diffraction." *Science* 302.5649 (2003): 1382-1385.

6 Siwick, Bradley J., et al. "Femtosecond electron diffraction studies of strongly driven structural phase transitions." *Chemical Physics* 299.2 (2004): 285-305.

7 Dwyer, Jason R., et al. "Femtosecond electron diffraction:'making the molecular movie'." *Philosophical Transactions of the Royal Society of London A: Mathematical, Physical and Engineering Sciences* 364.1840 (2006): 741-778.

8 Henneken, H., et al. "Quantum efficiencies of gold and copper photocathodes in the VUV and X-ray range." *Metrologia* 37.5 (2000): 485.

9 Prokhorenko, Valentyn I., et al. "Coherent control of retinal isomerization in bacteriorhodopsin." *Science* 313.5791 (2006): 1257-1261.

10 Prokhorenko, Valentyn I., Andrea M. Nagy, and RJ Dwayne Miller. "Coherent control of the population transfer in complex solvated molecules at weak excitation. An experimental study." *The Journal of chemical physics* 122.18 (2005): 184502.

11 Prokhorenko, Valentyn I., et al. "On the mechanism of weak-field coherent control of retinal isomerization in bacteriorhodopsin." *Chemical Physics* 341.1 (2007): 296-309.

12 Prokhorenko, Valentyn I., Alexei Halpin, and RJ Dwayne Miller. "Coherently-controlled two-dimensional photon echo electronic spectroscopy." *Optics express* 17.12 (2009): 9764-9779.

13 Nagy, Andrea, Valentyn Prokhorenko, and RJ Dwayne Miller. "Do we live in a quantum world? Advances in multidimensional coherent spectroscopies refine our understanding of quantum coherences and structural dynamics of biological systems." *Current opinion in structural biology* 16.5 (2006): 654-663.

14 Goswami, Debabrata. "Optical pulse shaping approaches to coherent control." *Physics Reports* 374.6 (2003): 385-481.

15 Brumer, Paul, and Moshe Shapiro. "Laser control of molecular processes." *Annual review of physical chemistry* 43.1 (1992): 257-282.

16 Seideman, Tamar, Moshe Shapiro, and Paul Brumer. "Coherent radiative control of unimolecular reactions: Selective bond breaking with picosecond pulses." *The Journal of Chemical Physics* 90.12 (1989): 7132-7136.
17 Discussions with R.J Dwayne Miller.

18 Albert Casandruc, thesis. TBP.

Chapter 2: The Design of a Stretched Pulse Normal Dispersion Regime Fiber Ring Oscillator Utilizing Non-Linear Polarization Rotation (NPR) for the Mode-locking Mechanism

During the course of this PhD work, two NPR fiber oscillators, duplicates of each other, were constructed for electron diffraction experiments. This chapter will compare fiber oscillators over other oscillator designs and explain why fiber oscillators were chosen. Also, the chapter will introduce the theory for the non-linear pulse evolution within such oscillators.The emphasis of this chapter will be on the experimental results for the novel oscillators developed in this work and on repeatable recipes used in the construction of these laser systems.

2.0 Advantages of Fiber Oscillators and Design Criteria for Electron Diffraction Experiments

As mentioned in the introduction, laser oscillators are fundamental to electron diffraction experiments, and novel technologies must be explored to improve electron diffraction setups. To begin with, laser oscillators are the primary source of ultrafast optical pulses and thus are the primary source of error in optical configurations. As the reference signal, these setups must be stable in repetition rate (rep. rate), amplitude and spatial profile of the pulse. In some applications the carrier-envelope phase (CEP) of the optical pulse must be locked together (CEP stability).

There are two main types of oscillators that are used in the field: solid-state oscillators and fiber oscillators. Solid-state oscillators employ free space cavities that are essentially non-continuous waveguides constructed with the use of optical elements at points in the cavity. It is useful to think in the picture of Gaussian optical-beam propagation when analyzing these cavities and applying the results of the ABCD matrix formulation [1]. There is an overall ABCD matrix that governs any free space cavity, and there are only at most two confined Eigen modes (two in the transverse and two in the saggital planes) since ABCD matrices are 2X2 matrices. Due to the low number of Eigen modes allowed, for the design of such cavities the region of stability in the overall parameter space must be large to tolerate environmental external forces and noise. As the cavity elements fluctuate in space, the cavity Eigen modes have to be allowed to fluctuate in a continuous manner. Mechanical noise is mapped onto the Eigen mode spatial distributions. Issues such as pump-signal overlap in the gain medium must be accurately managed given environmental fluctuations. Beam deviation and pointing error within free space cavities due to temperature changes and mechanical noise can inhibit cavity lasing. Thus, without confining the beam in a continuous unchanging waveguide structure, spatial stability may be hard to manage.

The effects of mechanical noise fluctuations in the context of the previous paragraph are greatly reduced in all-fiber oscillators or close to all-fiber oscillators because the optical pulse is guided in a continuous wave guided structure. If the fiber waveguide moves, the signal will still be bound within the fiber and there will be no free-space pointing and alignment error.

The pump signal in the fiber gain medium for single-mode fiber always overlaps with the signal. In almost all-fiber ring oscillators, beam deviation present in the focusing optics can still be coupled into the fiber if the fiber NA allows this. Once coupled into the fiber, the beam is rectified and propagates in the same manner within the fiber (particularly for single-mode fibers), thus, any memory of beam deviation is lost but at the expense of power loss due to the degraded coupling efficiency. However,

the power loss is recuperated due to the nearly perfect and constant pump and beam alignment, so even this coupling error is negligible. The cavity can still maintain the pulse and the lasing as compared to the effect of free space pointing error in solid state lasers. Therefore, fiber oscillators output high-quality optical beams and can recuperate from parasitic environmentally induced strains.

Heat management in fiber systems is superior to that of free-space oscillators. Heat is distributed along the length of the entire cavity, and because of the higher surface-to-volume ratio [2], local hotspots are diffused along the fiber length, eventually diffusing out through the increased surface area contact with air or cooling structures. In solid-state laser cavities, hotspots within the optical elements inherently change the placement of these elements and the cavity size, producing phase noise instabilities, for example. Thermal lensing in the gain crystal can cause spatial aberrations in the optical pulse and loss of cavity confinement. Fibers are much better at maintaining cavity confinement even with the presence of thermal lensing due to the wave-guiding nature and the thermal management.

From single-mode fiber oscillators a steady Gaussian spatial mode can be produced [3] because it is the only confined mode possible and higher-order modes are not guided (see section 2.1.1). The confinement offers another advantage: due to the confined smaller spot-size the peak intensity of the signal and pump are higher. Therefore, the pumping rate is higher (offering the ability to scale to high rep. rates) and the absolute gain level is higher for single-pass fiber amplifiers. Thus, higher output efficiencies can be achieved in fiber lasers. For example, rep. rates up to 10GHz [4-7] were reported in fiber designs. A 3Ghz fiber oscillator was used in the creation and compression of stable large-bandwidth supercontinuum pulses generated in photonic crystal fiber through Cherenkov radiation[8].

Because the optical pulse is propagating in a waveguide, nonlinearities arise due to an intensity dependence of the refractive index, which can contribute to many parasitic or beneficial effects such as self-focusing[9,10], self-phase modulation[11,12],self-steepening[13] and wave-breaking[14,15].

Self-focusing, self-steepening and wave-breaking provide limitations in fiber oscillator designs. For example, with self-focusing, the pulse can be focused within the fiber such that the peak intensity of the optical pulse exceeds the threshold for plasma formation. This causes a plasma filament to occur and can damage the fiber. Confinement can be lost due to the smaller spot size and higher numerical aperture (NA) in the fiber needed to contain the mode.

The fiber also introduces dispersion due to the frequency dependence of the refractive index values. If dispersion is not managed, the confined pulse continuously broadens in time and reduces its amplitude. Hence, dispersion must be managed in any stable fiber oscillator, which will be discussed later in this chapter.

Finally, fiber is very delicate and can break easily, especially along splice points where different fibers are connected. In non-controlled environments special protections must be in place for these fiber oscillators. The advantages and disadvantages of fiber oscillators as compared to free-space solid-state oscillators are given and summarized in table 1.

Advantage	Fiber Oscillator	Free-Space Cavity Oscillators
Phase Noise	Rep. Rate is stabilized because the influence of mechanical vibrations on fiber systems is less than that of solid-state systems.	
Amplitude Noise	Fiber is at an advantage because of pump signal overlap in the gain medium and high peak intensities.	
Spatial mode stability	Fiber is at an advantage because of continuous mode filtering and a confined single-mode within the cavity	
Power limitation/ Propensity for parasitic Non-Linearity		Free space cavity has an advantage because of reduced gain crystal length. Preventing parasitic non-linearities.
Scaling to higher rep.rates at constant pump power	Due to pump confinement a faster possible gain recovery, Scaling to higher rep-rates up to 10 Ghz is achievable[4-7].	
Extracted Efficiency	Due to confined modes, and high peak intensities extracted energy efficiency is higher.	
Gain Recovery	Gain recovery is faster (due to high intensity confined pump mode) and ASE noise is limited due to longer inversion lifetimes in fiber	

Table 1: Main advantages of fiber oscillators over free space oscillators.

The aforementioned power limitations can be managed by optical amplifying stages such as regenerative amplifiers[16] and large-core fiber amplifiers[17] placed after the oscillator. Extensive literature exists in how to design such systems and thus, solutions exist to counter the power limitations at the oscillator stage. The regenerative amplifier used in the laser system designed here will be discussed extensively in the next chapter.

Fiber development has been significantly enhanced by the telecommunication industry. Signal propagation in the infrared bands is favored due to the low attenuation with current fiber fabrication technology[20]. Single-mode fiber operation is also easier at higher wavelengths. Thus, it would be prudent to design a fiber system in the telecommunication bands due to the availability of fiber technology already developed from industry. However, according to table 2 the O-band is the minimal infrared wavelength used in the telecom industry, which is too far away from 266 nm. Generating a UV higher harmonic, a design constraint for electron diffraction experiments, is rather difficult using telecom wavelengths.

Band	Wavelength
O	1260–1360 nm
E	1360–1460 nm
S	1460–1530 nm
C	1530–1565 nm
L	1565–1625 nm
U	1625–1675 nm

Table 2 Prominent telecommunication bands for fiber optic systems[21]

However, due to the prominence of fiber amplifier technology, extensive doping techniques exist for the production of gain fiber from rare-earth metals such as ytterbium, erbium, neodymium and thulium. From, the absorption and emission cross section presented in fig. 1**,** it is seen that there is an emission peak at 1.03 µm for ytterbium doped fibers. Ytterbium doped fiber can theoretically produce a lasing output at 1.03 µm. The output can be converted to the 257 nm harmonic, its 4th harmonic, with the use of 2 second harmonic generation conversion stages. This lies above the band gap energy of most photocathode materials used in electron diffraction experiments. This technology exists in abundance in industry because of the ease of generating visible radiation through harmonic up-conversion from this wavelength and since a rare-earth doping method exists for ytterbium. Therefore, designing an ytterbium based fiber ring oscillator is advantageous for meeting the lab design criteria.

In the following section, a brief theoretical overview will be presented for the various processes that were used in building the 1.03 µm fiber ring oscillator source. References that guided in the source design were [22,29, 30].

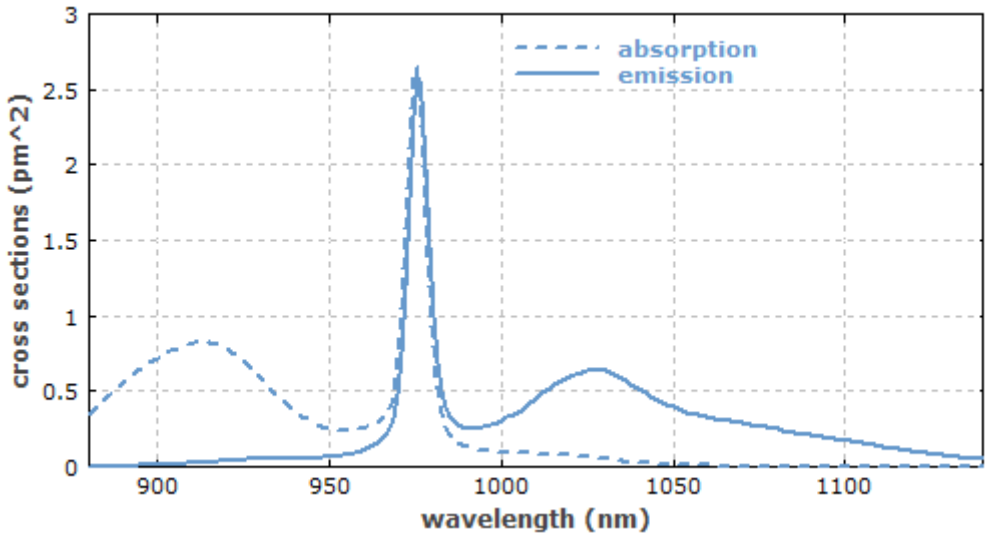

Figure 1: Taken from [23]. Absorption and emission cross sections for the relevant wavelength range of Ytterbium-doped germanosilicate used in the cores of Yb doped fiber.

2.1 Theoretical Considerations

This section will discuss the theoretical underpinnings for oscillator systems in general, and specifically fiber oscillators. In order to understand the dynamics of the oscillators that were built, it is first necessary to introduce the theory of pulse propagation in fiber structures, the 1-D non-linear Schrödinger equation and specific solutions relevant to fiber lasers. Also the concept of, dispersion, and mode-locked lasers with real and virtual saturable absorbers (SA) will be discussed extensively. Parts of this theory will be presented in more detail in subsequent chapters and thus, only a brief introductory treatment will be made here.

2.1.1 Pulse Propagation in Fiber Structures

The fiber used in the construction of the oscillator is a cylindrical waveguide consisting of a "core" and a "cladding". The cladding encloses the core in a torus structure. The core is at a slightly higher refractive index than the cladding. Thus, there is a critical angle between the core-cladding interfaces for which any ray at the critical angle or higher in relation to the propagation axis will undergo total internal reflection and remain in the core. The light can be efficiently transported through the fiber. There are different propagation pathways possible for rays at different launch angles at the fiber input. Each pathway can be viewed as a confined mode of the fiber in the simple ray picture [25] (see, fig. 3).

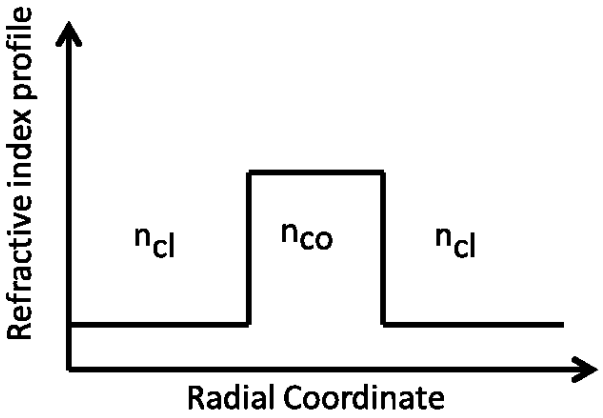

Figure 2: Example of a core cladding refractive index profile in the radial coordinate.

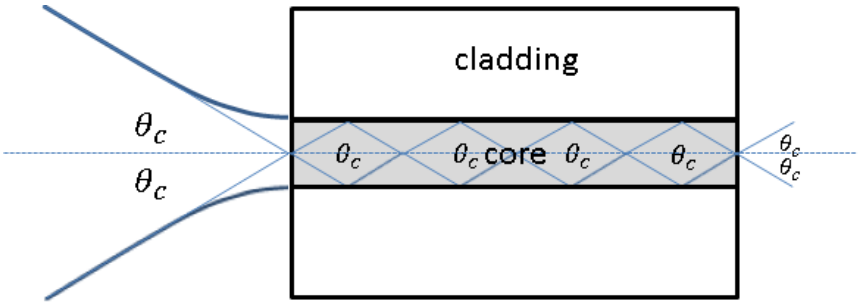

Figure 3: Momentum Ray diagram indicating total internal reflection in the fiber. For paraxial Gaussian beams the asymptotic divergence angle of the spatial distribution corresponds to the highest momentum angle in the Gaussian beam momentum representation. The mode at the end of the fiber, if

Gaussian like (i.e., single mode) will expand out to asymptotic divergence angle limit set by the critical angle.

The modal structure of propagating confined electromagnetic radiation in the fiber becomes clear once the corresponding Maxwell's wave equation is derived for such a cylindrical waveguide. For the radial step-index profile presented in fig. 2 the following wave equation in cylindrical coordinates can be derived. The derivation is a summary of what is discussed in Chapter 8 of [24]:

$$\frac{\partial^2 \mathrm{U}}{\partial \mathrm{r}^2} + \frac{1}{\mathrm{r}}\frac{\partial \mathrm{U}}{\partial \mathrm{r}} + \frac{1}{\mathrm{r}^2}\frac{\partial^2 \mathrm{U}}{\partial \varphi^2} + \frac{\partial^2 \mathrm{U}}{\partial \mathrm{z}^2} + \mathrm{n}^2 \mathrm{k_o}^2 \mathrm{U} = 0 \tag{1}$$

Where U is the electric or magnetic field, $\mathrm{n} = \mathrm{n_{core}}$ for $\mathrm{r} < \mathrm{a}$ and $\mathrm{n} = \mathrm{n_{cladding}}$ for $\mathrm{r} > \mathrm{a}$. $\mathrm{k_o}$ is the free space wavenumber.

The boundary conditions require that at $\mathrm{r} = \mathrm{a}$, $\mathrm{U_{cladding}} = \mathrm{U_{core}}$ and $\frac{\partial \mathrm{U_{cladding}}}{\partial \mathrm{r}} = \frac{\partial \mathrm{U_{core}}}{\partial \mathrm{r}}$.

The family of bound guided paraxial (i.e., confined to small momenta angles about the propagation, z axis) solutions that are relevant to most applications of fiber waveguides can be expressed as:

$$\mathrm{U}(\mathrm{r}, \varphi, \mathrm{z}) = \mathrm{u}(\mathrm{r}) \mathrm{e}^{\mathrm{i}l\varphi} \mathrm{e}^{\mathrm{i}\beta \mathrm{z}} \tag{2}$$

Where, $l = 0, \pm 1, \pm 2, \ldots$. l is the angular momentum wavenumber. β is the effective z propagation wavenumber, which will be discussed later in this section, and:

$$\mathrm{u}(\mathrm{r}) \propto \begin{cases} \mathrm{J}_l(\mathrm{k_{co}} \mathrm{r}), & \mathrm{r} < \mathrm{a} \\ \mathrm{K}_l(\mathrm{k_{cl}} \mathrm{r}), & \mathrm{r} > \mathrm{a} \end{cases} \tag{3}$$

Where, J is the first Bessel function of order l and K is the modified second Bessel function of order l.

The effective radial wavenumbers $\mathrm{k_{co}}, \mathrm{k_{cl}}$ are given in terms of β as:

$$\mathrm{k_{co}}^2 = (\mathrm{n_{co}} \mathrm{k_o})^2 - \beta^2 \tag{4}$$

$$\mathrm{k_{cl}}^2 = (\mathrm{n_{cl}} \mathrm{k_o})^2 - \beta^2 \tag{5}$$

Only a restricted set of $\mathrm{k_{co}}, \mathrm{k_{cl}}$ are possible solutions that satisfy the continuous boundary conditions for the electromagnetic field as introduced above. By determining this set of possible values of $\mathrm{k_{co}}$ and by using Eq. (4) β can be fully determined. The procedure to do this is outlined below.

From the aforementioned boundary conditions it follows:

$$\mathrm{k_{co}} \mathrm{a} \frac{J_{l \pm 1}(\mathrm{k_{co}} \mathrm{a})}{J_l(\mathrm{k_{co}} \mathrm{a})} = \pm \mathrm{k_{cl}} \mathrm{a} \frac{K_{l \pm 1}(\mathrm{k_{cl}} \mathrm{a})}{K_l(\mathrm{k_{cl}} \mathrm{a})} \tag{6}$$

It can be verified that:

$$\mathrm{k_{co}}^2 + \mathrm{k_{cl}}^2 = (\mathrm{n_{co}}^2 - \mathrm{n_{cl}}^2) \mathrm{k_o}^2 = constant = \frac{\mathrm{V}^2}{\mathrm{a}^2} \tag{7}$$

Plotting the left hand side (LHS) vs the right hand side (RHS) with respect to k_{co} , using Eq. (5) to find the corresponding k_{cl} and finding the intersections obtains a set of possible solutions for k_{co}, k_{cl} . k_{cl} is restricted to being strictly real or otherwise, the bound condition of the solution is violated, leading to propagating radial waves in the cladding. k_{co} must be real to prevent propagating waves in the core. Thus, the maximum value of $k_{co} = ((n_{co}{}^2 - n_{cl}{}^2)k_o{}^2)^{0.5}$. The points of intersection yield unique values of k_{co} which are denoted as k_{colm} $m = 1,2,3. etc$. It can be shown that, -*l* and *l* yield the same spatial mode amplitudes and values of k_{co}. A mode can be described with the integer set *l,m*. The constant on the RHS of Eq. (7) can be described as a parameter that limits the points of intersection and the possible modes at a given *l*. This is due to the real limitation on k_{co} thus creating the condition that $k_{co} < \frac{\sqrt{V}}{a}$. While the above Maxwell's equation is a scalar equation, it can be assumed that the modes are TE modes. This is because of the fact that these modes are under the paraxial approximation, where the transverse components of the mode wavenumbers are small. Therefore, the polarization state of each momentum vector (which in bound-charge isotropic media is always in the plane perpendicular to each momenta vector) is roughly always perpendicular to the propagation direction.

The V parameter given in Eq. (7) is important in controlling the amount of propagating modes that are confined in the fiber.

The number of modes existent in the fiber can be described as :

$$M_{\#} = \frac{4}{\pi^2}V^2 \tag{8}$$

For single mode operation from Eq. (8), the following condition can be concluded:

$$V = \frac{\pi}{2} \tag{9}$$

$$(n_{co}{}^2 - n_{cl}{}^2)^{\frac{1}{2}} = \frac{\pi}{2k_o a} \tag{10}$$

The cladding-core refractive index difference and the core size, a, constitutes the fiber design constraints. Using the Taylor series expansion for small ratios between cladding and core:

$$n_{co}(n_{co} - n_{cl}) \cong \frac{\pi}{2k_o a} \tag{11}$$

Knowing n_{co} and a one can solve for n_{cl}. The incoming mode momenta into the fiber must have angles to the fiber propagation axis that are below the critical angle for total internal reflection to be considered for confinement (see, Fig. 3). Solving Snell's law for the system, one can obtain:

$$\theta_c = \arcsin(NA) \tag{12}$$

$$NA = (n_{co}{}^2 - n_{cl}{}^2)^{\frac{1}{2}} \tag{13}$$

From the given fiber numerical aperture, lensing systems can be designed, to ensure proper coupling at the fiber's input.

While the above is valid as a powerful approximation for experimental setups, in order to calculate coupling efficiency between a general optical electric field distribution at the input of the fiber, an overlap integral will have to be performed[24].

For single mode operation, the approximately TE mode Bessel function within the core will consist of the central peak (its spatial period will be greater than twice fiber core size) and will be an attenuated function in the cladding, see Fig. 4. This effectively mirrors a Gaussian distribution and this will be denoted as a fiber single-mode Gaussian distribution.

The above modal analysis was for the monochromatic case, the wavelength range considered for the oscillator is within the relatively large single-mode bandwidth of the fiber. However, it is important to note that the modal-frequency dispersion and modal group velocity of the fiber will be different than the bulk material analogue and values specific to the fiber have to be considered instead.

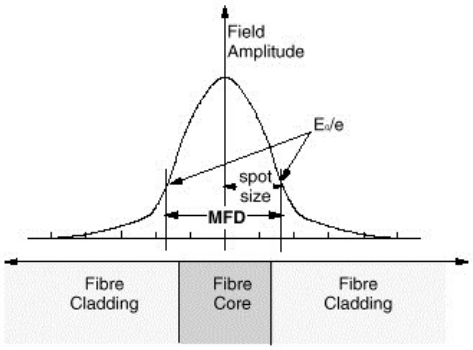

Figure 4: Mode-Field Diameter (MFD) of the approximately Gaussian distribution in single-mode fiber. Image obtained from [26].

2.1.2 1-D Nonlinear Schrodinger Equation

Of great importance to the study and understanding of fiber oscillators are the various linear and non-linear effects present as the optical pulse propagates within the fiber. The non-linear wave equation of interest can be derived from Maxwell's equations where the polarizability term has a non-linear dependence on the optical intensity of the propagating optical pulse. The derivation assumes a slow varying envelope approximation, meaning that the frequency bandwidth of the pulse is less than its central frequency[27]. In this section NLSEs that are of interest to the fiber oscillator system are presented. . The NLSE will be the central focus of chapter 4 and only a short description will be presented here. To start with, the simplified 1-D NLSE for the nonlinear propagation of a pulse through a medium in the one dimensional case without gain terms reads as [26]:

$$\frac{\partial U}{\partial z} = i\gamma|U|^2U - i\frac{\beta_2}{2}\frac{\partial^2 U}{\partial \tau^2} \tag{14}$$

Where, only the second order dispersion is included. γ is related to the nonlinear refractive index (n_2) and accounts for self-phase modulation (SPM) which is an effect that describes the frequency broadening of the pulse (intensity dependent additive phase in the time domain) because of the intensity dependent nature of the refractive index[28]. U is the normalized (to peak electric field amplitude) envelope amplitude, τ is time, defined in the travelling frame of the pulse (time window

travelling at the group velocity of the original optical pulse), and z is the propagation direction of the optical pulse.

For restricted 1-D systems such as the fiber systems being considered,

$$\gamma = \frac{n_2 \omega_o}{c A_{eff}} \tag{15}$$

ω_o is the central frequency, c is the speed of light in free space, A_{eff} is the effective mode area (i.e., the core size of the fiber).

For fibers there are two classes of solutions to Eq. (14) that are interesting to explore; namely, the so-called solitons and similaritons. In practice, both pulses can appear so the theory of both will be discussed. Solitons are pulses that maintain their amplitude profile save for an overall phase term as they propagate through the medium. Because of this property, solitons can be viewed as an Eigen-mode like solution to the non-linear equation. Solitons are generated due to the competition between SPM and dispersion. As the pulse propagates in a normal dispersive medium (meaning the refractive index decreases w.r.t wavelength) with negative n_2, second order dispersion would chirp the pulse in such a manner that bluer frequencies would head to later times of the pulse while redder frequencies will gravitate towards earlier times in the pulse. However, SPM generates instantaneous frequencies as [32] :

$$\omega_{afterSPM} = \omega_{original} - \gamma \frac{\partial |U|^2}{\partial \tau} \Delta z \tag{16}$$

ω is the instantaneous frequency along the temporal profile of the pulse. Thus, at the start of the pulse the derivative term in Eq. (16) is overall positive and there will be a frequency shift towards the blue, while the back of the pulse sees a red frequency shift. Therefore, redder components at the front of the pulse shifted because of dispersion undergo a frequency shift to the blue and bluer frequencies at the back undergo a frequency shift towards the red. Under certain conditions this results in a net instantaneous frequency conversion of zero[33].

The soliton solutions are a stability point that naturally arises even if the input pulse is far from the soliton form. This is because of the fact that parts of the pulse that do not meet this balancing act, quickly disperse away and the wave breaks into a train of dissipative pulses and the solitons[29].

The unnormalized soliton solution has an envelope function in the form of [29]:

$$U_{soliton} = \sqrt{P_o}\,\mathrm{sech}\left(\frac{\tau}{\tau_o}\right) e^{i k_s z} \tag{17}$$

And has a hyperbolic secant (sech) time profile. P_o is the peak power of the soliton, τ_o can be found from Eq. (19) as the soliton pulse duration and:

$$k_s = \frac{|\beta_2|}{\gamma \tau_o} \tag{18}$$

In analogy to the Eigen-mode solutions of linear equations there are higher order soliton solutions. The order of the soliton governs the relation between peak power achieved and soliton duration. The relation is known as the soliton area theorem given as:

$$N^2 = \frac{\gamma P_o {\tau_o}^2}{|\beta_2|} \tag{19}$$

N is the soliton order. For fundamental solitons which are present in the fiber oscillator, N=1.

A note: solitons can exist in anomalous dispersion regimes (opposite of normal dispersion) only if n_2 correspondingly becomes positive. This maintains the restriction that SPM additive phase contributions balances with phase from dispersion.

It would be beneficial to use this effect in a fiber oscillator because of the short temporal durations achievable with solitons, the ease of generating solitons and the inherent resistance solitons have to pulse broadening in a medium. Thus, steady state pulse conditions can easily be sought with soliton solutions and stable fiber oscillator can be achieved. However, it will be seen that there is even a better class of solutions for fiber oscillators.

To conclude with the basic NLSE it is important to note that the higher-order dispersion may have to be considered (for example third order dispersion or TOD). To reflect these changes Eq. (14) becomes [36]:

$$\frac{\partial U}{\partial z} = i\gamma|U|^2U - i\sum_{n=2}^{\infty}\frac{\beta_n}{n!}\frac{\partial^n U}{\partial \tau^n} \tag{20}$$

$$\beta_n = \frac{\partial^n k}{\partial^n \omega}|_{\omega_o} \tag{21}$$

n=2 because the term describing the group velocity (the n=1 term) is already considered in the moving frame of reference and the overall phase term of n=0 can be neglected without any loss of generality. Since all pertinent effects depend on the relative phase variation in the optical envelope. This is also why the central frequency phase term is omitted and the envelope is only modeled.

The above analysis will now be extended to a more complicated 1-D NLSE that can be used to closer model the dynamics of the pulse evolution in the fiber oscillator and factoring in additional non-linear effects. Due to the gain term introduced by a pumped doped fiber, the unitary (i.e. conservative) NLSE above is modified to a non-unitary NLSE [29]:

$$\frac{\partial U}{\partial z} = i\gamma|U|^2U - i\frac{\beta_2}{2}\frac{\partial^2 U}{\partial \tau^2} + \frac{g}{2}U \tag{22}$$

The gain coefficient is a function of both time and propagation coordinate (z). It is coupled to ordinary differential equations that describe the gain evolution[34], with parameters described in Table 3:

$$g = (\sigma_{em} N_o n - \sigma_{ab} N_o (1 - n)) \tag{23}$$

$$\frac{dn}{dt} = \left(-\sigma_{em} n + \sigma_{ab}(1 - n)\right)N_o|A|^2 - \frac{nN_o}{T_{sp}} \tag{24}$$

Parameter Symbol	Description
g	gain coefficient (cm^{-1})
σem	Emission cross section (cm^2)
σab	Absorption cross section (cm^2)
N_o	Total electron density that can undergo inversion transition (cm^{-3})
n	Electron density in upper state manifold (cm^{-3})
$\|A\|^2$	Unnormalized $\|U\|^2$ in $(\frac{W}{cm^2})$
Tsp	Spontaneous emission time (s)

Table 3: Parameter explanation of Eq. (20)-(24).

The two manifold electronic transition systems considered for the gain evolution will be described in chapter 3. For now it is sufficient to state that Eq. (24) describes the evolution of electrons in a ground manifold to an upper state excited manifold. The derivative is over the proper time coordinate and not in the frame of the propagating optical pulse. The absorption and emission cross section are both functions of optical frequency (for example, see fig. 1) and thus, the instantaneous phase of the pulse in a region of time dictates what value these functions take. g and n are both functions of time and the propagation coordinate.

Equations (23) and (24) are solved iteratively, where $|A|^2$ obtained from the previous propagation slice of Eq. (20) is used to calculate the population inversion at the propagation slice (Eq. (24)**)** , which is used in turn to evaluate the gain Eq. (23), allowing to recalculate $|A|^2$ using Eq. (20) and the updated gain value for the present propagation slice and so forth.

However, for a single-pass amplification where the optical pulse signal is considered to be ultrafast (shorter than the gain relaxation time) it can be assumed that the gain coefficient is a constant in time. For a gain saturated system, it can also be assumed that the gain coefficient is constant in the propagation coordinate. This is deemed the parabolic approximation for the NLSE [29]. For small gain coefficients, the term can be treated as a perturbation on the NLSE. It has been demonstrated[35] that a class of solutions, called similariton solutions, can be obtained that propagate in a self-similar manner (meaning whose profile shape type remains the same in frequency and time). At $z \to \infty$:

$$A(z,\tau) = A_o(z)(1 - (\frac{\tau}{\tau_o(z)})^2)^{\frac{1}{2}} e^{i\varphi(\tau)z} \quad (25)$$

For $\tau > \tau_o(z)$,$A(z,\tau) = 0$.

$$\tau_o(z) = 3(g)^{\frac{-2}{3}}(\frac{\gamma\beta_2}{2})^{\frac{1}{3}}(E_p)^{\frac{1}{3}}e^{\frac{gz}{3}} \quad (26)$$

$$A_o(z) = 0.5(gE_p)^{\frac{1}{3}}(\frac{\gamma\beta_2}{2})^{\frac{-1}{6}}e^{\frac{gz}{3}} \quad (27)$$

$$\varphi(\tau,z) = \left(\frac{3\gamma}{2g}A_o(z)^2 - \frac{g}{6\beta_2}\tau^2\right)z \quad (28)$$

E_p is the inputted pulse energy. $\varphi(\tau,z)$ is represented in Eq. (28) without the arbitrary phase constant. The z varying phase is linearly chirped (i.e., linearly chirped k_Z wavenumber) and can be viewed as the propagation wavneumbers matching the instantaneous frequency.

The z varying amplitude term arises from gain being present as the pulse traverses z. The similariton pulse broadens exponentially as a function of z. The phase derivative describing the instantaneous frequencies as a function of time is a negative linear function of time. This indicates that frequencies are linearly increasing over the pulse width (positive linear chirp), which is the case in normal dispersion material that is considered here.

The similariton spectrum has a parabolic profile that mirrors the temporal envelope function.. The spectral extent corresponds to the end frequencies in the chirp described by the derivative of Eq.(28)**.** Past these end frequencies there is a sharp cutoff.

Since Similariton solutions exhibit a linear chirp, they can easily be compensated by simple dispersion management (i.e., a grating system). They are the predominant solution under gain perturbation at $z \to \infty$ which is the case when the laser is at steady state (and the circulating intracavity pulse has undergone many roundtrips). These points make these solutions very important for fiber lasers as they are the solutions in the asymptotic limit (in the steady state dynamics).

Because of the linear chirp that is exhibited by similariton solutions, the frequency distribution and time amplitude of the pulse are similar. In fact, it can be seen from the instantaneous frequency distribution that the time amplitude distribution is the frequency distribution at a z magnified by the ratio $\frac{g}{3\beta_2}$.

If the gain can be viewed as a weak perturbation of the cavity one would obtain a slightly perturbed soliton type pulse. Thus, the intracavity pulse can vary from a soliton at one end of the range to a similariton at the other end depending on dispersion management in normal dispersion media.

The final topic of discussion in regards to the NLSE is the effect of Kerr dependent polarization rotation within the fiber medium. It is in fact this mechanism that plays a large role in obtaining pulse formation within the cavity from initial start-up laser conditions and is the principle intensity dependent effect (a virtual saturable absorber) used in mode-locking the spectrum, as discussed in the next section.

The NLSE including cross phase polarization modulation terms, under the slowly varying approximation (high birefringence), reads as [36]:

$$\frac{\partial U_x}{\partial z} = -\frac{\Delta\beta_1}{2}\frac{\partial U_x}{\partial \tau} - i\frac{\beta_2}{2}\frac{\partial^2 U_x}{\partial \tau^2} + i\gamma\left(|U_x|^2 + \frac{2}{3}|U_y|^2\right)U_x + \frac{g}{2}U_x \tag{29}$$

$$\frac{\partial U_y}{\partial z} = \frac{\Delta\beta_1}{2}\frac{\partial U_y}{\partial \tau} - i\frac{\beta_2}{2}\frac{\partial^2 U_y}{\partial \tau^2} + i\gamma\left(|U_y|^2 + \frac{2}{3}|U_x|^2\right)U_y + \frac{g}{2}U_y \tag{30}$$

U_x and U_y describe the electric field along a linear polarization orthonormal basis set. $\Delta\beta_1$ is the group velocity phase difference associated to the refractive index change between polarization axis ($\Delta\beta_1 = \frac{\Delta n}{c}$).

Without any nascent fiber birefringence [36]:

$$\frac{\partial U_+}{\partial z} = -i\frac{\beta_2}{2}\frac{\partial^2 U_+}{\partial \tau^2} + i\frac{2}{3}\gamma(|U_+|^2 + 2|U_-|^2)U_+ + \frac{g}{2}U_+ \tag{31}$$

$$\frac{\partial U_-}{\partial z} = -i\frac{\beta_2}{2}\frac{\partial^2 U_-}{\partial \tau^2} + i\frac{2}{3}\gamma(|U_-|^2 + 2|U_+|^2)U_- + \frac{g}{2}U_- \tag{32}$$

The above equations utilize a transform into the circularly polarized orthonormal basis given as:

$$U_+ = \frac{(U_x + iU_y)}{\sqrt{2}}$$

$$U_- = \frac{(U_x - iU_y)}{\sqrt{2}}$$

The first term on the right hand side of the high birefringence case (Eq.(29)), mathematically adds an overall delay to the optical pulse in polarization axis (one can see this by considering the frequency representation of the term, shown in chapter 4) and accounts for a net total delay between optical pulses travelling along the two orthogonal axes. The n_2 intensity dependent term now contains intensity contributions from both polarizations. This is because the intensity dependent variation of the refractive index sees overall intensity regardless of, i.e., the polarizability tensor remains scalar. The above equations employ the slowly varying intensity approximation.

The above is obtained by considering the two polarization states of light on the polarizability term in the original derivation of the NLSE [36].Due to intensity dependent coupling between polarization states, the amplitude electric field of one polarization state rotates such there is a component in each of the polarization basis vectors. This process iterates over the medium propagation coordinate. Details of this derivation are extensively covered in [36].

It is also sufficient to state here that Soliton or Similariton solutions (dependent on the strength of the gain perturbative terms) exist when considering the polarization cross phase modulation in the case of the low birefringence NLSE[29].

2.1.3 Mode-Locking Mechanisms of Laser Oscillators

The inherent goal in passively pulsed lasers systems is to lock the phases of spectral components that are allowed to lase within the cavity. It is prudent to briefly discuss what spectral components can propagate in such a laser cavity, this can be seen by the CW lasing conditions. The CW lasing conditions of these spectral components depends on the gain medium and the coherence of the lasing mode. If the phase after a roundtrip of the spectral component is not an integer multiple of 2π than interference with phase regions of the CW component at lower roundtrip numbers will cause an intensity drop in the intra-cavity power of the component and lasing will stop[1]. Thus, only spectral components satisfying this phase relation within the gain bandwidth of the oscillator can contribute to the final pulse build up in the mode-locked case.

There is a discrete train of CW spectral components that are allowed in the cavity (since the spacing of these CW lasing components are small, this is assumed to be a continuum) and if the phase differences between these components happen to be close to zero, by the Fourier series property (or integral if a continuum approximation is used), an optical pulse in time is produced. Furthermore, the peak amplitude of the pulse would be equivalent to the summation of the peak amplitudes of the train of spectral components, far exceeding and individual components value. Thus, pulsed operation exhibits higher local intensities around its peak than the background amplified spontaneous emission waveform.

If it is possible to construct a device that:

1) Filters the optical intra-cavity intensity so that intensities past a threshold can propagate within the cavity and,
2) Recovers on a fast time-scale.

Then, a pulse exhibiting the ideal properties discussed in the past paragraph can be allowed to propagate while other regions of the optical waveform in the cavity not exhibiting these spectral phase relations will be attenuated by the device. Only a small attenuation factor is necessary due to the exponential amplification of the pulse (and depletion of the gain medium after the pulse). Essentially, by tuning the pump power, the pulse in the waveform with the highest peak intensity will deplete the gain medium such that for times before and after the pulse interacts with the gain medium at roundtrips past steady-state, the population inversion has not recovered to a level where gain equals absorption within the cavity and attenuation caused by power out-coupling from the cavity.

A device that accomplishes this task is correspondingly named a real Saturable Absorber (SA). As the name suggests, this works on the concept that at steady state population inversion the SA material is close to transparent to the pumping signal (i.e., the stimulated emission rate of the SA balances with the absorption rate). The timescale to this steady state and thus transparency is dependent on the pump intensity. The SA will be rendered transparent for parts of the waveform that exhibit peak intensities past a threshold and absorptive/reflective for parts that do not meet this criterion. The relative transparency need not be great (modulation depth on the order of 1-5%[31]).

However, in the next section, I will discuss the success of a virtual SA scheme that is the dominant mode-locking mechanism in the fiber oscillator that was built. This scheme does not rely on material population inversion dynamics as in the case of the real SA but on the non-linearities that exist in the fiber and that was covered in section 2.1.2. The advantage to this scheme is that the response time of the virtual SA is instantaneous with intensity. In the real SA the response time dictates the inversion recovery, for example, which adds amplitude noise in the system because the pulse sees different initial conditions in the SA every roundtrip. Since this is not the case in virtual SA's noise is minimized.

Narrower subsets of pulses are allowed in virtual SA's. This is because in real SA's the inversion level saturates with pulse peak intensity; any pulse over the saturation value is allowed with negligible relative losses. This can cause double pulsing or pulse trains with different pulses to be outputted from the oscillator since the real SA cannot differentiate these pulses. However, in virtual SA's this effect is not present. The virtual SA scheme does not saturate with intensity, and due to the non-linear dependence of intensity, intensity changes are always highly impactful and cause large changes in the dynamics. Self-starting of virtual SA systems are than harder to achieve; however, once mode-locking is achieved pulses do not fluctuate in the pulse train. Therefore, for stable applications, even if self-starting may be hampered in virtual SA's, they should be the preferred scheme.

2.1.3.1 Non-linear Polarization Rotation (NPR) Mode-Locking: A Virtual SA

The predominant method of mode-locking similariton fiber cavities is via NPR which can be seen as an intensity dependent polarization rotation.

As can be seen from Eq. (29) to (32) the electric field amplitude along a polarization of the optical waveform is intensity coupled to the other orthogonal polarization. By only considering the Kerr rotation term, [36] has derived an analytic expression for the Kerr rotation term. From his derivation it can be seen that a linear state will not rotate, while a circularly polarized state will remain circularly polarized but in the orthogonal circularly polarized state. There are thus, linear polarization Eigen modes of the polarization effect.

By considering only the case of Eq. (31) and (32)**,** the polarization rotation will add no phase offsets between the polarization axes and thus the overall polarization state will be rotated but still maintained for an elliptical polarization. In terms of the general optical waveform* born from the random spontaneous emission source, at first the polarization state will vary across the overall optical waveform in a random (depolarized) manner. However, because of the random variation the system can find a state where for a given region in time the electric field amplitudes are Eigen-mode type solutions of the cavity; meaning, that at the entrance of the fiber, the optical waveform matches the initial condition of the previous roundtrip. Through competition in relation to the gain population this region will be amplified over others; the losses in relation to the gain for other regions will increase and thus, will be subdued. The cavity "Eigen-mode" has to match the initial phase (up to an arbitrary constant), amplitude and polarization of the initial condition at the previous roundtrip for the pulse to be in a steady state dynamic.

Now, it will be explained why this "Eigen-mode" will be amplified over other regions in the waveform. If there is a polarization based filtering within the cavity, for regions of the optical waveform where the polarization state and intensity do not match the initial conditions after passing through the polarization based filter, there can be either two outcomes: The waveform will walk in transformations until it will evolve into a polarization state with high out-coupling loss, due to the statistics over a large amount of transformations that result in that or walk in transformations until it reaches a repeatable state, where now walks in polarization are suppressed.

A more in-depth analysis of the conceptual discussion above starts with the inputted pulse polarization state at the entrance of the fiber portion of the cavity (see Fig. 5). After the PBS the overall waveform is in the P-polarization. After the QWP at the entrance of the fiber the state is rotated to an elliptical polarization that is the same across the optical waveform (linear states will not change and thus need to be converted to an elliptical state for the effect to happen). Due, to the intensity dependent polarization rotation in the fiber, portions of the optical waveform will be rotated differently. Thus, regions of the waveform will be in-coupled differently into the cavity after the PBS. This effectively modulates the optical waveform such that the intensity distribution is localized in time.

It can be experimentally shown that Eq. (31) and (32) ,operating under a specific gain value and a short input pulse (i.e. short region in time), can rotate an elliptical input state in a manner such that the intensity gained at a given time is exactly in the out-coupling S polarization across the narrow region in time and thus, the input intensity entering the fiber will have the same intensity profile across the region in time as the previous roundtrip. If cavity dispersion is managed and there is no overall gain filtering effects (the bandwidth of the pulse is the same as the previous roundtrip at the entrance of the fiber), than all initial conditions are met. If cavity dispersion is not managed than the pulse is likely to evolve into a soliton with dissipative waves, that are called Kelly sidebands [37]. This type of oscillator is called a normal dispersion oscillator.

If the optical waveform is in the high in-coupling polarization states for many round-trips in its evolution, than the asymptotic limit is reached and a similariton pulse will form. Once this limit is reached it can be experimentally shown that Eq. (31) and (32) yields similariton solutions where the polarization rotation meets the initial conditions described in the previous paragraph. Once this pulse is formed, to insure initial conditions are met and the same pulse is being coupled out of the cavity per round trip, the linear chirp that accumulates per additional roundtrip after convergence to the asymptotic limit is compensated after out-coupling by a double pass diffraction grating (DPG) [38].

This type of similariton oscillator is easier to achieve since the steady state solution does not rely as heavily on the gain effects being cancelled after out-coupling in its evolution prior to steady state, because of the wide plethora of input pulses that can evolve to a similariton in the asymptotic limit. In the case of the soliton formation, the gain memory may never result in the soliton formation or cause dissipative waves because of the narrow stability point that soliton formation exhibits when gain effects are considered. Due to the negative stretching of the pulse after the diffraction grating, this fiber oscillator type is accordingly named stretched-pulse oscillator. The oscillator example with the DPG is called a stretched pulse NPR fiber oscillator. Note, that if the diffraction grating does not compensate for dispersion in the prescribed way and there is net normal dispersion, the oscillator will have soliton formation like a normal dispersion oscillator.

The disadvantage for similariton solutions is that the linear chirp is only achieved in the asymptotic limit. Thus, the evolution of the system at the start has to still follow close to similariton evolution even in the presence of the now parasitic dispersion compensation. However, the chirp in the non-asymptotic limit can be highly non-linear and a linear additive variation can be neglected as a minor perturbation. Though, this can contribute to system instabilities. The amplitude reduction from the output coupling can affect the evolution of the pulse to the similariton limit. However, [39] has shown that the asymptotically limited similariton solution can be achieved from a variety of pulse evolutions and is robust to these effects.

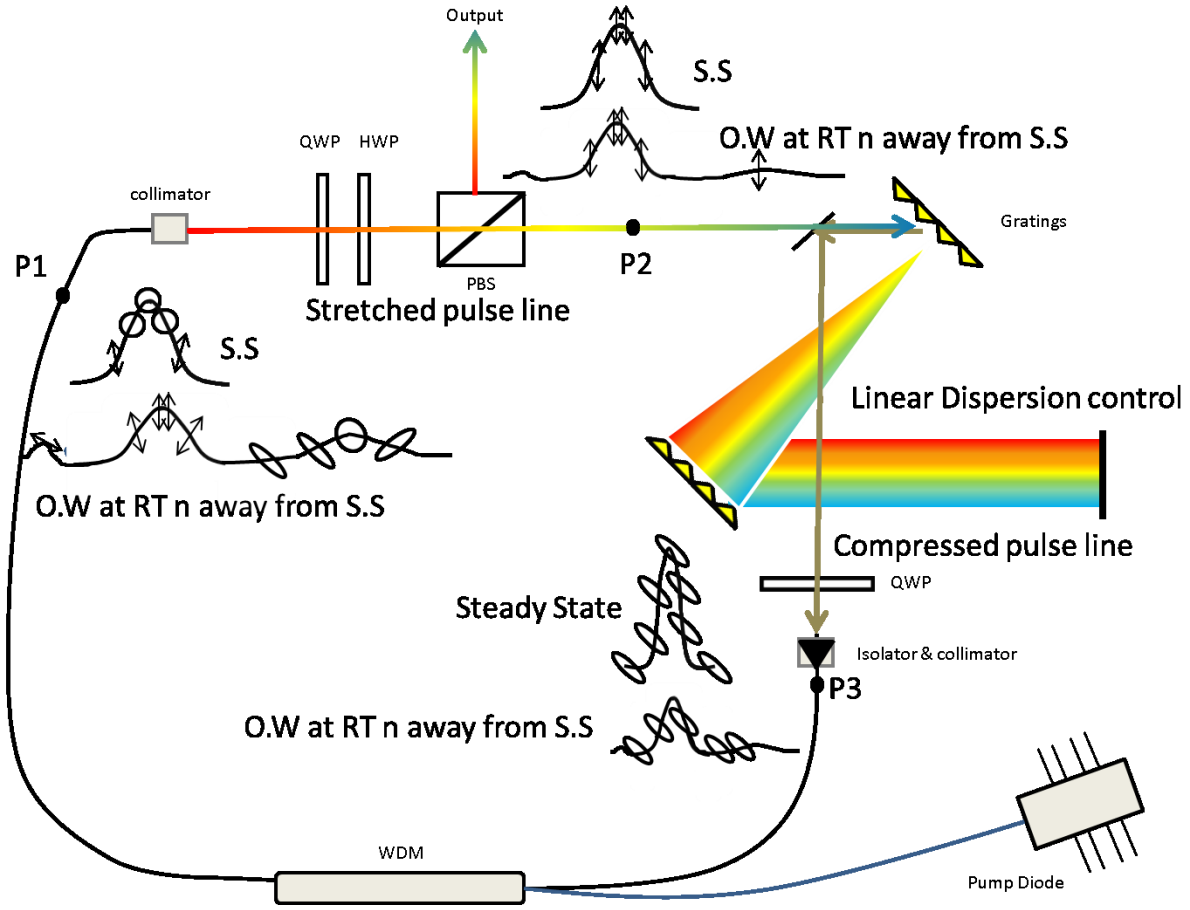

Figure 5: A descriptive picture of NPR mode locking. O.W: Optical Waveform, S.S: Steady State, RT: Round Trip. At P1 the optical waveform is stretched in time because of dispersion. At RT away from S.S, portions of the waveform will be polarization rotated such that the out-coupling loss will result in attenuation in the cavity. At this point the optical waveform has an intensity distribution already localized in small regions of time. Only a short region in time of the initial waveform will progress to steady state. Because of tight constrains on the intensity-dependent rotation and because of gain competition. At point P2, only the P-polarization (here depicted as vertical arrows, however, in the plane parallel to the paper) will be in-coupled. Thus, for example, the O.W at RT N will be truncated around the main peak. At P3 linear dispersion is compensated by the use of a DPG. The QWP at P3 inputs a uniform elliptical polarization across the O.W. This serves as the necessary initial condition to insure Kerr rotation across the entire O.W. The P polarization will not rotate and thus, this QWP is integral. Finally, the output pulse at S.S will be as described in the text (different to the intracavity S.S pulse). WDM stands for the wavelength Demultiplexor/Multiplexor and is used to the pump fiber to the cavity gain fiber.

Due to laboratory conditions, external environmental forces can exert strain on the fiber system. This locally causes the fiber to be birefringent [40] and the effect is even used to rotate the modal polarization within fiber [41] in industry. Thus, at these local regions of the fiber, the system equations are better described by Eq. (29) and (30). There is a polarization walk off represented by the first term of these equations. This additional birefringence must be reduced in the design of the setup by reducing environmental strain on fibers. Because of the walk off, these parasitic birefringent areas of the fiber cause limitations on the shortest duration of pulsed operation and can lead to multiple pulsing.

In the initial condition analysis above another fact must be considered. Directly, from Eq. (26) it can be seen that as the similarition propagates in the fiber, the pulse width in time increases. Since, Eq. (28) is never violated, this is due to the linear chirp now over additional frequencies added in a linear fashion in time to the ends of the previous frequency bandwidth and in the same ordering. Thus, spectral filtering must happen at the start of every round trip; to maintain initial conditions.

The added bandwidth at a certain fiber propagation length can be calculated as :

$$w_{min} = \frac{g}{3\beta_2}\frac{\tau_o(z_o)}{2} + \frac{g}{3\beta_2}\frac{\tau_o(z_1) - \tau_o(z_o)}{2} \tag{33}$$

Where the first term is the minimal frequency at z_o, which represents the end length of the first round trip after convergence.

It follows that :

$$w_{max} = -\frac{g}{3\beta_2}\frac{\tau_o(z_o)}{2} - \frac{g}{3\beta_2}\frac{\tau_o(z_1) - \tau_o(z_o)}{2} \tag{34}$$

Subtracting the above equations and substituting the equation Eq. (26) for τ_o gives:

$$\Delta w = \frac{g}{3\beta_2} 3(g)^{\frac{-2}{3}}(\frac{\gamma\beta_2}{2})^{\frac{1}{3}}(Ep)^{\frac{1}{3}} e^{\frac{gz_1}{3}} \tag{35}$$

This can be derived as the bandwidth conditions straight from Eq. (26) and the time derivative of Eq. (28). This verifies that calculating the bandwidth addition in the manner expressed above is correct and that instantaneous frequencies are appended to the ends of the previous bandwidth in a linear fashion and in the same ordering in time.

The added bandwidth is assumed to be attenuated primarily by the natural gain-filtering effect of the gain medium [42] and by the spectral transmission function of the DPG.

The amplitudes of the frequency components change vs propagation distance (this can be seen by the time shape of the pulse being maintained as new frequency components are added and by the gain dependence of the amplitude function). However, it is assumed that this is taken care of with the appropriate polarization rotation characteristics described above at steady state. Meaning the S-polarization out-couples intensity gained. There is a sharp frequency cut off that can be seen from Eq. (28). There is a minimum and maximum possible frequency value obtained from the time derivative Eq. (28). This is because of the amplitude function going abruptly to zero past the temporal width τ_o. Thus, frequency values at $|\tau| > |\tau_o|$ will exhibit zero amplitude to guarantee that the time amplitude function is zero past the temporal width. This frequency cut off in the spectrum is in contrast with spectra obtained from solitons.

Table 4 lists the advantages of similariton over soliton operation, which strengthens the reason why dispersion compensation is needed.

Advantage	Similariton	Soliton
Dispersive wave generation	Similaritons exhibit minimal dispersive wave generation[30]	Kelly sideband contributions exist due to dispersive wave contributions[30]
Perturbative recovery	Under perturbations similaritons are robust with a reduced wave-breaking as compared to solitons. [30]	Solitons undergo fission and fusion dynamics under perturbation.[43]
Evolution pathways	A large number of evolution pathways from the original optical waveform tend to similariton formation. However, this can lead to double pulsing in similariton cavities because of the increased number of valid regions of the optical waveform. This is also why perturbative recovery is easier with a similariton	A limited number of evolution pathways render soliton formation tougher to implement and also why perturbative recovery is lower in soliton pulses as compared to similaritons.
Energy scaling	Mismatch of amplitude in pulse build up does not cause depolarization as easily as soliton formation. Similariton formation is more robust in this regard.	Amplitude reduction/increase with the additional gain/absorptive term may cause soliton wave-breaking due to the non-linear part of the NLSE contributing less than the linear dispersion part or vice versa. Dispersion is not balanced anymore with the non-linearity (SPM). However, due to the dispersive solitons that can be produced, system is still robust but may be unstable [30].
Frequency Filtering	Frequency filtering may be necessary to counter the gain dynamics (non-uniform gain profile) of the fiber and to insure initial conditions.	Due to the perturbative gain term the soliton will undergo additional SPM frequency broadening (due to the energy conservation violation of the NLSE and intensity gradients being enhanced by the intensity dependent gain). Thus, in order to maintain the soliton initial conditions at every round trip additional frequencies have to be filtered before entering the fiber.

Table 4: Relative advantages of operating in similariton vs soliton pulse formation.

*The starting optical waveform is a summation of incoherent spontaneous emission over many round trips. If the CW lasing conditions are not met, the contribution of that spectral component in this summation is reduced.

Advantages	NPR mode-locking	Real SA mode-locking
Pulse duration	The intensity dependent polarization scheme used as a virtual saturable absorber fluctuates directly with pulse intensity. There is no delayed system response.	The Relaxation time of the inverted population in real SA's is essentially the time the SA cannot be used for intensity filtering. Thus, noise can persist after the pulse formation.
Noise	Reliant primarily on pump noise and thermal noise.	Reliant on pump noise, thermal noise, population recovery noise in the SA, pointing fluctuation error, etc. As well as gain recovery noise (explored in chapter 3)
Stability at higher repetition rates	Once initial conditions per roundtrip match, by the fact that the pulse is mathematically an Eigen-mode like analogue to the system NLSE, the pulse will be stable. The dynamics will match every roundtrip.	The SA population recovery noise will dominate the pulse dynamics at higher rep. rates. This is because the initial conditions of the ground state population will be different for every time the pulse passes through the SA.
Robustness to environmental strains	The out-coupling loss is dependent on the degree of Kerr polarization rotation. This is dependent on intensity. Thus, if cavity losses increase due to environmental effects, the output coupling loss decreases and for a given gain, the cavity can still be in a steady state. The system can adapt to environmental impacts through it being able to vary its losses through a feedback with the environmental impact.	See above arguments. More reactive to environmental instability.
High Rep-Rate	Easily possible due to modal confinement as already discussed	See above arguments. Less scalable.
Extracted Efficiency	Higher due to modal confinement and gain recovery dynamics	
System Response Time	Virtual SA scheme used is instantaneous	Output Modulated by population rise time and decay time. Saturation effects may decrease pulse selectivity.

Table 5: Compares NPR over real SA's.

2.1.4 Theory of Dispersion Management

As the pulse travels through the fiber portions of the cavity, the temporal width of the pulse will broaden and a frequency chirp across the pulse will develop as shown by Eq. (26) to Eq. (28). Therefore, to insure initial conditions are met at the entrance of the fiber after every roundtrip, a scheme to manage dispersion must be in place. To design such a scheme it is first prudent to delve into the theory of dispersion and obtain pertinent equations for the regime the oscillator operates in.

Optical pulses can be viewed as a summation of small bandwidth pulses at different central frequencies[1,25]. Each pulse centered at a specific central frequency has a corresponding group velocity inside the various optical elements in the cavity. Because of group velocities not being equivalent, the pulses at different frequencies have different time delays relative to each other as they propagate to a specific propagation coordinate position in the cavity. Dispersion terms are viewed as a Taylor series where coefficients are given by Eq. (21)**.** The physical meaning of each term can easily be seen from the frequency representation of Eq. (21) and each term approximately can be viewed as carrying an intuitive physical meaning:

Zero order dispersion, arises from the first term in the Taylor series expansion of momentum w.r.t angular frequency about the central angular frequency (first term in Eq.(21))[1]. It is a linearly increasing phase offset that arises as the pulse propagates along the medium. It can be viewed as the constant overall k_Z momentum (the propagation coordinate momentum in Eq. (2)**)** of the fiber mode across all specific instantaneous angular frequency along the temporal profile of the pulse, where z is the propagation coordinate.

First order dispersion, arises from the second term (i.e., second term in Eq.(21)) in the Taylor series expansion of momentum w.r.t angular frequency about the central angular frequency[1]. It can be viewed as the time delay assigned to a global group velocity applied to the entire train of different angular frequency centered pulses, and is a linear function of propagation coordinate. It is the average velocity of the envelope function of the optical field. If the original pulse can be viewed as having a small bandwidth first order dispersion is sufficient and all other orders are negligible. Second order dispersion, arises from the third term in the Taylor series expansion of momentum w.r.t angular frequency about the central angular frequency. It can be viewed as the additional time delays due to individual angular frequency centered pulses posing group velocity deviations from the global average velocity as they propagate to a given propagation coordinate position in the cavity. This is generally termed group velocity dispersion (GVD). For the fiber oscillator application this is sufficient and higher orders do not have to be considered. However, it is sometimes prudent to consider third order dispersion, which is the additional broadening of those sub-pulses centered at specific angular frequencies, (i.e. these sub-pulses are again decomposed into pulses centered at different sub-frequencies). Each additional dispersion term is the next iteration in this pattern[25]. The angular frequency width of each sub-pulse is dependent on the variation of the refractive index function on frequency. For slowly-varying functions, the bandwidth of each sub-pulse is higher and truncation can happen after a lower dispersion order.

For second order dispersion, the GVD parameter dictates pulse broadening and scales linearly with propagation length. The group velocity (V_g) is[1]:

$$V_g = \frac{dw}{dk}|w_o = \frac{c}{n(w) + w\frac{dn}{dw}}|w_o \tag{36}$$

w is the angular frequency and k is the angular momentum wavenumber. The propagation time per meter is simply:

$$\mathrm{TD} = \frac{1}{\mathrm{V_g}} \tag{37}$$

The timing delay change per angular frequency per length (group velocity dispersion), using the refractive index function of frequency is thus[1]:

$$\mathrm{GVD}|_{\mathrm{w}=\mathrm{w_0}} = \frac{\partial}{\partial \mathrm{w}}\frac{1}{\mathrm{V_g}}|_{\mathrm{w}=\mathrm{w_0}} = \frac{\partial^2 \mathrm{K}}{\partial \mathrm{w}^2}|_{\mathrm{w}=\mathrm{w_0}} = \frac{2\frac{\mathrm{dn}}{\mathrm{dw}} + \frac{\mathrm{d}^2\mathrm{n}}{\mathrm{d}^2\mathrm{w}}\mathrm{w}}{\mathrm{c}}|_{\mathrm{w}=\mathrm{w_0}} \tag{38}$$

GVD is entirely based on material refractive index variation with frequency. Thus, it is a material parameter, whose units are $\frac{\mathrm{s}^2}{\mathrm{m}}$.

Where, K is the total momentum of a fiber mode (wavenumber) with frequency w. In isotropic media such as the core of the fiber, this is independent of momentum direction. Under the assumption that only up to second order dispersion is sufficient and that the GVD does not vary substantially over the bandwidth (constrained bandwidth approximation), GVD can be employed in the following manner for calculations pertaining to pulse broadening at a certain propagation coordinate in material:

$$\Delta\mathrm{T} = \mathrm{GVD} * \Delta\mathrm{w} * \mathrm{L} \tag{39}$$

$\Delta\mathrm{T}$, is the new time duration of the pulse. $\Delta\mathrm{w}$ is the angular frequency bandwidth, L is the length. The sign of GVD dictates the direction of broadening of the frequencies. For positive GVD higher frequencies are delayed in time (normal dispersion [44], anomalous dispersion is the opposite).

For multiple optical components (quantity: #) that exist within the region L, labelled with the index j, Eq. (39) becomes, under a constant optical bandwidth:

$$\Delta\mathrm{T} = \sum_{\mathrm{j}=1}^{\#} \mathrm{GVD_j} * \mathrm{L_j} * \Delta\mathrm{w} \tag{40}$$

Eq. (40), will be used in obtaining the amount of total broadening that needs to be compensated for and deriving a scheme consisting of a DPG to implement this compensation per roundtrip.

2.2 Building the Fiber Laser Oscillator

2.2.1 Component Review, Alignment, CW Lasing

The theory presented in section 2.1 supports the creation of an all-fiber NPR mode locked laser oscillator with minimal optical components. However, because of the variety of evolution pathways that tend to a similariton, a theory analyzing a particular solution of the NLSE will not solve the problem. Primarily, the system is better described in terms of evolution pathways. Whereby, a starting

pulse undergoes propagation governed by Eq. (31) and (32) and then after partial out-coupling, is used as the initial solution for the next round trip. The set of all pulses used as initial solutions until convergence to the asymptotic similariton limit is termed the evolution pathway. As discussed in 2.1 if certain conditions are met throughout the evolution pathways, it will be valid (i.e., converge to a similariton). Thus, the final similariton pulse can be obtained by the asymptotic convergences of many different pulse evolutions and pathways. This fact is why stable pulses are so easily reached in similariton oscillators.

To find a particular valid pathway of the many possible ones by randomly creating an initial optical waveform is a statistically challenging problem. The number of outcomes that have to be explored will be computationally intensive. Analytic solutions can offer an alternative to the statistical approach, by finding an initial subset of optical waveform regions that will converge. However, this is still an ongoing problem.

It is sufficient to understand that the systems NLSE equations yield these asymptotic similaritons over a wide parameter space. It is thus, an emergent property of the NLSE system and the onus in artificially inducing these pulses (for example in the design of real SA) is removed. Thus, whether the system is well known theoretically is of less importance since the emergent nature of the solution guarantees the solution over a wide range of parameters.

Also, the exact asymptotic similariton has well defined analytic expressions in terms of the system parameters and lengths can be calculated merely by the one pass length of the roundtrip at this limit. Thus, similariton progression such as linear chirp (phase, roundtrip gain, etc.) can easily be deduced from these expressions and the roundtrip length. The probability that the original random waveform outputs a similariton type initial condition at a given region in time is high because of the extensive sampling of this random waveform. Thus, similariton convergence is virtually guaranteed from startup and therefore, the cavity is designed for rather the final steady state pulse rather than the buildup. Initial conditions and steady state conditions need only be designed for the final circulating similariton.

Given the previous discussion, it is prudent to design the system first experimentally and to heuristically optimize for mode-locked spectrum, average power and stability. Emphasis is placed on deriving a reproducible experimental technique to build up the fiber oscillator. This technique was tested by reproducing the same oscillator.

Furthermore, while the system equations shown in section 2.1 were for a continuous non-linear medium with gain, in practice, the system has multiple fiber segments of different types. The gain fiber is spliced to single mode fiber at 1.03um wavelength. This introduces boundary conditions and regions of validity of different NLSE equations describing each fiber. However, it is found by our experiments that not much in the fundamental analysis changes with this variation and one can still achieve similariton type operation.

The oscillator was designed to have a repetition rate of 30 MHz, an average power of 300 mW and auto-correlated pulse duration of sub 100 fs. The absorption cross section of Yb-doped fiber peaks at 976 nm as showed in fig. 1. Therefore, to pump this system efficiently it is necessary to obtain a pump close to the resonance peak. To minimized the required fiber length of gain fiber, we choose to pump with a 976 nm laser diode, which has a fiber pigtail and a fiber Bragg grating (FBG) for wavelength stabilization. The FBG consists of a fiber core with varying refractive index such that the overall transmission transfer function is narrowly peaked at the pump wavelength. Other wavelengths are

reflected and are not transmitted further. Appendix A1 has details of all materials used in the construction of the oscillators.

To maintain the continuous fiber nature of the cavity, the gain fiber is pumped by a fiber coupled pump diode spliced to a wavelength division multiplexor (WDM). The WDM works on the principle of evanescent wave coupling, shown in figure 6, where optical fields are coupled evanescently through the refractive index barrier of a double well index profile. The coupled evanescent wave propagates in the new fiber core with the same propagation constant (and thus, direction) and beam profile (provided both cores have the same dimensions and material). The modal solutions in the coupling fiber are dependent on the boundary conditions from the evanescent region. If the separation distance changes to less than the 1/e value of the evanescent decay region more than 50% in-coupling (for the oscillator WDM <1.0dB) can be achieved [45].

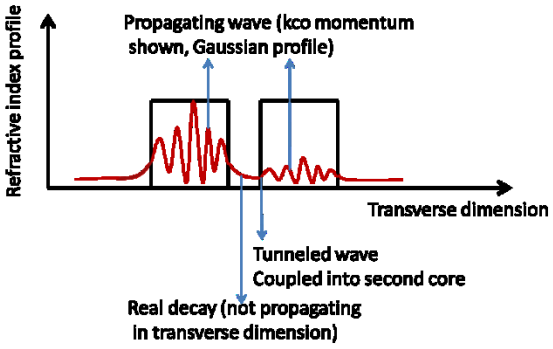

Figure 6: Evanescent coupling in the WDM.

The gain fiber is spliced with the common port of the WDM. The length of the gain fiber and single mode fiber (Corning Hi1060, MFD @1.03µm: 6 µm) constitute the bulk of effective length the pulse undergoes and thus, dictates the time the pulse spends in the oscillator (and rep.rate of the system). Both lengths have to be optimized for:

1) Gain recovery dynamics
2) Increase of random mechanical strains and thermal effects as a function of fiber length
3) Parasitic non-linear contributions such as self-focusing, self-steepening and wave breaking.
4) Fiber Losses
5) System dispersion and higher order dispersion contributions (parasitic)

The advantages of having long fiber lengths and thus a low-repetition rate are that the gain medium is always saturated by the time the pulse enters the gain medium per roundtrip. Thus, gain recovery noise due to varying gain initial conditions is absent since the effects of the initial conditions are not impactful anymore. Because of the saturated gain the single pass amplification is higher. However, limiting the fiber length has more advantages. Due to environmental stress and strain within the fiber and thermal expansion along the length of the fiber, phase noise and amplitude noise rises with increasing fiber length. These random noise sources are more deleterious than gain recovery noise which is controllable (by varying fiber lengths and pump power). With greater fiber lengths, third order dispersion and even linear dispersion become highly contributing effects. Thus, the dispersion compensation scheme will have to become more complicated and a restricted simple linear dispersion

compensation scheme may not be effective. If the fiber length starts to become comparable to the non-linear self-focusing length of the intracavity pulse, self-focusing can increase the effective NA necessary to contain the propagating mode and the mode is not contained in the fiber waveguide anymore. In essence, due to the smaller beam size, diffractive effects are higher and the spread of momenta angles is greater, thus violating the allowed angular spread of the fiber. Other effects that dominate in large fiber lengths, include the build-up of Brillouin scattered modes[48-50], the beta parameter (high non-linear phase), and fiber losses. However, an inherent advantage in using longer fiber lengths is that the asymptotic similariton solution can be achieved in one roundtrip. This substantially reduces the complexity of simulating the system since initial conditions are not changing in the initial pulse build up round trips.

In general, the gain recovery depends on the pumping power and the remaining depleted population after amplification, for a given dopant percent. The fiber lifetime is 1ms [46] thus, any rep.rate above 1 kHz sees no effects of the finite inversion lifetime. For long rep.rates due to the amplified spontaneous emission (ASE) noise will be present and may contribute to less pulse amplification. ASE contributes to lowering the saturated gain value. Competition between the CW build up and the pulse amplification can come into play, preventing lasing.

However, going to extremely high-rep. rates also poses specific problems. The gain medium is now not pumped to saturation. Thus, initial gain conditions for when the pulse enters the gain medium per round trip are different. The gain value may be higher or lower at different round trip numbers resulting in amplitude fluctuations of the pulse. This perturbation may result in amplitude noise. At higher rep.rates the inversion level is lower because of the reduced pumping time interval between subsequent round trips. Thus, losses in the cavity may overpower gain and loss of mode-locking will occur. It is prudent to carefully tune the fiber length so it is in the proper range to avoid such effects. The possible simulation model for this is derived rigorously in chapter 3, where the discussion centers on regenerative amplifier dynamics but can be applied here as well. Fig. 10 demonstrates gain recovery noise and fig. 11 shows the effects of fiber length on gain recovery time. The exact experimental procedure to determine the fiber lengths necessary will be discussed later in this section.

The ring oscillator is constructed with a free-space portion that contains the QWP, HWP, PBS, grating pair, isolator to insure propagation in one direction and QWP (see fig. 7). This free-space portion contains high NA components where point deviation is not critical. Every component in the free-space cavity can be replaced by a fiber analog for a true all fiber oscillator system.

The coupling between fiber ends in the cavity is accomplished by convex fiber collimators at 8mm focal lengths at the fiber ends. The fiber ends are placed at the focal point of the lenses. The beam will remain collimated after the lens and focused back into the fiber end. Small angular offsets or parallel transport of the beam on a lens surface is compensated for after the lens as the lens corrects these deviations to pass through the focal point. Limited pointing error is compensated for in this manner. The Rayleigh length of these collimators, given the input beam waist exceeds the free space cavity length and this was verified experimentally.

CorActive Yb doped gain fiber was spliced (appendix A1 has details of every component used in the cavity). The gain fiber undergoes multiphoton absorption and fluorescence in the visible blue range (explained in fig. 8). Thus, pump depletion can be approximated by the region of fiber that is fluorescent. Past this region, the population inversion can be in the net small signal absorption region for the 1.03 μm signal. Therefore, the fiber was cut in the fluorescent region such that at least 10% of the 500mW pump power was transmitted through the fiber. This corresponded to a gain fiber length of 1.3m. At this stage in the development a 5m length of Corning 1060Hi fiber was spliced to the input

port of the WDM and at this point in the development the length of signal mode passive fiber can remain arbitrary.

The fiber ends were connectorised with Thorlabs FC/APC connectors. The fiber connectors were polished manually using a three stage process. The first stage consists of polishing the connectorised end with a 5 µm grit roughness paper. Thus, the connectorised end would have features <5 µm in amplitude after this stage. The end is then polished with a 1 µm grit roughness paper, insuring at this stage, features <1 µm in amplitude and finally with a 0.3 µm grit roughness paper insuring features less than 0.3 µm in amplitude. Due to the optical wavelength being much larger than 0.3 µm, scattering off of these 0.3 µm features will contribute negligibly to the spatial electromagnetic distribution coming out of the fiber.

After the placement of connectors on the fiber ends, Thorlabs 8mm focal length variable FC/APC fiber collimators where attached to the connectors. The collimators where adjusted in distance to the fiber end such that the fiber end is exactly at the focal point. This was done by actively checking the collimation of radiation (at first the pump going through the fiber), with an IR card at different points in space.

The connectors with the collimators were mounted on Thorlabs KM100T mounts and then on optical posts. Optical posts lengths were minimized as much as possible to increase mechanical stability. The next step is to align the cavity such that the amount of light being coupled into C2 (refer to fig. 7) and into the passive fiber branch is at a maximum. There are in fact many methods that can optimize this alignment.

The first method is to have the single mode fiber unattached to the WDM. Power is found by measuring the power being transmitted out of the bare fiber end. Alignment is maximized by the two degrees of freedom on both mirror mounts (azimuthal and polar angles). The cavity at this stage corresponds to fig. 7. Once power is maximized, the PBS is inserted and rotated such that the power being transmitted through the single mode fiber is preserved. In a corresponding fashion a QWP and HWP is inserted before the PBS. There is a small angular offset within these optical components such that back reflections are not back coupled into the gain fiber.

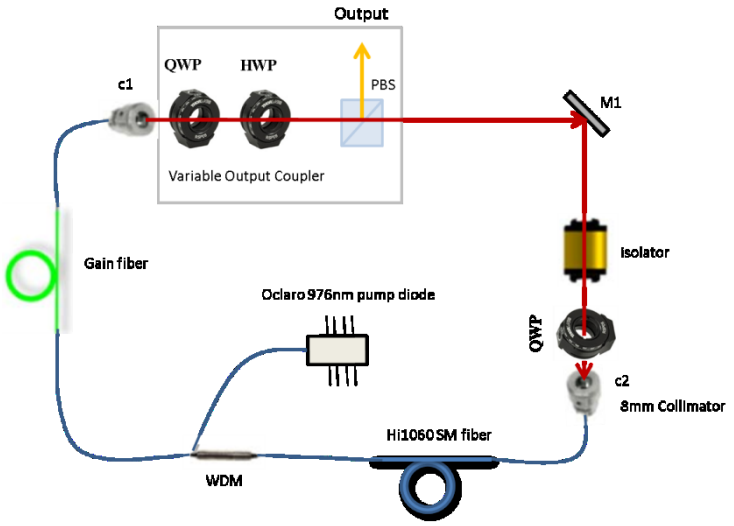

Figure 7: Connected cavity. Alignment is done with M1 and C2.

Another method that was found to be as efficient is to align the cavity using the fluorescence of the gain fiber (see fig. 8). This method is the favored one because if the single mode fiber is already

spliced with the WDM and the cavity is misaligned, one does not need to re-splice the single mode fiber. When the amplified spontaneous emission spectrum is coupled back into the gain fiber, the population inversion will be affected because of the competing decay rate (see Eq. (24)) introduced by the further stimulated emission from the in-coupled spontaneous emission. Then because of the depletion of upper state electrons further transitions to higher manifold states is suppressed, and fluorescent decay from these states is depleted. Since in-coupled spontaneous emission is iteratively amplified along the length of the gain fiber, the fluorescent suppression will be higher towards the end of the length and will vary in an exponential fashion. If the depletion length from the end of the gain fiber is maximized, by varying the alignment, the amount of in-coupled spontaneous emission increases and alignment is optimized (note that the spontaneous emission spatial profile is Gaussian due to the single-mode filtering in the fiber waveguide). If there is no isolator in the cavity at this stage, the gain fiber will have some in coupled power from the single mode fiber (since spontaneous emission travels along both directions in the gain fiber) and this effect will even be more enhanced.

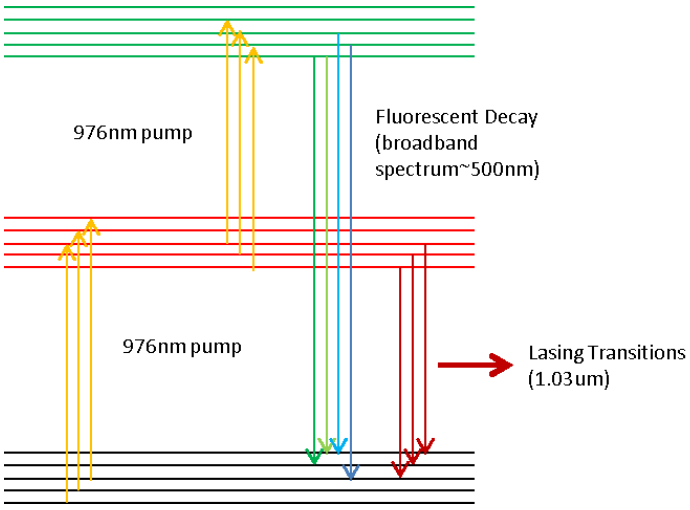

Figure 8: Explanation of the relevant multiphoton absorption pathway that can be used to check for proper alignment. Population inversion occurs at the red manifold. However, there are transitions to additional higher manifolds (multiphoton or singular photon absorption) at the pump wavelength. If the cavity is aligned, the circulating amplified spontaneous emission depletes the inverted population in the red manifold. This prevents additional transitions to higher manifolds due to lack of inverted population at the red manifold and increases pump absorption (due to an increased population in the ground manifold), limiting multiphoton absorption effects.

**A third way that is mainly used for coarse alignment is to overlap the two beams from the end of the fibers at spatial points along the free space portion using an IR card.*

Once alignment is accomplished and an isolator is placed in the cavity, a spectrometer is placed at the output of the PBS. By varying the wave plates, it is possible to out couple a certain percentage of the dominant lasing mode of the cavity. At this point there is no Kerr rotation due to the insufficient intensity of the CW mode. At a certain out-coupling loss, pump power lasing conditions are matched and the cavity begins to CW lase at a given wavelength if alignment is optimized enough. The lasing wavelength can be shifted by varying the cavity length, due to the coherent superposition condition and this can be accomplished attaching one fiber end output to a translation stage. The lasing wavelength roughly corresponds to the central wavelength of the mode-locked spectrum and gain profile. CW lasing was verified by a spectrometer (A narrow peak on the spectrometer whose width is on the order of the wavelength resolution of the spectrometer was optimized for. Maximization of this

peak over the ASE spectrum was used as an aligning tool). The polarization of the lasing mode is controlled by the output coupling scheme that allows only a **P** polarization after the PBS in the cavity.

Once cavity lasing is accomplished**,** the lasing amplitude is optimized by varying the cavity alignment and verified with a power meter and low pass 1 μm filter. After alignment, the length of the gain fiber was varied to increase the power output of the CW lasing. Because of pump depletion, the end region of the gain fiber can still be net absorptive to the CW signal, lowering the total gain. To verify this, the gain fiber is cut down until the maximum amplitude (out-coupling parameters were varied after each cut) of the CW lasing mode stops increasing. Thus, 10 cm cuts were done to the 1.5m gain fiber. After the first cut the CW lasing amplitude increased, meaning that the gain fiber was depleted near the end (if not one would have to add gain fiber and check). The process was continued until the amplitude was maximized. The gain fiber was at a length of $0.9\text{m} \pm 5$ cm m at the end of this process. The cavity round trip time is now calculated to be:

$$\mathrm{RT} = \frac{\mathrm{L}_1}{\frac{\mathrm{dw}}{\mathrm{dk}_1}|\mathrm{w}_\mathrm{o}} + \frac{\mathrm{L}_2}{\frac{\mathrm{dw}}{\mathrm{dk}_2}|\mathrm{w}_\mathrm{o}} + \frac{\mathrm{L}_3}{\mathrm{c}} \tag{41}$$

$$\mathrm{Rep.\,Rate} = \mathrm{RT}^{-1} \tag{42}$$

$$\frac{\mathrm{dw}}{\mathrm{dk}_\mathrm{x}}|\mathrm{w}_\mathrm{o} = \frac{\mathrm{c}}{\mathrm{n}_\mathrm{x}(\mathrm{w}) + \mathrm{w}\frac{\mathrm{dn}_\mathrm{x}}{\mathrm{dw}}|\mathrm{wo}} \tag{43}$$

Where, the derivative relationship is the group velocity of a pulse centered on the CW wavelength. The derivative is at the corresponding lasing frequency (i.e. at $\mathrm{w}_\mathrm{o} = \frac{\mathrm{c}}{\lambda_\mathrm{o}}$, λ_o is the free space lasing wavelength obtained from the readout of the spectrometer). The dispersion relation is a scalar (reduced from a tensor) due to the isotropy of the dispersion relationship in contained core fiber modes, which is the case for single-mode fiber at these lengths. L_1 is the gain fiber length, L_2 is the length of passive Corning Hi1060 single mode fiber and L_3 is the free-space length of the cavity. Group velocity contributions through the isolator, PBS, HWP and QWP are assumed to be negligible. The group velocity consideration for the DPG arrangement that will be added to the cavity will be assumed to be equivalent to the free-space phase velocity for the calculation.

Fiber Type	Group Velocity	Group Velocity Dispersion
CorActive SM gain fiber	$\sim 2.3 * 10^8 \frac{\mathrm{m}}{\mathrm{s}}$	$39 \frac{\mathrm{fs}^2}{\mathrm{mm}}$
Hi1060 SMF	$\sim 2.3 * 10^8 \frac{\mathrm{m}}{\mathrm{s}}$	$26 \frac{\mathrm{fs}^2}{\mathrm{mm}}$

Table 6:[47] group velocity and dispersion values for the fibers used in the cavity.

Cavity Region	Length	Individual Trip Time
Gain Fiber	0.68m (this value was the final gain fiber length, deviation from 0.90m will be explained later in this section)	2.9ns
SMF Hi1060 Corning	~6m	26ns
Free Space Portion (with the inclusion of the DPG)	0.91m	3ns
Total RT	~32ns, (31MHz)	

Table 7: Cavity Round Trip Time Calculation

2.2.2 Tuning the Diffraction Gratings

The next step in building the stretched-pulse oscillator is to introduce the diffraction gratings as described in section 2.1.3.

From, Eq. (46) the variable total broadening introduced by the diffraction gratings could dictate the global pulse broadening within the pertinent bandwidth of the output pulse from the cavity. Tuning this delay parameter can compensate for total cavity dispersion and dispersion from previous cavity roundtrips. Total cavity dispersion consists of dispersion with non-fiber optical elements and fiber dispersion. By varying the input chirp of the pulse into the fiber, the effective total time delay of an instantaneous frequency per propagation increment step is lower in the fiber. While, the diffraction grating is a distinct element from the fiber, if a negative chirp is added by it, the effective length of pulse broadening past the transform limited version of the pulse is reduced. This results in a higher ratio of non-linear length to dispersion length. This can approximately be represented as an effective β_2 that is lower than the nascent fiber β_2. According to Eq. (26) and (27)**,** this effectively translates to a lower similariton pulse duration and higher amplitude. Eq. (28), shows a positive chirp, thus, the grating stretcher being at a negative GVD is ideal.

The gratings used in the oscillator are reflective gold gratings with a saw-tooth profile maximized for the negative first order transmission in the horizontal polarization **(P)**. The grating transmission efficiency is 92% per pass in the **P** polarization. For the resulting four pass system this translates to a grating transmission efficiency of 72%. Including mirror losses in the arrangement, the overall efficiency is 69%. The gratings are Edmund optics 600 line/mm gratings. The corresponding GVD[51] of the system can be found to be:

$$\theta_1 = \arcsin\left(\frac{\lambda}{g} - \sin\theta_o\right) \tag{44}$$

$$\beta_2|w_o = -\frac{\lambda}{\pi c^2}\left(\frac{\lambda}{g}\right)^2 \frac{1}{\cos\theta_1{}^3} \tag{45}$$

Total group velocity delay (s^2) is then:

$$\text{GVDelay} = \beta_2 d \tag{46}$$

λ (1.03 μm) is the free space wavelength of central frequency w_o. g is the groove spacing of the gratings, θ_1 is the first order angle, from the normal of the grating pair. θ_1 is listed for the most efficient incoming angle operation (45 degrees). d is the normal distance between the two gratings.

Grating Parameter (Edmund Optics)	Value
g	600 lines/mm
$\lvert\theta_1\rvert$	0.785 rad
β_2	$-3.63 * 10^{-24}\ \frac{s^2}{m}$

Table 8: Grating parameters for the double pass diffraction grating arrangement.

The overall β_2 for this grating arrangement is $-3.63 * 10^{-24}\ \frac{s^2}{m}$. The minimum grating spacing is calculated from the highest dispersive optical element other than the fiber. The GVD of the isolator is

$178\,\frac{fs^2}{mm}$ [52]. The isolator length is 25.4mm. This yields a normal distance of 1.25mm for the gratings (a negligible amount).

The grating pair is inserted into the cavity as shown in Fig. 9. The first order from the first grating is found using the grating first order angle calculated above. A power meter is placed after the grating and the power of the amplified spontaneous first order emission is optimized by rotating the first grating (which should ideally be at an incident angle of 45 degrees). The first orders are then propagated to the second grating mounted on a linear translation stage, such that its surface is normal to the stage translation direction. This grating should be parallel to the first grating. If this condition is met, the first order output from this grating consists of a set of parallel beams that do not deviate angularly. The angle of the second grating was tuned such that these beams are parallel. The distance of the mirror used for the backward pass to the second grating is irrelevant to the overall dispersion, since Eq. (46) scales only with the normal distance between the two gratings. Therefore, the mirror was placed as close as possible to the grating to avoid additional round trip time. The mirror was tuned such that the back reflection was slightly below the first, first order line in the second diffraction grating and such that the back reflected spot was directly below the incoming beam spot on the first diffraction grating. The back reflected spot was tuned to be as close in height to the first spot, while still being able to put an output mirror from the system that does not clip the first beam. A retro-reflector need not be considered for the distance range being implemented. After insertion of the grating pair the system was re-aligned using the fluorescent length technique outlined above.

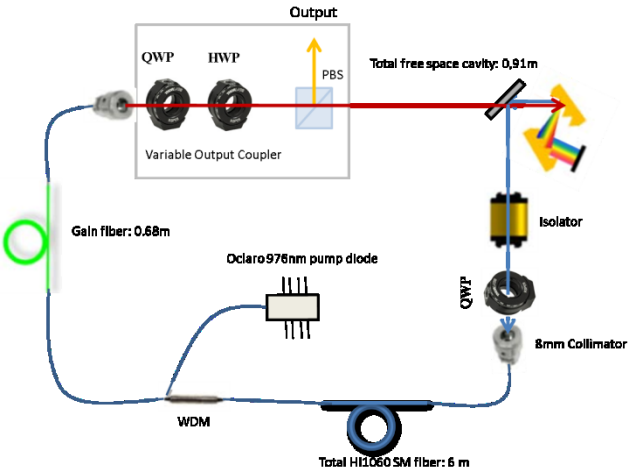

Figure 9: The grating pair is inserted into to the cavity after the PBS. The polarization state after the PBS for cavity coupling is in the P polarization which is what the gratings is optimized for (92% reflection).

A QWP after the isolator was placed in the system as a critical component to ensure an overall elliptical polarization across the optical waveform. At this stage, it is prudent to achieve mode-locking of the fiber oscillator. The net cavity dispersion is in the normal region and all non-negligible contributions now come from the fiber. To mode-lock the system a spectrometer was placed at the output of the cavity. The HWP and QWP were rotated in a random manner. Due to the high amount of evolution pathways to similaritons, mode-locking points in parameter space are dense and stable under small parameter adjustments. Mode-locking should occur rather quickly with this type of parameter adjustment. If no mode-locking was found, the QWP at the entrance of the SMF was incremented to a new position and the procedure was again carried out. If again the oscillator did not mode-lock easily under this random algorithm, the diffraction grating distance was increased by 1 cm.

2.3 Results Discussion

Once mode-locking was found, a pulse train (with the cavity repetition rate) can be observed using an InGaAs fast photodiode (model number DET10A/M, Thorlabs). Peak amplitude scales linearly with the output power and the trace on the photodiode output gives an account of the amplitude noise fluctuations of the pulse. The trace on the photodiode output gives an account of the amplitude noise fluctuations of the pulse. At first cavity parameters such as the wave plates and DPG spacing was varied to minimize the noise. As will be discussed in more detail in the next section, noise originates either from the gain recovery of the gain fiber or by birefringence and wave breaking throughout the fiber length. The first noise source is reduced by varying once more the length of the gain fiber and the second type of noise is reduced by controlling the SMF length. Due to population depletion after a pulse enters the gain fiber, for subsequent round trips, after pumping in between round trips there can still be a portion of the gain fiber that is depleted and hence an absorptive portion. This can result in the overall gain oscillating as a function of round trip number (gain final conditions are different, therefore gain initial conditions are different for subsequent cycles), translating in amplitude fluctuations for the pulse (deemed amplitude bifurcation), this is demonstrated in Fig. 10. Hence, to ensure that the gain stays constant, this depletion region must be removed, so that the pumping time needed for a desired overall gain matches the rep.rate period. In sum: For a given pump time (far from the saturation pump time) and a constant pump signal, increasing fiber length will decrease gain obtained even if the saturation gain of the fiber increases (as indicated in Fig. 11). The achieved gain within the rep. period may be insufficient to balance absorption and out-coupling loss to maintain a net cavity gain of 1, so this process can even result in rep.rate fluctuations as the pulse train seizes due to the lasing being stopped for given time intervals.

More information of this process can be found in [53-55]. A simple simulation tool was used for Fig. 11 where the rate equations were solved as described by Eq. (23) and (24). References [53-55] indicate these effects at μs periods, while the effect is more negligible for higher rep.rates in fiber amplifiers, due to the intricate balance of parameters in fiber oscillators slight modulations in one system parameter can cause ergodic behavior in this highly non-linear system. For example, the amplitude modulation can violate initial conditions and result in higher out coupling losses that the gain cannot compensate. The pulse will decay in energy over subsequent round trips and pulsed operation may seize, resulting in rep.rate deviations (and amplitude fluctuations) in the pulse train.

Thus, the gain fiber was cut and respliced at approximately 5 cm intervals to maximize the signal amplitude on the photodiode pulse train and also to reduce the amplitude fluctuations. Stability was achieved in the first oscillator at new gain length of 0.70+/-0.03m. Gain recovery, will be discussed in great detail in chapter 3 for the solid-state case.

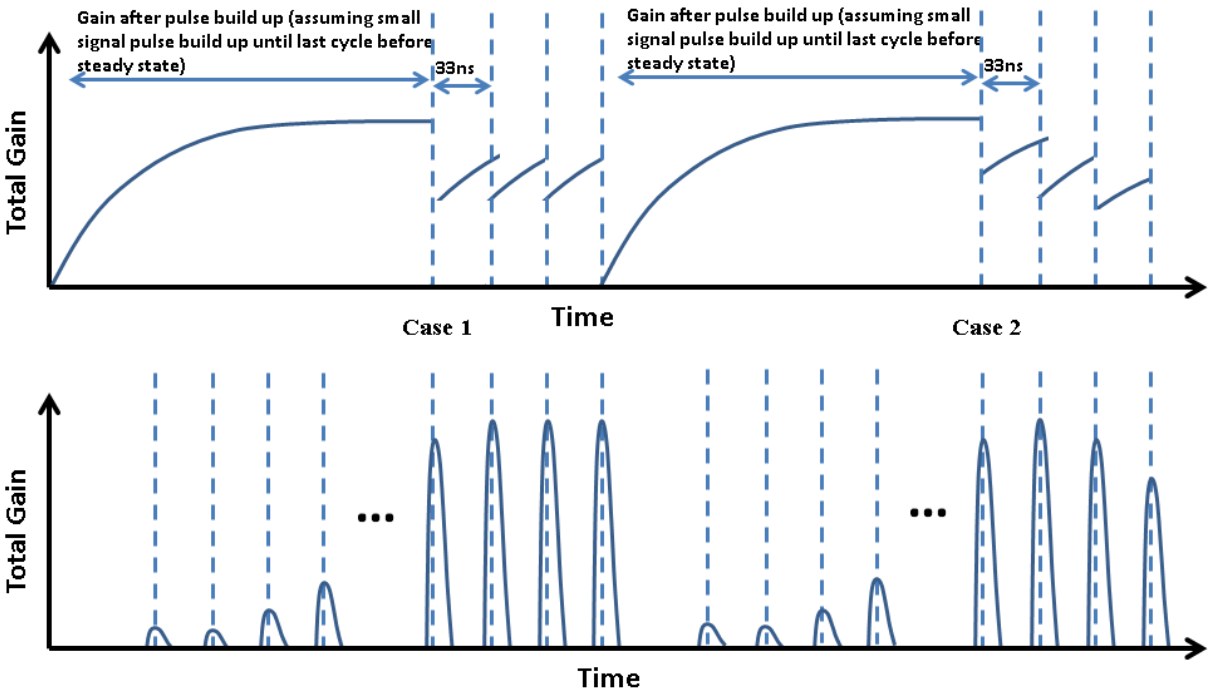

Figure 10: Gain recovery dynamics. In case 1 steady state can be achieved in the pulse amplitude. This is because the gain population relaxes to the same level at the end of the pulse input and increases to the same level before the next pulse input. In case 2, the gain relaxation and pumping oscillates producing different amplitude values of the pulse each time it is inputted in the gain medium. This can cause bifurcation or chaotic behavior.

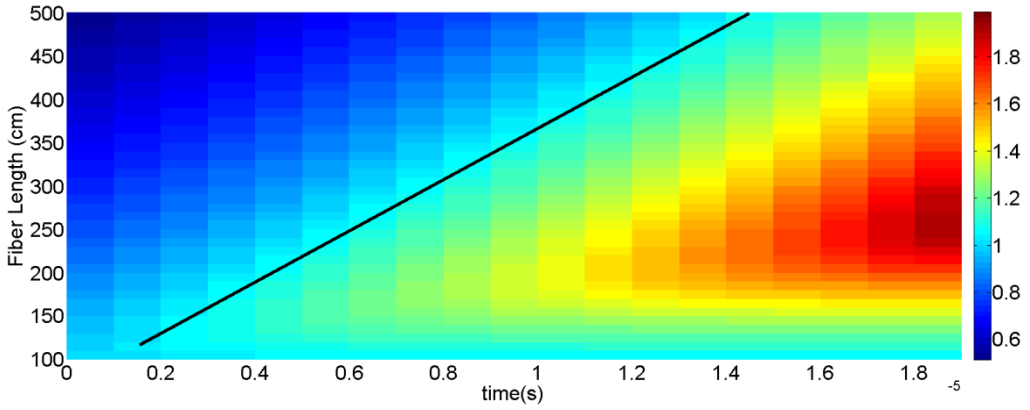

Figure 11: Simulation based pumping time required to obtain a total gain level (represented by the colour) at different fiber lengths (ranging from 100cm to 500cm). The solid black line indicates the linear increase of pumping time to a given gain level (G=1.05) as fiber length is increased.

It is now prudent to list values obtained for the first oscillator that was built. The second oscillator will be discussed later. Mode-locking was initially achieved at a grating distance of 8.3 cm, see Figure 13. In this arrangement the DPG compensates for the one pass linear chirp that accumulates. However, given the discussion in relation to the effective dispersion in the system NLSE, if the DPG distance is increased, it may be possible to achieve shorter pulse durations and higher mode-locked bandwidths as seen in this example. A grating compressor was placed at the output of the oscillator and the pulse was compressed to an autocorrelation trace of FWHM ~93.5fs, see fig. 14. This output pulse can be

approximated as the same as the intracavity pulse before compression, for the following analysis. The compressor contained the same gratings and arrangement as the intracavity DPG. The spacing between the compressor gratings to achieve the minimal auto correlated pulse width was ~2.8cm (see, fig. 12 for setup). The pedestal of the autocorrelation trace indicates third order dispersion (TOD) that was uncompensated. Figure 13 demonstrates the spectral profile. From this a FWHM bandwidth of 40nm is obtained.

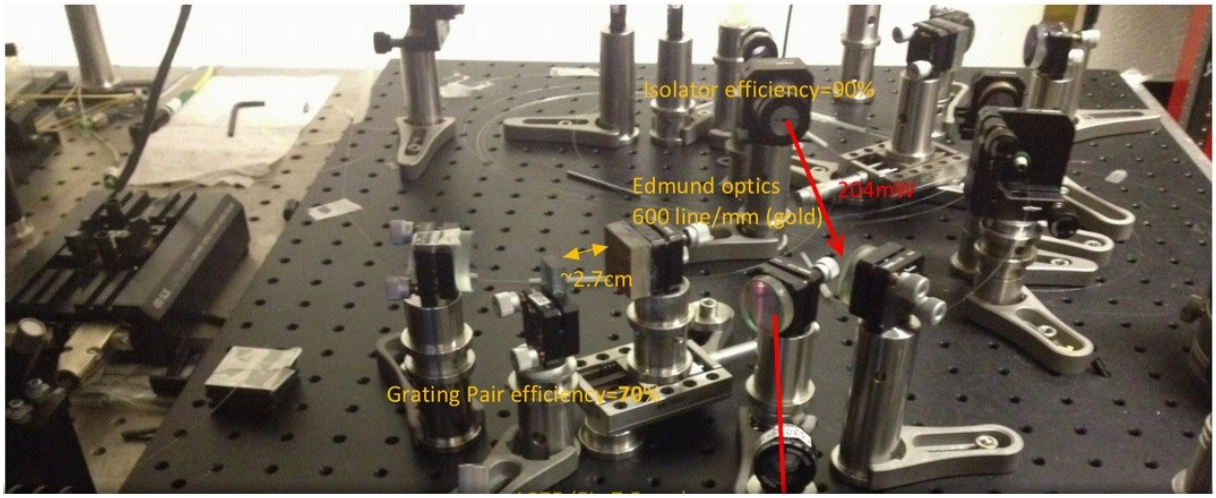

Figure 12: Compressor setup at output of cavity. Grating distance of ~2.8 +/- 0.1cm.

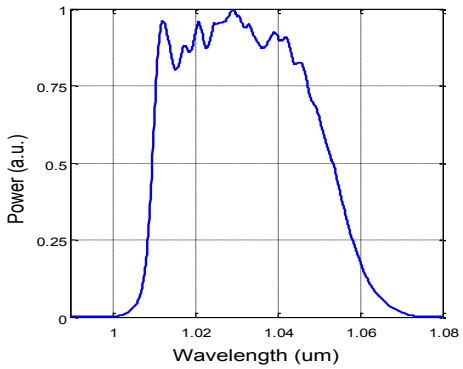

Figure 13: Spectral energy density obtained with an intra-cavity grating distance of 8.3cm and FWHM of 40nm. An average power of 300mw corresponds to this spectrum, and repetition rate of 31 MHz.

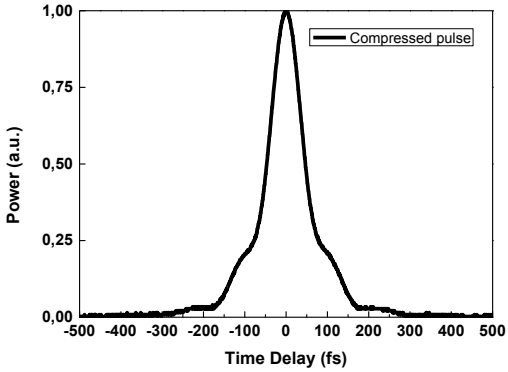

Figure 14: Auto correlated pulse of FWHM ~93.5fs corresponding to the spectrum of Figure 13. Compressor grating was at a distance of 2.8cm.

From table 6 the highest GVD coefficient is $39\frac{\mathrm{fs}^2}{\mathrm{mm}}$. From equation Eq. (28) the instantaneous frequency is given as:

$$\frac{\partial\phi}{\partial\tau} = w_o + \frac{\mathrm{g}}{3\beta_2}\tau \tag{47}$$

From Eq. (46), the total temporal pulse width right before the diffraction gratings (thus, at the output of the cavity) can be obtained as:

$$\Delta\mathrm{t} = 3.63 * 10^{-24}\,\frac{\mathrm{s}^2}{\mathrm{m}} * (2.8\mathrm{cm} - 0.125\mathrm{cm}) * \mathrm{c} * 2 * \pi\frac{40\mathrm{nm}}{1.03\mu\mathrm{m}^2} = 6.9\mathrm{ps} \tag{48}$$

This corroborates nicely with the autocorrelation measurement effectuated on this oscillator output before compression.

Therefore, using Eq. (48) and the highest dispersion coefficient in table 6:

$$w_{max} = w_o + \frac{\mathrm{g}}{3\beta_2}\frac{\Delta\mathrm{t}}{2} \tag{49}$$

$$\mathrm{g} = (\mathrm{w_{max}} - \mathrm{w_o})3\beta_2\frac{2}{\Delta\mathrm{t}} = 3(39000\frac{\mathrm{fs}^2}{\mathrm{m}})\frac{1}{3.63 * 10^{-24}\,\frac{\mathrm{s}^2}{\mathrm{m}} * (2.8\mathrm{cm} - 0.125\mathrm{cm})} = 1.20\mathrm{m}^{-1} \tag{50}$$

For this arrangement. From table 7 giving the cavity lengths, this means that the total gain in the gain fiber is $\mathrm{G} = 2.32$. It is now useful to solve for the intracavity power in the steady state from the overall gain value and the output power. The following equation can be obtained at steady state:

$$\frac{P_{out} + P_{in}}{G} = P_{in@fiber} = (1 - \alpha_{gr})(1 - \alpha_{coupling})P_{in} \tag{51}$$

Where α_{gr} is the normalized percent loss in the grating and $\alpha_{coupling}$ is the normalized percent losses in the coupling back into the fiber. All other losses are negligible and are omitted from the analysis. α_{gr}~0.30, $\alpha_{coupling}$~0.20 (previously obtained from the alignment procedure). Rearranging for P_{in}:

$$P_{in} = -\frac{P_{out}}{\left(1 - G(1 - \alpha_{gr})(1 - \alpha_{coupling})\right)} = 1.00\ \mathrm{watts} \tag{52}$$

The efficiency is thus 30% (average output power is 300mw). It can directly be seen from (52) that $\mathrm{G} > \frac{1}{(1-\alpha_{gr})(1-\alpha_{coupling})}$. This places an upper bound for the losses given an overall gain, G.

Necessary gain filtering to maintain similariton propagation was achieved primarily through the frequency transmission function of the DPG and the gain filtering effect of the gain fiber.

It was also observed that once mode-locking was achieved the pump power could be reduced from the maximal current used of 850mA (corresponding to 625 mw) to 300mA (corresponding to 175mw) and mode-locking was still occurring. This indicates that the cavity itself recovers the pulse under a wide parameter space due to the intensity dependent polarization rotation that occurs. If gain is minimized,

the peak intensity of the pulse will be lower and non-linear polarization rotation will be minimized. Thus, the out-coupling loss of the cavity lowers accordingly. Therefore, if constant losses such as losses in the DPG and in-coupling are minimal as compared to the reduced gain, the overall cavity loss is reduced with lower gain and the cavity absorption does not exceed the gain. This is yet another advantage to NPR mode-locking as compared to other schemes where there is a constant out-coupling loss and therefore, cavity lasing is tightly constrained to pump power and a specific crystal gain.

2.3.1 Deviations from the Similariton Model

It is worthy to note that referring to Fig. 15, the output spectrum does not entirely corroborate a pure similariton spectrum. There are four experimentally relevant reasons for this:

1) The gain coefficient profile of the gain fiber is not constant as a function of propagation length but is a decaying exponential function. Thus, the system NLSE used is only approximate.
2) The spectrum of the out coupled pulse is not that of the intracavity pulse (refer to subsection 2.1.3 in the discussion of the polarization rotation intensity profile in the out coupling polarization coordinate).
3) TOD is uncompensated for and not considered in the system NLSE.
4) The system does not consist of one continuous fiber block but discrete fiber sections (SMF, gain fiber, SMF pigtail of the WDM). Once again deviating from the system equations.
5) Added birefringence in the fiber from mechanical strain and gain recovery noise contribute to deviations.
6) Higher order non-linearities, i.e. self-steepening are not considered in the system NLSE.
7) The DPG spacing parameter offers an extra degree of freedom that can account for some of these effects but does not perfectly balance with all.

Parameters (i.e., by varying the diffraction grating inter-distance to 9cm) were varied to obtain the spectrum in fig. 15. This spectrum is closer to the similariton profile (parabolic around the peak). However, there are two additional side band peaks that deviate from the norm. Varying the DPG further than 9cm resulted in the loss of stability and mode-locking.

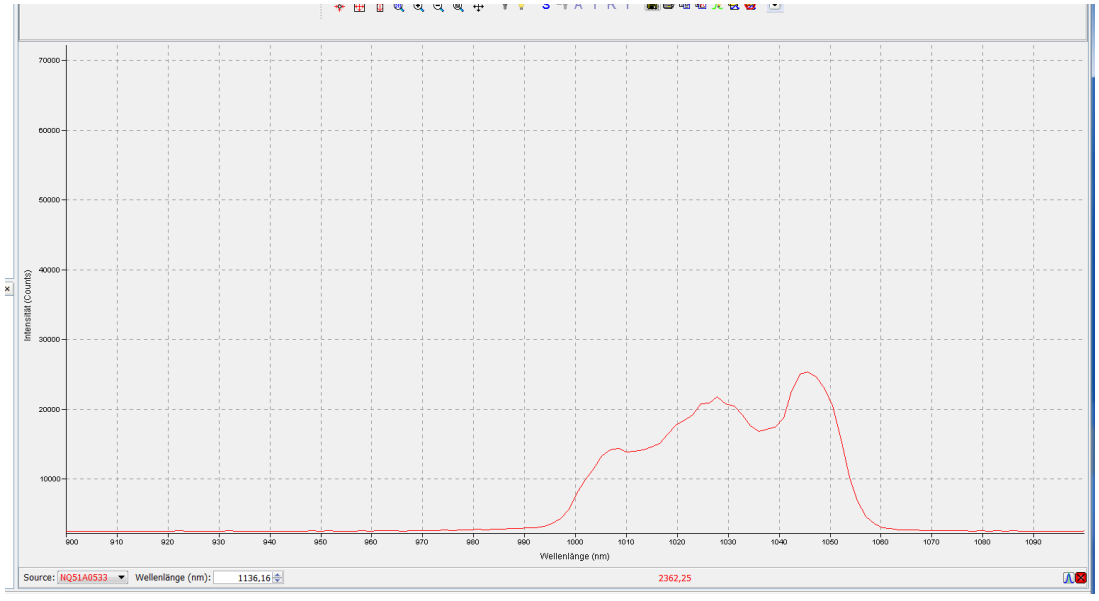

Figure 15: Spectrum obtained that resembles more closely a similariton spectrum. Side-band generation is visible as well.

2.3.2 Final fiber lengths and cavity arrangement of first oscillator:

Please refer to table 8 for final fiber lengths and free-space lengths. The final cavity inter-grating distance was 9cm. The cavity sketch and picture is presented in Fig. 16.

a)

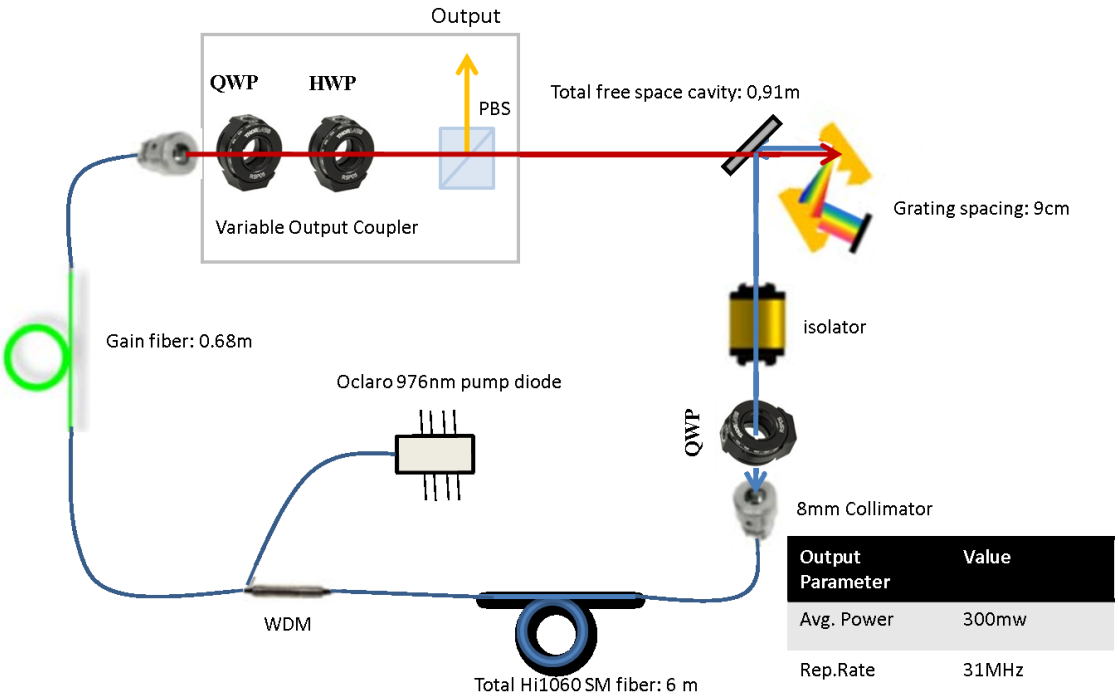

Output Parameter	Value
Avg. Power	300mw
Rep.Rate	31MHz
Pulse Duration (before Compression)	1,1ps (1.6ps autocorrelated)

b)

Figure 16: a) Picture of the final setup and b) Sketch indicating fiber lengths.

2.3.3 Spectra and Cavity Arrangement of Second Oscillator

A listed goal for the second oscillator that was built was to improve the spectrum of the first oscillator and to generate a spectrum closer to the similariton profile at the output or a Gaussian spectrum. A Gaussian spectrum can yield more information of the pulse duration and minimize the pedestal in the auto correlated pulse. In order to control this, parasitic non-linearities such as additional birefringence that induces different NLSE (Eq. (29) and (30)) regions in the cavity that limit the evolution of the similariton pulse or inhibit it were reduced. The length of the SMF was decreased. Varying the SMF length can be compared to the fine tuning knob of the experiment, while varying the gain length is akin to the coarse knob. This is because a lot more SMF has to be cut to decrease the rep.rate period on relevant time scales, compared to the amount of gain fiber needed to substantially change the gain and the gain pumping time of the system.

This may have also reduced the effective length of higher order non-linearities such as self-steepening (will be discussed in chapter 4) that contributes to side band creation.

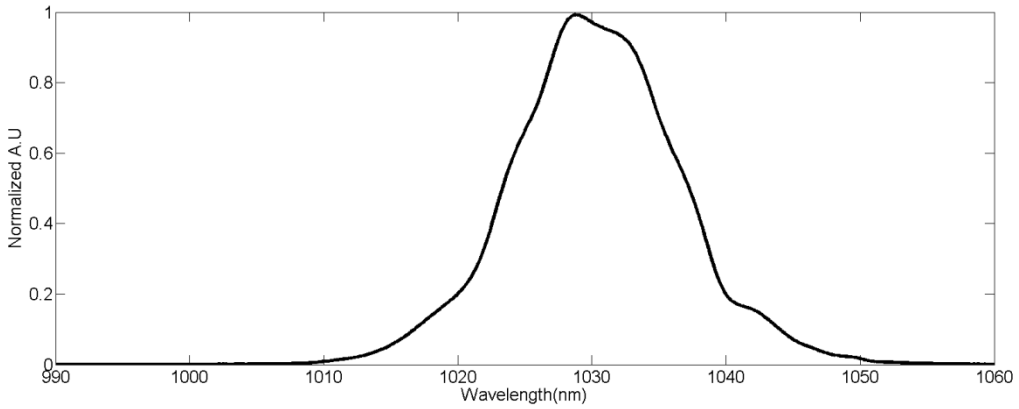

Figure 17: Closer to Gaussian spectrum observed in OSC 2. More of an emphasis in cutting down the Hi1060 SM fiber to match the gain dynamics and to limit parasitic non-linearity over large fiber lengths was placed.

Cavity Region	Length	Individual Trip Time
Gain Fiber	0.59m	2.5ns
SMF Hi1060 Corning	~3.83m	16.6ns
Free Space Portion (with the inclusion of the DPG)	1.24m	5.4ns
Total RT	~24.5ns, (41MHz)	

Table 9: Cavity arrangement of second oscillator.

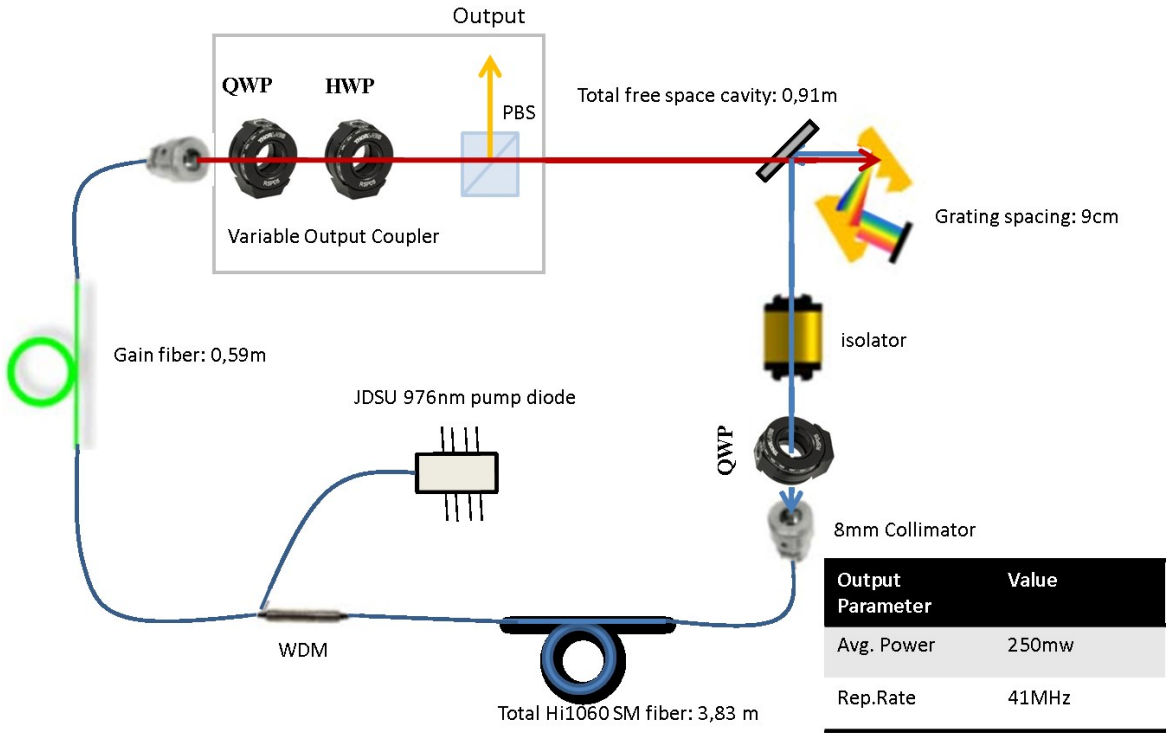

Figure 18: Schematic of OSC 2 Design.

2.3.4 Other Results

A RIN evaluation[56] was obtained for Osc 1 and results are presented :

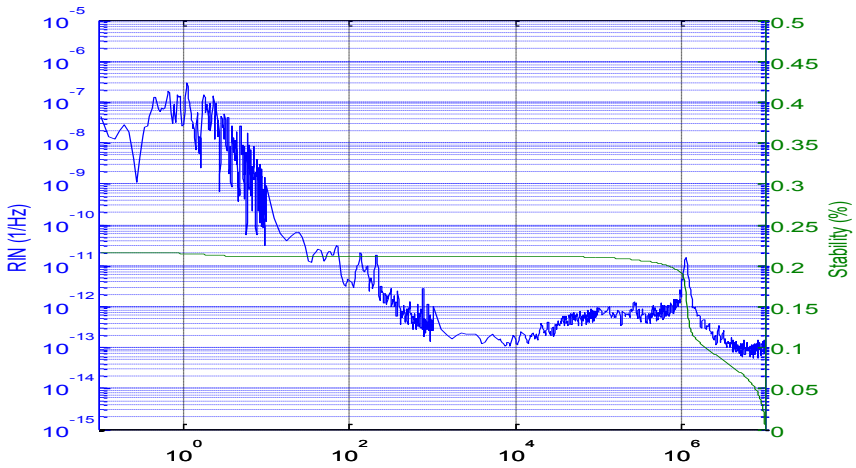

Figure 19: RIN noise evaluation of Osc 1. Frequencies past 10000 Hz are substantially attenuated. Average stability is 0.2%.

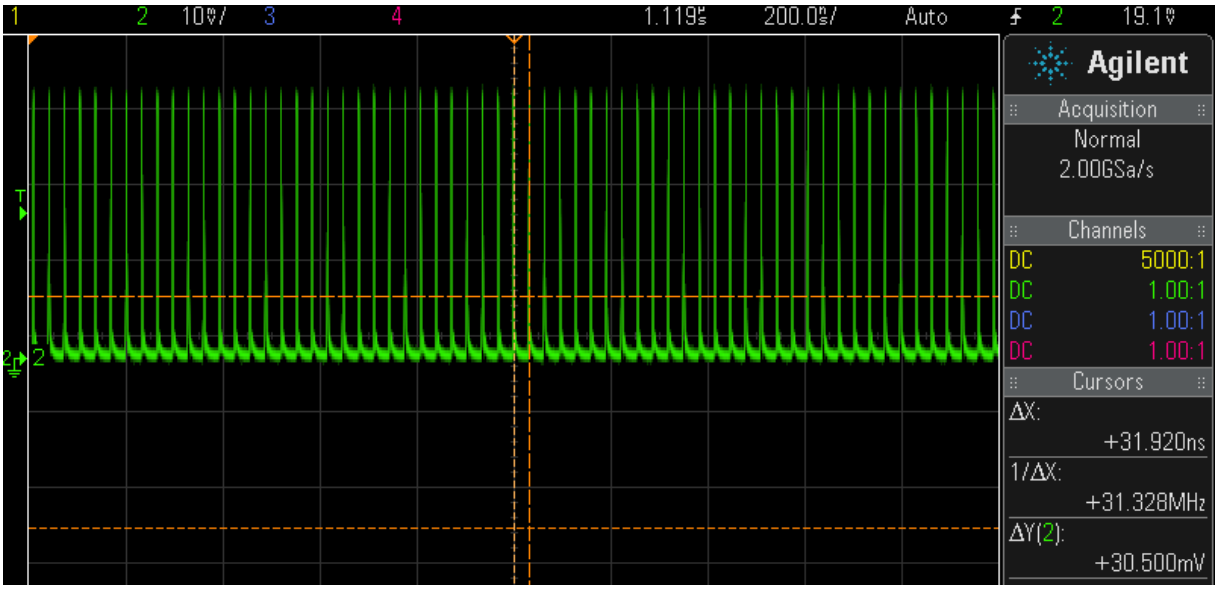

Figure 20: Amplitude stability of oscillator 1 over a large time window. This photodiode trace corroborates well with the RIN measurement of 0.2% amplitude fluctuations.

The wide bandwidth pulses achieved with this type of fiber oscillator, the high average power of 300mw and the sub 90fs compressed pulse duration of the oscillator has never been achieved before in this combination to the best of my knowledge. The characterization of the system is also novel. The system self-starts in the sense that if the pump current is turned to 800mA mode locking will happen. The self-starting stability is a surprising result and the exact reasons why will be explored in future work.

2.4 Spectrometer as a Valuable Tool for Multiple Pulsing Evaluation

The spectral profile is inherently different from the spontaneous emission profile and has sharp cut-offs due to the similariton character of the pulse. Once mode-locking was achieved, the QWP at the entrance of the SMF was perturbed to increase the bandwidth of the mode-locked spectrum. As well, all other wave-plates were varied. The HWP contributes the most to out-power coupling (due to the fact that it rotates the global polarization state to align with the out-coupling axis of the PBS). Under small perturbations, power can be out-coupled in a linearly increasing manner while maintaining the spectral profile of the pulse (due to the dense mod-locking points in parameter space). The QWP at the pump side was varied to maximize spectral bandwidth, while the HWP was varied carefully to out-couple as much power as possible while still maintaining the spectrum. The diffraction grating spacing was also tuned to increase the spectral bandwidth.

The oscillations on the spectral energy density profile of the spectrometer indicate double pulsing within the cavity. The period of oscillation in this spectral domain scales inversely with the separation in time of the two pulses. For example, in frequency space the measurement on the spectrometer is the spectral energy density($J * s$) which would be:

$$|B(w)|^2 = |A_1(w)|^2 + |A_2(w)|^2 + A_1(w)^* A_2(w)\, e^{i\tau_o w} + A_2(w)^* A_1(w)\, e^{-i\tau_o w} \tag{53}$$

Where the above is obtained by taking the modulus square of:

(54)

$$B(w) = A_1(w) + A_2(w)e^{i\tau_o w}$$

B is the spectral energy density of the final optical waveform describing the two pulses separated by τ_o.

For two identical pulses of different amplitude constants the above reduces to:

$$|B(w)|^2 = |A_1(w)|^2 + |A_2(w)|^2 + \frac{2}{h}|A_1(w)|^2 \cos(\tau_o w) \quad (55)$$

Where, $h = \frac{A_2(w)}{A_1(w)}$ for this two identical pulse arrangement. From the triangle inequality, it can be shown that $|B(w)|^2$ is never zero unless h=1. Therefore, a perturbative oscillation on the original spectrum will be observed in this case.

In lambda space (with lambda values corresponding to free-space values), the above becomes (now in units of $(\frac{J}{nm})$):

$$|B(\lambda)|^2 = [(1+h)|A_1(\lambda)|^2 + 2h|A_1(\lambda)|^2 \cos\left(\tau_o \frac{c}{\lambda}\right)]\frac{c}{\lambda^2} \quad (56)$$

The oscillation amplitude can determine h and the oscillation period can determine τ_o. Thus, the secondary pulse amplitude can be determined and its delay in time can be fully mapped. For more complicated arrangements in this double pulsing scenario Eq. (53) can determine the dynamics. The following analysis can easily be extended to triple pulsing, etc.

Spectrometer property	Value	Timing interval that can be determined
Window size	100nm	$2\frac{{\lambda_o}^2}{c\Delta\lambda} = 35\text{fs}$
Resolution	5nm	$2\frac{{\lambda_o}^2}{c\Delta\lambda} = 70\text{ps}$

Table 10: Typical values of the spectrometer that were used in the experimental set up are indicated in this table. From the window size obtained from when the spectrum goes to the noise level and from the resolution, one can obtain the minimal pulse delay that can be detected and the maximal pulse delay that can be detected from the spectrometer at central wavelength for both calculations assumed to be ~1.03 μm. Factor of 2 arises from the assumption that one could only detect the modulation if it goes to a max and zero.

Therefore, pump power as well as the cavity parameters just listed were tuned to reduce these oscillations, i.e. by lowering pump power. If double pulsing is occurring and the variations of the above listed parameters do not reduce the double pulse, than wave-breaking is the most likely the cause. Reducing the fiber length will reduce the effective length of these higher order non-linearities (not reflected in the above system NLSE).

There are several ways to know that the cavity is mode-locked without the use of a spectrometer. With the use of an IR viewer one can see the scattered radiation of the first order line on the second diffraction grating. The width of the line corresponds directly to the bandwidth of the locked pulse in the cavity. The intensity profile of the line corresponds to the spectral shape.

Other aspects can be characterized such as double pulsing that occurs on the ns timescale, amplitude deviations that are not time-fluctuating, and rep. rate fluctuations on the ns scale (phase noise), with

the use of a photodiode. Double pulsing below the 35fs limit can be characterized by the use of an auto correlator (double pulsing would result in 3 pulses on the autocorrelation with the same time delay as the double pulse).

2.5 After the Oscillator: Accousto-Optic Modulator (AOM), Stretcher Fiber and Pre-Amplifier

For inputting the pulse into the regenerative amplifier (REGEN) discussed in the next section, it is important to down convert the repetition rate and to stretch the pulse to 500ps (the measurement was verified with a fast RF oscilloscope). At this stage it is important to have polarization stability, because of the REGEN being polarization sensitive. Amplitude fluctuations of the pulse train being inputted into the REGEN will result if the polarization state is not maintained. The pulse was stretched to 500ps by the use of a double pass stretcher fiber system (to maintain the polarization state of the pulse). After the stretcher fiber a polarization maintaining (PM) fiber AOM was used to down-convert the repetition rate to a pulse train period of 10μs (it is only necessary that the incoming rep. period is longer than the cavity period of the pulse inside the REGEN). Due to the losses in the stretcher/AOM system, a fiber pre-amplifier was used before the AOM. The system is described in Fig 21. The pulse energy after the stretcher+fiber pre-amplifier+AOM was 1.6nJ. Losses are summarized in Table 12.

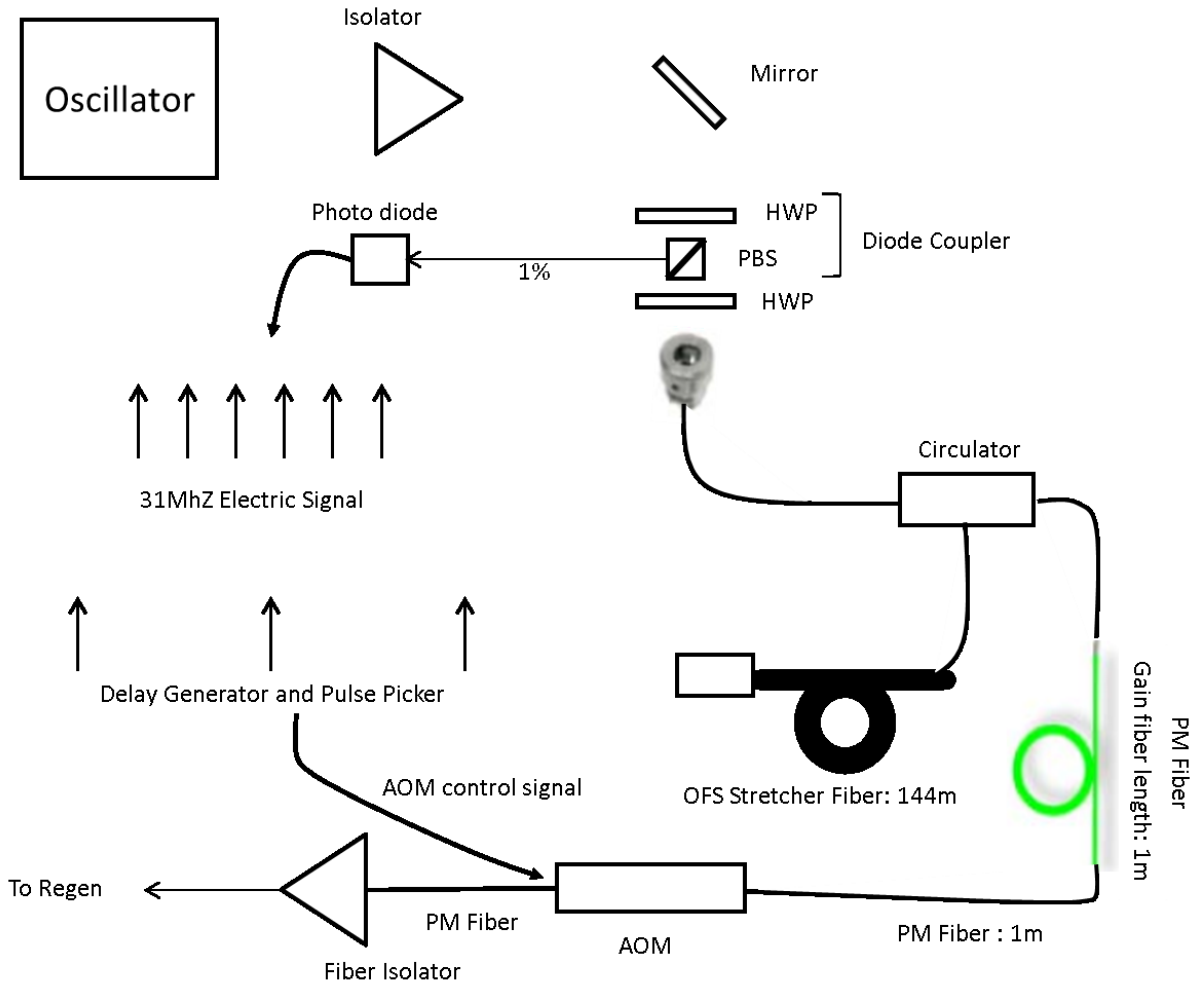

Figure 21: System after the oscillator. HWP at entrance of circulator ensures proper polarization in the PM fiber branch.

The double pass system of the stretcher fiber works as follows: Light goes through the circulator and into port 2 (which is the port for incoming light).The faraday rotator and mirror introduces a π phase in the polarization state of the signal after the stretcher fiber, the pulse is then sent back into the stretcher fiber, canceling out the polarization effects in the stretcher fiber. On the second pass light is now circulating backwards. The fiber circulator then outputs light into port 3 which is the port for backward propagating light. The circulator directionally selects which port light is outputted to. After port 3 light is then passed through a gain fiber.

The stretcher fiber is optimized for the in coupling of a higher order mode (but still single-mode) that carries a lower modal third order dispersion. The modal second order dispersion coefficient is such that given a gold compressor consisting of 1200lines/mm, and optimized at 45 degrees input angle, the spacing between the diffraction gratings is 1 meter.

Losses are high because of the fiber diameter core mismatch between the Hi1060 single mode fiber **(~6μm)** and the smaller core of the stretcher fiber**(2.86μm)**. Table 11 contains pertinent stretcher fiber parameters. This translates into both aperture losses and losses because of the overlap integral between the single mode higher order mode of the stretcher fiber and the single mode Gaussian of the corning fiber. Furthermore, Light is outputted and inputted from/to the fiber into Hi1060 fiber through an adapter and connectors, increasing the losses. As well, due to the length of the fiber, absorptive losses in the fiber are non-negligible. The losses in the AOM arise because of coupling losses within the AOM box. The AOM was ordered from Gooch&Housego and cannot be modified in the lab.

Property of stretcher fiber	Value
Fiber length	137.4m
GVD	18.935 ps^2
Insertion loss per end	>3dB

Table 11: Pertinent properties of the OFS custom stretcher fiber (Obtained from OFS).

The length of the Gain fiber was optimized at saturation. Pump power was decreased to preserve spectrum and to minimize gain filtering effects (see fig**.** 22).

Component	% insertion Loss
Stretcher Fiber	80%
AOM	60%
Overall Losses	92%
Fiber Pre-Amplifier	Overall Gain: 2
Pulse Output	$10\text{nJ} * 0.2 * 2 = 1.6\text{nJ}$

Table 12: Gain and Losses in fiber stretcher and AOM stages.

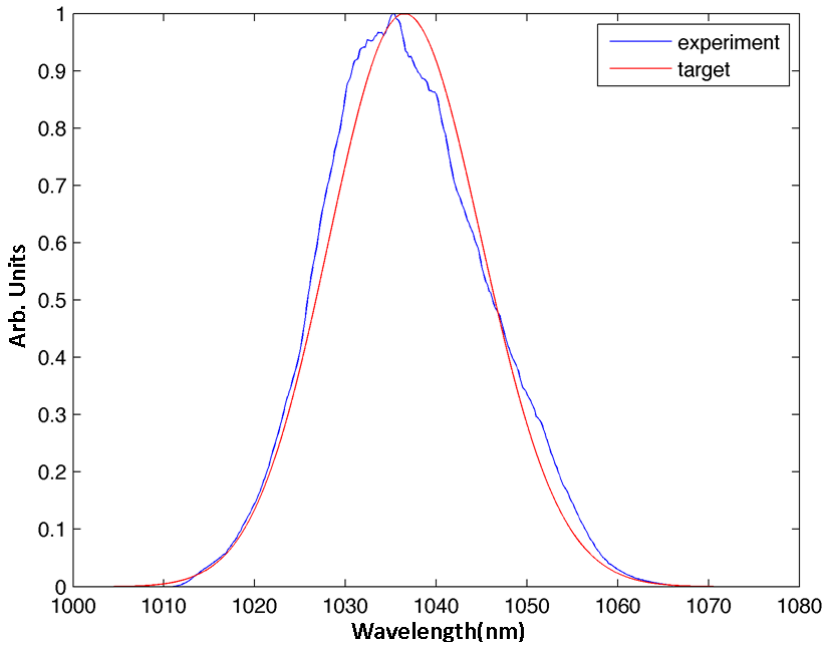

Figure 22: Normalized spectrum after the gain fiber system (at a pump power of 600mW). The target spectrum consists of sech^2 fit to the desired central wavelength of the amplified pulse to be fed into a large core fiber amplifier system. This is not pertinent for the final system consisting of the fiber oscillator regenerative amplifier system. Due to the relatively good fit with a sech^2 profile, any autocorrelation of the stretched pulse can assume a sech^2 input to calculate the pulse duration. Data was fitted and plotted by Damian Schimpf.

2.6 Summary

Two NPR mode-locked stretched pulse fiber ring oscillators at 1.03 μm have been constructed. Both of which have average powers between 250-300mW at rep rates of 31 MHz and 44Mhz. Pulses were compressed to durations lower than 90fs, and amplitude fluctuations were minimized. The average stability of intensity fluctuations is roughly 0.2%, which surpasses the amplitude noise performance of Ti:Sapphire lasers (Coherent) currently being used in electron diffraction experiments. Experimental results match well with the theoretical description of the system both of which were extensively discussed in this chapter. Both the average power of the oscillators, the stability and the footprint out-compete laboratory Ti:Sapphire systems and demonstrate that these novel fiber oscillators can be used for electron diffraction experiments.

The oscillator pulses were in-coupled to an AOM PM fiber system, a stretcher fiber and a fiber PM pre-amplifier. The pulse energy is 1.6 nJ at the output of this system. The next chapter will explore the construction of a regenerative amplifier to achieve pulse energies on the order of 0.5mJ.

2.7 Experimental Extensions and Future Prospects

The first oscillator that was described in this section was used in an experiment during my time at MIT. The experiment consisted of generating Cherenkov radiation [57] in a short (3.3cm) segment of photonic crystal fiber. The average power of the oscillator was sufficient to generate an octave spanning spectrum. More details of the experiment can be found in [57]. The supercontinuum pulses at the output of the photonic crystal fiber were compressed to sub 11fs at an average power of 7.5mW.

The next steps for the oscillators will be to integrate fiber components for the free-space components to increase stability and to minimize the footprint of the oscillator even further. Fiber wave plates can be constructed from inducing controlled strain on the fiber and creating a corresponding birefringence, the gratings can be replaced with fiber engineered Bragg gratings and the PBS, isolator can be constructed with fiber pigtailed components.

The coupling and mode shaping into the stretcher fiber will be accomplished by taper splicing the Corning fiber to the stretcher fiber. This will substantially reduce losses.

Chapter 2 Bibliography

1 Yariv, Amnon, and Pochi Yeh. *Photonics: optical electronics in modern communications (the oxford series in electrical and computer engineering)*. Oxford University Press, Inc., 2006.

2 Galvanauskas, Almantas. "High power fiber lasers." *Optics and photonics news* 15.7 (2004): 42-47.

3 Stutzki, Fabian, et al. "26 mJ, 130 W Q-switched fiber-laser system with near-diffraction-limited beam quality." *Optics letters* 37.6 (2012): 1073-1075.

4 Carruthers, Thomas F., and Irl N. Duling. "10-GHz, 1.3-ps erbium fiber laser employing soliton pulse shortening." *Optics letters* 21.23 (1996): 1927-1929.

5 Clark, T. R., et al. "Phase noise measurements of ultrastable 10 GHz harmonically modelocked fibre laser." *Electronics Letters* 35.9 (1999): 720-721.

6 Wu, Chiming, and Niloy K. Dutta. "High-repetition-rate optical pulse generation using a rational harmonic mode-locked fiber laser." *Quantum Electronics, IEEE Journal of* 36.2 (2000): 145-150.

7 Sobon, Grzegorz, et al. "10GHz passive harmonic mode-locking in Er–Yb double-clad fiber laser." *Optics Communications* 284.18 (2011): 4203-4206.

8 Chen, Hung-Wen, et al. "3 GHz, Yb-fiber laser-based, few-cycle ultrafast source at the Ti: sapphire laser wavelength." *Optics letters* 38.22 (2013): 4927-4930.

9 Chong, Andy, et al. "All-normal-dispersion femtosecond fiber laser." *Optics Express* 14.21 (2006): 10095-10100.

10 Renninger, William H., Andy Chong, and Frank W. Wise. "Self-similar pulse evolution in an all-normal-dispersion laser." *Physical Review A* 82.2 (2010): 021805.

11 Stolen, R. H., and Chinlon Lin. "Self-phase-modulation in silica optical fibers." *Physical Review A* 17.4 (1978): 1448.

12 Tomlinson, W. J., R. H. Stolen, and C. V. Shank. "Compression of optical pulses chirped by self-phase modulation in fibers." *JOSA B* 1.2 (1984): 139-149.

13 Lin, Gong-Ru, Ci-Ling Pan, and Ying-Tsung Lin. "Self-steepening of prechirped amplified and compressed 29-fs fiber laser pulse in large-mode-area erbium-doped fiber amplifier." *Lightwave Technology, Journal of* 25.11 (2007): 3597-3601.

14 Liu, Xueming. "Mechanism of high-energy pulse generation without wave breaking in mode-locked fiber lasers." *Physical Review A* 82.5 (2010): 053808.

15 Ilday, F. Ö., et al. "Self-similar evolution of parabolic pulses in a laser." *Physical review letters* 92.21 (2004): 213902.

16 Calendron, Anne-Laure, et al. "High power and high energy Yb: KYW regenerative amplifier using a chirped volume Bragg grating." *Conference on Lasers and Electro-Optics*. Optical Society of America, 2009.

17 Galvanauskas, Almantas, et al. "High peak power pulse amplification in large-core Yb-doped fiber amplifiers." *Selected Topics in Quantum Electronics, IEEE Journal of* 13.3 (2007): 559-566.

18 Sciaini, Germán, and RJ Dwayne Miller. "Femtosecond electron diffraction: Heralding the era of atomically resolved dynamics." *Reports on Progress in Physics* 74.9 (2011): 096101.

19 Dwyer, Jason R., et al. "Femtosecond electron diffraction:'making the molecular movie'." *Philosophical Transactions of the Royal Society of London A: Mathematical, Physical and Engineering Sciences* 364.1840 (2006): 741-778.

20 Kahn, Joseph M., and John R. Barry. "Wireless infrared communications." *Proceedings of the IEEE* 85.2 (1997): 265-298.

21 R. Paschotta, article on 'Optical Fiber Communications' in the Encyclopedia of Laser Physics and Technology, accessed on 2015-06-24

22 Bülend Ortaç, Ammar Hideur, Thierry Chartier, Marc Brunel, Cafer Özkul, and François Sanchez, "90-fs stretched-pulse ytterbium-doped double-clad fiber laser," Opt. Lett. **28**, 1305-1307 (2003)

23 R. Paschotta, article on 'Ytterbium-doped Gain Media' in the Encyclopedia of Laser Physics and Technology, accessed on 2015-06-24

24 Yablon, Andrew D. *Optical fiber fusion splicing*. Vol. 103. Springer Science & Business Media, 2005.

25 Saleh, Bahaa EA, Malvin Carl Teich, and Bahaa E. Saleh. *Fundamentals of photonics*. Vol. 22. New York: Wiley, 1991.

26 Image was obtained from the following website: http://www.snipview.com/q/Mode_field_diameter

27 Rothenberg, Joshua E. "Space–time focusing: breakdown of the slowly varying envelope approximation in the self-focusing of femtosecond pulses." *Optics Letters* 17.19 (1992): 1340-1342.

28 Shen, Yuen-Ron. "Principles of nonlinear optics." (1984).

29 Rühl, Axel. *The normal dispersion regime in passively mode-locked fiber oscillators*. Cuvillier Verlag, 2008.

30 Mukhopadhyay, P. K. "Femtosecond pulse generation and amplification in Yb-doped fibre oscillator-amplifier system." *Pramana* 75.5 (2010): 787-805

31 Keller, Ursula, et al. "Semiconductor saturable absorber mirrors (SESAM's) for femtosecond to nanosecond pulse generation in solid-state lasers." *Selected Topics in Quantum Electronics, IEEE Journal of* 2.3 (1996): 435-453.

32 Kaertner, Franz. Ultrafast Optics. Lecture notes, 2013.

33 Boyd, Robert W. *Nonlinear optics*. Academic press, 2003.

34 Saleh, Bahaa EA, Malvin Carl Teich, and Bahaa E. Saleh. *Fundamentals of photonics*. Vol. 22. New York: Wiley, 1991.

35 M. E. Fermann, V. I. Kruglov, B. C. Thomsen, J. M. Dudley, and J. D. Harvey. Self-similar propagation and amplification of parabolic pulses in optical fibers. *Physical Review Letters*, 84:6010–6013, 2000.

36 "Mode locked fiber lasers: theoretical and experimental developments."
PhD diss., Department of Physics and Astronomy, University of Aarhus, 2006.

37 Renninger, W. H., A. Chong, and F. W. Wise. "Dissipative solitons in normal-dispersion fiber lasers." *Physical Review A* 77.2 (2008): 023814.

38 Buckley, J. R., et al. "Femtosecond fiber lasers with pulse energies above 10 nJ." *Optics letters* 30.14 (2005): 1888-1890.

39 Finot, Christophe, et al. "Parabolic pulse evolution in normally dispersive fiber amplifiers preceding the similariton formation regime." *Optics express* 14.8 (2006): 3161-3170.

40 Ulrich, Rashleigh, S. C. Rashleigh, and W. Eickhoff. "Bending-induced birefringence in single-mode fibers." *Optics letters* 5.6 (1980): 273-275

41 Thorlabs: fiber waveplates

42 Oktem, Bulent, Coşkun Ülgüdür, and F. Ömer Ilday. "Soliton–similariton fibre laser." *Nature Photonics* 4.5 (2010): 307-311.

43 Gatz, S., and J. Herrmann. "Soliton collision and soliton fusion in dispersive materials with a linear and quadratic intensity depending refraction index change." *Quantum Electronics, IEEE Journal of* 28.7 (1992): 1732-1738.

44 R. Paschotta, article on 'Dispersion' in the Encyclopedia of Laser Physics and Technology, accessed on 2015-06-24

45 Ishio, Hideki, Junichiro Minowa, and Kiyoshi Nosu. "Review and status of wavelength-division-multiplexing technology and its application." *Journal of Lightwave Technology* 2 (1984): 448-463.

46 R. Paschotta, *et al.*, "Lifetime quenching in Yb doped fibers", Opt. Commun. 136, 375 (1997)

47 Obtained from Cor-Active, and Corning

48 Liu, Anping. "Suppressing stimulated Brillouin scattering in fiber amplifiers using nonuniform fiber and temperature gradient." *Optics express* 15.3 (2007): 977-984.

49 Kovalev, V. I., and R. G. Harrison. "Suppression of stimulated Brillouin scattering in high-power single-frequency fiber amplifiers." *Optics letters* 31.2 (2006): 161-163.

50 Keiser, Gerd. *Optical fiber communications*. John Wiley & Sons, Inc., 2003.

51 Vodopyanov, K. L. "Handbook of nonlinear optics, by Richard L. Sutherland." *Optics & Photonics News* 8 (1997): 54-55.

52 Thorlabs correspondance

53 Desurvire, Emmanuel, C. Randy Giles, and Jay R. Simpson. "Gain saturation effects in

high-speed, multichannel erbium-doped fiber amplifiers at λ= 1.53 μm." *Lightwave Technology, Journal of* 7.12 (1989): 2095-2104.

54 Bononi, Alberto, and Leslie Rusch. "Doped-fiber amplifier dynamics: A system perspective." *Lightwave Technology, Journal of* 16.5 (1998): 945-956.

55 J. Dörring *et al.*, "Period doubling and deterministic chaos in continuously pumped regenerative amplifiers", Opt. Express 12 (8), 1759 (2004)

56 R. Paschotta, article on 'Relative Intensity Noise' in the Encyclopedia of Laser Physics and Technology, accessed on 2015-06-26

57 Chen, Hung-Wen, et al. "Yb-fiber oscillator based, few-cycle ultrafast source at 850nm." *Lasers and Electro-Optics Pacific Rim (CLEO-PR), 2013 Conference on*. IEEE, 2013.

Chapter 3: The Design of a Regenerative Amplifier for Pulse Amplification

In order to provide sufficient energy for down source electron diffraction and pump probe experiments, the pulse energy from the oscillator must be amplified to hundreds of μJ, as described in the introduction. This chapter will describe the design of a regenerative amplifier that achieved 400 μJ pulse energies, and how to scale the design to achieve ideal pulse energies >1mJ.

Single pass fiber amplifiers hold potential as an amplification source to 1mJ pulse energies, however, there are extensive problems with these amplifiers such as:

1) Peak intensities and intensity gradients of the confined mode can generate parasitic non-linearities that introduce self-steepening effects, pulse breaking or SPM that results in practically incompressible optical waveforms (for example, instantaneous frequencies are not linearly chirped).
2) Peak intensities generated by self-focusing mechanisms may damage the fiber (i.e., photo darkening effects) or plasma effects.
3) Brillouin scattering may generate amplified optical radiation that damage optical components.

However, there are solutions to these problems and mJ fiber sources have been developed[11]. The advantages of designing a solid-state regenerative amplifier (REGEN) are: that the accumulated non-linear phase is lower (due to the larger beam size) and the length of the solid-state material (on the scale of mm). The extractable energy is higher, due to higher doping possible in solid-state material (hence-wise, why the propagation length through the crystal is small as compared to fiber) and the technology is safer for downstream (and upstream) components.

The REGEN consists of a closed free-space cavity with a gain crystal. The crystal is pumped and a population inversion is achieved. The signal pulse is coupled into the cavity by the use of a PBS, Pockel Cell arrangement that actively rotates its polarization state so that the pulse is trapped in the cavity for a given amount of time. After multiple passes through the gain crystal, the pulse is coupled out of the cavity through a polarization rotation by the re-activation of the Pockel cell.

The REGEN is inherently a laser cavity and the first stage of its construction is to get CW lasing with the pumping of the gain crystal. The CW lasing output is maximized through optimizing the alignment of the cavity and pump. As well, cavity losses are characterized at this stage. The second step is to Q-switch the REGEN. In the Q-switched operation, the Pockel cell is further aligned to optimize the Q-switching signal. As well, the average Q-switched power roughly corresponds to the pulse amplification power. In the last step, the pulse is seeded into the cavity. Again the Pockel cell alignment is optimized to maximize the pulse amplification.

In the design of the REGEN the following considerations must take place to achieve a desired pulse energy and average power: The choice of the gain crystal, the choice of the pump source and pump spot size, the signal spot size and the cavity design. As well transient gain recovery noise must be evaluated if higher rep.rates are desired.

3.1 Choice of Gain Crystal

The choice of the doped gain crystal at the signal wavelength has to satisfy the following conditions:

1) Pumping efficiency must be high to avoid gain recovery noise.
2) Overall gain must be adequate, i.e., the crystal must be capable of generating desired inversion populations given a pump power.
3) Crystal length should be at a minimum to insure non-linear effects are minimized (as described in point 1) above).
4) Thermal lensing should be minimized in the crystal to prevent cavity losses due to cavity Eigen-mode walk off.
5) Quantum defect of the crystal (defined below) should be low to insure efficient energy extraction and to minimize heating effects.

There are two choices of gain crystals that are readily available from industry and that show good agreement with points 1)-5), Yb:KGW and Yb:KYW. Extensive literature exists for REGEN's designed in the wavelength range of 1.03-1.04 μm using these materials[2-4].The pertinent material values are compared in Table 1.

Property	Yb:KYW	Yb:KGW
Optical Axis labels	Nm, Np, Ng	Nm, Np, Ng
Max. Absorption cross-section	$\sim 1.75 * 10^{-19} \mathrm{cm}^2$ along Nm @981nm	$\sim 1.6 * 10^{-19} \mathrm{cm}^2$ along Nm @981nm
Max. Avg. Emission cross-section 1.02-1.045 μm	$\sim 0.25 * 10^{-19} \mathrm{cm}^2$ along Nm	$\sim 0.22 * 10^{-19} \mathrm{cm}^2$ along Nm
Fluorescence Lifetime	0.3 ms	0.3 ms
Thermo-optic coefficients	dn_p/dT=-13.08 x 10^{-6} K^{-1} dn_m/dT=-7.61 x 10^{-6} K^{-1} dn_g/dT=-11.83 x 10^{-6} K^{-}	dn_p/dT=-15.7 x 10^{-6} K^{-1} dn_m/dT=-11.8 x 10^{-6} K^{-1} dn_g/dT=-17.3 x 10^{-6} K^{-1}

Table 1: Important material properties for Yb:KYW and Yb:KGW[5].

From Table 1 it can be deduced that Yb:KYW has lower thermo-optic coefficients and exhibits a lower thermal lensing effect as compared to Yb:KGW. The emission and absorption cross section of Yb:KYW is slightly higher than Yb:KGW. Therefore, of these two crystal choices, Yb:KYW was chosen as the gain crystal in the REGEN cavity.

3.2 Determining Crystal Parameters: Crystal Length, Crystal Doping

Simulations were carried out to determine the optimal crystal doping and crystal length. The average value of the emission cross section for the desired wavelength range shown in Table 1 was used. The simulation was done in two parts, rate equations based on the pump wavelength were used to determine the pumping time necessary to achieve a desired overall crystal gain. The pumping time also determines the maximal rep.rate the REGEN can output at a given pulse energy. In the second stage, using the overall gain derived by the rate-equations, a Franz-Nodvik simulation was carried out to determine the pulse energy. The maximum non-linear phase accumulated (b-integral) was determined within the Franz-Nodvik simulation.

3.2.1 Rate Equations

Yb:KYW can be viewed as a quasi-2 level manifold system[5]. Meaning, that electronic transitions can occur to an upper state manifold, of densely packed energy levels (average spacing of energy levels within these manifolds are on the order of phonon energies). The ground state manifold again consists of densely packed energy levels with similar spacing , see fig. 8 chapter 2.There are two pertinent assumptions:

1) It is assumed that if a transition occurs to a manifold, the electron quickly relaxes (in comparison to the signal pulse duration) into a thermal equilibrium distribution set by the Maxwell Boltzmann distribution within the manifold. Therefore, there is no memory of the original energy level in the manifold that the transition occurred to.
2) Another assumption is that the amount of possible electron transitions to the excited manifold (the density of states) far exceeds the density of electrons undergoing the transition. As well, the density of electrons undergoing the transition is negligible in comparison with the density of electrons in the lower manifold.

The first assumption is important because the backward transition of an electron to the ground manifold (or vice-versa) is not dependent on the original energy level of the forward transition. The electron is in a superposition state over many energy levels in the manifold set by the thermal occupancy conditions of the Maxwell Boltzmann distribution. Therefore, since transitions between manifolds are not dependent on the pathway of previous transitions, a singular constant transition probability for a specific wavelength, described by the transition cross section, can be used. The second assumption yields that the probability that a transition occurs, described by the transition cross section is not influenced by electron densities in the manifold. The electron population in the upper manifold negligibly influences the occupation of energy levels and the occupancy of energy levels in the ground manifold does not change in an impactful way. However, the transition cross section to the higher manifold (the absorption cross section) is different than the transition cross section to the lower manifold (the emission cross section) because the occupancy of energy levels in each manifold is different.

Given the above assumptions, the rate equations describing this manifold system are[6]:

$$\frac{dn_2N_o}{dt} = \left(-\sigma_{em}\, n_2 + \sigma_{ab}(1 - n_2)\right)N_o\frac{I}{hv} - \frac{n_2N_o}{T_{sp}} \tag{57}$$

$$\frac{dn_1N_o}{dt} = \left(\sigma_{em}\, n_2 - \sigma_{ab}(1 - n_2)\right)N_o\frac{I}{hv} + \frac{n_2N_o}{T_{sp}} \tag{58}$$

$$n_1N_o = (1 - n_2)N_o \tag{59}$$

Where, the transition cross-sections σ are functions only dependent on the wavelength.

Variable name	Definition
t	Time(s)
n_1	Fractional population density in ground manifold (cm^{-3}) normalized to N_0.
n_2	Fractional population density in upper manifold (cm^{-3}) normalized to N_0.
N_0	Total electron density (cm^{-3})
I	Pump intensity ($\frac{W}{cm^2}$)
T_{sp}	Spontaneous emission time
σ_{em}	Emission cross section (cm^2)
σ_{ab}	Absorption cross section (cm^2)
hv	Photon energy (J)

Table 2: Variable definitions for rate-equation model

Equation (59) is derived from the condition that the overall electron density is always conserved. The relation was substituted in Eq. (57) and (58).

The spontaneous emission decay rate is assumed to decay into a wide range of wavelengths, with a negligible power contribution to the pump wavelength and can be assumed to yield no contributions to generating pump photons. As well, ASE is neglected at this point in the model due to the solid angle this radiation goes into. Therefore, the contribution that is aligned with the pump beam is negligible.

Because of absorption and stimulated emission the pump intensity changes as a function of propagation coordinate in the crystal. The pump intensity propagation equation can be described as follows[6]:

$$\frac{dI}{dz} = \left(\sigma_{em}\, n_2 - \sigma_{ab}(1 - n_2)\right) N_0 I \tag{60}$$

Where, the coefficient on the LHS is accordingly named the gain coefficient (g) and carries units cm^{-1}.

3.2.2 Steady State Properties of the Yb:KYW Gain Crystal

At a certain population inversion the decay rate of the spontaneous emission and stimulated emission exactly balances with the upward absorption rate of pump photons. The net change in electron density as a function of time is thus zero if the pump intensity remains constant. Steady state conditions can be derived by substituting zero for the derivative in Eq. (57). Due to Eq.(59), population values for all manifolds can be found as a function of pump intensity, yielding:

$$n_2 = \frac{\sigma_{ab}}{\sigma_{em} + \sigma_{ab} + \frac{hv}{I}\frac{1}{T_{sp}}} \tag{61}$$

$$n_1 = \frac{\sigma_{em} + \frac{hv}{I}\frac{1}{T_{sp}}}{\sigma_{em} + \sigma_{ab} + \frac{hv}{I}\frac{1}{T_{sp}}} \tag{62}$$

$$\frac{n_2 N_o}{T_{sp}} = \left(-\sigma_{em}\, n_2 + \sigma_{ab}(1 - n_2)\right) N_o \frac{I}{hv} \tag{63}$$

It can be seen from the above that the steady state n_2 saturates with pump intensity. If $I \to \infty$, Eq. (61) approaches:

$$\lim_{I\to\infty} n_2 = \frac{\sigma_{ab}}{\sigma_{em} + \sigma_{ab}}$$

For a crystal of a differential propagation slice of size Δz, the steady-state population variation with pump intensity can be assumed to be zero due to the negligible pump variation within this differential slice. Integrating Eq. (60) and using the steady state condition described in Eq. (63) yields an approximation:

$$I(\Delta z) \approx I(0) - hv \frac{n_2(I(0))N_o}{T_{sp}} \Delta z \tag{64}$$

Where n_2 is solved by using $I(0)$ and its steady state equation (to explicitly make this apparent, n_2 is shown in Eq. (64) as a function of I(0)). For the next slice in the propagation coordinate, $I(0) \to I(\Delta z)$ and:

$$I(2\Delta z) = I(\Delta z) - hv \frac{n_2(I(\Delta z))N_o}{T_{sp}} \Delta z \tag{65}$$

n_2 for this propagation slice is solved by using $I(\Delta z)$ and its steady state equation.

However, the full exponential form, for example at the above step:

$$I(2\Delta z) = I(\Delta z) e^{\Delta z N_o \left(\sigma_{ems}\, n_2(I(\Delta z)) - \sigma_{abs}(1 - n_2(I(\Delta z)))\right)} \tag{66}$$

Was used in the simulation due to the exponential form being a more accurate approximation (reduces the effect of the slowly varying slice approximation).

This process is done iteratively throughout the entire crystal length, yielding a pump intensity at every discrete slice of the crystal. Δz is made smaller until convergence in the simulation outputs (i.e., integrated population inversion, end slice pump intensity become independent of slice step-size). It is also clear, that at steady state, pump absorption in the crystal is dictated by the spontaneous emission decay rate. If this rate is omitted, the crystal can be viewed as totally transparent to the pump as shown in Eq. (64), (65) and (66).

Obtaining the steady state inversion at each slice from the simulation allows the calculation of the overall steady-state gain in the crystal:

$$G = e^{\Delta z \sum_{i=1}^{i=N} \left(\sigma_{ems}\, n_{2i} - \sigma_{abs}(1 - n_{2i})\right) N_o} \tag{67}$$

σ_{ems} , σ_{abs} are now the average cross sections of the signal wavelengths that need to be amplified, N is the maximal slice number.

This calculation yields the following information for the following parameters in table 3:

Parameter	Value
Crystal Length	3mm
Doping Concentration	5%
T_{sp}	0.3ms
N_o*	$30.1 * 10^{19}\text{cm}^{-3}$
σ_{em}	$2.25 * 10^{-19}\text{cm}^2$
σ_{ab}	$1.75 * 10^{-19}\text{cm}^2$
σ_{ems}	$0.3 * 10^{-19}\text{cm}^2$
σ_{abs}	$0.02 * 10^{-19}\text{cm}^2$

Table 3: Parameters of simulation. * N_o is calculated from the small signal gain value of Yb:KYW doped at 5%, N_o at other concentrations can be deduced from this value by: $\frac{\text{doping\%}}{5\%} N_o@5\%$.

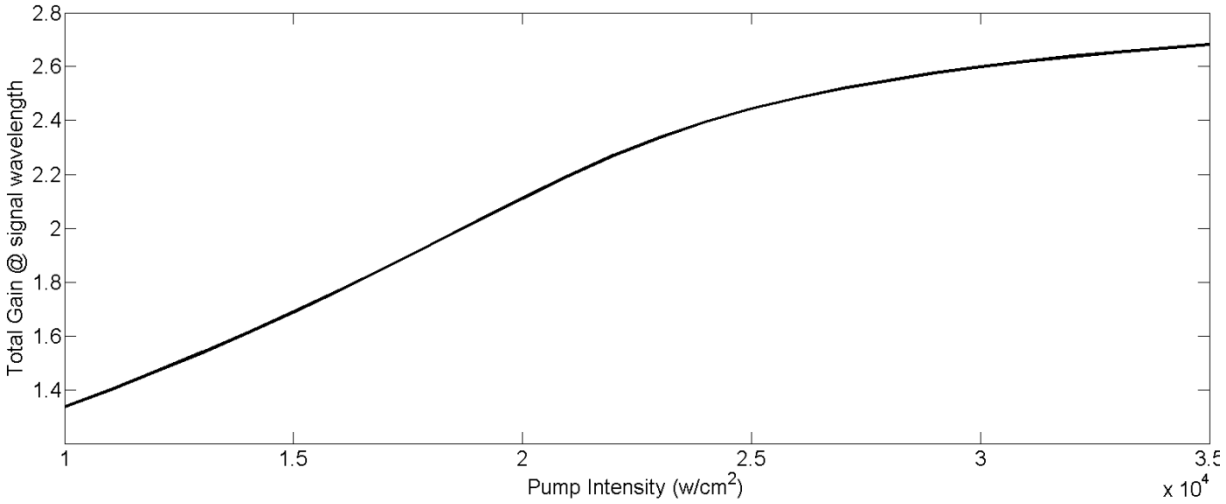

Figure 1: Total Gain as a function of average pump intensity. It can be seen that gain saturates past $23\frac{\text{kw}}{\text{cm}^2}$.

Fig. 2 illustrates the dependence of the saturation gain value and crystal length at a constant pump intensity. Intuitively it may be deduced that shorter crystals have lower saturation gain (at a constant given pump intensity), however this relationship is not always followed. For long crystals, even when all propagation slices are saturated, the pump intensity still decays as a function of propagation coordinate. Therefore, at propagation slices towards the end the population inversion will not be adequate for net gain at the signal wavelength and thus the overall absorption from these end slices will effectively lower the overall gain of the crystal.

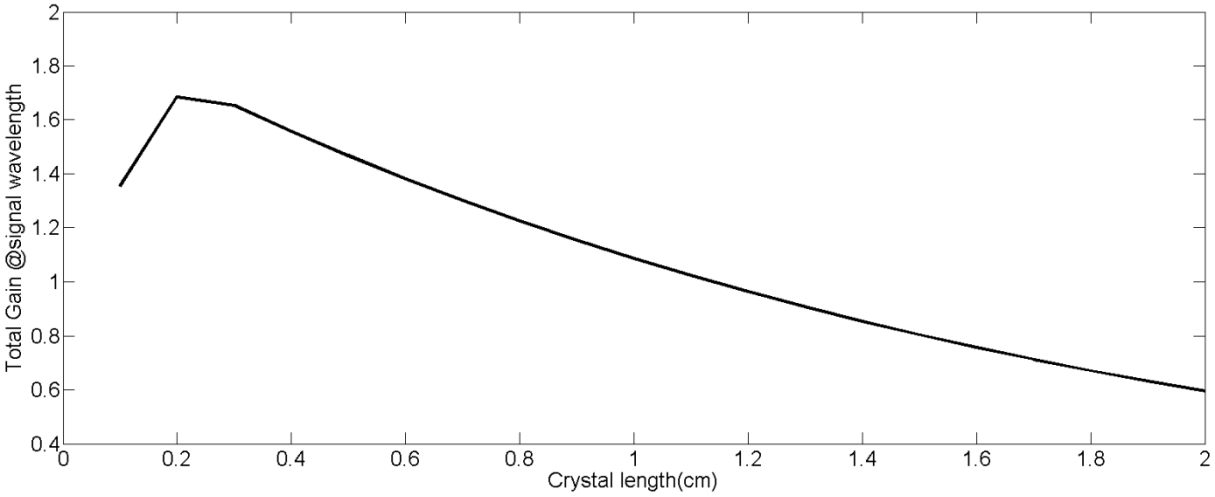

Figure 2: At a pump average intensity of $15\frac{\mathrm{kw}}{\mathrm{cm}^2}$ (kept low to demonstrate the effect), total saturation gain is plotted vs crystal length. As can be seen there is an optimal crystal length given a doping concentration (in this case 5%), and a pump intensity.

3.2.3 Pumping Gain Dynamics of the Yb:KYW Gain Crystal

The steady state conditions derived in the previous section offer insight into the maximal possible gain the crystal can be pumped to given a pump power. However, the time required to pump such a crystal is also important to explore. Pumping time for Yb:KYW amplifiers are on the order of ms[7] and therefore, this imposes maximal rep.rate constraints of the REGEN before gain recovery noise starts to dominate or pulse energy drops.

Following the same iterative approach of the algorithm introduced in the previous section but extending it for the time coordinate, for a differential propagation and time increment, Δz, Δt it can be assumed that the population inversion is insensitive to pump variation both in time and space. The pump intensity is a constant within the Δz, Δt slice. Therefore, under constant pump intensity within the time-slice Eq. (57) can be integrated from the nth time interval to the n+1th time interval $(n\Delta t, (n+1)\Delta t)$ to yield the following analytic expression and recursion:

$$n_2(n\Delta z, (n+1)\Delta t) = \frac{\left(n_2(n\Delta z, n\Delta t) - \frac{\sigma_{ab} * I}{h\nu}\right) e^{\left(-\Delta t\left(\frac{1}{T_{sp}} + \left(\frac{\sigma_{em} + \sigma_{ab}}{h\nu}\right)I\right)\right)}}{\frac{1}{T_{sp}} + \left(\frac{\sigma_{em} + \sigma_{ab}}{h\nu}\right)I} + \frac{\sigma_{ab}}{\sigma_{em} + \sigma_{ab} + \frac{h\nu}{I}\frac{1}{T_{sp}}} \quad (68)$$

The intensity used in Eq. (68) is $I((n-1)\Delta z, n\Delta t)$ coming out of the previous z slice at the end of the previous time interval.

The intensity recurrence is defined as:

$$I(n\Delta z, (n+1)\Delta t) = I((n-1)\Delta z, n\Delta t) e^{\left(\sigma_{em} n_2((n-1)\Delta z, n\Delta t) - \sigma_{ab}(1 - n_2((n-1)\Delta z, n\Delta t))\right) N_o \Delta z} \quad (69)$$

As mentioned previously, these equations can be simulated in an iterative fashion. The initial condition for each time step of Eq. (68) is the $n_2(n\Delta z, n\Delta t)$ term on the RHS and the initial condition for each time step of Eq. (69) is the $I((n-1)\Delta z, n\Delta t)$ term on the RHS. It is assumed that for a differential interval in time n_2 in Eq. (69) is equivalent to the final value of the previous time step, i.e.,

it is slowly varying in time w.r.t the time interval. This is verified by varying the increment size of t and z until convergence is found.

The boundary condition is such that at $z = 0$:

$$I(0, t) = I_o$$

I_o is the constant input average pump intensity.

The initial conditions (at time t=0) is:

$$n_2(n\Delta z, 0) = c_n$$

Where c_n is a constant for each slice number n. It will be shown below that, c_n is the remaining population density at a crystal slice after the signal pulse is amplified and coupled out of the REGEN cavity.

It is also assumed that the propagation of the pump through the crystal is on a much shorter timescale than the timescales considered for the simulation. Therefore, while there is a small delay in time between crystal slices this is assumed to be negligible and at a given timestamp all propagation slices through the crystal is evaluated in an iterative fashion. As can be seen from the above ($(\Delta z, \Delta t)$ are independent parameters).

For the same parameters as table 3**,** fig.3 demonstrates the pumping time to saturation for different pump intensities. It can thus be deduced that the greater the pump intensity, the faster the total crystal gain will reach saturation, for a given crystal length.

Thus, there are two ways to reduce pump time:

1) Increase the pump intensity.
2) Decrease the crystal length.

However 2) has the disadvantage of lowering the total gain if the length is in the region where total pump absorption at steady state does not result in slices towards the end being absorptive.

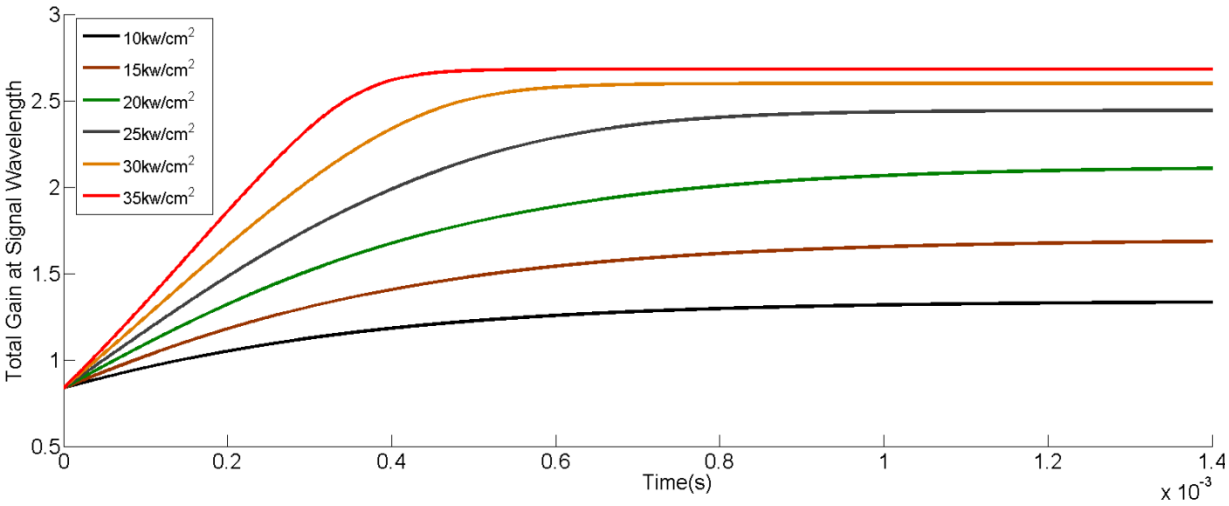

Figure 3: Indicates the dependence of total gain on pump time at different pump intensities.

The results obtained from this model are in good agreement with results reported in [7] for the corresponding pump average intensity of $23\frac{\text{kw}}{\text{cm}^2}$ (i.e., pumping time of approximately 0.4ms).

Therefore, from these calculations it is already apparent that if saturation gain is desired, and the signal pulse depletes the inversion population, the maximum rep. rate for a pump average intensity of roughly $15\frac{\text{kw}}{\text{cm}^2}$ is roughly 1kHz and for a pump intensity of $25\frac{\text{kw}}{\text{cm}^2}$ is roughly 2.5 kHz.

The signal pulse does not deplete entirely the gain population and these upper bounds are high. True upper bounds of rep.rates and gain recovery dynamics will be explored in section 2.2.5.

3.2.4 Pulse Amplification: The Franz-Nodvik Algorithm

The recurrence relationship for the pulse amplification used is named the Franz-Nodvik algorithm. It assumes that the signal pulse is at a short timescale in comparison with the spontaneous emission rate of the crystal. Therefore, this rate can be omitted and Eq. (57), (58), (60) integrate analytically to the following relations[10], defined in terms of fluence ($\frac{\text{J}}{\text{cm}^2}$) :

$$\text{J}(\text{K}+1) = \text{T}\text{J}_\text{S}\ln(\text{G}(\text{k})\left(\text{e}^{\frac{\text{J}(\text{K})}{\text{J}_\text{S}}} - 1\right) + 1) \tag{70}$$

$$\text{g}(\text{K}+1) = \text{g}(\text{K}) - \frac{1}{\text{J}_\text{S}}(\frac{\text{J}(\text{K}+1)}{\text{T}} - \text{J}(\text{K})) \tag{71}$$

g is the gain coefficient. Thus,

$$\text{G}(\text{K}+1) = \text{e}^{\text{g}(\text{K}+1)} \tag{72}$$

J_S is the saturation fluence defined as:

$$\text{J}_\text{S} = \frac{\text{hv}}{\sigma_{\text{em}} + \sigma_{\text{ab}}} \tag{73}$$

K is the pass number through the crystal of the pulse, T is the single-pass transmission within the cavity.

The algorithm is faster to implement than the rate-equation technique and thus, for pulse amplification this approach was used.

While, it is not necessary to partition the crystal in z-slices for the Franz-Nodvik algorithm the b-integral [11] was also calculated from an average intensity of the pulse fluence at a crystal increment divided by the pulse duration of 500ps. The major reason the crystal was partitioned was to obtain the population inversion density after the pulse amplification. These initial values for the population

inversion will be fed into the pumping time simulation to obtain the final gain for the next inputted pulse. This is necessary to analyze gain recovery transients and noise. Thus, the crystal was treated as a series of slabs of slice thickness Δz that were solved in series using the Franz-Nodvik equations, where the inputted fluence was the outgoing fluence of the previous crystal slice. This was done to the desired cavity pass number of the signal through the crystal.

After pulse amplification at the desired pass number, the upper state population was found according to:

$$n_2(n\Delta z) = \frac{\frac{g(K, n\Delta z)}{N_o \Delta z} + \sigma_{abs}}{\sigma_{ems} + \sigma_{abs}} \tag{74}$$

By re-arrangement of Eq.(67).
This is useful to determine the pumping initial conditions in between pulses and to evaluate any output pulse amplitude fluctuations or transients from the system.

The algorithm was verified by reproducing the same figures as in [10] with their parameters.

3.2.5 Competition with Q-Switching

The natural build-up of the ASE noise to the laser mode will be suppressed due to competition of the gain with the pulse amplification. This is true if the initial total energy of the pulse within the modal area of the cavity mode is higher than that of the ASE (calculated from the total ASE power contained in the modal area multiplied into the cavity roundtrip time).

The assumption is made that this is always the case due to the fact that ASE initially is outputted within a solid angle of 4π, thus the amount of power contained in the cavity mode is negligible.

3.2.6 Putting It All Together: Final Simulation Values, Gain Recovery Dynamics, Determined Output Values

It is now prudent to simulate the overall system-crystal pumping, pulse amplification and gain recovery dynamics (fig.4-7) to obtain the pulse energy outputted from the REGEN and to obtain gain recovery pulse energy fluctuations. The latter will determine the maximal rep.rate the system can afford before gain recovery instability becomes a major effect. In all simulations the pump was assumed to be continuous and the pumping effect within the pulse amplification time negligible.

Simulation parameters are found in Table 4.

Parameter	Value
J_S	$6.01\frac{J}{cm^2}$
T	0.97
Signal Spot Size @crystal	$400\mu m$
Pulse duration	500ps
J(0), initial fluence	$3.2\frac{mJ}{cm^2}$
Pump Spot	$400\mu m$
Pump Intensity	$23.9\frac{kW}{cm^2}$
Crystal Length	3mm
Crystal Doping	5%
Crystal Axis For Amplification and Pump	Nm

Table 4: Parameter values for Franz-Nodvik simulation

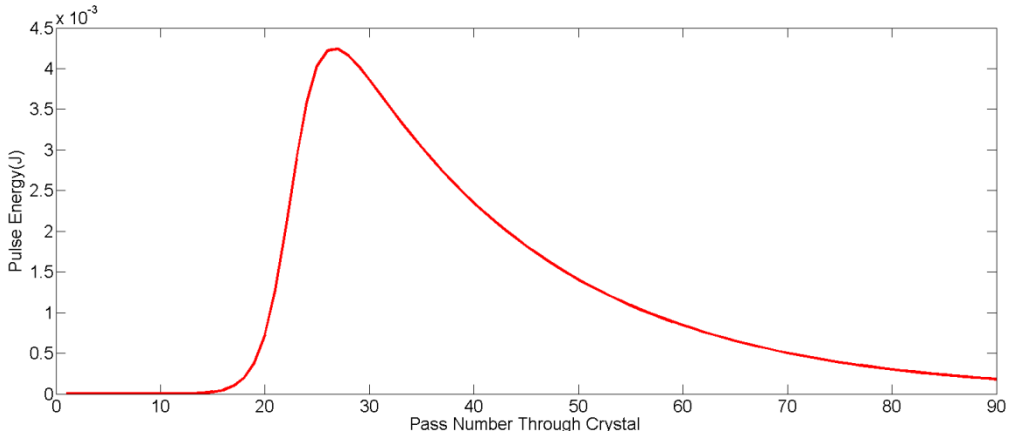

Figure 4: Pulse energy as a function of crystal pass number (Each cavity round trip sees two passes). This pulse energy curve was taken at entering pulse number 9 into the multipass cavity (when gain transients were stabilized.

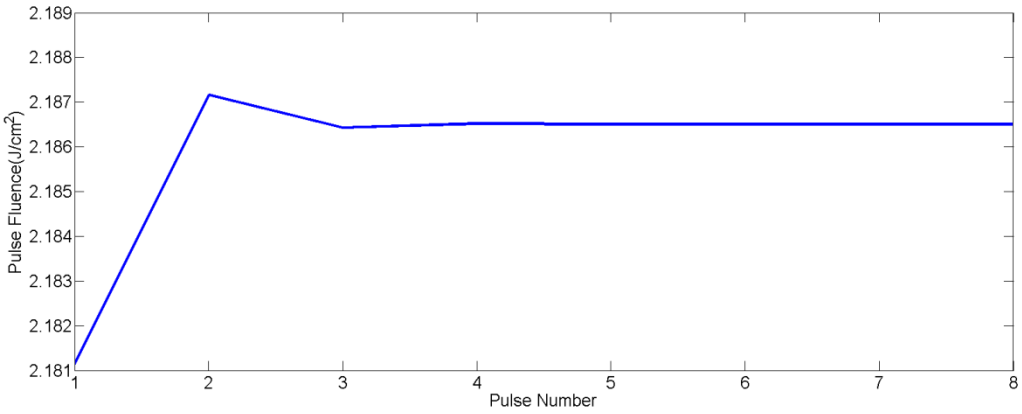

Figure 5: Pulse fluence at a constant pass number (pass 14 taken from above figure). Pulses are separated by 0.5ms (2 kHz rep.rate). Transients settle after 9 pulses and there is no gain recovery bifurcation[12].

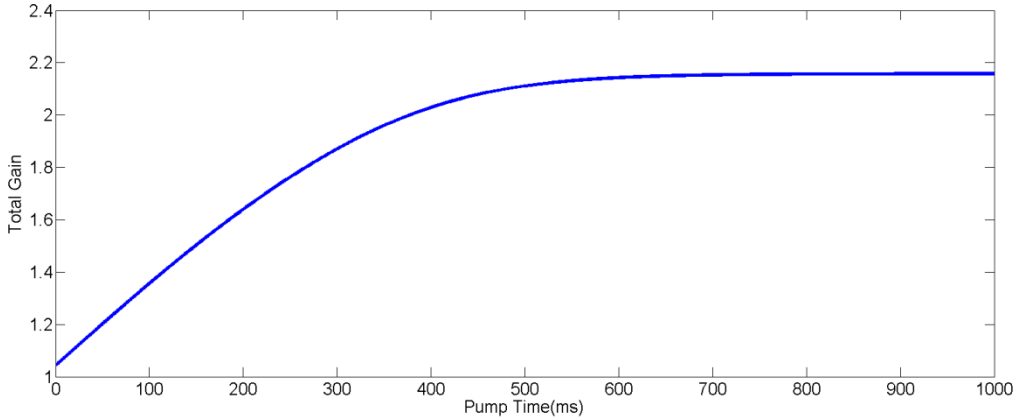

Figure 6: Pump time for the system after stable pulse fluence occurs (i.e. after pulse 9). At t=0, gain is above 1, which indicates that population inversion does not fully deplete after amplified pulse exits the cavity.

It was found that transients decay and there is no bifurcation up till a rep.period of 0.1ms (10 kHz). As shown in fig.7.

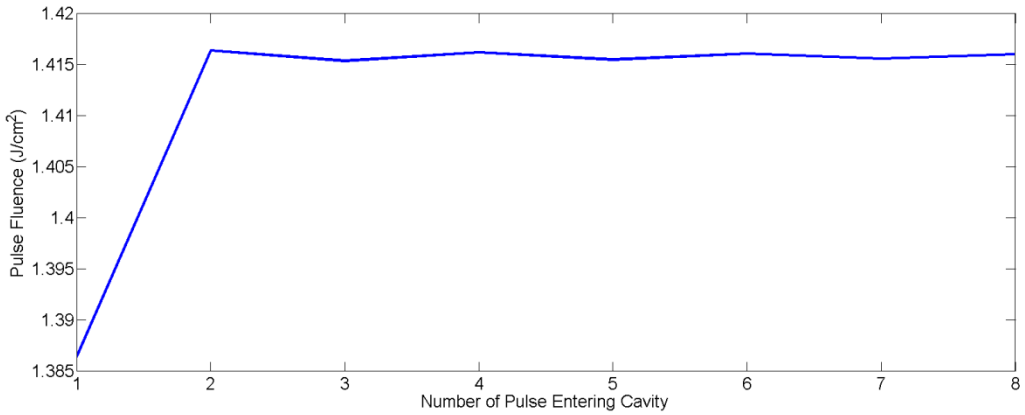

Figure 7: Pulse fluence bifurcation at 10 kHz. As can be seen when rep.rate increases pulse fluence is lower and bifurcation starts.

The b-integral for the system was found to be 0.1 using the non-linear index coefficient found in [11].

3.2.7 Extension of the Theory: Using Franz-Nodvik for the Calculating Pump Time

During the course of the design of this REGEN discussion centered on whether the Frantz-Nodvik equations which offer a computationally fast algorithm can be used to find the pumping time of the crystal, i.e., to reverse the Franz-Nodvik simulation to simulate the pumping of the gain medium rather than the depletion. I have found the corresponding corrections to the algorithm that would make this possible for spontaneous emission timescales on the order of ms and have computationally implemented it. The exact issues that arise with just using the Franz-Nodvik algorithm as is (with a reversal of signs in Eq. (71)) is that during the pumping cycle, which is on the order of ms, the ultrafast approximation does not work anymore, and spontaneous emission characteristic times must be considered. The algorithm was then used in the group for the evaluation and design of a 2μm Ho:YLF amplifier.

Firstly, the system is partitioned in time slices, Δt and in crystal propagation slices, Δz. Partitioning the crystal in propagation slices is not necessary (making the algorithm computationally fast due to a reduction of dimensionality) but is still carried out to obtain local population inversion information along the crystal. The pump fluence per slice Δt is calculated (for constant intensity the fluence does not change at different time intervals) and the Franz-Nodvik simulation is carried out on the series of crystal slices. The remaining pump fluence from one crystal slice (calculated from the Franz-Nodvik simulation) is fed into the next crystal slice at the given time slice (the approximation that the pump propagation through the crystal is ultrashort compared to the pump time is used here as well). The population inversion from the gain calculation is as well obtained for each crystal slice at a given time stamp. However, at the next time stamp the population inversion is multiplied by $e^{-\frac{\Delta t}{T_{sp}}}$. This is because, if the intensity terms of Eq. (57) are neglected, than the equation integrates to:

$$n_2((n+1)\Delta t) = n_2\,(n\Delta t)e^{-\frac{\Delta t}{T_{sp}}}$$

Therefore, the spontaneous emission decay rate to an approximation can be viewed as an overall exponential decay term on the population. To factor this loss numerically, before the next time step is calculated, the slice population is multiplied into this exponential decay factor. Convergence was obtained by varying the time step and propagation step. This procedure was compared with the rate equation formulation for a Ho:YLF crystal whose spontaneous emission characteristic time is on the order of ~15ms. Appendix B1 lists the simulation results which match.

3.2.8 Extension of the Theory: More Efficient Pumping Process by Pump Splitting

The rate equation simulation was extended to the case of pumping the crystal from both sides where each side would have half of the input pump intensity. Interference effects (i.e., intensity cross terms) from the two counter-propagating beams are omitted due to the incoherent radiation of the pump source. While, the overall pump intensity is the same, the gain pumping time to saturation drastically decreased and the gain saturation level rose. This can be explained by the spontaneous emission decay rate dynamics. If the intensity is halved, than the rate contributions to the population inversion of the intensity as well will be halved (omitting the spontaneous emission rate term for the time being). Thus, the pumping time will increase by a factor of two. However, since both sides of the crystal are being pumped the net pumping time to a given gain will be the same. Now when the effects of the spontaneous emission term are considered, it can be seen that for higher pump intensities, the loss through spontaneous emission will be higher (since the absolute population value does not linearly scale with pump intensity). Thus, propagating this intensity from one slice to another if the local intensity is double, the pumping rate will now be less than double (due to this spontaneous emission loss channel). Thus, the two cases are not equivalent anymore, and the efficiency for the pump split arrangement is higher and the pumping time to gain saturation is lower.

To illustrate the effect: using an overall pump intensity of $23\frac{kW}{cm^2}$, and the same crystal parameters, the following figures (fig. 8) were generated:

a)

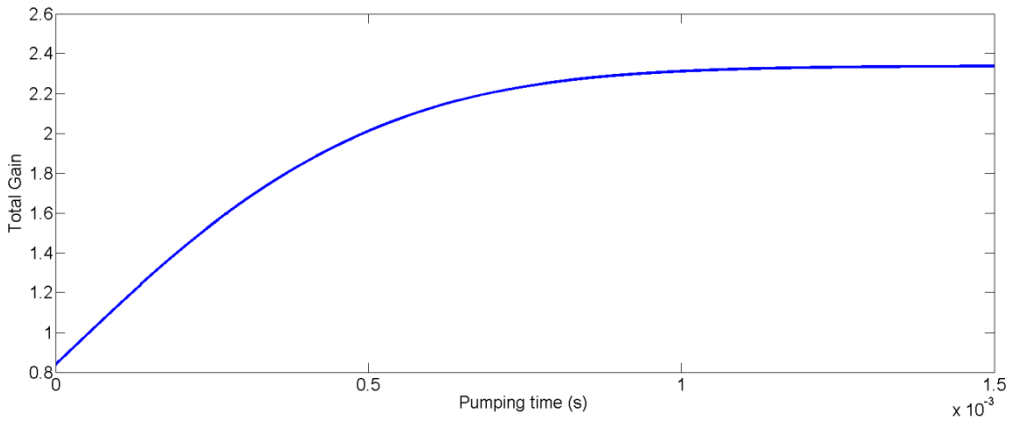

b)

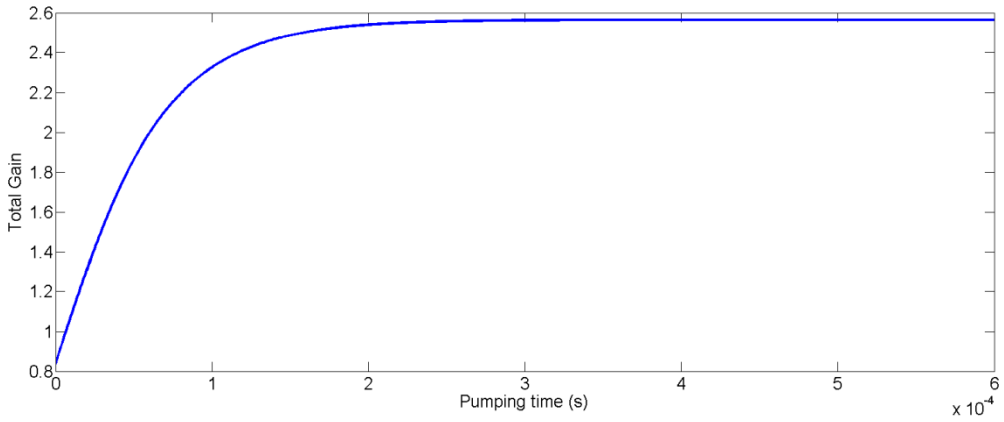

Figure 8: a) Total gain vs pumping time of arrangement where the pump only propagates in one direction) arrangement where pump is split and enters the crystal from both ends. Pumping time is reduced by a factor of ~7.5 and overall gain is increased by a factor of ~1.1.

3.3 Cavity Design

The cavity design parameters were taken from the parameters of the simulation. The signal spot size at the crystal should be <200µm, and the pump line spot-size should be 400µm. By using [2] as a reference cavity and by checking stock items for available mirrors the following cavity was designed, using the software tool, ReZonator. The reason the signal spot-size is smaller than 400µm is due to various experimental factors: 1) Available mirrors from stock items would not generate the desired spot-size at the Pockel cell (P.C) branch of the cavity, given the overall cavity length condition. 2) The pump beam profile at the focus was not top-hat or Gaussian but contained many structures. Therefore, in order to minimize aberrations in the signal beam profile, the spot size had to be reduced to avoid pump spot size regions with these structures.

#	Typ	Label	Parameters
1		M1	
2		L2	L=354mm
3		M3	R=229mm; Alpha=10°
4		L5	L=136mm
5		F1	F=200mm; Alpha=0°
6		L9	L=119mm
7		M4	R=229mm; Alpha=10°
8		L6	L=50mm
9		L7	L=500mm
10		M5	R=1000mm; Alpha=10°
11		L8	L=275mm
12		M6	

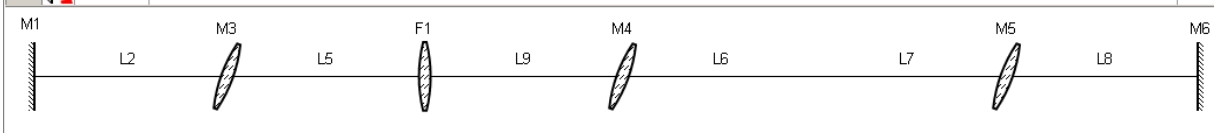

Figure 9: Input cavity into reZonator, using mirror stock items found from two sources: Eksma and Altechna. Total cavity length is 1.434m.

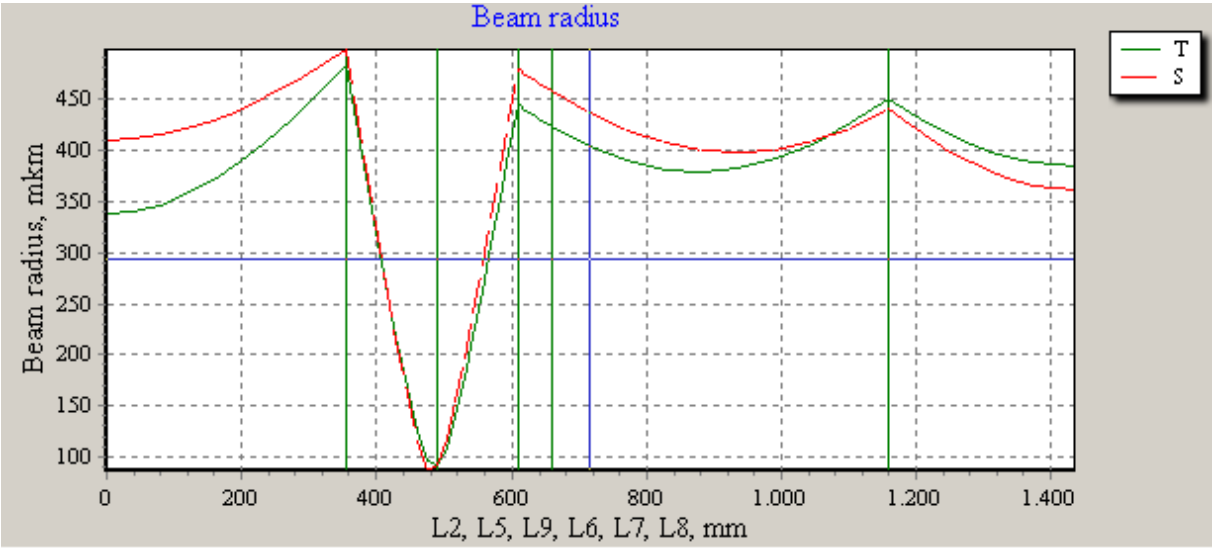

Figure 10: Caustic beam profile in micrometers for both the tangential and sagittal planes of the beam within the cavity. At crystal, beam radius is 92.8µm in both the tangential and sagittal planes.

Thermal lensing must be considered for Yb:KYW crystals, a focal length range of 125mm to 1000mm was considered in the cavity design, see fig. 11 for the stability plot.

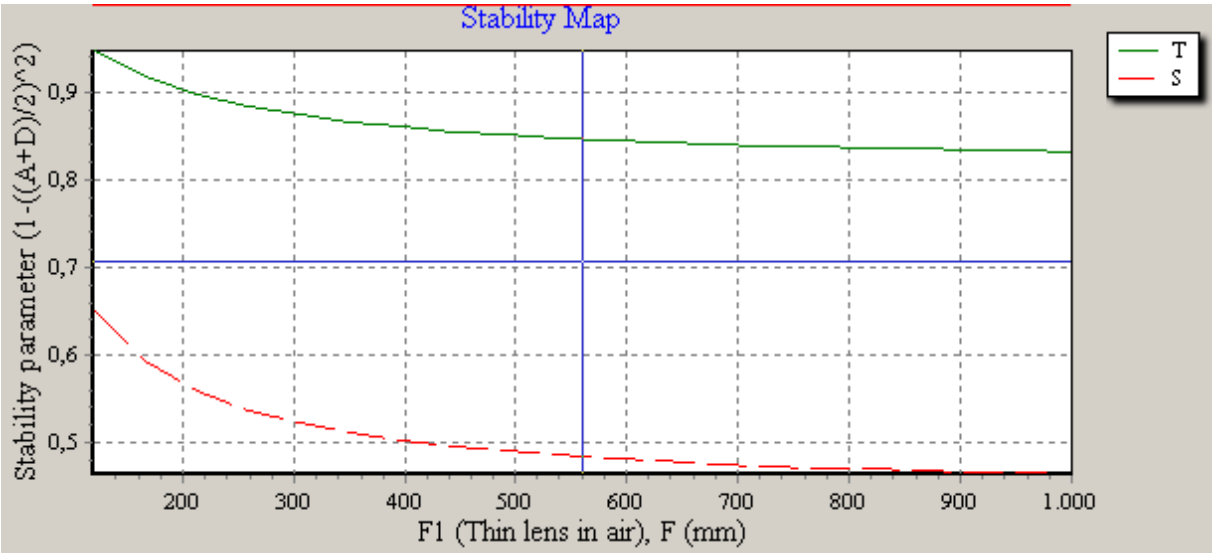

Figure 11: Stability map of both the transverse and sagittal planes of the beam from 125mm to 1000mm focal lengths. Within this range, stability is between 1 and -1 satisfying the stability criterion for the cavity.

The pump was coupled into the cavity through M1 which is a dichroic mirror that is reflective at 1.03 µm and transmissive at 981nm and the out-coupling optics (PBS, QWP, Pockel cell) were placed between M5 and M6. M6 was an out coupling end mirror without coupling transmission of 1.5%.

3.4 Experimental Setup

Diagrams of the experimental setup are given in fig. 12. Refer to appendix B2 for complete materials list.

The polarization dynamics are summarized in fig. 13. The crystal is orientated such that the intracavity P-Polarization is aligned with the Nm axis.

Mirror	Radius of Curvature	Reflectivity, Transmission
M6	∞	98,5%,1.5 (+/- 0.5)%
M5	1000mm	99,7%,-
M4	229mm	99,7%,-
M3	229mm	99,7%,-
M1	∞	1030nm: 99%, 981nm: 95%

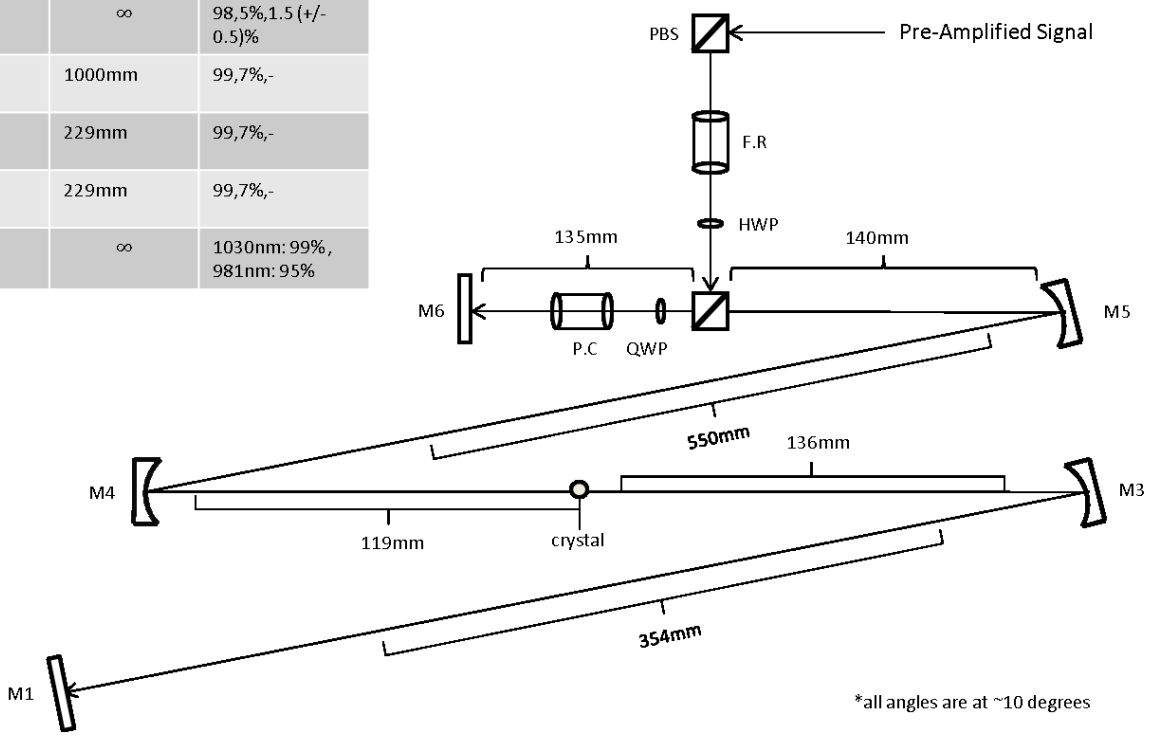

Figure 12: Cavity diagram showing all measurements. Accuracy is +/-2mm. Degree accuracy is +/-2 degrees. Second branch of the cavity is defined all cavity components after the cavity PBS on the M5 side. The pump is collinear with the signal and coupled into the dichroic mirror, M1. The pump line consists of a custom designed lensing system from DPM Photonics that focuses the beam to ~400um at the crystal. P.C: Pockels Cell, F.R: Faraday Rotator, PBS: Polarization Beam Splitter, H/QWP: Half/Quarter Wave-Plate, M: Mirror.

a)

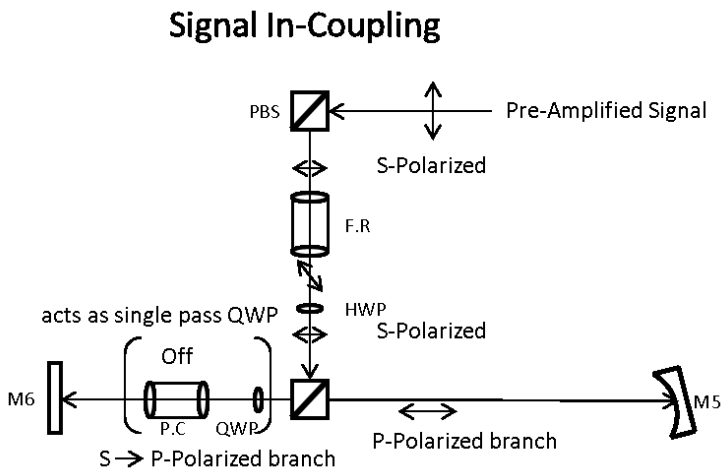

b)

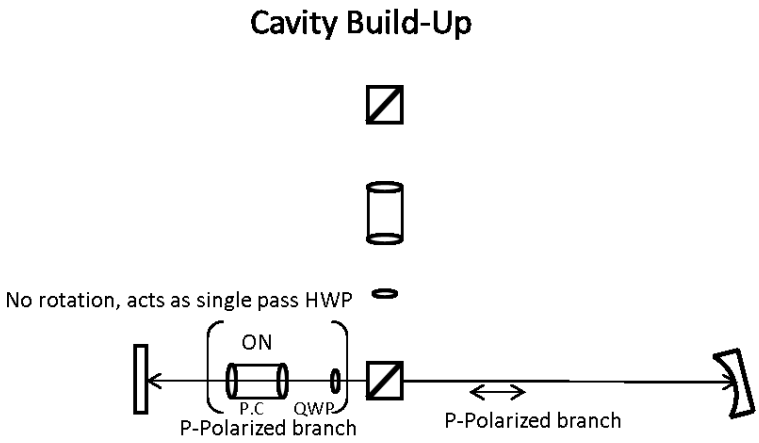

c)

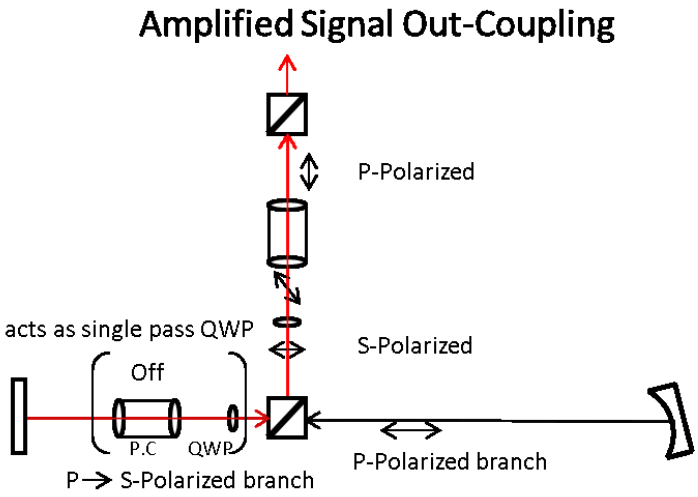

Figure 13: a) The Pulse signal is in-coupled into the cavity. At this stage the Pockel cell (P.C)[8, for Pockel cell alignment, see 9] is off. The QWP is orientated in such a way that after reflection at

M6(which adds a π phase shift and the second pass through the QWP, the polarization is converted to the P-state. The P-state is then passed through the cavity PBS and coupled into the second cavity branch. b) In the pulse build-up (where the pulse remains in the cavity), the P.C is turned on at the QWP voltage. After the double pass through the P.C and QWP the net polarization state does not change (2π phase with mirror M6). Therefore, the state will remain in the P-polarization and will propagate in the second branch of the cavity. c) At out-coupling the P.C is turned off (retrieving the initial arrangement). After the double pass through the P.C and QWP there will be a net -½ π phase shift and the P polarization will be converted in the S-polarization. The pulse will couple out of the cavity after the cavity PBS. After the HWP, the polarization state is tilted at 45 degrees, and in a 0 phase shift relative to the signal in a) at that point. The Faraday rotator (F.R), being insensitive to propagation direction [8], rotates the phase along the same direction as in a) i.e., clockwise, and the polarization state will now be in the P-polarization (½ π). This will couple into the out-put of the system through the out-coupling PBS.

According to fig. 13 , the P.C rise time and fall time must be less than the round-trip time of the second branch of the cavity. The total cavity length is 1.434m which translates to a round trip time of ~9.6ns. The P.C (from Dohrer Elektrooptik) consisted of a double cell rubidium titanyl phosphate (RTP), with a transmittance of 98.5%, an extinction ration greater than 200:1 (at no voltage) and an aperture of 3.6mm. The two crystals are orientated such that extra birefringence caused by thermal effects is compensated for. The P.C was switched at quarter wave voltage with a Birdman CMOS switching circuit that had a measured rise time and fall time (to zero) of 8.7ns.

3.5 Experimental Results

For the following experiments as a benchmark case the crystal that was used was not a 5% doped crystal but a 2%, 3mm, Yb:KYW Np cut crystal. This was to insure that at this stage, pulse build-up will not damage optical components. Repeated alignment was done within the cavity that could cause damage to these components. Once the cavity is properly aligned and studied, the crystal will be replaced by the 5% 2.5mm crystal. All data presented here is for the 2%, 3mm crystal.

3.5.1 CW Lasing

CW lasing of the cavity was obtained and maintained with the placement of the PBS and Quarter Wave plate. The lasing with all cavity components is given in fig. 14.

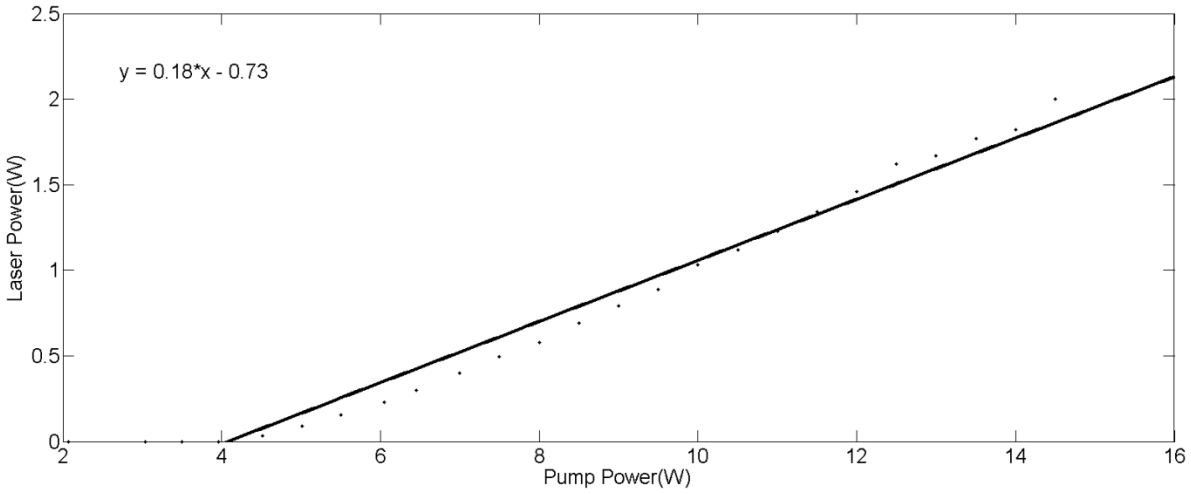

Figure 14: Lasing curve of cavity with all optical components (including QWP, PBS, P.C). Output-coupler was 2(0.5)%. The slope efficiency was found to be 18%.

From fig. 14 the lasing threshold is found to be at a pump power of 4W. Simulations show that this translates to a threshold gain of 1.11. The inverse of the threshold gain is the total cavity transmission which then is equivalent to ~0.90. Therefore, the roundtrip losses are ~10%. The single pass loss of each mirror is 0.3%, the output coupler is ~2%, the dichroic in-coupling mirror is 1%, and thus, the remainder should be in the PBS, P.C, and QWP system.

$$L_{P.C+PBS+QWP} = 10\% - 100\%(1 - (0.997^6)(0.99)(0.98)) = 5.29\%$$

Laboratory measurements of the losses given an alignment seed signal centered at 1.03um confirm the above analysis. The measured insertion percent loss through the P.C+QWP is ~1.5(0.3)% and through the PBS, ~1 (0.3)%. This yields a double pass loss of ~5%.

Updated simulation parameters with the exact beam radius at the crystal, the crystal used for this experiment and the losses yield at a pump power of **14W**, a maximal pulse energy of ~440μJ.

3.5.2 Q-switched operation

Before operation in amplified pulsed mode, the cavity was operated in the Q-switched laser head. The Q-switched average power relating to the pump power is shown below.

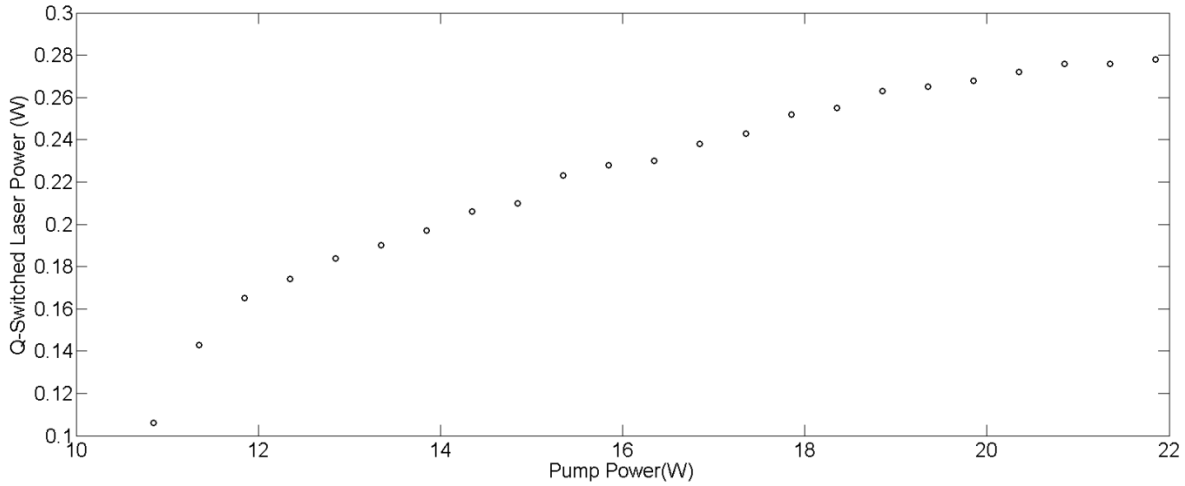

Figure 15: Full saturation curve of the Q-switched laser head power vs pump power at a rep.rate of 1 kHz. Saturation pump power is approximately 18.5W. Each point represents the maximal power extracted by varying cavity on times.

From fig. 16, it can be seen that the optimum rep.rate of the Q-switched laser head occurs at 1kHz. For Higher rep.rates, the lower pulse energies can be explained by the gain recovering to a lower value due to the shortened pump time betweeen pulses. The lower pulse-energy that occurs at higher than 1kHz rep.rates is explained by thermal effects that build up in between pulses, due to a longer exposure of the inverted population with the pump time. Substantial bifurcation was found at 5kHz, were the second pulse had ~1/4 the pulse energy as the first, see fig. 17b.

The cavity-on time necessary to generate a Q-switched average power on the order of 0.1W -0.3W is in the range of 654ns-744ns (at higher pump power, the cavity build up time is reduced). This is illustrated in fig. 17.

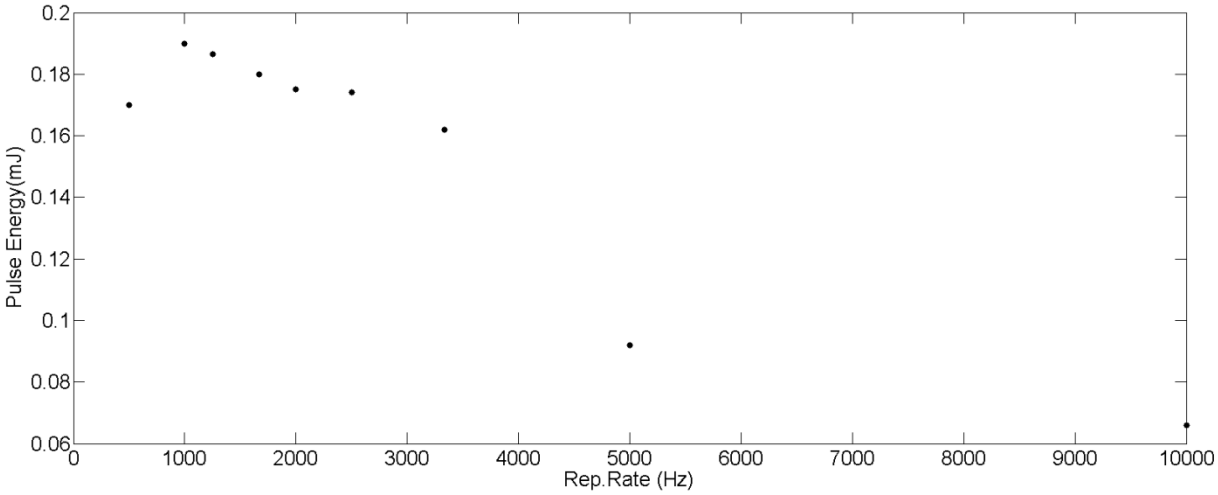

Figure 16: Pulse energy variation with rep.rate. Roll-over occurs at ~32500Hz.

a)

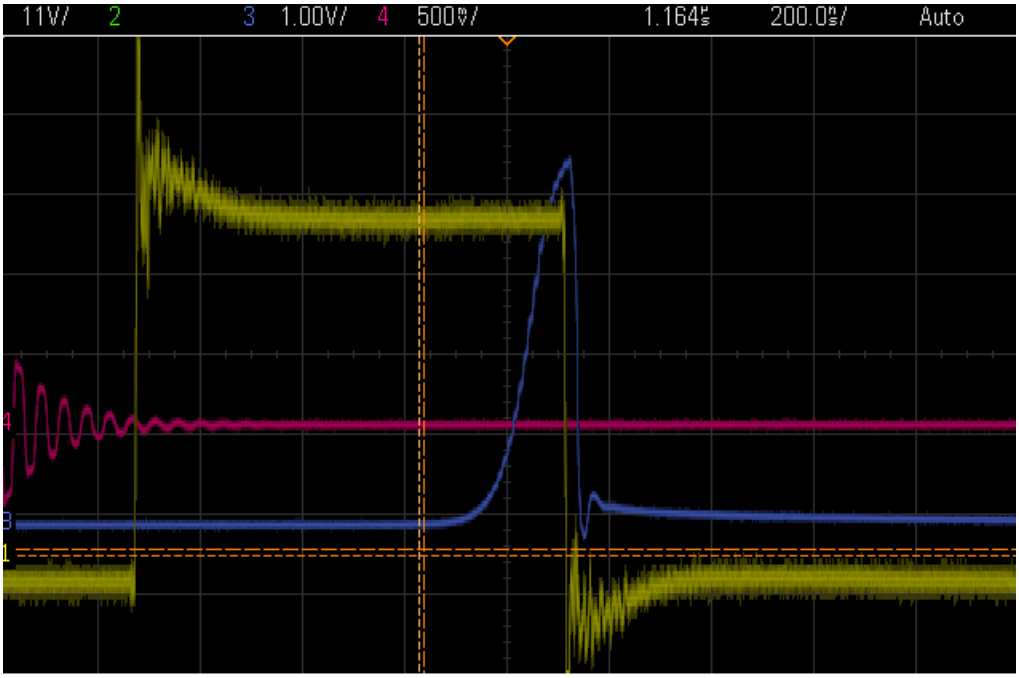

b)

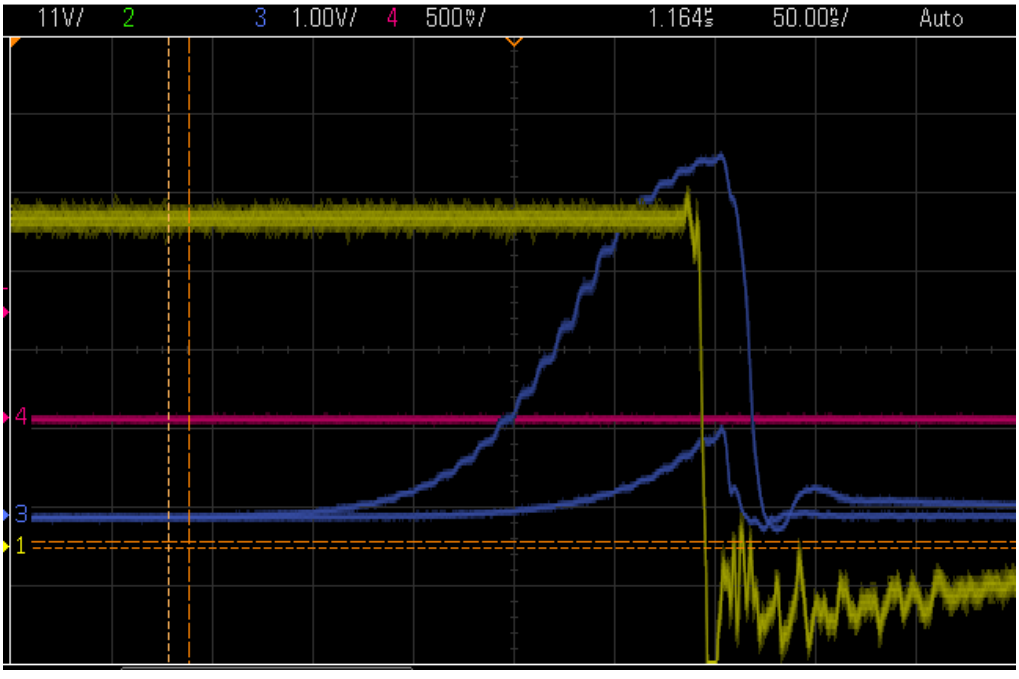

Figure 17: a) Example Q-switched signal of the diode monitoring the intracavity buildup (through the 2% output coupler . The pulse build up is the blue curve, the P.C switching signal is the yellow curve and the scope trigger signal (can be ignored) is the red curve. B) Stable bifurcation that occurs at a rep.rate of 5 kHz. Second pulse is ¼ the energy of the first.

3.5.3Amplified Pulsed operation

After the cavity was optimized in the Q-switch regime, the cavity was operated in the pulse amplification head. The input signal coupled into the cavity was a 1 kHz signal coming from the stretcher AOM system. The signal pulse energy at this point was 1.3nJ, due to losses in the stretcher fiber in-coupling and fiber AOM losses. The signal pulse energy coupled into the cavity was 0.8nJ.

In the pulsed amplification regime, the cavity on time is shorter than the Q-switched time. As well, the extracted energy was higher due to the higher peak intensity in pulsed operation at the last trip through the gain medium before extraction.

The average amplified pulse power at a pump power of 13.5W was found to be 396 µJ, which corresponds well with the simulations. The pulse reaches maximum amplification in 36 roundtrips (see, fig. 18). The simulation parameters at an input pulse energy of 0.8nJ yields 27 round trips. The discrepancy arises because the signal pulse is not matched to the cavity Eigen-mode at the start. Therefore, the effective energy in the Eigen mode is lower due to the lower overlap integral. As well, the higher order modes present in the signal at the start create modulations on the beam profile in the crystal, influencing the amplification across the beam. Thus, while these modes are being filtered in the first roundtrips, the amplification process in the proper cavity Eigen mode is hampered and effectively creates more passes in the crystal that are needed. Due to crystal heating, at higher rep.rates the beam quality suffered and pulse amplification was hampered (discussed in recommendations).

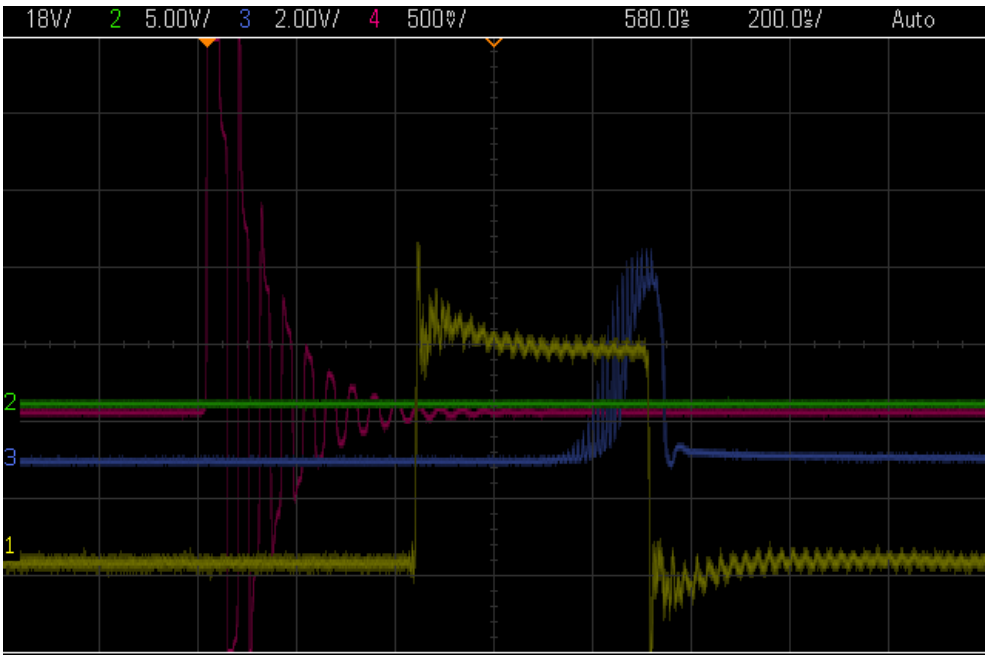

Figure 18: Intra-cavity build-up of signal pulse. Pulse peaks correspond to the round-trip number and are separated in time by the cavity roundtrip time (~10ns).

Unfortunately, further data could not be taken due to a pump diode failure that occurred.

3.6 Extensions and Recommendations

A pulse energy of 0.4mJ was extracted at 1 kHz. Due to the nice match with simulations, it can be deduced that replacing the crystal with a 5% 2.5mm Yb:KYW crystal with polarization orientated along the Nm axis should achieve amplification past 1mJ as simulations in the first section have shown.

It was also experimentally determined that the pump beam profile from the fiber pump system (LIMO, refer to appendix B2) was not adequately coupled into the core of the fiber delivery system. Greater than 40% of the power was coupled into the cladding. Due to these higher order modes, the pump beam focusing optics was inadequate to focus the beam to a flat topped profile or Gaussian profile at the crystal. As well, power in these modes was filtered out before the crystal. Simulations show that the input pulse intensity only extends the pulse time in the cavity. However, the absolute maximal amplified pulse energy is only strongly dependent on the stored energy. If the pump beam profile can be made to a top hat profile and can match with the 100um signal spot the complete stored energy reservoir can be accessed. The experiments were done at an output coupling of 2% (single pass). As well, a dichroic mirror was used for the other cavity end mirror that had an insertion loss at 1.03um of 1%. These losses contributed to high cavity losses that were found through experiment. The system will be updated with a low output coupler (0.5%) and a better dichroic mirror.

The REGEN was also un-cooled during all data acquisition. Power stability will greatly increase if the crystal is cooled to room temperature due to the reduction in thermal effects limiting beam quality.

Finally, the next step is to build up the pulse compression stage. It was already experimentally shown that a 273fs auto correlated pulse was achieved after compression of the pulse coming from the stretcher fiber. Due to the small crystal length, dispersive broadening can be viewed as negligible. As well, due to the low non-linear phase (b-integral), uncompressible phase variations are also at a minimum. The compressed pulse duration should not change significantly from this figure. Gain narrowing effects however, may increase the compressed pulse duration.

Chapter 3 Bibliography

1 Brooks, Christopher, and Fabio Di Teodoro. "1-mJ energy, 1-MW peak-power, 10-W average-power, spectrally narrow, diffraction-limited pulses from a photonic-crystal fiber amplifier." *Optics Express* 13.22 (2005): 8999-9002.

2 Calendron, Anne-Laure, Hüseyin Çankaya, and Franz X. Kärtner. "High-energy kHz Yb: KYW dual-crystal regenerative amplifier." *Optics express* 22.20 (2014): 24752-24762.

3 Calendron, Anne-Laure, et al. "High power and high energy Yb: KYW regenerative amplifier using a chirped volume Bragg grating." *Conference on Lasers and Electro-Optics*. Optical Society of America, 2009.

4 Buenting, Udo, et al. "Ultrafast Yb: KYW regenerative amplifier with combined gain spectra of the optical axes Nm and Np." *Lasers and Applications in Science and Engineering*. International Society for Optics and Photonics, 2008.

5 Obtained from the EKSMA company website

6 Saleh, Bahaa EA, Malvin Carl Teich, and Bahaa E. Saleh. *Fundamentals of photonics*. Vol. 22. New York: Wiley, 1991.

7 Papadopoulos, Dimitrios N., et al. "Broadband high-energy diode-pumped Yb: KYW multipass amplifier." *Optics letters* 36.19 (2011): 3816-3818.

8 Yariv, Amnon, and Pochi Yeh. *Photonics: optical electronics in modern communications (the oxford series in electrical and computer engineering)*. Oxford University Press, Inc., 2006.

9 http://goochandhousego.com/wp-content/uploads/2014/07/QS-align_roll_discussion6h-EF-04_v2a.pdf

10 Lowdermilk, W. H., and J. E. Murray. "The multipass amplifier: Theory and numerical analysis." *Journal of Applied Physics* 51.5 (1980): 2436-2444.

11 R. Paschotta, article on 'B Integral' in the Encyclopedia of Laser Physics and Technology, accessed on 2015-06-24

12 Jochen Dörring, Alexander Killi, Uwe Morgner, Alexander Lang, Max Lederer, and Daniel Kopf, "Period doubling and deterministic chaos in continuously pumped regenerative amplifiers," Opt. Express **12**, 1759-1768 (2004)

13 Yumashev, K. V., et al. "Z-scan measurements of nonlinear refraction and Kerr-lens mode-locking with Yb3+: KY (WO4) 2." *Optical and quantum Electronics* 32.1 (2000): 43-48.

Chapter 4: New Split-Step Method for Generalized Non-Linear Equations Applied to White-Light Generation in Bulk Material

4.1 Introduction

In order to develop new light sources for the coherent control of molecules it is first important to develop the simulation tools necessary to accomplish this goal, as stated in the thesis introduction. In this chapter, a novel numerical scheme was implemented to simulate the non-linear propagation of light in bulk material and the white-light generation that extends the spectrum.

4.1.1 Niche of the New General Split-Step Method

Within this chapter is presented, the first methodology to my knowledge that is entirely based on the Strang Fourier Split Step scheme and that can model extremely complex non-linear equations in all three spatial dimensions and time. Amongst a wide plethora of fields, these non-linear equations mostly arise in physical and mathematical disciplines such as Non-Linear Optics[1-3], Plasma Physics[4,5], Fluid Dynamics[6,7], and General Chaotic and Dynamical Systems[8,9].

Split-step methods are based on modelling the non-linear equation in an iterative fashion in one propagation coordinate. Per propagation step, the non-linear equation is usually decomposed in a series of coupled equations in terms of each operator (named flows of the equation). These operators are defined as terms of the non-linear equation that act in modifying the solution per propagation increment. The operators can be applied using Fourier transforms[10], in a discretized fashion or Finite Difference (FD) methods[11]. The advantage of using the split-step operator method over other conventional methods lies in the ease of use of the method and the low computational error introduced by the method due to its spectral nature[12]. It is limited mainly only by the Nyquist Criterion and its Fourier nature makes it easy to use on a quadrature grid. Also, the well-defined Fast Fourier Transform algorithm (FFT) is available in most scientific computing software and is optimized for a reduced number of operations which makes this approach, in general, faster than other conventional methods [11]. The reduced operations needed for the Split-Step Fourier Method (SSFM) and the ease of implementation render this method the most ideal for modelling non-linear equations. This will be the inherent goal in the derivation of this new SSFM. That is, to render it intuitive and well-defined for the user to use.

The Split-Step Fourier Method has been extensively explored in one dimensional systems such as the one-dimensional cubic Non-Linear Schrodinger Equation (NLSE) that models the substantive spectral broadening of light (accordingly named supercontinuum generation) as it propagates in fiber. Past studies focused primarily on estimating step-size dependent error and deriving adaptive step-size algorithms for the implementation of the method[13-15]. Other studies explored the stability of the method under various permutations such as introducing Finite-Difference Methods (FD) in the implementation of the operators used in the split-step scheme[16] or around certain bound solutions of a NLSE such as soliton formation[17].

However, extensions of the method itself have not been comprehensively explored until now. For example, the method has not been extended into a 3-D scheme in the spatial coordinates in a generalized sense. Studies have explored the prospect of using Bessel discretization for certain NLSE equations[23]. However, these discretization schemes do not translate to easy representations in a

domain that can reduce the operator expression (such as derivative terms) to easy algebraically defined expressions in terms only of independent variables. As well, they are limited to the study of spherically symmetric solutions. The easiest method that accurately does this is to use a Fourier split-step scheme and define spatial operators accordingly.

Another problem that needs to be considered is to extend this method to beyond cubic NLSE type equations. Taking the previous example of optical spectral generation, cubic NLSE equations well model supercontinuum generation in 1-D systems but do not model all the intricate processes that occur in Bulk material. The added terms and effects that need to be considered while propagating light in Bulk material in the generation of new spectral components for White-Light Generation (WLG) yield far from cubic 3-D NLSE type equations.

Other known computational methods used in the solutions of non-linear differential equations include the Runge-Kutta methods [19], Crank Nicholson methods [20], symplectic [21], relaxation methods [12,22] or combinations of such methods. Each of these methods bares a certain level of accuracy and stability that scales with grid step sizes, computation cost and inherent complexity. However, the computational time, the implementation ease, the low amount of operations and the adaptability of the newly derived extended SSFM offers an attractive alternate. As well, it is important to have a variety of methods since for some systems the stability of one method can be low, while another outperforms it. The advantages of this extended SSFM in relation to other methods will be briefly discussed over others as the derivation is carried through.

To demonstrate the usefulness of this method to the community the chapter will be divided into two broad topics: The derivation of the general method and the types of non-linear partial differential equations it models and its specific application to a complicated Non-Linear Schrödinger equation (NLSE) that is integral to the physics community. The NLSE chosen for the demonstration of the method describes white-light generation (WLG) in bulk Kerr media.

4.1.2 Description of the White-Light Generation Process

Non-linear Optical processes in bulk materials such as white light generation (WLG) are integral to a variety of optical systems and optical applications. WLG is a process where the pump signal generates a broadband optical spectrum that can span multiple octaves and whose spectral components are coherently locked to each other [23]. Within the optics community, this process is used for many applications such as single-cycle pulse generation [24,25], seeding optical-parametric amplifiers (OPA) [26,27,28,29] and two dimensional spectroscopy [30]. This non-linear process relies heavily on a high input optical intensity gradient generated from pulses in the femtosecond to picosecond range and consists of the combination of several non-linear and linear processes.

The pump pulse produces a change in the second order (non-linear) refractive index, which becomes a function of pump intensity. This produces both spatial lensing effects (such as self-focusing) and a phase variation within the envelope of the pulse creating a corresponding frequency broadening accordingly named self-phase modulation (SPM). SPM is the non-linear phenomena solely responsible for the actual generation of new frequencies in conventional systems omitting delayed effects such as stimulated Raman scattering[35]. Thus, WLG is inherently energy conserving and does not rely on an optical gain medium as in the case of a laser. To produce broader spectra and to control the WLG effect, one needs to control the interactions of the nonlinear and linear effects(such as dispersion and diffraction) that directly or indirectly influence the temporal gradient of the optical intensity through SPM. Of interest is additional higher order non-linear/linear effects such as space-time focusing [32],

plasma absorption, scattering and plasma refractive index effects that influence the intensity and the spectral generation.

The corresponding NLSE describing all of these effects and the addition of plasma absorption and scattering was shown to be accurately described in Gaeta et al [34]. As an example to the general method the equation outlined in Gaeta et al. will be simulated.

4.1.3 Organisation of Information in this Chapter

In the first section of this chapter a detailed derivation of the general method as applied to an outlined general non-linear partial differential equation will be presented. The second section of the chapter will introduce the specific physical system being studied (that of WLG in bulk material). The third section will discuss the general method as applied to this system and the fourth section will discuss the relevant sampling stability conditions for both the general method and applied to the specific system. The final section will present the results obtained from the simulation of the specific WLG equation and discuss these results as they apply to the extensive literature on the subject. Appropriate appendices will be referenced in the text.

4.2 Derivation of the General Method

To start the derivation of the general method, first a discussion of the type of solutions that the method aims to find will be carried out and the general form of non-linear partial differential equations the method can be applied to will be presented. The method will then be derived in a manner that reviews the general derivation of the SSFM.

I consider non-linear equations in which bound L-2 normed solutions are described. The general form of non-linear equations of which I consider in this chapter writes as:

$$\frac{\partial \mathrm{u}}{\partial \varsigma} = \wp \mathrm{u} + \mathbb{Q}\mathbb{N}\mathrm{u} \tag{75}$$

This equation is defined in a unit-less coordinate system and for unit-less quantities. Where, x,y are the transverse unit-less coordinates, τ is the unit-less time coordinate. ς, is the unit-less propagation coordinate.

$\wp$ is composed of a series over derivative operators $(\nabla, \frac{\partial}{\partial \tau})$. $\wp$ can be described as functions over derivative operators, where the functions correspond to the series convergence if the deriviative operators are replaced by variables in Eq. (76)**.**

$$\wp = \sum_{\mathrm{n}=0}^{\infty} \sum_{\mathrm{j}=0}^{\infty} \mathrm{c_n c_j} \nabla^{\mathrm{n}} \frac{\partial^{\mathrm{j}}}{\partial^{\mathrm{j}} \tau} \tag{76}$$

$\mathrm{c_n}$, $\mathrm{c_j}$ are complex constants. $\nabla^{\mathrm{n}} \equiv \frac{\partial^{\mathrm{n}}}{\partial^{\mathrm{n}}_{\mathrm{x}}} + \frac{\partial^{\mathrm{n}}}{\partial^{\mathrm{n}}_{\mathrm{y}}}$.

It can be shown that any summation of functions that can yield the Eq. (76) series representation can globally be described in an Eq. (76) series representation and thus, $\wp$ can be described as a summation of these functions. The reason for why $\wp$ is defined as in Eq. (76) will become clear later in this

section. If $\wp$ consists of a series of functions over derivatives it is assumed that this is a finite series (if not, see note in appendix C0.2).

$$\mathbb{Q} = \left(c_1 + c_2 \frac{\partial}{\partial \tau}\right) \tag{77}$$

c_1, c_2 are complex constants.

$$\mathbb{N} = \beta(|u|, \dots, |u|^j, u, u^*, v(x_\perp, \tau)) \tag{78}$$

β is a function whose arguments are the independent coordinate variables in space and time and distributions, some of which can be based on the absolute value of u to an arbitrary j^{th} order. Where, I use the notation $x_\perp$ to mark the set of unit-less transverse coordinates. $v(x_\perp, \tau)$ represents a set of functions based on $x_\perp, \tau$. For example, v can be spatial or temporal derivative functions of u such as its modulus powers. u is assumed to be an analytic function to at least the maximal derivative term used in an operator defined above and possesses norms up to L^j . Otherwise, Eq. (75) possesses branch points and discontinuities and unbound solutions which are not considered in this chapter, or further regions of validity may have to be imposed.

As stated above the assumption is made that there is an *integrably bound* L-2 norm[36] solution to Eq. (75) and thus, with the application of the operators that are about to be defined, u always remains integrably bound in L-2. Because, of the L-2 norm, the Fourier transform of u always exists, justifying the use of a Fourier method. Integrably unbound L-2 solutions are not considered due to the fact that these solutions are not relevant to physical applications (energy is not conserved).

Eq.(75) will now be split into a series of operators that are applied in an iterative sense along the propagation coordinate in the goal of producing a solution given initial and boundary conditions which is u inputted into the first slice of the propagation coordinate. In order to accomplish this goal, the operators will first be defined, then how they are applied will be studied and finally the complexity of the application method will be reduced.

To outline the method and the proof of its validity $\mathbb{QN}$ is split into distinct operators. $\mathbb{QN}$ can be expanded as:

$$\alpha = \mathbb{QN} = \left(c_1 \mathbb{N} + c_2 \left(\frac{\partial \mathbb{N}}{\partial \tau} + \mathbb{N} \frac{\partial}{\partial \tau}\right)\right) \tag{79}$$

α will be split into two operators once more.

$$\alpha = \alpha_1 + \alpha_2 \tag{80}$$

Defined as:

$$\alpha_1 = c_1 \mathbb{N} + c_2 \left(\frac{\partial \mathbb{N}}{\partial \tau}\right) \tag{81}$$

and,

$$\alpha_2 = c_2 \mathbb{N} \frac{\partial}{\partial \tau} \tag{82}$$

The reasons for doing this will become clear as the methodology is defined. However, at this stage I have decoupled α into an operator solely defined on distributions, and an operator defined by a distribution and a derivative operator. This decoupling simplifies the mathematics as will be seen later and is a rather intuitive way to deal with this operator.

At this point, it is clear to see which operators are linear and which operators are not. $\wp$ is the straight forward linear operator. As well, the commutation relation between all terms and combinations of terms in $\wp$ can trivially be shown to be zero using the commutation of partial derivatives of independent variables (see appendix C0 for proof). This means that the ordering of how each term in this operator is applied does not matter. Therefore, this operator carries minimal computational error and can be applied in one step due to the irrelevance of the ordering of its terms (its application will become clear later in this section).

α_1 is a non-linear operator solely and in a function form acting on distributions and not on derivative operators. It follows also that each term in α_1 and combinations of terms carry a commutation relation of zero. Thus, this operator can be applied in one step.

α_2 is named the augmented non-linear operator. It is defined as a series of difference operators and distributions acting on u. The form of α_2 is a combination of the linear operator and α_1 form and exists because of terms produced in the derivative cross products of α.

To proceed in implementing the following operators in an effective way to model Eq. (75) it is first necessary to reduce the complexity of some of these operators with the use of the Fourier representation, as done in traditional pseudo-spectral techniques [14]. The reason why $\wp$ is defined as a series and only this type of non-linear partial differential equation is considered is because in the inverse Fourier space of τ and the transverse spatial coordinates, these operators become defined as replacing the dummy variable in the series with $-i\mathrm{w}$ and $(-i\mathrm{kx}, -i\mathrm{ky})$ where w is the corresponding angular frequency variable of τ (also unit-less) and $(\mathrm{kx}, \mathrm{ky})$ are the corresponding spatial angular frequency variables of x,y (also unit-less). Therefore, these partial differential equations become easy to solve in a Fourier based method. This is explained in more detail below.

Since, $\wp$ consists of derivative terms of independent variables and has no dependence on functions of u itself, in its corresponding combined inverse space (kx,ky,w), the operations in $\wp$ are defined by functions of the independent variables rather than differential operations and becomes easier to implement:

To make this clear, using the series representation of $\wp$, in the Fourier domain, -iw only needs to be substituted for $\frac{\partial}{\partial \tau}$ and $-i\mathrm{kx}, -i\mathrm{ky}$ for $\nabla_{\mathrm{x}}^1, \nabla_{\mathrm{y}}^1$ and their powers to obtain the Fourier representation of the operator. This follows straight forward from the Fourier identities [37], the fact that series expansions w.r.t to the operator exists and of course because terms self-commute and commute with each other (please appendix C0 for pertinent proofs). Therefore, in the inverse space (kx,ky,w), $\wp$ is applied as :

$$\wp = \sum_{\mathrm{n}=0}^{\infty} \sum_{\mathrm{j}=0}^{\infty} \mathrm{c_n c_j}((-i\mathrm{kx})^{\mathrm{n}} + (-i\mathrm{kx})^{\mathrm{n}})\ (-i\mathrm{w})^{\mathrm{j}} \tag{83}$$

Which if $\wp$ is defined as a function over derivative variables, is equivalent to replacing the derivative variables of the function with the Fourier representation of the variables (above listed), obtaining a functional representation in the Fourier inverse domain. See appendix C0.2 for the proof and

convergence conditions for when it is possible to have a functional representation in the inverse domain. Thus, in the Fourier inverse domain the function is evaluated over these now numerical variables. This is of great benefit since in its Fourier space $\wp$ is a function over numerical variables instead of derivative operators and can be easily evaluated.

In contrast to $\wp$, it would be of no benefit to consider α_1 in any inverse space since it is of a functional form with no derivative operators and therefore it is considered in the original space it is written in.

In order to avoid any FDTD errors, the derivatives of the functions in α_1 are evaluated as Fourier operations, meaning the Fourier identity for the derivative outlined above is used and the term is transformed back into the time domain. Evaluating the derivative this way for a given step size and sampling at the appropriate Nyquist conditions (explained and derived in section 4.5, appendix C2), is more accurate than doing a numerical difference operation. There is no matrix truncation for one, and the difference operation averages the effects of the individual frequency components of the function, while using the Fourier identity does not. This only negligibly adds to computational time. For functions in α_1 that are defined in terms of an additional differential equation (i.e. for functions whose derivatives are defined instead), the appropriate time domain integration method is used, i.e. Runge-Kutta, etc. This does not take away much from the stability and accuracy of this simulation method over others for these types of nonlinear differential equations, since this step would have to be undertaken in those methods as well and this method still minimizes the use of these numerical difference techniques.

It will later be demonstrated that the complexity of α_2 can be reduced and then a suitable way to apply it will be found but first it is of importance to understand how $\wp$, α_1, α_2 can be applied to obtain the solution to Eq. (75). This lies in understanding how they are used in the following set of ordered differential equations that yield an approximation of u coming out of a propagation slice into the next slice [13]. Partial solutions$u_{\wp}$, $u_{\alpha 1}$, $u_{\alpha 2}$ are obtained that are defined as the solution to the below series of differential equations involving $\wp, \alpha_1, \alpha_2$ applied in the shown specific order within the step being considered. From this, [13, Eq.8-10] has shown that the overall solution of u coming from the step can thus be approximated. The specific ordering, named Strang symmetrisation [12] is needed because each of the 3 operators have a nonzero commutation relation to the others. Therefore, their ordering influences the result introducing numerical error. [12] has shown that the Strang symmetrisation scheme significantly reducing the computational error, to one that is proportional to the square of the propagation step size. From [13] the equations are updated to reflect the new 3 operator symmetric split step scheme:

$$1.\begin{cases} \dfrac{\partial u_{\wp}(\varsigma)}{\partial \varsigma} = \wp u_{\wp}(\varsigma), & \forall \varsigma \in [\varsigma_k, \varsigma_{k+\frac{1}{4}}] \\ u_{\wp}(\varsigma_k) = u(\varsigma_k), & \text{u coming from previous slice} \end{cases}$$

$$2.\begin{cases} \dfrac{\partial u_{\alpha 2}(\varsigma)}{\partial \varsigma} = \alpha_2 u_{\alpha 2}(\varsigma), & \forall \varsigma \in [\varsigma_k, \varsigma_{k+\frac{1}{2}}] \\ u_{\alpha 2}(\varsigma_k) = u_{\wp}(\varsigma_{k+\frac{1}{4}}) \end{cases}$$

$$3.\begin{cases} \dfrac{\partial u_{\wp}(\varsigma)}{\partial \varsigma} = \wp u_{\wp}(\varsigma), & \forall \varsigma \in [\varsigma_{k+\frac{1}{4}}, \varsigma_{k+\frac{1}{2}}] \\ u_{\wp}\left(\varsigma_{k+\frac{1}{4}}\right) = u_{\alpha 2}\left(\varsigma_{k+\frac{1}{2}}\right), \end{cases}$$

$$4.\begin{cases}\dfrac{\partial u_{\alpha 1}(\varsigma)}{\partial \varsigma} = \alpha_1 u_{\alpha 1}(\varsigma), & \forall \varsigma \in [\varsigma_k, \varsigma_{k+1}] \\ u_{\alpha 1}(\varsigma_k) = u_{\wp}\left(\varsigma_{k+\frac{1}{2}}\right)\end{cases}$$

$$5.\begin{cases}\dfrac{\partial u_{\wp}(\varsigma)}{\partial \varsigma} = \wp u_{\wp}(\varsigma), & \forall \varsigma \in [\varsigma_{k+\frac{1}{2}}, \varsigma_{k+\frac{3}{4}}] \\ u_{\wp}\left(\varsigma_{k+\frac{1}{2}}\right) = u_{\alpha 1}(\varsigma_{k+1}),\end{cases}$$

$$6.\begin{cases}\dfrac{\partial u_{\alpha 2}(\varsigma)}{\partial \varsigma} = \alpha_2 u_{\alpha 2}(\varsigma), & \forall \varsigma \in [\varsigma_{k+\frac{1}{2}}, \varsigma_{k+1}] \\ u_{\alpha 2}\left(\varsigma_{k+\frac{1}{2}}\right) = u_{\wp}(\varsigma_{k+\frac{3}{4}})\end{cases}$$

$$7.\begin{cases}\dfrac{\partial u_{\wp}(\varsigma)}{\partial \varsigma} = \wp u_{\wp}(\varsigma), & \forall \varsigma \in [\varsigma_{k+\frac{3}{4}}, \varsigma_{k+1}] \\ u_{\wp}\left(\varsigma_{k+\frac{3}{4}}\right) = u_{\alpha 2}(\varsigma_{k+1}),\end{cases}$$

Where the final $u_{\wp}(\varsigma_{k+1})$ calculated from the 7th step becomes u entering the next slice labelled (ς_{k+1}) in the propagation direction and the above 7 steps are repeated iteratively. Fig. visually represents the above iteration. The methodology of generating u, how the operators $\wp, \alpha_1, \alpha_2$ are applied, the ordering of how they are applied and to what they are applied to have just been shown. However, the above procedure can be simplified because the above differential equations can be solved analytically or "close to" analytically for all operators, yielding:

For the first step:

$$u_{\wp}(\varsigma) = e^{\wp(\varsigma-\varsigma_k)}u(\varsigma_k) \tag{84}$$

Coming out of the first step than:

$$u_{\wp}\left(\varsigma_{k+\frac{1}{4}}\right) = e^{\frac{1}{4}\wp\Delta\varsigma}u(\varsigma_k) \tag{85}$$

For the second step:

$$u_{\alpha 2}(\varsigma) = e^{\int_{\varsigma_k}^{\varsigma}\alpha_2(\varsigma')d\varsigma'}u_{\wp}\left(\varsigma_{k+\frac{1}{4}}\right) \tag{86}$$

The integral arises since the α_2 operator contains functions based on u, where u is a function of ς. However, since the interval $[\varsigma_k, \varsigma_{k+\frac{1}{2}}]$ is considered to be small and u and its derivatives are considered to be slowly varying relative to the step size of ς, a mean value theory [37] can be employed. Where, the value of α_2 in the exponent with u given from the end of the previous operator step is used.

This gives a value at $\varsigma_{k+\frac{1}{2}}$ (at the end of the step) of:

$$u_{\alpha 2}\left(\varsigma_{k+\frac{1}{2}}\right) = e^{\frac{1}{2}\alpha_2(u_{\wp}\left(\varsigma_{k+\frac{1}{4}}\right))\Delta\varsigma} u_{\wp}\left(\varsigma_{k+\frac{1}{4}}\right) \tag{87}$$

At the end of the third step:

$$u_{\wp}\left(\varsigma_{k+\frac{1}{2}}\right) = e^{\frac{1}{4}\wp\Delta\varsigma} u_{\alpha 2}\left(\varsigma_{k+\frac{1}{2}}\right) \tag{88}$$

At the end of the fourth step, again employing a mean value theory and using the value of u coming from the previous step for all functions of u in α_1 at ς_{k+1}, the following is obtained:

$$u_{\alpha 1}(\varsigma_{k+1}) = e^{\alpha_1(u_{\wp}\left(\varsigma_{k+\frac{1}{2}}\right))\Delta\varsigma} u_{\wp}\left(\varsigma_{k+\frac{1}{2}}\right) \tag{89}$$

At the end of the fifth step the following is obtained:

$$u_{\wp}\left(\varsigma_{k+\frac{3}{4}}\right) = e^{\frac{1}{4}\wp\Delta\varsigma} u_{\alpha 1}(\varsigma_{k+1}) \tag{90}$$

At the end of the sixth step:

$$u_{\alpha 2}(\varsigma_{k+1}) = e^{\frac{1}{2}\alpha_2(u_{\wp}\left(\varsigma_{k+\frac{3}{4}}\right))\Delta\varsigma} u_{\wp}\left(\varsigma_{k+\frac{3}{4}}\right) \tag{91}$$

And at the end of the final step:

$$u_{\wp}(\varsigma_{k+1}) = e^{\frac{1}{4}\wp\Delta\varsigma} u_{\alpha 2}(\varsigma_{k+1}) \tag{92}$$

Where now,

$$u(\varsigma_{k+1}) = u_{\wp}(\varsigma_{k+1}) \tag{93}$$

The proof of the integration of these steps is discussed in appendix C0.4. An example proof for these steps is shown in appendix C4.

The following scheme is then equivalent to:

$$u(\varsigma_{k+1}) = e^{\frac{1}{4}\wp\Delta\varsigma} e^{\frac{1}{2}\alpha_2\Delta\varsigma} e^{\frac{1}{4}\wp\Delta\varsigma} e^{\alpha_1\Delta\varsigma} e^{\frac{1}{4}\wp\Delta\varsigma} e^{\frac{1}{2}\alpha_2\Delta\varsigma} e^{\frac{1}{4}\wp\Delta\varsigma} u(\varsigma_k) \tag{94}$$

Where, the non-linear operators dependent on functions of u are calculated at u outputted from the previous operator step.

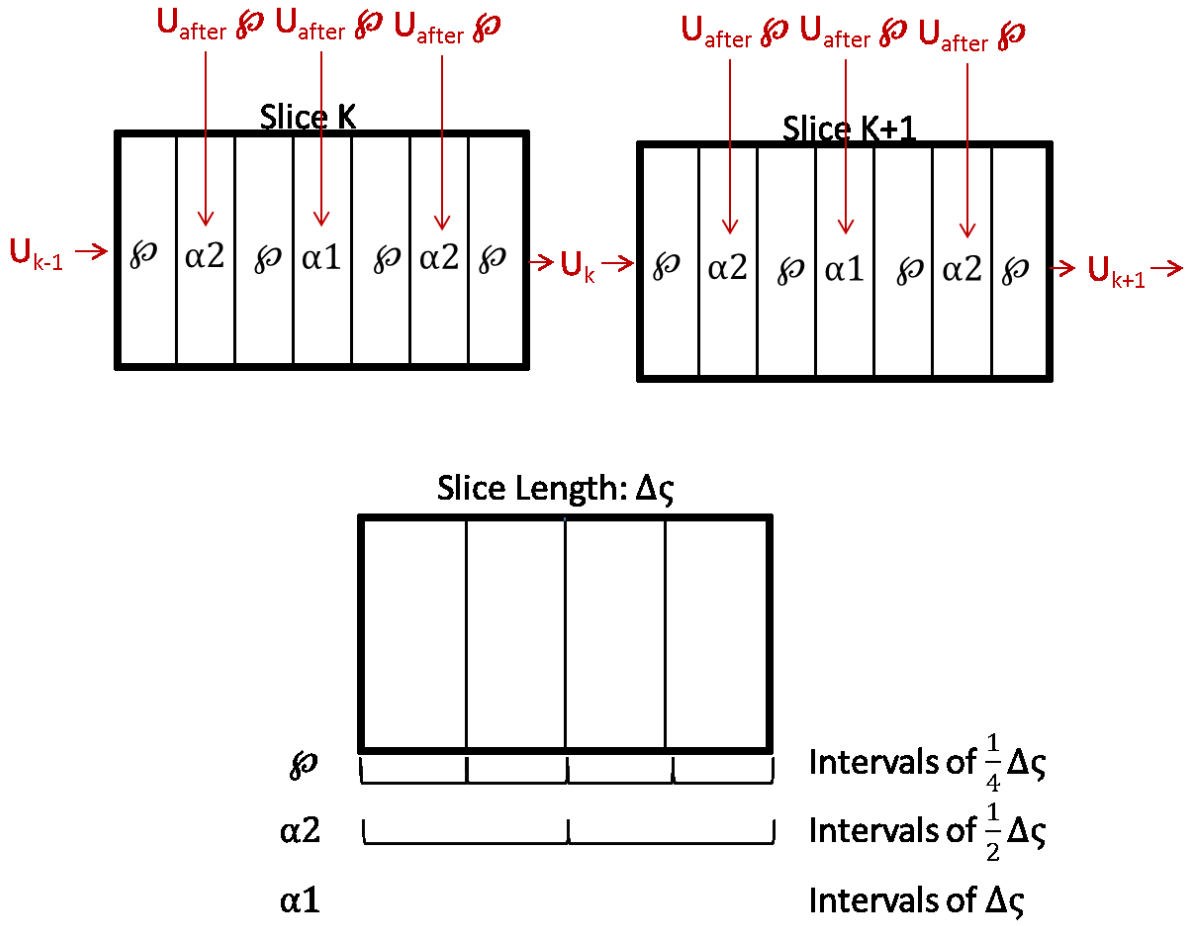

Figure 1: Graphical representation of steps 1-7. U_{k-1} is calculated from the output of the slice numbered k-1 and is used as the initial U in slice K. The updated U from the previous iterative sub steps in slice K is used to calculate the operator values for the pertinent sub step. Each operator is applied in intervals equivalent to the slice length divided by the amount of times the operator is applied in the slice.

The above ordering can be modified to fulfill different symmetrisations. In general, terms that are fast varying relative to others should be the ones most extensively split in the symmetrisation, as one would need to "sample u interacting with these terms" more often. The symmetrisation is not a hard constraint and is dependent on the problem and the computational resources. For the WLG problem, this symmetrisation was found to be the most stable in the set of symmetrisations that was considered and converged rather quickly with varying the propagation coordinate step size.

Therefore, the exponential of each operator is multiplied with u, which means the equivalent Maclaurin series expansion of the exponential with respect to the propagation coordinate is applied (which translates to substituting the argument of the exponential, which is linear w.r.t the propagation coordinate) into the well-known exponential Maclaurin series valid everywhere in the propagation coordinate domain space). Appendix C0 outlines in more detail how this procedure is done. Appendix C4 details the proof for why the Maclaurin series is applied. In the case where the operator is defined only as functions of the independent domain variables the numerical value of the exponential can be computed directly and then multiplied into u at the appropriate domain coordinates.

It can be derived (see appendix C0) that the Maclaurin series expansion of the exponential of an operator that is equivalent to a series of derivative terms with constant coefficients, multiplied into u in the original space is equivalent to the inverse Fourier transform of the exponential of the representation of that operator in the Fourier space (i.e., frequency space) applied to the representation of u in the Fourier space. If the representation of the operator converges to a function in Fourier space, the exponential of that operator in Fourier space will be the exponential of a function over independent numerical domain variables and can be computed directly in this space as stated in the paragraph above.

Given the above discussion, it is not prudent to evaluate the Maclaurin series expansion of the exponential operator of $\wp$ in the original space. Each term of the Maclaurin series will consist of a series expansion of derivative operators acting on u. therefore, numerical differentiation will have to be employed and both truncation in the terms of the Macluarin series and the series representation of each term will have to be employed. Instead, the exponential of $\wp$ representation in its Fourier space can be used. If the representation of $\wp$ reduces to a functional form, than the exponent can be directly calculated. If not, each term in the Maclaurin expansion will have to be calculated in this Fourier space for each domain value and both truncation in the Maclaurin series and truncation in the series representation of each term of the series will have to be used. However, numericial differentiation is avoided and this is a better approach than evaluating $\wp$ in its original space where its defined in terms of derivative operations (again, see appendix C0 for the rigorous proof and the procedure). The error then only depends on the numerical Fourier transform algorithm being implemented and the step size in the propagation direction. The Fourier error can be reduced if certain conditions of the sampling step sizes are maintained (i.e., the Nyquist criterion).

In the exponential form of the α_1 operator the function is applied in the original domains without need of a Maclaurin expansion since there are no derivative operators, and all is defined in terms of functions of the independent variables already (see appendix C0 for more details).

The complication factors in, in how the α_2 operator is applied. There are several ways in which this operator can be implemented. The operator can be implemented in the original domain and then truncated after some terms in the Maclaurin series expansion with respect to α_2 of the corresponding exponential. This yields time derivative operator terms that act on u. Less accurate finite difference methods would be required to evaluate the derivative terms acting on u after the expansion. However, as mentioned in the previous paragraph for greater accuracy and reduced computational requirements,

an equivalent version of the α_2 operator that has no Maclaurin series expansion required should be used.

The exponential expression of α_2 is simplified by first expanding the exponential operator in its Maclaurin series w.r.t to the propagation coordinate (where the step size $\frac{1}{2}\Delta\varsigma$ in the constants of α_2 is included for ease of writing):

$$e^{\alpha_2} = 1 + c_2\mathbb{N}\frac{\partial}{\partial\tau} + \frac{1}{2!}(c_2\mathbb{N})^2\frac{\partial}{\partial\tau}^2 + \frac{1}{3!}(c_2\mathbb{N})^3\frac{\partial}{\partial\tau}^3 \ldots \tag{95}$$

The above assumes the derivative commutes $\mathbb{N}$ and can be algebraically rearranged in the product. However, this is not completely true and an approximation. Please see appendix C4.3 for when this series expansion is valid and its limitations and the fix to this problem. $\mathbb{N}$ is calculated with the mean-value approximation outlined in steps 1-7.

Now, it can be seen that ($R = c_2\mathbb{N}$) :

$$e^{\alpha_2(\tau,\ldots)}u(\tau,\ldots) = [1 + R(\tau,\ldots)\frac{\partial}{\partial\tau} + \frac{1}{2!}R(\tau,\ldots)^2\frac{\partial}{\partial\tau}^2 + \frac{1}{3!}R(\tau,\ldots)^3\frac{\partial}{\partial\tau}^3 \ldots]u \tag{96}$$

The left hand side of Eq. (96) is obtained by carrying out the following integral operation, where I define w' as an additional independent variable, and $u(w',\ldots)$ as equivalent to the distribution given by the Fourier transform of u to the inverse variable domain of τ (ie, $u(w',\ldots) = u(w,\ldots)$):

$$\begin{aligned}\int_{-\infty}^{\infty}\left[1 + R(\tau,\ldots)(-iw') + \frac{1}{2!}R(\tau,\ldots)^2(-iw')^2 + \frac{1}{3!}R(\tau,\ldots)^3(-iw')^3 \ldots\right]u(w',\ldots)e^{-iw'\tau}dw \\ = \left[1 + R(\tau,\ldots)\frac{\partial}{\partial\tau} + \frac{1}{2!}R(\tau,\ldots)^2\frac{\partial}{\partial\tau}^2 + \frac{1}{3!}R(\tau,\ldots)^3\frac{\partial}{\partial\tau}^3 \ldots\right]u \\ = e^{\alpha_2(\tau,\ldots)}u(\tau,\ldots)\end{aligned} \tag{97}$$

Therefore,

$$\begin{aligned}e^{\alpha_2(\tau,\ldots)}u(\tau,\ldots) = \int_{-\infty}^{\infty}\left[1 + R(\tau,\ldots)(-iw') + \frac{1}{2!}R(\tau,\ldots)^2(-iw')^2\right. \\ \left. + \frac{1}{3!}R(\tau,\ldots)^3(-iw')^3 \ldots\right]u(w',\ldots)e^{-iw'\tau}dw'\end{aligned} \tag{98}$$

Where, R is unaffected by the Fourier integral since the integral is only over the independent variable w'. As well, since u is L2-normed each term in the Fourier integral is bound with the assumption that there is an integrably bound solution in L-2 to Eq.(75) with the initial input u, the overall summation of Fourier integrals in the right hand side of Eq. (98) yields an integrably bound solution in L-2.

Eq.(97) can be simplified further by using the Maclaurin series identity to the series within the Fourier integral in (97), yielding:

$$e^{-c_2\mathbb{N}iw'} = \left[1 + R(\tau, \dots)(-iw') + \frac{1}{2!}R(\tau, \dots)^2(-iw')^2 + \frac{1}{3!}R(\tau, \dots)^3(-iw')^3 \dots\right] \tag{99}$$

Where, the definition of R on the left hand side of Eq.(99) is used. Please note, the argument of the exponential now consists of a function defined on 4 independent variables: w', τ and the variables describing the transverse spatial coordinates and the following relation is obtained through substituting Eq.(99) into Eq. (98):

$$e^{\alpha_2(\tau,\dots)}u(\tau, \dots) = f_{w'}\{e^{-c_2\mathbb{N}iw'}u(w', \dots)\}|_\tau \tag{100}$$

$f_{w'}$ means the Fourier transform over w' at τ. This identity is used which gets past truncation errors and lets e^{α_2} be applied to u in terms of Fourier transform integrals.

It is worth noting that the derivative term $\mathbb{N}$ is assumed to be re-arrangeable in the product terms (power terms of $\mathbb{N}$) in the above expansion. This is an approximation. However, appendix C4.3 presents the case that overcomes this approximation and also justifies why this approximation is physically relevant.

$\overline{\alpha_2}$ is defined as the name of the operator $-c_2\mathbb{N}iw'$ when the above derived substitution identity is used.

The semantics of the α_2 operator will become clear once the general steps that are applied with all of these operators in their respective spaces are stated. Let Z be the series of operations:

$$\begin{aligned} Z = \text{fft}\, k\chi, k\psi, w, \rightarrow \chi, \psi, \tau e^{\frac{1}{4}\wp(k_x,k_y,w)\,\Delta\varsigma}\, \text{fft}\, \chi, \psi, \tau, \rightarrow k\chi, k\psi, w \text{fft} w' \\ \rightarrow \tau e^{\frac{1}{2}\overline{\alpha_2}(w',\tau,\dots)\,\Delta\varsigma}\, \text{fft}\, k\chi, k\psi, w, \rightarrow \chi, \psi, w e^{\frac{1}{4}\wp(k_x,k_y,w)\,\Delta\varsigma}\, \text{fft}\, x, y, \tau \rightarrow k\chi, k\psi, w \end{aligned} \tag{101}$$

χ, ψ represent the transverse spatial dimensions. For the α_2 operator it is explicitly written now with the step size factored out of its constant and with the $\frac{1}{2}$ symmetrisation adjustment to the step-size. I remind the reader that $\text{fft}_{w'} \rightarrow \tau e^{\frac{1}{2}\overline{\alpha_2}(w',\tau)\Delta\varsigma}u(w', \dots)$ means that u is first converted into the frequency domain (because it has the same representation in w'), secondly the exponent is applied at a value τ , thirdly, the inverse Fourier transform on the frequency domain of the updated total function at only that τ is carried out, fourthly, the process is repeated for all τ . At the input of this step $u(\chi, \psi, w)$ is sent and after this step an updated $u(\chi, \psi, \tau)$ is found.

The full symmetrisation yields:

$$u(\chi, \psi, \tau, \varsigma') = Ze^{\alpha_1\Delta\varsigma}Zu(\chi, \psi, \tau, \varsigma' - \Delta\varsigma) \tag{102}$$

This is done iteratively overall all steps in the propagation coordinate, ς.

One can see from the above treatment the power of this exponential operator theory. At the heart of traditional FDTD methods or Runge-Kutta methods the differential operators are replaced, with a numerical difference scheme. However, this method yields a step size dependent error and is inherently a computational approximation to the derivative terms. However, by using the Fourier representation of derivative terms, there is no violation in the nature of the derivative term, the derivative operator term is simply being replaced by its equivalent algebraic integral representation. There is no step size dependent error in this sense and provided that the Fourier transform can be represented by the FFT algorithm accurately, i.e. if the Nyquist criterion is met, there is no other over all errors in computing these derivatives.

Applying an FDTD or Runge-Kutta method to solve the differential equations in steps 1-7 also bears more error in the integration than the preceding method. For example taking step 1, a FDTD method would look like:

$$u_{\wp}(\varsigma_{k+\frac{1}{4}}) = u_{\wp}(\varsigma_k) + \frac{\partial u_{\wp}(\varsigma)}{\partial \varsigma}|\varsigma_k(\frac{1}{4}\Delta\varsigma) \ = u_{\wp}(\varsigma_k) + \wp u_{\wp}(\varsigma_k)(\frac{1}{4}\Delta\varsigma) \tag{103}$$

Where, the operators can be carried out in the Fourier treatment or with Taylor series expansions (specifically those with differential operators). The more pronounced error in the integration arises because the mean value theorem would still have to be applied for these methods as well, and these methods turn out to be a computational approximation of the analytic solution under the mean value approximation. However, the exponential method outlined in this chapter is the true analytic solution of the integration under the mean value approximation. Runge-Kutta methods bare the same form albeit more developed as (103). Therefore, it will always out-compete applying Runge-Kutta methods for the longitudinal propagation. The exponential describes the step without making the extra assumption that the system is discretized, it still respects the continuous nature of the problem while other methods do not make this distinction. Adaptive recursive or implicit methods can overcome the mean-value approximation itself, but these are substantially more complex methods that lie out of the scope of this chapter. The computational costs increase and the stability of such methods may be an issue or hard to evaluate.

In sum, the system acts in an exponential manner to the propagation coordinate, since it equates to the derivative of this coordinate with no functional coefficient, thus, the most accurate, stable and intuitive way to model it would be in an exponential form.

4.3 Defining the Equation and Explaining the WLG Process

In this section, the preceding method will be applied to a specific problem in physics: Namely, WLG in bulk material. As stated in the introduction, the various linear and non-linear processes involved in the spectral broadening of the input pump signal in the material can be modeled by the corresponding NLSE. Fig. 2 and fig. 3 and their captions in subsection 4.2 will illustratively explain the dominant temporal and spatial effects of WLG in bulk material.

4.3.1 Defining the NLSE Equation

The NLSE considered in this section, that describes the various effects contributing to WLG, is taken from [34] with trivial corrections (please see footnote in appendix C1):

$$\frac{\partial u}{d\varsigma} = \frac{i}{4}\left(1+\frac{i}{\omega_o\tau_p}\frac{\partial}{\partial\tau}\right)^{-1}\nabla_\perp^2 u - i\frac{L_{df}}{L_{ds}}\frac{\partial^2 u}{\partial\tau^2} + i\left(1+\frac{i}{\omega_o\tau_p}\frac{\partial}{\partial\tau}\right)\left[\frac{L_{df}}{L_{nl}}|u|^2 u - \frac{L_{df}}{L_{pl}}\left(1-\frac{i}{\omega_o\tau_c}\right)\rho u + i\frac{L_{df}}{L_{mp}}|u|^{2(m-1)}u\right] \quad (104)$$

The derivation was carried out by updating the Maxwell's equations with the appropriate polarizability term covering all effects in Table 1. Both the slow-varying envelope approximation was used and the paraxial approximation. The L constants represent various non-linear and linear lengths for physical processes. They are all outlined in appendix C1 and taken from [34]. The equation is over reduced unit-less coordinates. Where, ς labels the propagation coordinate, τ_p is the RMS value of the original pulse duration and ω_o is the angular central frequency of the original pulse. ρ represents the normalized plasma distribution being created by the optical intensity. The first two terms are the linear terms of the equation.

ρ , the normalized plasma density term is a function of u. The optical radiation undergoes multi-photon absorption to produce a plasma, meaning unbound charge carriers, in the material. The plasma that is created is assumed to be static, meaning the dynamics of the plasma density occurs over a much broader timescale than the pulse duration. The plasma density is defined by a linear first order non-homogenous differential equation:

$$\frac{\partial\rho}{\partial\tau} = \alpha\rho|u|^2 + |u|^{2m} \quad (105)$$

m is a constant and is related to the order of photo-absorption.

It is verifiable that Eq. (104) is of the general form of Eq. (75), and thus, the above derived method can be used. The equation is defined in unit-less coordinates $\chi = \frac{x}{Sp}$,$\psi = \frac{y}{Sp}$ where x,y are the normal transverse coordinates to the propagation axis of the input optical field. Sp is a constant in meters usually equal to the spot size, rendering χ , ψ unit-less. The unit-less spatial gradient is the second derivative over χ, ψ.

$$\nabla_\perp^2 = \nabla_\chi^2 + \nabla_\psi^2$$

As well, $\tau = \frac{t - z/v_g}{\tau_p}$ where, z is the propagation coordinate, v_g is the group velocity (constant) and τ_p is the RMS value of the initial input electrical field making τ unitless. Eq. (104) models the WLG

propagation in a frame of reference travelling at the group velocity of the input pulse and thus, is in terms of τ. Due to the slow-varying approximation, the linear phase term of the propagation coordinate is omitted.

The unit-less z propagation coordinate is given as $\varsigma = z/L_{df}$, where L_{df} is in meters and represents the diffraction length (the Rayleigh length for an input Gaussian).

The above differential equation describes the evolution of the input envelope electric field normalized to the peak amplitude. The electric field at the input plane of the crystal (from free space) is described as:

$$E = Ae^{-(\frac{x^2+y^2}{2Sp^2}+\frac{t^2}{2\tau p^2})}e^{i(w_o t+\varphi)}$$

Where, w_o is the central frequency and φ is a phase. A is the peak amplitude. u, the normalized envelope of the electric field is related to E as follows:

$$u = \frac{|E|}{A} = e^{-(\frac{x^2+y^2}{2Sp^2}+\frac{t^2}{2\tau p^2})}$$

It is sufficient only to solve (104) in the appropriate coordinates to obtain the full solution of E within the crystal and at the terminal point of the crystal. The final u obtained yields the output E as follows:

$$E = Aue^{i(w_o t+\varphi)}e^{i(kz)}$$

With the appropriate transform to unit coordinates. Where k is the momentum of the central frequency w_o in the material and z is the total crystal length.

The coefficient lengths are defined for an input that is a radial Gaussian beam and therefore, this equation is implicitly defined for an initial value Gaussian in time and boundary value Gaussian in space. However, the equation can model any arbitrary inputted electric field amplitude profile as long as the paraxial approximation at the input can be used justifying the use of the full 3-D split step technique above derived.

4.3.2 Illustration of Relevant Physical Effects Described by the NLSE

Table 1, summarizes the physical meaning of each term on the right-hand side of the equation. [34] references work that presents an extensive discussion of these terms.

Term	Physical Process
$\frac{i}{4}\left(1+\frac{i}{\omega\tau_p}\frac{\partial}{\partial\tau}\right)^{-1}\nabla_\perp^2 u$	Space-time Focusing: Diffractive term coefficient (function of temporal derivative). Accounts for the dependence of diffraction, i.e., spatial propagation in transverse dimensions long the propagation axis, on the frequency of the optical radiation. Diffractive term: Accounts for spatial propagation in transverse dimensions along the propagation axis.
$-i\frac{L_{df}}{L_{ds}}\frac{\partial^2 u}{\partial\tau^2}$	Dispersion term assuming constant group velocity dispersion (GVD) across generated spectral components.
$i\left(1+\frac{i}{\omega\tau_p}\frac{\partial}{\partial\tau}\right)$	Self-Steepening term (in paragraph below).
$\frac{L_{df}}{L_{nl}}\lvert u\rvert^2 u$	Non-linear term describing Self-Phase Modulation (SPM) and Kerr-lensing both due to the intensity dependent nature of the refractive index.
$-\frac{L_{df}}{L_{pl}}\left(1-\frac{i}{\omega_o\tau_c}\right)\rho u$	Plasma term describing plasma scattering and effects due to the refractive index variation of the plasma population.
$i\frac{L_{df}}{L_{mp}}\lvert u\rvert^{2(m-1)}u$	Plasma absorption term describing the effect of multiphoton absorption.

Table 1: Physical meaning of derived terms in Eq. (104).

a)

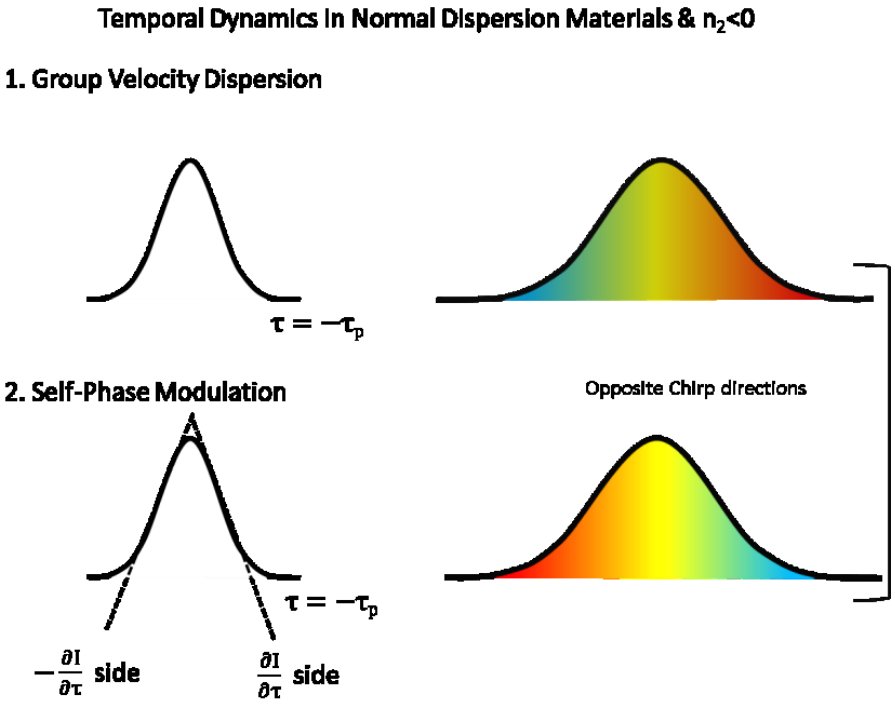
Temporal Dynamics in Normal Dispersion Materials & n_2<0
1. Group Velocity Dispersion
$\tau = -\tau_p$
2. Self-Phase Modulation
Opposite Chirp directions
$\tau = -\tau_p$
$-\frac{\partial I}{\partial \tau}$ side
$\frac{\partial I}{\partial \tau}$ side

b)

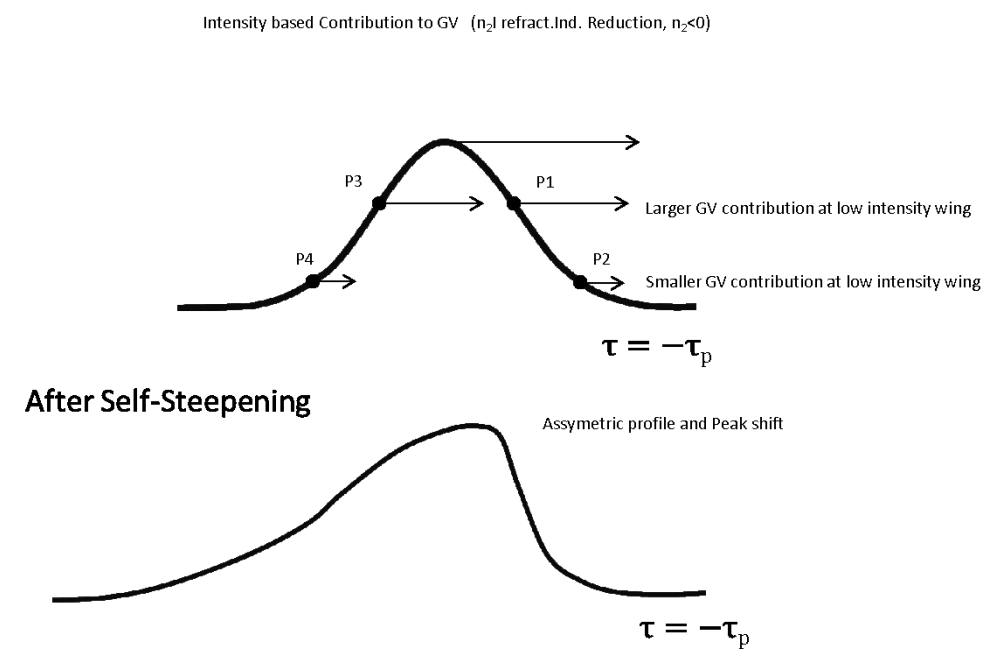
3. Self-Steepening
Intensity based Contribution to GV (n2I refract.Ind. Reduction, n2<0)
P3
P1
Larger GV contribution at low intensity wing
P4
P2
Smaller GV contribution at low intensity wing
$\tau = -\tau_p$
After Self-Steepening
Assymetric profile and Peak shift
$\tau = -\tau_p$

c)

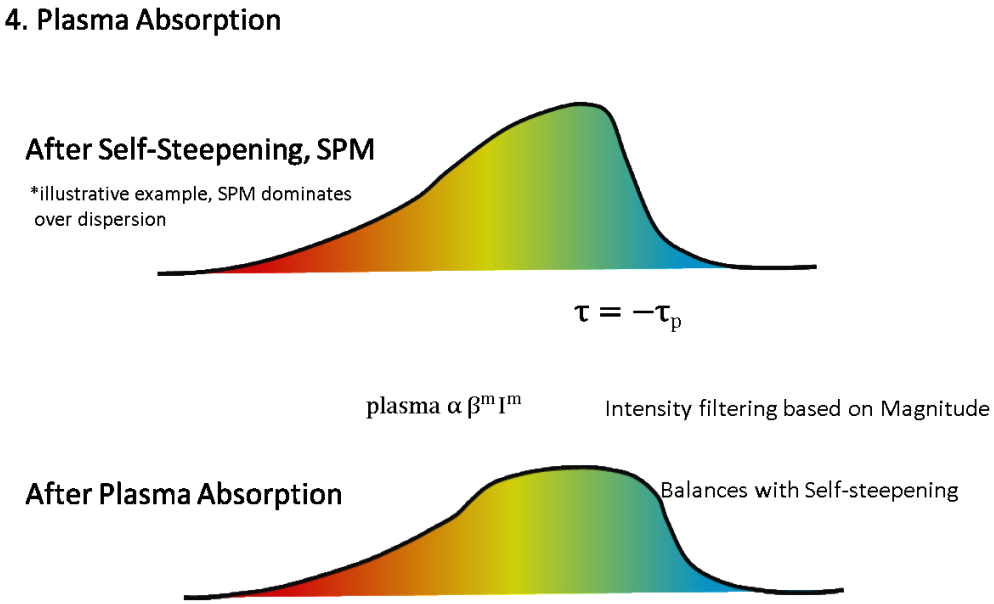

d)

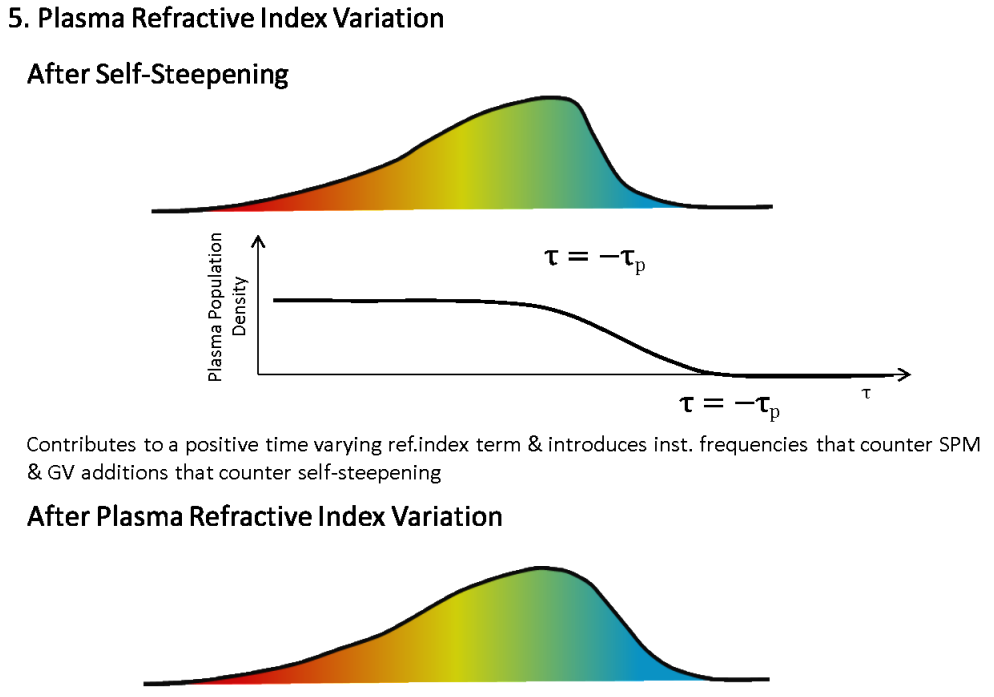

Figure 2: a) Illustration of the effect of group velocity dispersion (explained extensively in chapter 2) and the effect of SPM (refer to Eq. (16) in chapter 2). SPM generates instantaneous frequencies in the opposite direction of the GVD reorganization of frequencies (references for SPM and GVD are found in chapter 2). b) Self-Steepening imposes a group velocity delay at different intensity points along the pulse because of the intensity dependent refractive index (int.dep.ref.index) term. For example, for a reducing term ($n_2 < 0$) P1 has a higher negative velocity and heads towards P2 at the front of the pulse. P4 has a lower negative velocity than P3 and thus the net delay between these two points increases. The peak also shifts at a maximal negative velocity. This gives a steepened edge on the front

of the pulse and a shifted peak towards the front, creating an asymmetric pulse profile. For $n_2 > 0$ the case is reversed. c) Multi-photon plasma absorption exponentially increases with intensity (this can be deduced from the plasma equations presented in [34]) . Therefore, intensities are filtered by magnitude, where the peak will be reduced more than the wings of the pulse. This reduces the peak intensity and reduces the steepened slope generated by self-steepening, creating a balance. This also prevents the peak intensity to rise above the damage threshold of the material. This extends the amount of time the pulse can stay in the material[34] and through SPM over a greater length; broader frequency bandwidth can be generated. d) Plasma refractive index variation is positive and counters SPM frequency generation (in the buildup region of the plasma density, where it is a strongly varying function of time). As well, the positive refractive index term counters the group velocity delay dynamics of the negative int.dep.ref.index term in the self-steepening process. This broadens the pulse and reduces the self-steepening effect.

a)

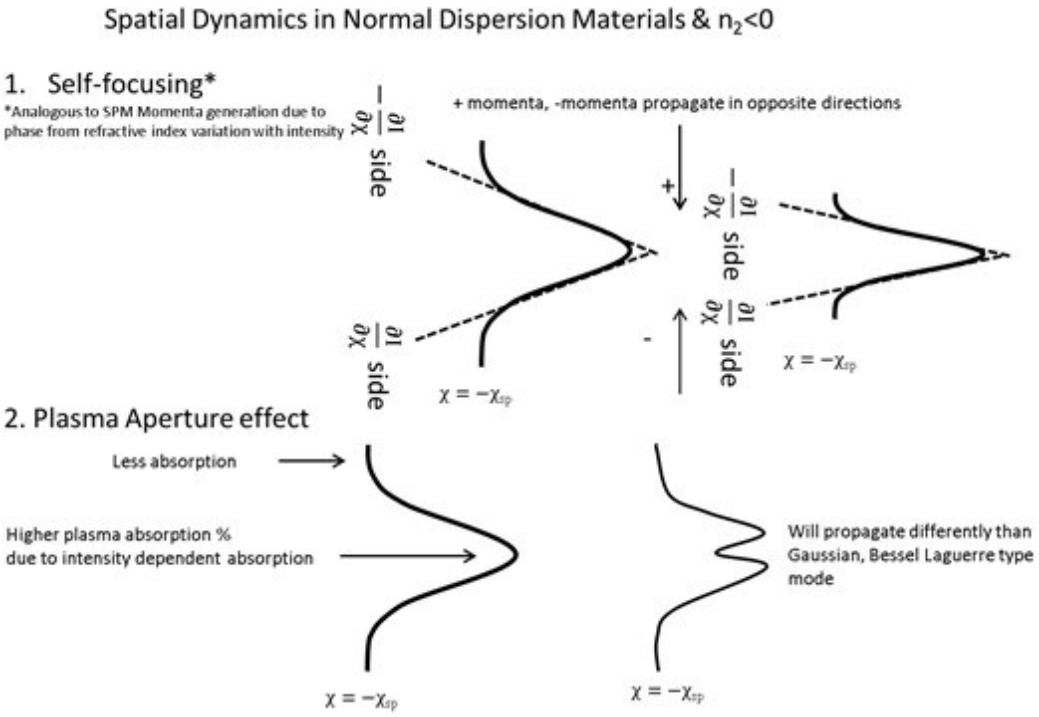

b)

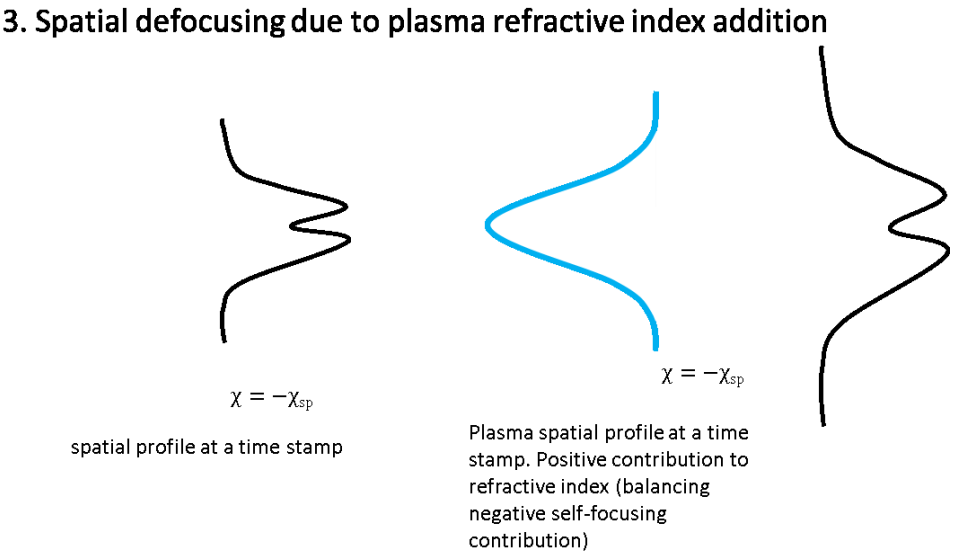

Figure 3: a) Self-focusing is demonstrated. It is an analogy to SPM, where the int.dep.ref.index generates spatially instantaneous momenta proportional to the spatial derivative of the intensity[33, chapter 2]. These momenta propagate to compress the pulse, in a lensing effect (in the negative case of the int.dep.ref.index). The plasma term generates a time dependent absorptive aperture that represents exponentially higher absorption for higher intensity. This generates a donut type mode (refer to Results section 4.6.3). b) The time-dependent plasma refractive index addition counters the negative int.dep.ref.index and defocuses the pulse. This prevents self-focusing to focus the beam to peak intensities that damage the crystal, and can extend the WLG process.

Since the extensive numerical method above derived is primarily to account for self-steepening (through the additional time derivative operation), it is worth presenting a brief overview of this effect.

Self-steepening is a term that explains the effects of the additional group velocity dispersion a due to the dependence of the refractive index on the optical intensity. This effect contributes to a shift of the peak intensity and an asymmetric steepening of the optical pulse. The peak shifts to the back of the pulse for a positive second order coefficient of the refractive index w.r.t the expansion of the refractive index with the optical electric field (n_2) and to the front for a negative coefficient[42]. This is because the self-steepening term in the simple NLSE goes as [42]:

$$i\varepsilon\frac{\partial(\gamma|u|^2u)}{\partial\tau} = i\varepsilon\gamma\frac{\partial(|u|^2)}{\partial\tau}u + i\varepsilon\gamma\frac{\partial(u)}{\partial\tau}|u|^2 \tag{106}$$

γ is the-non-linear coefficient used for the SPM term. Where ε is the self-steepening coefficient. The first term on the right hand side can be viewed as responsible to account for the fast varying effect of self-steepening. It is responsible for the amplitude intensity reorganizing due to enhanced SPM generation at the steepened slope and its interaction with the intensity dependent GV. The second term reorganizes the instantaneous phase variation, because of the additional intensity dependent group velocity change, and generates the steepening to begin with. It is responsible for the slower and global effects of self-steepening. Due to the time reorganization of the second term being intensity dependent, there is an additional instantaneous frequency generation effect, for more details appendix C2.2 rigorously explores the effects of self-steepening. Instantaneous frequencies generated through SPM

scale with the first derivative of the optical intensity. For positive n_2, the asymmetric steepening of the optical waveform interacts with SPM in a manner that generates bluer frequencies.

The derivative operator acting on u with a time-dependent distributional coefficient adds numerical complexity to the problem and is why traditional split-step methods cannot be used and where the above derived method can be used for WLG in bulk. It is this physical operation and the 3-D spatial nature of the differential equation that justifies using the numerical method above derived. As well, self-steepening is responsible for creating an optical shock in the material with a high peak intensity that can eventually damage the material. Therefore, including this very important effect can provide upper bound estimates for crystal lengths used in experiments. As well, it can evaluate if plasma absorption is sufficient to balance out this effect in materials.

In (104), the self-steepening term is described by:

$$\frac{-1}{\omega_o \tau_p}\frac{\partial}{\partial \tau}\left[\frac{L_{df}}{L_{nl}}|u|^2 u - \frac{L_{df}}{L_{pl}}\left(1-\frac{i}{\omega_o \tau_c}\right)\rho u + i\frac{L_{df}}{L_{mp}}|u|^{2(m-1)}u\right].$$

An over-arching way of understanding these non-linear terms is that $i\left(1+\frac{i}{\omega_o \tau_p}\frac{\partial}{\partial \tau}\right)$ acts on an overall intensity profile given as:

$$\gamma_{effective}|u_{effective}|^2 = \frac{L_{df}}{L_{nl}}|u|^2 - \frac{L_{df}}{L_{pl}}\left(1-\frac{i}{\omega_o \tau_c}\right)\rho + i\frac{L_{df}}{L_{mp}}|u|^{2(m-1)} \quad (107)$$

4.4 Defining the Split Step Operators and Split Step Method for the NLSE

The exact operator method will now be derived for Eq.(104) in this section. In accordance with the method, the first step is to partition the crystal medium into a series of steps in the propagation coordinate where the solution of one step is fed into the input of the proceeding step. The solution coming out of a step is calculated by applying a series of operations on the input field distribution. These operations are based on the coefficient functions that act on u in each term on the right hand side of the differential equation. The procedure follows the method derived in section 4.2. All that remains is to group the terms in the NLSE in corresponding linear, non-linear and augmented non-linear operators.

The first 2 terms on the right hand side given as: $\frac{\mathrm{i}}{4}\left(1+\frac{\mathrm{i}}{\omega_o\tau_p}\frac{\partial}{\partial\tau}\right)^{-1}\nabla_\perp^2-\mathrm{i}\frac{L_{df}}{L_{ds}}\frac{\partial^2}{\partial\tau^2}$ can be grouped together to produce one corresponding operation. These terms are grouped together because they are both linear operators of the spatial domain and time domain that are not functions of u and commute with each other. It will be shown later that the grouping of both these terms has a simple representation. The operators in these two terms act on independent domains: The spatial domain and the temporal domain and therefore in independent inverse domains: The momentum domain and the frequency domain. Since, the commutation relation between these two terms is zero, meaning that the ordering of how each term in this operator is applied does not matter.

Therefore, for the straight forward linear operator, it is defined as:

$$\widehat{\mathrm{A}}=\frac{\mathrm{i}}{4}\left(1+\frac{\mathrm{i}}{\omega_o\tau_p}\frac{\partial}{\partial\tau}\right)^{-1}\nabla_\perp^2-\mathrm{i}\frac{L_{df}}{L_{ds}}\frac{\partial^2}{\partial\tau^2} \tag{108}$$

$\widehat{\mathrm{A}}$ is composed of two functions (each term on the right hand side) that are over derivative operator parameters. $\widehat{\mathrm{A}}$ has the following series expansion:

$$\widehat{\mathrm{A}}=\sum_{n=0}^{\infty}\sum_{j=0}^{\infty}c_n[(-1)^j(\frac{\mathrm{i}}{\omega_o\tau_p})^j+d_n](\frac{\partial}{\partial\tau})^j\nabla_\perp^n \tag{109}$$

Where, $c_n=0$ when $n\neq 2$, otherwise $c_n=\frac{\mathrm{i}}{4}$. $d_n=0$ if $n\neq 0$, otherwise, $d_n=-\mathrm{i}\frac{L_{df}}{L_{ds}}$. The above was derived with the binomial expansion substitution of $\left(1+\frac{\mathrm{i}}{\omega_o\tau_p}\frac{\partial}{\partial\tau}\right)^{-1}$, which is meant to be the functional description of that series (this can be seen in the original derivation of Eq. (104)). Therefore, $\widehat{\mathrm{A}}$ is in the form of Eq. (76), which converges to a summation of two functions (described in Eq. (108)) and $\widehat{\mathrm{A}}$ satisfies the conditions to be considered as $\wp$ in section 4.2.

By corollary **C**0.2 the derivative terms in the functional representation of $\widehat{\mathrm{A}}$ in Eq. (108) can be replaced by the Fourier variables to obtain the operator (labelled as $\widehat{\mathrm{A}}(k_\chi,k_\psi,w)$) that is applied in Fourier space, in accordance with the discussion in appendix C0 and section 4.2. This yields:

$$\widehat{\mathrm{A}}(k_\chi,k_\psi,w)=-\frac{\mathrm{i}}{4}\left(1+\frac{1}{\omega_o\tau_p}w\right)^{-1}(k_\chi{}^2+k_\psi{}^2)+\mathrm{i}\frac{L_{df}}{L_{ds}}w^2 \tag{110}$$

w is the angular frequency of τ, k_χ, k_ψ are the angular frequencies of χ,ψ. The region of validity for the series convergence in the inverse space must be considered, see appendix C3. The operator series expansion in the frequency domain converges to Eq. (110) within the bandwidth of the slow varying

approximation used for Eq. (104). Thus, when applying the $\widehat{A}$ exponential operator, no series truncation is needed (see note in appendix C0.2).

In terms of the angular frequency (ω) of t (united proper time) for the entire expression of u w is related to it as:

$$w = \tau_p(\omega - \omega_o) \tag{111}$$

Where, ω_o is the central angular frequency of the input pulse.

I am then left with terms on the right hand side of the considered differential equation whose coefficients are functions of u, ρ and also functions of u, ρ and the time differential operator. I group the terms whose coefficients are just functions of u in to another operator which is called the nonlinear operator acting on χ, ψ, τ:

$$\begin{aligned}\widehat{B}(\chi,\psi,\tau) = i\left[\frac{L_{df}}{L_{nl}}|u|^2 + \frac{L_{df}}{L_{pl}}\left(1+\frac{i}{\omega_o\tau_c}\right)\rho + i\frac{L_{df}}{L_{mp}}|u|^{2(m-1)}\right] \\ + \left(\frac{-1}{\omega_o\tau_p}\right)\left[\frac{L_{df}}{L_{nl}}\frac{\partial}{\partial\tau}|u|^2 + \frac{L_{df}}{L_{pl}}\left(1+\frac{i}{\omega_o\tau_c}\right)\frac{\partial}{\partial\tau}\rho + i\frac{L_{df}}{L_{mp}}\frac{\partial}{\partial\tau}|u|^{2(m-1)}\right]\end{aligned} \tag{112}$$

ρ is found by solving its ordinary differential equation using a Runge-Kutta 4th order method (RK4) with u inputted into the operator. u inputted in the operator function is the u after previous operators are applied. This is also true for the $\widehat{C}$ operator shown below. The RK4 method is sufficient for this non-homogenous first order ODE.

In contrast to $\widehat{A}$, it would be of no benefit to consider $\widehat{B}$ in any inverse space and I consider it in the original χ, ψ, τ space. Also, it can be shown that each term in $\widehat{B}$ has a commutation relation of zero with any other term or combination of other terms. Therefore, as in the case with $\widehat{A}$ ordering of individual terms do not matter.

The remaining are now the terms with coefficients that are both functions of u, ρ and the time differential operator. I call this operator the augmented non-linear operator:

$$\widehat{C} = \left(\frac{-1}{\omega_o\tau_p}\right)\left[\frac{L_{df}}{L_{nl}}|u|^2\frac{\partial}{\partial\tau} + \frac{L_{df}}{L_{pl}}\left(1+\frac{i}{\omega_o\tau_c}\right)\rho\frac{\partial}{\partial\tau} + i\frac{L_{df}}{L_{mp}}|u|^{2(m-1)}\frac{\partial}{\partial\tau}\right] \tag{113}$$

$$\overline{C(w',\tau)} = \left(\frac{-1}{\omega_o\tau_p}\right)\left[\frac{L_{df}}{L_{nl}}|u|^2 + \frac{L_{df}}{L_{pl}}\left(1+\frac{i}{\omega_o\tau_c}\right)\rho + i\frac{L_{df}}{L_{mp}}|u|^{2(m-1)}\right](-iw') \tag{114}$$

The symmetrisation is obtained by studying the physical effects of each operator (Table 2). Dispersion and Diffraction do not rely on the slow-varying (or mean field approximation) of u and thus, they must be sampled more because they can be relatively faster varying in the propagation slice. As well, the self-steepening effect, being a higher order effect does not contribute as much as the physical processes in the B operator. Therefore, it will be sampled once in the propagation slice.

Using the analysis of section 4.2 for the linear, non-linear and augmented operator, the following is obtained:

$$\begin{aligned} Z = \mathrm{fft}\, k\chi, k\psi, w, \rightarrow \chi, \psi, \tau e^{\frac{1}{4}\hat{A}(k_{\chi'}, k_{\psi'}, w)\Delta\varsigma}\, \mathrm{fft}\, \chi, \psi, \tau, \rightarrow k\chi, k\psi, w\, \mathrm{fft}\, w' \\ \rightarrow \tau e^{\frac{1}{2}\overline{C(w', \tau)}\Delta\varsigma}\, \mathrm{fft}\, k\chi, k\psi, w, \rightarrow \chi, \psi, w e^{\frac{1}{4}\hat{A}(k_{\chi'}, k_{\psi'}, w)\Delta\varsigma}\, \mathrm{fft}\, x, y, \tau \rightarrow k\chi, k\psi, w \end{aligned} \tag{115}$$

Yielding:

$$u(\chi, \psi, \tau, \varsigma') = Z e^{\hat{B}\Delta\varsigma}\, Z u(\chi, \psi, \tau, \varsigma' - \Delta\varsigma) \tag{116}$$

Eq.(115) and (116) are iteratively implemented over all steps in ς.

Table 2 gives an additional physical interpretation of each operator.

A	B	C
Spatio-Temporal focusing, dispersion, diffraction	SPM, Kerr Lensing, plasma effects on refractive index, plasma scattering, plasma absorption, intensity envelope and plasma envelope contribution to self-steepening	Remaining Self-steepening contributions: Derivative of amplitude electric field

Table 2: Physical interpretation of each operator used in the specific WLG bulk problem.

4.5 Nyquist Criterion and Pseudo-Spectral Criterion for Spatial Grid Sizes

In this section grid size considerations will be considered in order to reduce global step-size error. Provided that the Nyquist criterion for the sampling intervals is satisfied for the original input pulse, the error originates from: Under-sampling the instantaneous phase variation contributions from the exponential operators, the exponential error due to decaying exponential terms in the operator, commutation error between operators, and error due to the mean-value approximation used. The appropriate Nyquist criterion when applied to the phase terms is sufficient to subdue the phase error [43] making this method, through its pseudo-spectral nature extremely precise. The real exponential error can be reduced in a similar way: By considering characteristic lengths of these exponential decaying terms. **This is rigorously derived in appendix C2.**

For the real exponential error, the exponential operator method scales with exponential error relative to the step size in the longitudinal coordinate. The exponential argument is the absolute value of the difference of the magnitude of the mean field and the actual field used in the functional terms of the real exponential argument. Therefore, at coarse step sizes there is the potential that this method starts to diverge and violate energy conservation while other methods do not. However, this acts as a natural step size filter since while other methods are more stable at coarser steps, the error increases. Thus, if accuracy is the prime metric, this method always converges to a low error solution when refining the propagation step size. As well, due to an additional error reduction property that can be applied and is not present in other methods, the Nyquist criterion, the error in other coordinates is greatly reduced to only the presence of numerical floating point error.

One can also use the Euler type or Runge-Kutta type form shown in Eq.(103). This may allow for low accuracy but course resolution simulations. The operator method is easily convertible into any one of these other numerical schemes. And ignoring steps 1 to 7 and just applying an overall Runge-Kutta method, the operator form reduces nicely to the traditional implicit Runge-Kutta method acting on discretized spatial coordinates. However, this system bares lots of instabilities through convolution operators acting on convolution operators introduced by these types of stiff nonlinear equations that arise in the spatial and temporal discretization and mean value approximation. If these discretisations are omitted the implicit Runge-Kutta methods becomes less accurate and stable unless it becomes more complex to account for the numerical difference operators.

In general, acquiring a proper upper bound calculation for the longitudinal step size is rather difficult: Unless, the mean field "slow-varying" approximation can quantitatively be defined. This would involve a numerical recursion scheme. Physical properties of the system being studied [45] can help. For example, [46] derives longitudinal step size conditions based on commutation relations and uncertainty relations between operators. As well, adaptive propagation step-size algorithms, for example, outlined in appendix C2 can reduce error.

There are two main topics to consider when defining the step size:

1) The step size should be appropriate such that the exponent terms do not vary faster than the Nyquist criterion defined for the system (otherwise there could be under-sampling errors that iteratively grow) producing aliasing effects and low sampling resolution effects.

2) Under most cases a good first estimate of propagation step size corresponds to the inverse of the highest ratio of coefficients in (104) (i.e., $\max(\frac{1}{\omega\tau_p}, \frac{L_{df}}{L_{ds}}, \frac{L_{df}}{L_{nl}}$, etc)).

At the start of the simulation sampling is at or below the Nyquist criterion for the input pulse. The propagation step size is calculated from point 2). If however, the step sizes need to be varied, the simulation parameters are updated accordingly. Specific discussion and definition of the Nyquist criteria, how sampling intervals are updated, why they need to be varied are in appendix C2**.**

4.6 Numerical Results from the WLG Simulation

The overall goal of this section is to show that the above derived numerical method can accurately simulate the WLG equation introduced in section 4.3. Self-Steepening and the 3-D spatial nature of Eq.(104) are the main terms that require the elaborate numerical scheme derived above. A numerical study of all temporal effects will be explored in this section. Published experimental results from [49] will be compared to the simulation outcome for that system. The spatial profiles of spectral components and the overall beam fluence will be presented to explore the spatial nature of the method.

In order to set up an accurate simulation of the WLG, material values for YAG were used and listed in appendix C1. As well, input parameters for the pump pulse and simulation sampling intervals are listed in appendix C1.

4.6.1 Pertinent Simulation Results on/ and Verification of Physical Effects in the Temporal Domain

Next, to illustrate the effects of dispersion in anomalous dispersion materials such as YAG, the GVD is made higher than the actual value for YAG (80 times higher in fig. 4, 5) and the pulse intensity is reduced to minimize the non-linear effects (to10^{15} $\frac{\mathrm{W}}{\mathrm{m}^2}$). The non-linear effects were not turned off but minimized through lowering the pulse intensity, because the goal is to show that the system approaches the case where only dispersion acts on the optical profile when the non-linear effects are reduced and the dispersive term is raised, which is what is to be expected. Explanations are in the figure captions. Fig. 4 – 7 are all plotted for temporal intensities at the central propagation axis and a Gaussian envelope input pulse of 194 fs RMS in duration and 76 µm RMS in spatial extent. The central wavelength is 3.1 µm.

a)

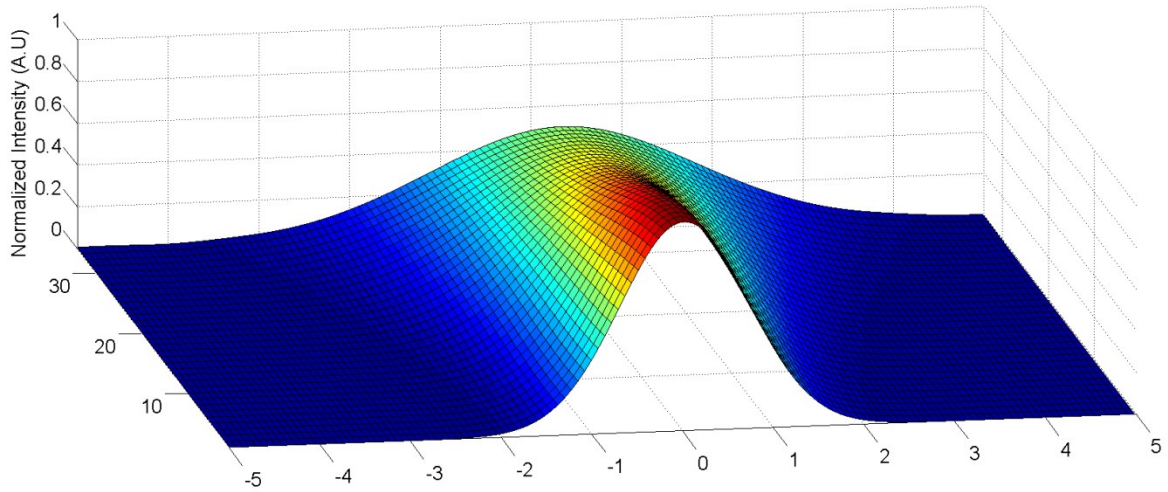

b)

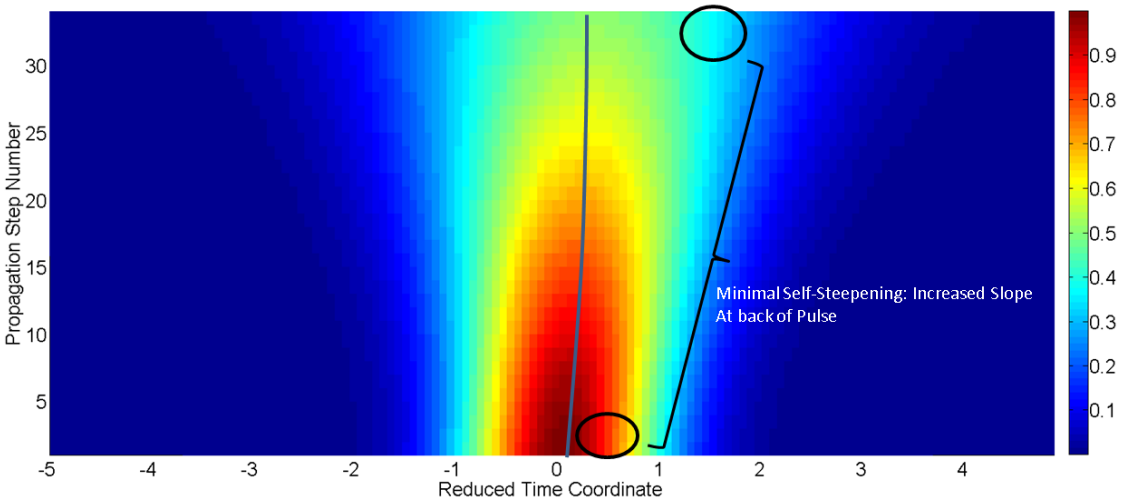

Figure 4: a) Input pulse intensity is lowered and Dispersive term is raised. The pulse broadens in time and its amplitude is reduced as is what is expected in the simple dispersive case. The non-linear shift of the peak intensity due to self-steepening is still present, however, minimized. b) Self-Steepening is still present. $n_2 > 0$ in YAG, and the slope at the back of the pulse is higher (however, negligibly so) and the peak is shifted backward in time. This effect is more pronounced at the beginning due to the higher peak intensity (the pulse has not broadened yet due to dispersion), and less pronounced at the end due to the low peak intensity from dominant dispersive pulse broadening. The peak shift is indicated by the solid blue line in the figure.

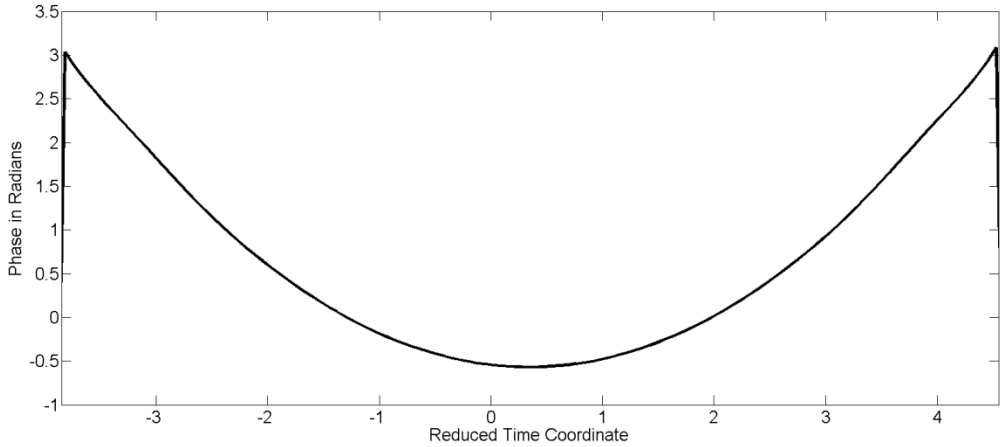

Figure 5: Temporal phase at propagation slice 34. A parabolic phase profile is obtained with a positive derivative slope. This corresponds to the case of anomalous dispersion where a negative linear chirp is introduced in the pulse profile (higher frequencies are at the front of the pulse, i.e., negative times). From the peak shift due to self-steepening, a shift of the parabola minimum is observed. Also, due to self-steepening the right side is slightly compressed. The phase offset is due to the global phase variation with the propagation coordinate (due to the intensity dependent propagation wavenumber) of the pulse envelope.

In the following figures, the dispersion term was kept artificially high (albeit lower than the first case, 20 times the value for YAG) and the pulse intensity was raised (to $5 * 10^{16}\ \frac{W}{m^2}$). The goal is to show the non-linear pulse compression that occurs between the interplay of SPM and dispersion. This effect occurs in anomalous dispersion materials with positive n_2 and in normal dispersion materials with negative n_2. The effect is well known in literature [51, 52] and is the predominant mechanisms for solitons in fiber (see chapter 2.1.2). SPM frequencies are generated in the reverse order as the effect of dispersion on the instantaneous frequencies (see fig. 6 b)). Therefore, at the beginning propagation slices higher frequencies and lower frequencies both go towards the center of the pulse, effectively compressing the pulse. After they reach the center they head away, broadening the pulse again.

In this case self-steepening was turned on. As the blue and the red frequencies head towards each other, due to the additional positive index contribution from self-steepening, the bluer frequencies compress relative to each other and the redder frequencies expand relative to each other. This causes local intensity features that can break the pulse (optical wave-breaking [34]). As well, the self-steepening enhances temporal gradients that cause more SPM. The SPM is thus, even more unbalanced with dispersion and the higher frequency differences drive these parts of the pulse away from the main pulse through the higher dispersion. If the characteristic length for this effect lies before the overall pulse compression, the optical wave can still be compressed, if it is after, wave-breaking will occur after pulse compression. Simulations using this novel technique can give information about crystal lengths for non-linear compression factoring in all of the pertinent effects such as self-steepening, which as mentioned above plays a role in the compression.

a)

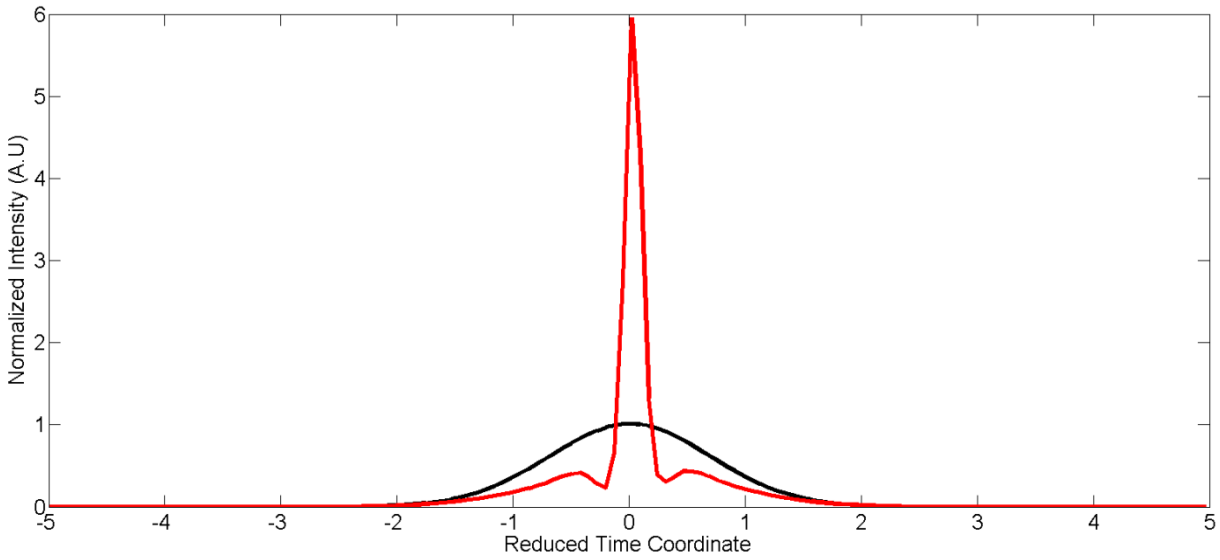

b)

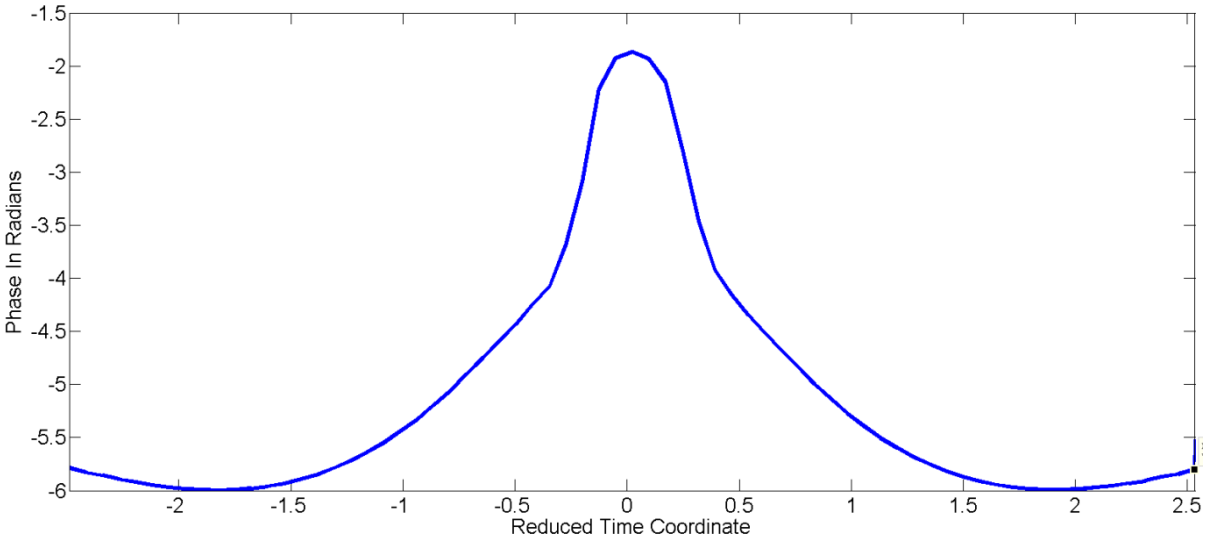

c)

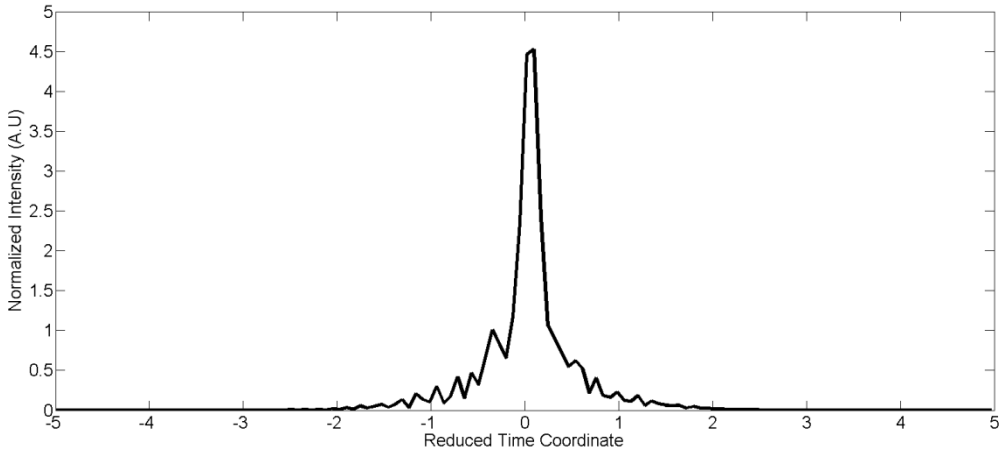

Figure 6: a) Pulse compression occurs near propagation step 15 (red curve), roughly at 6 μm in this artificial dispersive system. Initial optical intensity is shown as the black curve. To illustrate the effect, the dispersion parameter is higher than material value for YAG. Bandwidth increases through SPM and temporal compression occurs with the anomalous dispersion. Due to the increased bandwidth ultrashort pulses are obtained. SPM is in a positive feedback loop due to the higher intensity gradients that are generated as the pulse compresses, enhancing the generation of the ultrashort pulse. b) Phase demonstrates a still existing linear chirp in the opposite direction of fig. 5 around the peak. This is due to the instantaneous phase contribution of SPM chirping the pulse in the opposite manner of dispersion in this case (anomalous dispersion, $n_2 > 0$). Therefore, transform limited pulse compression occurs slightly before this step. In the wings of the pulse, the intensity gradient is reduced. SPM generation is reduced. There the chirp is in accordance to anomalous dispersion seen in fig. 5. The constant phase offset of -1.87 radians is due to the constant phase variation of the pulse amplitude with the propagation coordinate (due to the overall propagation wavenumber). c) Example of wave-breaking after pulse compression. On the blue side (in this case left side due to the slice being after pulse compression), wave-breaking is more pronounced due to compression. On the right side wave-

breaking is present due to interference modulation of the various pulses centered at different red frequencies during the expansion when they traversed to the right side of the pulse. The slope on the right side is higher due to self-steepening for$n_2 > 0$.

As can be seen, in the anomalous dispersion dominated case with $n_2 > 0$, self-steepening is reduced. Also, self-steepening happens on the red side of the pulse because it happens on the trailing edge of the pulse. If SPM dominates over dispersion, than bluer frequencies would be found on the right side of the pulse for $n_2 > 0$, due to the high modulation induced by the self-steepened intensity gradient.

As described in [34] wave-breaking caused by self-steepening is reduced by plasma effects. This is because as discussed in section 4.3.2, plasma reduces peak intensity regions while maintaining lower intensity regions.

Using the material value of dispersion for YAG, yields fig. 7. Here the intensity is kept at 5*10^16 $\frac{W}{m^2}$. The figure shows that plasma counters wave-breaking and the high peak intensity due to self-steepening. Self-steepening occurs on the red side of the pulse, due to the signs of n_2 and GVD. The wave-breaking characteristic length is increased and the pulse can remain in the crystal for longer propagation lengths.

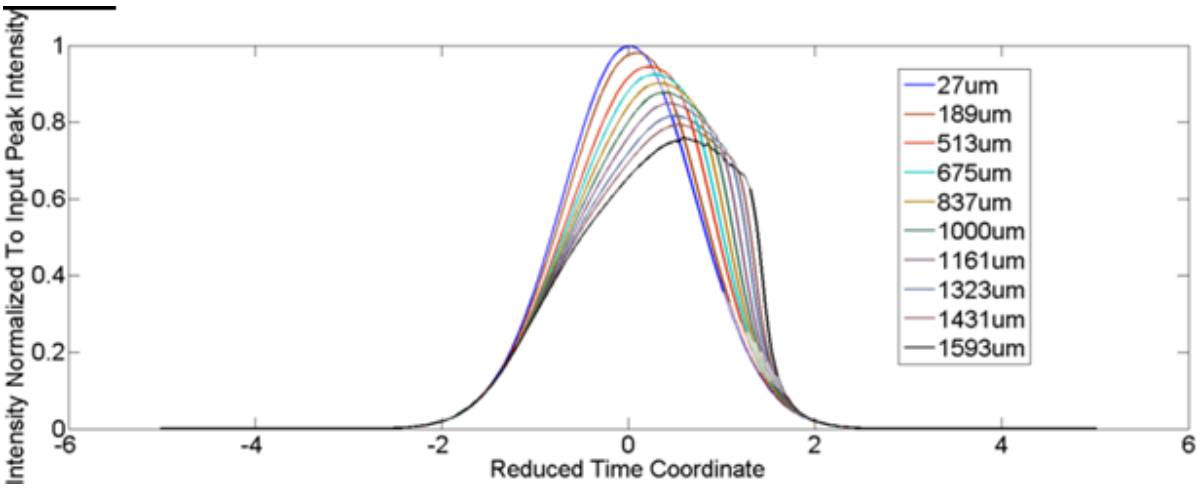

Figure 7: Pronounced self-steepening of the optical pulse propagating through the crystal. The temporal intensity profile of the spatial center of the pulse is plotted for various propagation distances in the crystal. The intensity is normalized to the peak pulse intensity of the input: 5*10^16 $\frac{W}{m^2}$. The intensity profile corresponds well with [34] and supports the findings in that paper.

4.6.2 White-Light Generation: Simulation Spectrum compared to Experiment

The white-light spectrum of the system will now be evaluated and compared to experimental data in literature. [49] has experimentally found the spatially integrated spectral density of WLG in a 2mm YAG crystal with an input temporal and spatial Gaussian centered at 3.1 μm, spatial $1/e^2$ value of 50 μm, temporal power FWHM of 85fs and input peak power of 76MW. The comparison between this simulation technique, the experimental data and their simulation is shown below. The range of the simulation was set at a wavelength above 1700nm, due to the zero dispersion point in YAG. The GVD was assumed to be unchanging through the spectral window, which is a source of error. Other sources of error include the fixed absorption order and all that is discussed in appendix C3. The bandwidth range exceeds the slow varying approximation used in the derivation of the white-light equation shown in this chapter. The ideal radially symmetric Gaussian input that was assumed in the experiment may not have been the case. Material values were taken directly from [49] without change.

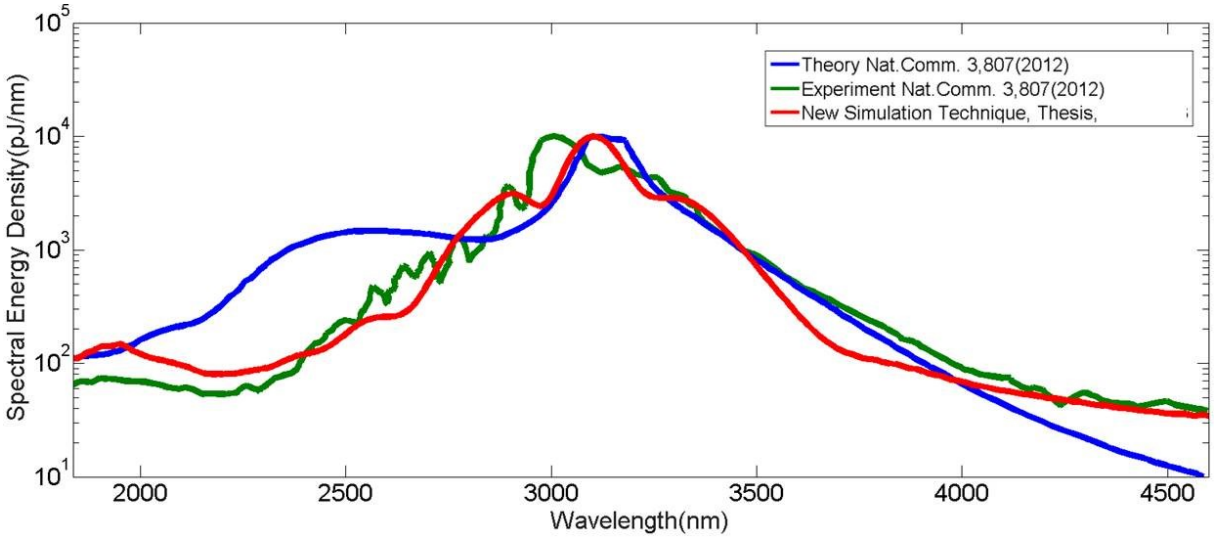

Figure 8: Comparison of experimental data from [49] and the simulation (shown in red). Simulation fit is in excellent agreement to the experimental data (within less than a factor of 3 everywhere). The theory fit in [49] diverges considerably on the blue side of the spectrum. Data from [49] was collected using the grab it! App and was collected by A. Choudhuri. The same input spatial and temporal distribution was used as in section 4.6.1.

4.6.3 Spatial Effects

In this section spatial information will be explored to demonstrate the 3+1D information that can be obtained from this simulation and a discussion of what can be done with this information will be presented.

4.6.3.1 Frequency Spatial Modes

The spatial configuration of the various frequency components is useful for many downstream applications. For example, knowing the spatial profile of a given frequency range in the white-light generation can yield all information necessary to spatially shape the mode after the crystal to spatial distributions ideal for in-coupling into fiber systems or OPA stages. As well, the inherent nature of how WLG happens can be explored and systems can be designed that maximize the generation of frequencies from manipulating various spatial effects. An example of the latter will now be shown in this section. Taking the system modelled in section 4.6.2 as the reference, spatial-frequency modes at the crystal are shown in fig. 9. Fig. 9 corresponds to the end propagation slice and it can be seen that the spatial distribution of a frequency component can focus differently in the crystal than another. This is due to different spatial distributions from the WLG interacting with the lens caused by the spatially varying refractive index. In the figures below, pump corresponds to the central wavelength of the input signal.

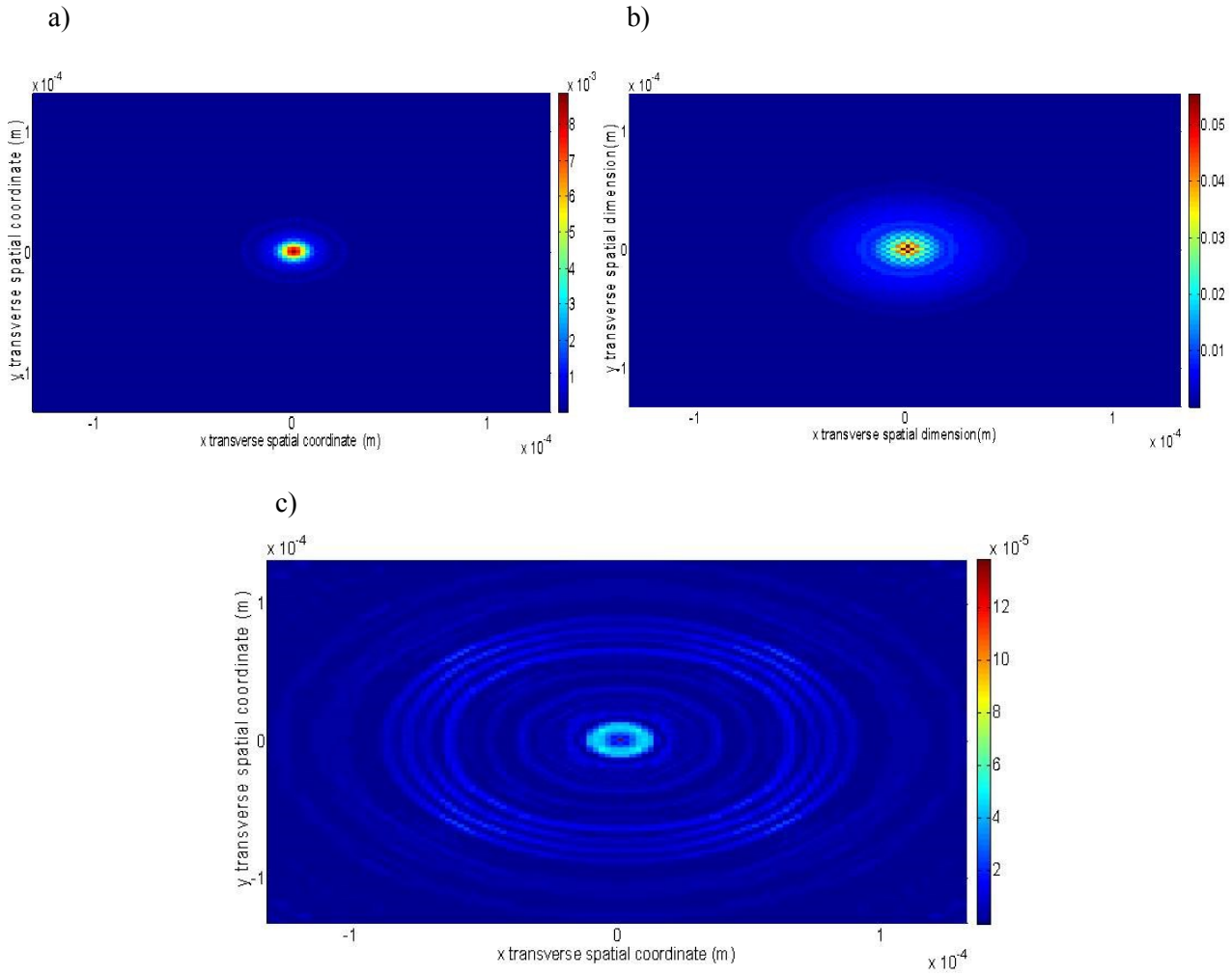

Figure 9: fluence(J/m^2) at end of crystal, spatial distributions. a) The spectral fluence spatial mode corresponding to a small range of frequencies about 3.5 µm. b) The spectral fluence spatial mode corresponding to a small range of frequencies about 3.1 µm (pump frequency). c) The spectral fluence spatial mode corresponding to a small range of frequencies about 2 µm. Aliasing effects are present due to the inadequate sampling intervals in momentum space. Low resolution effects are present due to the inadequate spatial sampling interval. This can be reduced if window sizes are made bigger, i.e.,

through the adaptive algorithm outlined in appendix C2.2, however simulations were done on a desktop computer with limited resources.

As explained in the image captions, due to simulations being run on a desktop machine, errors above include slight under-sampling error (for example, low resolution error leading to the pixelated spatial profiles). Momentum under-sampling (or spatial window extent being too small) generates the slight aliasing in Fig. 9, for example. u is undergoing aliasing, therefore it fills more of the spatial window up to atleast a boundary of the window. Thus, this yields convolution effects with the rectangular window (rectangular sinc function convolved with u in momentum space) which also has the effect of increasing the aliasing. However, these errors do not take away much from the accuracy of the simulation as shown by the experimental comparison and will be fixed by simulating the data on a more powerful machine. Appendix C2.2 presents an adaptive step-size algorithm that fixes under-sampling errors.

The conclusion of the above figures is the following: the pump central frequency becomes defocused into a Bessel-like function as it progresses through the crystal, while the other frequency components become more focused. The other frequency components exhibit the same ring like effect. The pump wavelength fluence density is the highest (refer to fig. 9) at all times in the crystal. Therefore, in regions of the optical waveform where the pump is present, due to the higher fluence, it will generate more plasma; the plasma will defocus the optical signal more in those regions.

Intensity regions in the spatial profile of the optical waveform that have lower intensity see less of the plasma absorption and scattering effects. Therefore, the peak gradients can become more pronounced before plasma absorption/scattering reduces the peak intensity increase (and thus, reduces the gradients). Since SPM generates instantaneous frequencies in proportion to intensity gradients, more frequency components can be generated at the wings of the spatial distribution. This is one of the contributing reasons for why these ring patterns appear. For example, see Fig. 9a). The other contributing factor is that instantaneous momenta added from the spatially varying refractive index can increase nearer to the wings of the spatial optical waveform, due to the intensity gradients that can accumulate before peak intensities reach plasma absorption or scattering-defocusing thresholds. Thus, these momenta cause areas in the spatial distribution to focus differently, creating rings. The final contributing effect and perhaps the most pertinent is due to the modulation of the distribution that arises in momentum space due to self-focusing. Self-focusing and SPM are analogous effects as described above. In SPM case, modulation in the frequency spectrum is seen due to interference effects of regions in the waveform that generate the same frequency but at different times. The self-focusing analogue would be that there is modulation in momentum space due to the same momenta being generated at two different spatial points. These modulations are radially symmetric in this case due to the radial symmetry of the equation given a radially symmetric input. The modulations in momentum space translate to modulations in real space due to the propagation property that in the far field, the momentum space is mirrored in real space[53]. Thus, the modulations in momenta space from the self-focusing effect manifest in this ring type pattern for a given frequency. These are the three major contributors to the ring effects seen in the frequency generation and in the pump.

4.6.3.2 Spatial Fluence Profile of the WL Pulse

a)

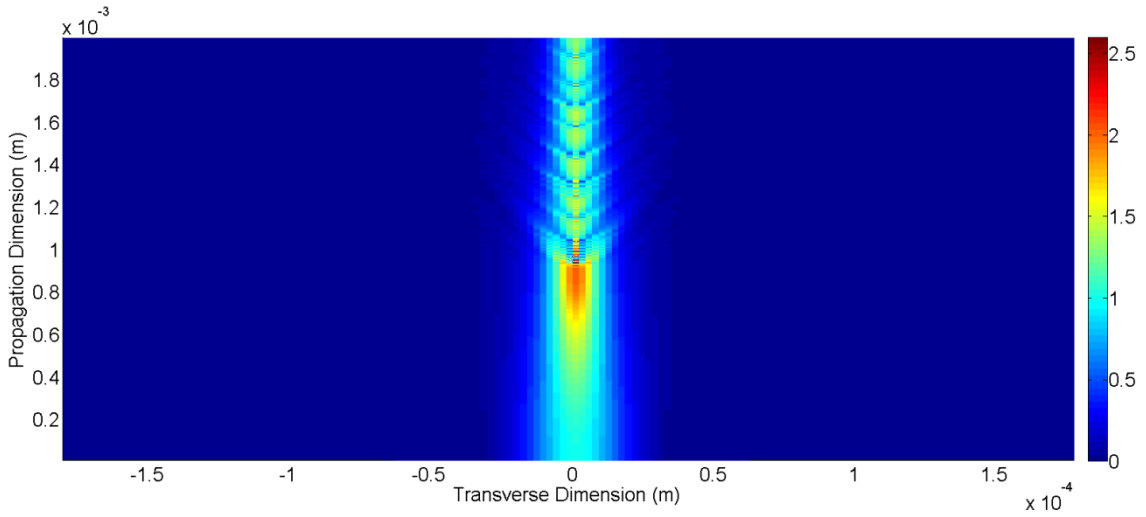

b)

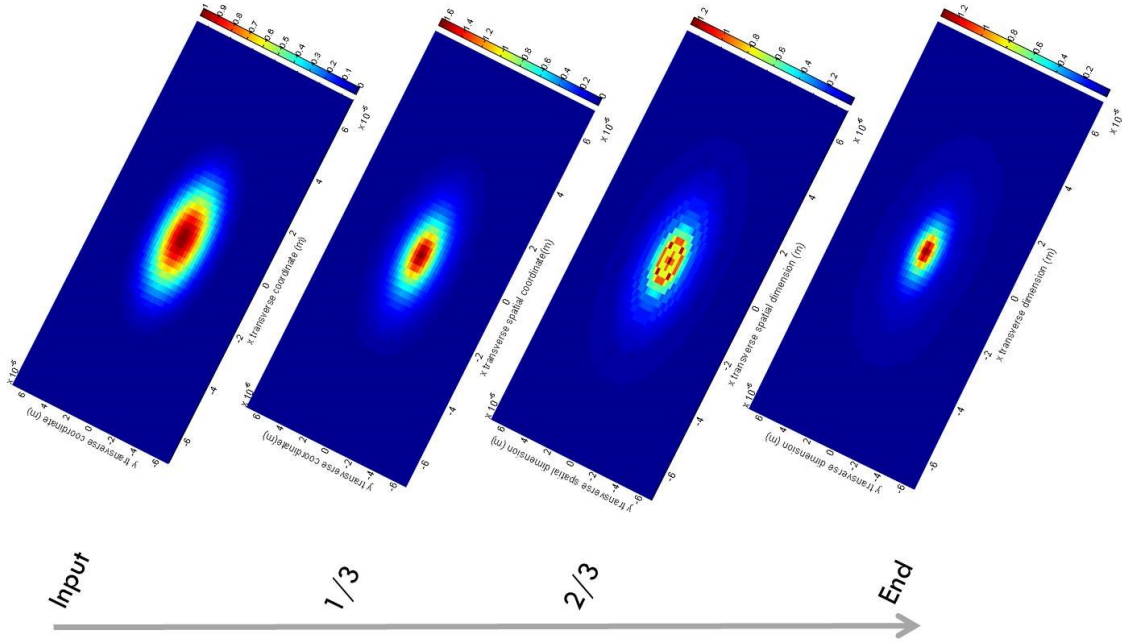

Figure 10: a)Spatial Fluence normalized to input peak fluence, fluence along a transverse dimension is plotted against propagation distance in the crystal (input of 4.6.2 is radially symmetric). b) Different view of a): at certain propagation distances the fluence is plotted against the two transverse coordinates to highlight the ring formation.

Due to plasma absorption and scattering effects, a donut mode is observed to form that then focuses due to the spatially varying intensity dependent refractive index. The maximum fluence decreases due to absorptive losses until the focusing effect at the end dominates and it increases again. In intermediate propagation steps, the center of the beam focuses and then defocuses due to plasma scattering, creating rings due to the intensity dependent focusing conditions within the fluence. This generates cycles in the plasma filament.

4.7 Conclusions and Extensions

A novel and fast 3+1D simulation technique based on the symmetric split-step Fourier method has been developed in this chapter. The novel numerical technique can solve generalized NLSE type equations not accessible with traditional split-step approaches and does not intrinsically have the same numerical errors that are present in Runge-Kutta type methods for partial differential equations. These generalized NLSE equations are important in optics, notably white-light generation in bulk material. This novel numerical technique was implemented to create a simulation of WLG in bulk. Results are compared to published experimental data and a good match between the simulation and the experiment is shown, even with spatial under-sampling errors. A top-down view of every aspect of WLG can be achieved with this simulation as was shown in extensively in section 4.6. Also, an adaptive algorithm to avoid under-sampling is shown in appendix C2.

Extensions include to implement Raman terms in the simulation and to adjust the equation of [34] to generalize it for a broader frequency range (see appendix C3 and C4). The only limitation is the derived equations that the numerical technique is used to implement. This novel numerical technique does not add any constraints or numerical approximations above the Nyquist criterion for Fourier based methods. Also another extension would be to adjust the scalar equation to account for polarization. This is easily accomplished, as described in appendix C3. The method can be applied to each of the two coupled scalar equations that arise (see Eq. (31) and (32) in chapter 2, for an example).

A transmission phase mask simulation has been developed but not shown in this chapter to take obtained spatial frequency modes from the WLG simulations and to shape them to desired inputs for downstream optics.

Results were shown with an input Gaussian beam (radially symmetric). This was only to match the experimental beam profile used in [49]. However, this new numerical technique can model any arbitrary input signal.

As a final remark, all simulation results were done on a desktop computer and each simulation run took no longer than 5 hours to complete.

Chapter 4 Bibliography

1. Hasegawa, Akira, and Yūji Kodama. *Solitons in optical communications*. No. 7. Oxford University Press, USA, 1995.

2. Anderson, Dan, and Mietek Lisak. "Nonlinear asymmetric self-phase modulation and self-steepening of pulses in long optical waveguides." *Physical Review A* 27.3 (1983): 1393.

3. Nakatsuka, Hiroki, D. Grischkowsky, and A. C. Balant. "Nonlinear picosecond-pulse propagation through optical fibers with positive group velocity dispersion." *Physical Review Letters* 47.13 (1981): 910.

4. Taniuti, T., and H. Washimi. "Self-trapping and instability of hydromagnetic waves along the magnetic field in a cold plasma." *Physical Review Letters* 21.4 (1968): 209.

5. Ruderman, M. S. "Propagation of solitons of the derivative nonlinear Schrödinger equation in a plasma with fluctuating density." *Physics of Plasmas (1994-present)* 9.7 (2002): 2940-2945.

6. Peregrine, D. H. "Water waves, nonlinear Schrödinger equations and their solutions." *The Journal of the Australian Mathematical Society. Series B. Applied Mathematics* 25.01 (1983): 16-43.

7. Dysthe, Kristian B. "Note on a modification to the nonlinear Schrodinger equation for application to deep water waves." *Proceedings of the Royal Society of London. A. Mathematical and Physical Sciences* 369.1736 (1979): 105-114.

8. Sato, Mikio. "Soliton Equations as Dynamical Systems on a Infinite Dimensional Grassmann Manifolds (Random Systems and Dynamical Systems)." (1981).

9. Temam, Roger. *Infinite dimensonal dynamical systems in mechanics and physics*. Vol. 68. Springer Science & Business Media, 1997.

10. Agrawal, Govind P. *Nonlinear fiber optics*. Academic press, 2007.

11. Taha, Thiab R., and Mark I. Ablowitz. "Analytical and numerical aspects of certain nonlinear evolution equations. II. Numerical, nonlinear Schrödinger equation." *Journal of Computational Physics* 55.2 (1984): 203-230.

12. Besse, Christophe, Brigitte Bidégaray, and Stéphane Descombes. "Order estimates in time of splitting methods for the nonlinear Schrödinger equation." *SIAM Journal on Numerical Analysis* 40.1 (2002): 26-40.

13. Balac, Stéphane, and Fabrice Mahé. "An Embedded Split-Step method for solving the nonlinear Schrödinger equation in optics." *Journal of Computational Physics* 280 (2015): 295-305.

14. Sinkin, Oleg V., et al. "Optimization of the split-step Fourier method in modeling optical-fiber communications systems." *Journal of lightwave technology* 21.1 (2003): 61.

15. Heidt, Alexander M. "Efficient adaptive step size method for the simulation of supercontinuum generation in optical fibers." *Lightwave Technology, Journal of* 27.18 (2009): 3984-3991.

16. Dehghan, Mehdi, and Ameneh Taleei. "A compact split-step finite difference method for solving the nonlinear Schrödinger equations with constant and variable coefficients." *Computer Physics Communications* 181.1 (2010): 43-51.

17. Liu, X., L. J. Qian, and F. W. Wise. "Generation of optical spatiotemporal solitons." *Physical review letters* 82.23 (1999): 4631.

18. Nehmetallah, G., and P. P. Banerjee. "An adaptive spherical Fourier Bessel split-step method for tracking optical bullets." *Optics & Photonics 2005*. International Society for Optics and Photonics, 2005.

19. Ascher, Uri M., Steven J. Ruuth, and Raymond J. Spiteri. "Implicit-explicit Runge-Kutta methods for time-dependent partial differential equations." *Applied Numerical Mathematics* 25.2 (1997): 151-167.

20. Mastorakis, Nikos E. "An Extended Crank-Nicholson Method and its Applications in the Solution of Partial Differential Equations: 1-D and 3-D Conduction Equations." *WSEAS Transactions on Mathematics* 6.1 (2007): 215.

21. Fuchssteiner, Benno, and Athanassios S. Fokas. "Symplectic structures, their Bäcklund transformations and hereditary symmetries." *Physica D: Nonlinear Phenomena* 4.1 (1981): 47-66.

22. Besse, Christophe. "A relaxation scheme for the nonlinear Schrödinger equation." *SIAM Journal on Numerical Analysis* 42.3 (2004): 934-952.

23. Bellini, Marco, and Theodor W. Hänsch. "Phase-locked white-light continuum pulses: toward a universal optical frequency-comb synthesizer." *Optics letters* 25.14 (2000): 1049-1051.

24. Alfano, Robert R. "The supercontinuum laser source." (1989): 458.

25. Serebryannikov, E. E., Eleftherios Goulielmakis, and A. M. Zheltikov. "Generation of supercontinuum compressible to single-cycle pulse widths in an ionizing gas." *New Journal of Physics* 10.9 (2008): 093001.

26. Zhang, Xiaomin, et al. "Acquiring 1053 nm femtosecond laser emission by optical parametric amplification based on supercontinuum white-light injection." *Optics letters* 31.5 (2006): 646-648.
27. Manzoni, Cristian, et al. "Coherent synthesis of ultra-broadband optical parametric amplifiers." *Optics letters* 37.11 (2012): 1880-1882.

28. Johnson, Philip JM, Valentyn I. Prokhorenko, and R. J. Miller. "Enhanced bandwidth noncollinear optical parametric amplification with a narrowband anamorphic pump." *Optics letters* 36.11 (2011): 2170-2172.

29. Johnson, Philip J., Valentyn I. Prokhorenko, and R. J. Miller. "Bandwidth-Enhanced Noncollinear Optical Parametric Amplification via Anamorphic Pumping." *International Conference on Ultrafast Phenomena*. Optical Society of America, 2010.

30. Krebs, N., et al. "Two-dimensional Fourier transform spectroscopy in the ultraviolet with sub-20 fs pump pulses and 250–720 nm supercontinuum probe." *New Journal of Physics* 15.8 (2013): 085016.

31. Couairon, Arnaud, and André Mysyrowicz. "Femtosecond filamentation in transparent media." *Physics reports* 441.2 (2007): 47-189.

32. J. E. Rothenberg, Opt. Lett. **17**, 1340 (1992).

33. G. Yang and Y. R. Shen, Opt. Lett. **9**, 510 (1984).

34. Gaeta, Alexander L. "Catastrophic collapse of ultrashort pulses." *Physical Review Letters* 84.16 (2000): 3582.

35. Shankar, Ramamurti, Ravi Shankar, and Ramamurti Shankar. *Principles of quantum mechanics*. Vol. 233. New York: Plenum Press, 1994. (Chapter 1).

36. Stein, Elias M., and Guido L. Weiss. *Introduction to Fourier analysis on Euclidean spaces*. Vol. 1. Princeton university press, 1971.

37. Titchmarsh, Edward Charles. *Introduction to the theory of Fourier integrals*. Vol. 498. Oxford: Clarendon Press, 1948.

38. Guandalini, A., et al. "Spatio-temporal characterization of few-cycle pulses obtained by filamentation." *Optics express* 15.9 (2007): 5394-5404.

39. A. Couairon, J. Biegert, C. P. Hauri, W. Kornelis, F. W. Helbing, U. Keller, and A. Mysyrowicz, "Self-compression of ultrashort laser pulses down to one optical cycle by filamentation," J. Mod. Opt. 53, 87-96 (2006).

40. Q. Feng *et al.,* IEEE J. Quantum Electron. **QE-33**, 127 (1997).

41. M. Mlejnek *et al.,* Opt. Lett. **23**, 382 (1998).

42. J. R. de Oliveira, M. A. de Moura, J. M. Hickmann, and A. S. L. Gomes, "Self-steepening of optical pulses in dispersive media,"J. Opt. Soc. Am. B9,2025–2027 (1992).

43. Oppenheim, Alan V., Ronald W. Schafer, and John R. Buck. *Discrete-time signal processing*. Vol. 2. Englewood Cliffs: Prentice-hall, 1989.

44. Verwer, J. G., W. H. Hundsdorfer, and B. P. Sommeijer. "Convergence properties of the Runge-Kutta-Chebyshev method." *Numerische Mathematik* 57.1 (1990): 157-178.

45. Heidt, Alexander M. "Efficient adaptive step size method for the simulation of supercontinuum generation in optical fibers." *Lightwave Technology, Journal of* 27.18 (2009): 3984-3991.

46. Rieznik, A., et al. "Uncertainty relation for the optimization of optical-fiber transmission systems simulations." *Optics express* 13.10 (2005): 3822-3834.

47. Iizuka, Keigo. *Elements of Photonics, In Free Space and Special Media*. Vol. 1. John Wiley & Sons, 2002. (Appendix A).

48. Pedrotti, Frank L., and Leno S. Pedrotti. "Introduction to Optics 2nd Edition." *Introduction to Optics 2nd Edition by Frank L. Pedrotti, SJ, Leno S. Pedrotti New Jersey: Prentice Hall, 1993* 1 (1993).

49. Silva, F., et al. "Multi-octave supercontinuum generation from mid-infrared filamentation in a bulk crystal." *Nature communications* 3 (2012): 807.

50. Strichartz, Robert S. *A guide to distribution theory and Fourier transforms*. Singapore: World Scientific, 2003.

51. Alfano, Robert R. "The supercontinuum laser source." (1989): 458.

52. Liu, Jiansheng, Ruxin Li, and Zhizhan Xu. "Few-cycle spatiotemporal soliton wave excited by filamentation of a femtosecond laser pulse in materials with anomalous dispersion." *Physical Review A* 74.4 (2006): 043801.

53. Goodman, Joseph W. *Introduction to Fourier optics*. Roberts and Company Publishers, 2005.

Appendix A1: Materials List

1. Yb-fiber Oscillator		
Item	**Part #**	**Vendor**
Yb164, gain fiber	YB 501-PM	CorActive
Hi 1060, single mode bar fiber	HI 1060	Corning
Hi 1060 PM		Corning
WDM 980/1030nm	WDM6-12-P-1-L-0	Lightel
1030nm Wideband Polarization Insensitive Optical Isolator	IS-1030-P-2-3-3-0	AC photonics
980nm Wideband Polarization Insensitive Optical Isolator	IS-98-P-2-3-3-0	AC photonics
Fiber pigtailed collimator	CFS8-1030-FC	Thorlabs
Kinematic Optic Mount	KM100T	Thorlabs
Adapter for 8mm -> SM1 thread	AD8F	Thorlabs
BreadBoard 18x24"	MB1824	Thorlabs
Kinematic Mirror Mount (Compact)	KMS	Thorlabs
Continuous rotation Mount	RSP05	Thorlabs
Half-waveplate 1030nm	WPF1212-L/2-130	Photop
Quarter waveplate 1030nm	WPF1212-L/4-130	Photop
Polarization Beam-splitter cube	PBS-1030-50	CVI
976nm Laser Diode	S30-7602-720	JDSU
4-Channel laser diode controller	LDC-3900	ILX lightwave
Combination module (2A current source, 8W TEC)	LCM-39440	ILX lightwave
14-pin butterfly laser diode mount	LDM-4984	ILX lightwave
Current source/Laser diode mount cable	CC-305S	ILX lightwave
TE controller/Laser diode mount interconnect cable (6ft.)	CC-505S	ILX lightwave

2. Stretcher & Amplifier Stage		
Item	**Part #**	**Vendor**
Yb doped, single mode, single clad	PM-YSF-HI	Nufern
PM WDM 980/1030nm	WDM-PM-9830-L-7-0-1W	AFW
Fiber AOM/driver	PM fibre-Q, polarization maintaining 1030nm Fibre-coupled Acousto-Optic Modulator (and driver)	Gooch&Housego
1030nm Circulator	PMOC31030P21111-100nm	compoTron GmBH
Fiber Stretcher	Custom	OFS
Faraday Mirror	FFDM-2246-122101	Haphit
Fiber Pigtailed Isolator	FPIS-1053-FH1P10-320-N (1053nm High power PM isolator for pulse power)	Haphit
Panda PM fiber	PM980	Corning

Appendix B1: Results of Updated Franz-Nodvik Algorithm for Crystal Pumping

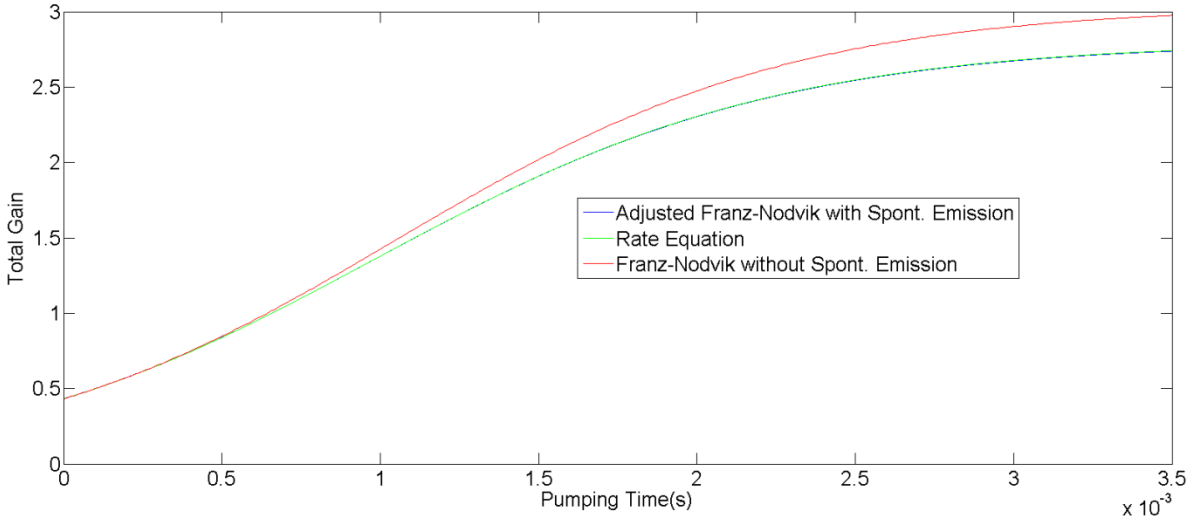

Figure 19: Simulations done on a Ho:YLF system. For a 1 cm 1% doped crystal ($7.6 * 10^3 \frac{\mathrm{w}}{\mathrm{cm}^2}$ pump intensity). Exact fit between the adjusted Franz-Nodvik algorithm factoring in spontaneous emission time and the rate equation is obtained. Without adjusting the Franz-Nodvik algorithm with spontaneous emission (red curve) total gain deviates towards the higher values.

Appendix B2: Materials list

The materials list is given in table 5.

Part List	Company	Notes
Yb:KYW	Eksma	Ng aligned, 2.5mm, 2% doped
Flat Dichroic Mirror	Altechna	99% Reflection At 1.3um
Flat Out-coupler	Eksma	1.5(0.5)% transmission at 1.03um
Mirror	Altechna	1000mm radius curvature
Mirror	Altechna	229mm radius curvature
Mirror	Altechna	229mm radius curvature
PBS	Optosigma	High Damage Threshold
Pockel Cell	Doehrer	RTP double cell
Electronic Switching	Birdmann	<9ns rise time
QWP	Thorlabs	
Custom Design Pump Lens	DPM Photonics	
Pump Diode	LIMO	Wavelength stabilised 976nm
Custom Made Crystal Mount		

Table 5: Materials list. All Mounts were ordered from Thorlabs.

Appendix C0: Essential Proofs of Section 4.2

C0.0 Fourier convention used

The Fourier convention used is:

$$F(w) = \int_{-\infty}^{\infty} f(t) e^{iwt} dt$$

$$f(t) = \frac{1}{2\pi} \int_{-\infty}^{\infty} F(w) e^{-iwt} dw$$

Where w represents angular frequency and t represents the time domain. The coefficient $\frac{1}{2\pi}$ is omitted in equations and derivations (for clarity) but assumed in this chapter. The convention to represent this integral in quick form is:

$$f(t) = f_w\big(F(w)\big)|_t$$

C0.1 Proof that any series expansion of derivative operators multiplied into u is equal to the inverse Fourier transform of substituting the derivatives with the representation of the derivatives in Fourier space into the series expansion and multiplying into the representation of u in the Fourier space.

In this section the following result will be proved:

If

$$Q = \sum_{n=0}^{\infty} \sum_{j=0}^{\infty} c_n \nabla^n c_j \frac{\partial^j}{\partial \tau^j}$$

Than

$$Qu = f_{k_x, k_y} \left(f_w \left(\left[\sum_{n=0}^{\infty} \sum_{j=0}^{\infty} c_n \left((-ik_x)^n + (-ik_y)^n \right) c_j (-iw)^j \right] \bar{\bar{u}}(w, k_x, k_y) |_\tau \right) |_{x,\, y}$$

If the operator can be represented in the form:

$$Q = \sum_{n=0}^{\infty} \sum_{j=0}^{\infty} c_n \nabla^n c_j \frac{\partial^j}{\partial \tau^j} \tag{117}$$

(c_n , c_j are constants, the del operator acts over x,y spatial coordinates, or normalized spatial coordinates, τ is the time coordinate, or normalized time coordinate) which is true for the $\wp$ operator, than

$$Qu = [\sum_{n=0}^{\infty} c_n \nabla^n \sum_{j=0}^{\infty} c_j \frac{\partial^j}{\partial^j \tau}] u \tag{118}$$

The operators ∇^n , $\frac{\partial^j}{\partial^j \tau}$ commute and the order of how they are applied on u does not matter. This follows for the commutation of partial derivatives over independent variables.

Eq.(118) is Fourier transformed in the w domain. Using the Fourier identity for derivative terms to any order, the following is obtained:

$$Qu = \sum_{n=0}^{\infty} \sum_{j=0}^{\infty} c_n \nabla^n c_j \, [f_w((-iw)^j \, \bar{u}(w,x,y))]|_\tau \tag{119}$$

Since the integral does not act over x,y, ∇^n can be factored out of the integral. The property of summation of integrals was used to place the Fourier integral within the summation.

Now, to evaluate the del operators over x,y the following 2D Fourier integral can be used:

$$Qu = \sum_{n=0}^{\infty} \sum_{j=0}^{\infty} f_{k_x, k_y}(c_n \, ((-ik_x)^n + (-ik_y)^n) c_j \, [f_w((-iw)^j \, \bar{\bar{u}}(w, k_x, k_y))|_\tau)|_{x, y} \tag{120}$$

Where the Fourier identity of the del operator is used. The summation property of integrals was used.

The integrals commute because they are evaluated over independent variables. The ordering of how the integral is evaluated does not matter.

Also, due to the summation property of integrals, the integrals can be factored outside of the summation. This simplifies Eq. (120) to:

$$Qu = f_{k_x, k_y} (f_w(\left[\sum_{n=0}^{\infty} \sum_{j=0}^{\infty} c_n((-ik_x)^n + (-ik_y)^n) \, c_j \, (-iw)^j\right] \bar{\bar{u}}(w, k_x, k_y))|_\tau)|_{x, y} \tag{121}$$

From equality of Eq.(121) and Eq. (118), Eq. (118)is equivalent to the Fourier transform of the series expansion of the Fourier representation of derivative operators multiplied into the Fourier representation of u. Concluding the proof. ■

$\wp$ is of the same form as Q above, and these proofs apply to $\wp$.

C0.2 Corollary: A series expandable function of derivative operators multiplied into u, in the original space, equals to the inverse Fourier transform of the same function where the derivative arguments are replaced by the representation of the derivatives in the Fourier space multiplied by the representation of u in the Fourier space.

The double summation in Eq. (121) mathematically matches the same expansion as Eq. (117) with variable labels replaced. Therefore, the function described is simply the function of the Q operator over derivative arguments replaced by $-\mathrm{iw}^{h}$ for the time derivatives and $-\mathrm{ik_x}^{\mathrm{v}} + -\mathrm{ik_y}^{\mathrm{v}}$ for the spatial del operator, ∇^{v} used in the functional arguments. Therefore,

$$\mathrm{Qu} = f_{\mathrm{k_x,\,k_y}}\left(f_{w}([\mathrm{Q}(-\mathrm{iw}, (-\mathrm{iw})^{h}, (-\mathrm{iw})^{\max}, -\mathrm{ik_x} \pm \mathrm{ik_y}, (-\mathrm{ik_x})^{\mathrm{v}} + (-\mathrm{ik_y})^{\mathrm{v}}, \ldots, (-\mathrm{ik_x})^{\max} + (-\mathrm{ik_y})^{\max})]\bar{\bar{\mathrm{u}}}(\mathrm{w}, \mathrm{k_x}, \mathrm{k_y}))|_{\tau}\right)|_{\mathrm{x,\,y}} \tag{122}$$

An important caveat to the above is that Eq. (122) is true if the series in Eq. (121) converges to a function within the inverse domains. If values in the domain are outside the region of convergence of the series, the full series form of Eq. (121) will have to be employed. For the convergence condition of $\wp$, see discussion in appendix C3.

A note: If the operator is defined as a series over derivatives that does not have a functional representation (i.e., the series does not converge to a function) or if the operator is defined as an infinite series of functions, than the above method derived in section 4.2 is still valid but with a slight difference. The Maclaurin expansion of the exponential operator will be over this series. This means that the full series will be substituted for the variable in the exponential Maclaurin expansion. By the proof in C0.1 and C0.3 (below) the application of the operator to u is equivalent to taking the inverse Fourier transform of the exponential Maclaurin expansion with the Fourier variables substituted in the series multiplied into the Fourier representation of u. While this avoids having to do numerical derivatives, the series terms of the Macluarin expansion will need to be truncated, and the general Maclaurin expansion will need to be truncated, generating numerical error.

C0.3 Proof of the Exponential Fourier Representation of $\wp$

In this section the following result will be proved:

$$\mathrm{e}^{\wp(\tau,\ldots)}\mathrm{u}(\tau, \ldots) = f_{(\mathrm{K}\chi,\,\mathrm{K}\psi,\,\mathrm{w})}\,[\mathrm{e}^{\bar{\bar{\wp}}}\bar{\bar{\mathrm{u}}}]|_{(\chi,\psi,\tau)}$$

Expanding the exponential $\wp$ operator w.r.t to the propagation coordinate in a Maclaurin series yields:

$$e^{\wp} = 1 + \wp + \frac{1}{2!}(\wp)^2 + \frac{1}{3!}(\wp)^3 \ldots \tag{123}$$

The step size is factored into$\wp$, for ease of writing. In the above multiplicative ordering (or additive ordering) does not have to be defined since derivative operators commute like algebraic variables.

From the above, an equivalent application of the exponential operator goes as:

$$e^{\wp(\tau,\ldots)}u(\tau,\ldots) = [1 + \wp + \frac{1}{2!}(\wp)^2 + \frac{1}{3!}(\wp)^3 \ldots]u \tag{124}$$

$\wp$ is equivalent to a global summation of derivative terms with constant coefficients as indicated in Eq. (76).

$(\wp(\tau,\ldots))^n$ in expanded form is equivalent to a summation of products of powers of spatial derivative and temporal derivative terms. Using the Fourier representation of derivative terms and then factorizing, the following can be obtained:

$$(\wp(\tau,\ldots))^n u(\tau,\ldots) = f_{(K\chi,\, K\psi,\, w)}\,[((\bar{\wp}))^n \overline{u}]|_{(\chi,\psi,\tau)} \tag{125}$$

$\bar{\wp}$ is simply the series of $\wp$ substituted with the fourier variable representation of the operators as indicated in C0.1. The expansion and factorization is straight-forward to obtain and is equivalent to the algebraic case of variables (i.e., ordering of operations does not matter) since derivative terms commute like algebraic variables and in the K_χ, K_ψ, w space the variables used represent real numbers (are in fact algebraic variables).

From the identity of Eq. (125) **,** for each term in the RHS of Eq. (124), the following is true ($\overline{\wp}$, $\overline{u}$ denotes the Fourier representation of $\wp$ and u):

$$\text{term}(\wp)u = f_{(K\chi,\, K\psi,\, w)}\,[\text{term}(\bar{\wp})\overline{u}]|_{(\chi,\psi,\tau)}$$

Therefore, Eq. (124) is equivalent to:

$$e^{\wp(\tau,\ldots)}u(\tau,\ldots) = f_{(K\chi\ K\psi\ w)}\,[[1 + \bar{\wp} + \frac{1}{2!}(\bar{\wp})^2 + \frac{1}{3!}(\bar{\wp})^3 \ldots]\overline{u}]|_{(\chi,\psi,\tau)} \tag{126}$$

The summation on the RHS, over algebraic variables, can be represented as (straightforwardly, using the Maclaurin series identity without defining a multiplicative ordering-since all algebraic properties including product commutation hold):

$$e^{\wp(\tau,\dots)}u(\tau,\dots) = f_{(K\chi,\, K\psi,\, w)}\,[e^{\bar{\wp}}\bar{u}]|_{(\chi,\psi,\tau)} \tag{127}$$

Following the discussion in C0.2 $\bar{\wp}$ can be described as a function in this momenta frequency space.

This concludes the proof of the identity. ■

Please note that the constant step size coefficient Δz is factored into $\wp$.

Also, if the functional representation of $\wp$ in the Fourier space cannot be obtained due to the series not converging to a function, than the full expansion of Eq. (126) will have to be considered, where the series representation of $\overline{\wp}$ is used. Truncating terms both in the series representation of each term based on $\overline{\wp}$ in the Maclaurin series and in the Maclaurin series on the rhs of Eq. (126) will need to be done.

C0.4 Proof of solution of differential equations in steps 1-7

It can be seen directly by differentiationg the Maclaurin series of the exponential operator multiplied into u. Since the operator itself does not rely on the propagation coordinate (for example, a mean field approximation is used), the analytic integration of steps 1-7 with an arbitrary operator including convolution operators always yields the exponential operator form as a solution. See appendix C4 for example verification.

Appendix C1: Explanation of Constants in the NLSE

In Si Units:

Name	Symbol	Value
Speed of light	c	$3.0 * 10^8 \frac{\mathrm{m}}{\mathrm{s}}$
Nonlinear refractive index	n_2	$7 * 10^{-20}$
Central angular Frequency	ω	$6.08 * \frac{10^{14}}{\mathrm{s}}$
β_2	GVD	$-4.08 * 10^{-25} \frac{\mathrm{s}}{\mathrm{m}}$
k_o	In material Wavenumber corresponding to: ω	$3.61 * \frac{10^6}{\mathrm{m}}$
β^n	nth photon absorption coefficient	$7.63 * 10^{-266} \frac{\mathrm{m}^{2n-3}}{\mathrm{W}^{n-1}}$
σ	Inverse Bremsstrahlung cross section	$2.6 * 10^{-24} \mathrm{m}^2$
τ_c	Electron collision time	$3fs$
E_g	Material band gap energy	$6.5eV$
A_o	Peak amplitude of the envelope	Described in section

	electric field	4.6

Name	Symbol	Equation
Nonlinear length	L_{nl}	$(\frac{c}{\omega n_2 I_o})$
Dispersion Length	L_{ds}	$\frac{\tau_p{}^2}{\beta_2}$
Diffraction Length	L_{df}	$\frac{k_o s_p{}^2}{2}$
Peak Intensity	I_o	$n_o c \frac{\lvert A_o \rvert^2}{2\pi}$
Multi-Photon Absorption	L_{mp}	$\frac{1}{\beta^m I_o{}^{(m-1)}}$
Plasma density	ρ_o	$\frac{\beta^m I_o{}^m \tau_p}{m\hbar\omega}$
Reduced plasma density	ρ	$\frac{\rho_e}{\rho_o}$ ρ_e is the electron density at a given time
Multi-Photon Absorption Length*	Lpl	$\frac{2}{\rho_o \sigma \omega \tau_c}$
Avalanche Ionization Coefficient	α	$\frac{\sigma I_o t_p}{n_o{}^2 E_g}$

* This term was modified from the original term in [chapter 4, 34]. Due to a typo error formula was incorrect (units did not match).

Appendix C2: Nyquist Criteria and Sampling conditions

C2.1 Initial Sampling Conditions

This appendix will now proceed in deriving initial sampling requirements and show the adaptive step-size algorithm used in the simulation.

It is now prudent to derive the initial sampling intervals.

The above NLSE is only valid for a reduced angular frequency range angular (inverse variable of τ) from $-0.5\omega_o\tau_p < \omega < 0.5\omega_o\tau_p$ as stated in [chapter 4, 34] due to the slow-varying approximation. This means, a bandlimited approach can be assumed and thus, the Nyquist criterion can be applied to calculate the spacing in τ needed. For the FFT algorithm used, sampling is at the Nyquist Criterion.

Thus the spacing in τ, according to the Nyquist criterion, $d\tau$ is:

$$d\tau \leq \frac{2\pi}{2(0.5\omega_o\tau_p)} = \frac{2\pi}{\omega_o\tau_p} \tag{128}$$

Where, ω_o corresponds to the central frequency of the initial input pulse. The range of τ is set to a desired domain length ($\Delta\tau$-user specified) and then $d\omega$, in angular radian units is calculated as:

$$d\omega \leq \frac{2\pi}{2(0.5\Delta\tau)} = \frac{2\pi}{\Delta\tau} \tag{129}$$

The arrays are designed such that the window size is an integer multiple of the spacing and that there are an even amount of array elements. The positive endpoint of the windows is reduced in magnitude by one step size in relation to the negative endpoint of the window, due to the periodic nature of the FFT for even arrays. If this is satisfied in one domain it is automatically satisfied in the inverse (frequency) domain. These condition assures that frequency domain values (and vice-versa, this also applies for the time domain when taking the inverse fft) corresponding to the frequency array element number are what is expected (i.e., frequency values corresponding to the fft are the value obtained from incrementing with the spacing in Eq.(129) from the minimal frequency-$0.5\omega_o\tau_p$). The even condition insures that the matrix swapping needed in the Matlab fft algorithm does not introduce element swapping error. Due to these conditions, the zero frequency is always sampled.Array sizes for the FFT algorithm in Matlab samples only at equality in the above Nyquist expressions (FFT assumes a periodic function with the window size and uses a Fourier series summation to accomplish this).

The amount of data points for both the frequency range and the time range are the same:

$$\#\text{of data points} = \Delta\tau\omega_o\tau_p \tag{130}$$

For the Spatial resolution there are no imposed upper bounds in momentum. The upper bound in momenta is introduced from the maximum frequency bound introduced in [chapter 4, 34] and using the paraxial approximation. The Nyquist criterion for the normalized angular k_χ, k_ψ momenta, reads as:

$$|k_{\chi}, k_{\psi}| \leq \frac{n_o(1.5\omega_{central})1.5\omega_{central}Sp}{c\tau_p} \tag{131}$$

In Eq. (131) for upper momentum bounds, the static refractive index is used, which makes Eq. (131) an estimate of the upper bound. Due to the intensity dependent nature of the index of refraction the maximal momenta can be higher than this upper bound estimation (this is taken into account by the adaptive step size algorithm shown in the next subsection).

Given a spatial grid size that is a free user parameter in the model (just like the temporal grid size) the spatial step size and the momenta step sizes can be defined in the same way as derived above for the temporal step and angular frequency step sizes.

$$d\chi, \psi \leq \frac{1}{2(\frac{n_o 1.5\omega_o Sp}{c\tau_p})} = \frac{2\pi c\tau_p}{3(n_o\omega_o Sp)} \tag{132}$$

The range of χ, ψ is set to a desired domain length and then dk_{χ}, k_{ψ} is calculated as:

$$dk_{\chi}, k_{\psi} = \leq \frac{2\pi}{2(0.5\Delta\chi, \psi)} = \frac{2\pi}{\Delta\chi, \psi} \tag{133}$$

$$\#\text{of spatial data points} = (2\Delta\chi, \psi \frac{n_o 1.5\omega_o Sp}{c\tau_p})^2 \tag{134}$$

At the start, the spatial and temporal grid sizes should be chosen such that the input signal decays to zero before the edges of the window. However, this is not a strict requirement given the use of the adaptive step-size algorithm described below. The adaptive step-size algorithm can be used to account for the expanding domain windows and the changes in the required sampling increments and thus avoid aliasing errors.

C2.2 The Adaptive Step Size Algorithm

While the frequency range is limited by the slow varying approximation, extending the frequency ranges can still yield insight to the system response over the increased bandwidth. For example, fig.8 in the results section demonstrates that the simulation still fits experimental results over frequency ranges that violate the slow-varying approximation. Window sizes need to be updated due to the various non-linear and linear effects. For example, the temporal and spatial window size should be increased, due to the GVD walk off the optical pulses and diffractive expansion in the transverse spatial coordinates. The following method offers a rigorous adaptive algorithm to adjust the original Nyquist Criteria.

C2.2.1 Phase Contributions: Part of Algorithm that Evaluates the Effects of the First Derivative

In the consideration of the step-size not only is it important to calculate the original step-size from the Nyquist conditions of the system but also to factor the additional instantaneous phases from the operators. In the respective domains the operators add instantaneous phase (i.e., frequencies) that

translates to higher maximal values in the inverse domain. For example, considering the self-phase modulation term in time translates to a broadening of the frequency domain. In order to evaluate the new domain boundaries a checking algorithm is employed in this computational method. The exponential operators can have both imaginary and real arguments in respective domains. The derivative of the imaginary arguments w.r.t to the domain being considered at values in the domain yields the additional instantaneous phase contribution at that domain value. For real arguments, the negative terms and positive terms are considered differently. For the negative terms, it is assumed that the derivative w.r.t to the domain being considered at a domain value yields the characteristic length of the decaying exponent at a domain value. From this, new sampling conditions are obtained at every propagation slice and verified with the original.

In section C2.2.1 and C2.2.2, only the imaginary argument terms of the exponential A, B and C operators are considered. All derivations in these subsections are over the imaginary argument terms of these exponential operators.

For imaginary terms, for operators acting over the same 3 dimensions, for a given domain in the subset, and propagation slice number (#+1):

For the (K_χ, K_ψ, w) domain subset:

$$\frac{\partial \varphi_{\#+1}}{\partial \mathrm{x}} = \frac{\partial \varphi_0}{\partial \mathrm{x}} + \sum_{\mathrm{n}=1}^{\mathrm{n}=\#} \frac{\partial \varphi_{\mathrm{A}}}{\partial \mathrm{x}} \tag{135}$$

x is a place holder for the domain being considered in the subset. φ_{A} stands for the imaginary arguments of the exponential operator A, φ_0 is the original phase of the input pulse (note that the step size increment in the propagation coordinate is included as a coefficient within the imaginary argument).

If the input pulse is transform limited the first term in Eq. (135) is zero. Thus, the maximal inverse domain value to the domain being considered is simply $\max(\frac{\partial \varphi_{\#+1}}{\partial \mathrm{x}})$. Max is calculated over the full set of values (K_χ, K_ψ, w).

With the above considerations, the new Nyquist criterion for the domain being considered yields:

$$dx_{\#+1,imaginary} \leq \frac{0.5 * 2 * \pi}{\max(\mathrm{abs}(\frac{\partial \varphi_{\#+1}}{\partial \mathrm{x}}))} \tag{136}$$

If the original sampling interval increment, dx_0, in the respective domain is smaller or equal to this updated sampling interval increment than there is no need to adjust the sampling interval in the domain being considered. The window size of the inverse domain is:

$$\Delta x^{-1}{}_{\#+1,imaginary} = 2\frac{0.5 * 2 * \pi}{dx_{\#+1,imaginary}} \geq 2 * \max(\mathrm{abs}(\frac{\partial \varphi_{\#+1}}{\partial \mathrm{x}})) \tag{137}$$

x^{-1} indicates an inverse domain (for example the temporal domain for frequency and spatial for momentum).

To guarantee that the endpoints of the inverse domain are well sampled, $dx_{\#+1,imaginary}$ is always taken to be smaller than the equality condition in Eq. (136). As well, a value is chosen such that the even array and integer multiple conditions of the domain window to the step size (described in subsection C2.1) is maintained.

From Eq. (135), it can be seen that the window size in the inverse domain (barring contributions from the exponential C operator explained below) can be calculated before the start of the simulation since the exponential A operator only relies on the frequency, momentum range and propagation step size and does not rely on the u inputted into the iteration. As an illustrative example, I will now calculate the spatial and temporal window size that accounts for dispersive and diffractive effects from the exponential A operator. This is a lower bound calculation since it does not factor in the C operator effects. The derivative with respect to w, K_χ, K_ψ for the exponential A operator argument can be analytically derived. Then the maximum phase derivative is multiplied into the total normalized propagation length:

$$\frac{\partial \widehat{\mathrm{A}}(\mathrm{k}_\chi, \mathrm{k}_\psi, \mathrm{w})}{\partial w} = \frac{\mathrm{i}}{4}\frac{1}{\omega_\mathrm{o}\tau_\mathrm{p}}\left(1+\frac{1}{\omega_\mathrm{o}\tau_\mathrm{p}}\mathrm{w}\right)^{-2}(\mathrm{k}_\chi{}^2+\mathrm{k}_\psi{}^2)+\mathrm{i}2\frac{\mathrm{L_{df}}}{\mathrm{L_{ds}}}\mathrm{w} \tag{138}$$

$$\frac{\partial \widehat{\mathrm{A}}(\mathrm{k}_\chi, \mathrm{k}_\psi, \mathrm{w})}{\partial K_{\chi/\psi}} = -\frac{\mathrm{i}}{4}\left(1+\frac{1}{\omega_\mathrm{o}\tau_\mathrm{p}}\mathrm{w}\right)^{-1}(2\mathrm{k}_{\chi/\psi}) \tag{139}$$

Since the χ and ψ domains are equivalent in size (rectangular window) the above equation is only calculated for the χ domain. Using Eq. (137) and the equality condition, the following can be obtained:

$$\Delta\tau_{endslice} = 2\max(\mathrm{abs}(\frac{1}{4}\frac{1}{\omega_\mathrm{o}\tau_\mathrm{p}}\left(1+\frac{1}{\omega_\mathrm{o}\tau_\mathrm{p}}\mathrm{w}\right)^{-2}(\mathrm{k}_\chi{}^2+\mathrm{k}_\psi{}^2)+2\frac{\mathrm{L_{df}}}{\mathrm{L_{ds}}}\mathrm{w}))\Delta\varsigma \tag{140}$$

Where, $\Delta\varsigma$ is the length of the crystal in reduced propagation coordinates.

$$\Delta\chi/\psi_{endslice} = 2\max(\mathrm{abs}(\frac{1}{4}\left(1+\frac{1}{\omega_\mathrm{o}\tau_\mathrm{p}}\mathrm{w}\right)^{-1}(2\mathrm{k}_\chi)))\Delta\varsigma \tag{141}$$

Therefore, to account for dispersion and diffraction the spatial and temporal lower bound window sizes are given by Eq. (140) and (141).

The domains are grouped together as (K_χ, K_ψ, w), (χ, ψ, τ),(χ, ψ, τ, w'). When considering the domain subsets, the C operator introduces an additional order of complexity due to its 4 domain nature. The exponential C operator imposes phase on the frequency representation and on the (χ, ψ, τ) as will be seen. Firstly, the instantaneous phase in the frequency domain contribution is derived. Eq. (135) is updated as follows for the frequency derivative:

$$\frac{\partial \varphi_{\#+1}}{\partial \mathrm{w}} = \frac{\partial \varphi_0}{\partial \mathrm{w}} + \sum_{\mathrm{n}=1}^{\mathrm{n}=\#} \frac{\partial \varphi_{\mathrm{A}}}{\partial \mathrm{w}} - (\mathrm{f}(\tau, K_\chi, K_\psi))\mathrm{d}\varsigma \tag{142}$$

Where, $\mathrm{f}(\tau, K_\chi, K_\psi)$ is obtained from $\mathrm{f}(\tau, \chi, \psi)$, the coefficient of $(-iw')$ in the C operator exponential argument. $\mathrm{d}\varsigma$ is the propagation step and is explicitly shown for the C operator term. This accounts for the maximal time delay generated by the group velocity dependence to the intensity varying refractive index which is described in the self-steepening effect and thus the exponential C operator. Thus, Eq. (142) calculates the temporal window from both the linear dispersion and from the group velocity effects of the self-steepening term.

The above can be upper bound estimated as:

$$\frac{\partial \varphi_{\#+1}}{\partial \mathrm{w}} = \frac{\partial \varphi_0}{\partial \mathrm{w}} + \sum_{\mathrm{n}=1}^{\mathrm{n}=\#} \frac{\partial \varphi_{\mathrm{A}}}{\partial \mathrm{w}} - \max(\mathrm{f}(\tau, \chi, \psi))\mathrm{d}\varsigma \tag{143}$$

The C operator acts in the same way as the B operator when considering the spatial domain. Therefore, Eq. (135) is applied for the K_χ, K_ψ domains.

The rest of the effects of the exponential C operator acts on (χ, ψ, τ) and its effect will now be considered in that domain set. The instantaneous phase contribution of the exponential C operator will be derived now in the (χ, ψ, τ). For the imaginary term of the C operator, it can be visualized that the effective operation is to create a new optical field by taking the values of the incoming optical fields and delaying them by the imaginary coefficient of w (labelled as $\mathrm{f}(\tau)$) in the exponential argument. This is in-line with the explanation given in section 4.3 for the self-steepening term. Thus, the C operator is grouped with the B operator (effectively it is over (χ, ψ, τ)). To calculate how its instantaneous phase contribution should be considered, the exponential C operator can be seen as reorganizing the phase information from the input phase as follows:

$$\varphi_{\mathrm{C}} = \varphi_{\mathrm{O}}(\chi, \psi, \tau - \mathrm{f}(\tau, \chi, \psi)\mathrm{d}\varsigma) \tag{144}$$

Labelling,

$$\mathrm{G} = \tau - \mathrm{f}(\tau\, , \chi, \psi)\mathrm{d}\varsigma \tag{145}$$

The phase derivative is given as:

$$\frac{\partial \varphi_{\mathrm{C}}}{\partial \tau} = \frac{\partial \varphi_{\mathrm{O}}(\chi, \psi, \mathrm{G})}{\partial \mathrm{G}} [1 - \frac{\partial \mathrm{f}(\tau\, \chi, \psi)}{\partial \tau} \mathrm{d}\varsigma] \tag{146}$$

Eq. (144) is equivalent to reorganizing the phase slices in time by the offset term $\mathrm{f}(\tau)\mathrm{d}\varsigma$. In Eq. (146) the first term, if the multiplication is expanded, is equivalent to adjusting the delay of the

instantaneous frequencies, as described in section 4.3. Meaning that, due to the GV intensity based adjustment; parts of the envelope containing a certain instantaneous frequency will be delayed relative to others. The second part of the term introduces instantaneous frequencies through the additional phase modulation that occurs with intensity dependent GV's. It can be viewed as SPM that occurs due to an intensity dependent GV that stretches or compresses the envelope and thus the instantaneous phase that it carries.

Numerically, the phase is reorganized by the offset term $\mathrm{f}(\tau)\Delta\varsigma$, as in Eq. (144), and then the numerical derivative is calculated.

For the χ, ψ domains the phase derivative is:

$$\frac{\partial \varphi_{\mathrm{C}}}{\partial\, \chi, \psi} = [\frac{\partial \varphi_{\mathrm{O}}(\chi, \psi, \mathrm{G})}{\partial \chi, \psi} |_{\mathrm{G}} = \mathrm{const}] + \frac{\partial \varphi_{\mathrm{O}}(\chi, \psi, \mathrm{G})}{\partial G} [\frac{\partial \mathrm{f}(\tau\, \chi, \psi)}{\partial \chi, \psi} \mathrm{d}\varsigma] \tag{147}$$

The above numerically translates to reordering φ_{O} as described in the previous paragraph, then taking the numerical derivative with adjacent spatial coordinate slices.

For the sake of simplicity the ordering of how the exponential B and C operators are applied are omitted from the analysis. u inputted into the slice is used for the exponential C operator calculation. Therefore, the instantaneous phase is thus:

$$\frac{\partial \varphi_{\#+1}}{\partial \mathrm{x}} = \frac{\partial \varphi_{0}}{\partial \mathrm{x}} + \sum_{\mathrm{n}=1}^{\mathrm{n}=\#} \frac{\partial \varphi_{\mathrm{B}}}{\partial \mathrm{x}} + \frac{\partial \varphi_{\mathrm{C}}}{\partial \mathrm{x}} \tag{148}$$

Where $\frac{\partial \varphi_{\mathrm{B}}}{\partial \mathrm{x}}$ is the derivative of the exponential B operator imaginary argument (the propagation step size for the exponential B and C operator is factored into the argument and not explicitly shown here). In this case the exponential B operator term in Eq. (148) can be evaluated by just considering the exponential arguments of the operator (updated with u outputted from the previous slice). However, the C operator term cannot be evaluated in such a manner. The original phase distribution must be reordered going into each propagation slice due to the reordering effect of the exponential C operator. From this algorithm one can deduce the new bandwidth of the momentum domains as well as the frequency domain (w).

This yields for the sampling condition:

$$dx_{\#+1,imaginary} \leq \frac{0.5 * 2 * \pi}{\max(\mathrm{abs}(\frac{\partial \varphi_{\#+1}}{\partial \mathrm{x}}))} \tag{149}$$

To guarantee that the endpoints of the inverse domain are well sampled, $dx_{\#+1,imaginary}$ is always taken to be smaller than the equality condition in Eq. (149).

C2.2.2 Additional Considerations: The Second Derivative of the Phase

Due to the frequency generation from the intensity variant refractive index, not only does the bandwidth in the frequency domains need to be extended, as shown above, but the new resolution in the (angular) frequency domains change (momentum, time-frequency). The (angular) frequency step-

size needs to be updated. As already stated, the intensity variant phase derivative obtains the instantaneous frequency. As used above, the maximum first derivative obtains the maximum frequency. Therefore, the minimum of the second derivative w.r.t the inverse domain of question, will obtain the minimal change in frequency. This will directly determine the new sampling step size in the inverse frequency domains: The step-size must be at this minimal frequency change or below. The incoming phase of u need not be considered here, as the minimum difference between frequencies is all that is important. However, additional constraints must be considered (see fig. 11).

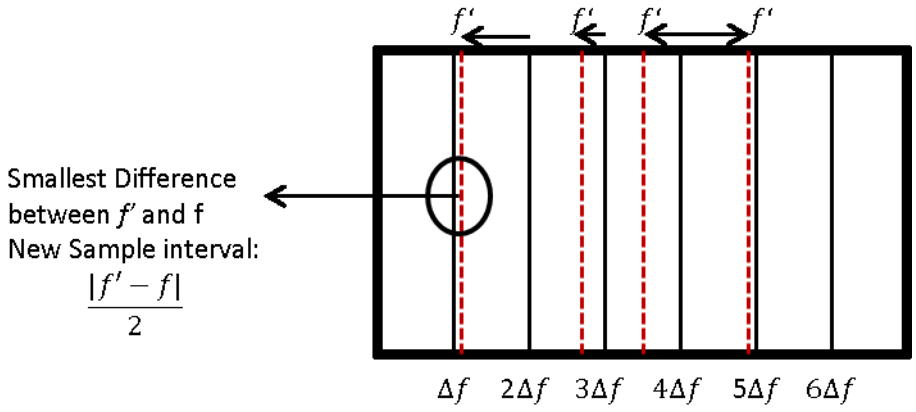

Figure 11: Not only does the minimal frequency variation have to be considered, but the absolute difference between the new frequencies and the incoming frequency grid as depicted in this diagram. This consideration yields Eq.(150). The factor of half is maintained to insure adequate sampling.

With these additional constraints, for the B and C exponential operators, in the (χ, ψ, τ) domains the grid spacing in the inverse domains have to satisfy:

$$\mathrm{df_{new}} \leq 0.5\min(\min(\mathrm{rem}\left(\frac{\frac{\partial^2 \varphi_B}{\partial x^2}\mathrm{dx}}{\mathrm{df}}\right), \mathrm{df} - \mathrm{rem}\left(\frac{\frac{\partial^2 \varphi_B}{\partial x^2}\mathrm{dx}}{\mathrm{df}}\right)), \min(\mathrm{rem}\left(\frac{\frac{\partial^2 \varphi_B}{\partial x^2}\mathrm{dx}}{\mathrm{df}}\right), \mathrm{df} - \mathrm{rem}\left(\frac{\frac{\partial^2 \varphi_B}{\partial x^2}\mathrm{dx}}{\mathrm{df}}\right))) \tag{150}$$

In Eq.(150), the propagation step size is factored into the derivative terms. dx is the domain step-size being considered. df is the original frequency step (inverse domain of x). Rem is the remainder function evaluated at all coordinate value, it is a 3-D array. The inner mins are also 3-D arrays. The outer min represents the operation of evaluating the minimum of the two global mins for the two inner mins. It is evaluated over two scalars. This is always computed below the equality condition.

The last consideration is that due to the Fourier series nature of the FFT, the minimal spacing calculated in Eq.(150) has to be a divisor of the maximal frequency. A spacing is chosen that is less

than the upper bound in Eq.(150) but satisfies the integer multiple criterion and the even array criterion.

Going back to the beginning of section C2.2.1, in discussion of the exponential A operator and C operator for the (K_χ, K_ψ, w) domains, the second derivative there to is evaluated, exactly in the same manner as the above analysis. Physically, time and space shifts from the linear GVD and spatial diffraction can shift in intervals smaller than the grid spacing causing low-resolution sampling errors.

C2.2.3 Putting it all together

The minimum step-sizes calculated from the above first derivative and second derivative contributions are then used for all respective domains. For example the second derivative step-size of the B and C exponential operator is compared with the first derivative step-size of the A and C exponential operator and the minimal value is used. The A and C exponential operator second derivative is compared to the first derivative of the B and C exponential operator. The u array is expanded accordingly; the array is subdivided into the new smaller slices using the initial original slice values. It is then padded to the corresponding maximal size needed. The operators are then applied and the same process is repeated for the next propagation slice.

C2.2.4 Effects of the Negative Exponential Arguments in the Algorithm

For negative real exponential arguments, the decaying exponential argument should not go to e^{-1} within the sampling interval increment. To insure this, the sampling interval should be 0.5 the value or less where the decaying exponential argument would go to e^{-1}. The characteristic inverse length where this occurs for the domain (K_χ, K_ψ, w) is in the w subdomain and occurs because of the exponential C operator:

$$\mathrm{L_{dw}}^{-1} = \max(\mathrm{f}(\tau, \chi, \psi))\Delta\text{çat slice \# } + 1 \tag{151}$$

The above is obtained using the approximation of the exponential C operator discussed in the appendix C2.2.1.

Therefore, the new sampling condition is calculated as:

$$dx_{\#+1,decay} = \frac{0.5}{\max(\mathrm{L_{dw}}^{-1})} \tag{152}$$

For the domain of interest, the original sampling interval increment should be smaller or equal to:

$$\min(dx_{\#+1,decay}, dx_{\#+1,imaginary}) \tag{153}$$

For the exponential B operators the same analysis can be carried for the (χ, ψ, τ).

To further the discussion, the step-size in the propagation coordinate introduces a linear scaling for all phase and decaying exponential effects described above. Thus, by reducing this step-size the onus of tuning other domain step-sizes is reduced.

C2.3 The Impact of the Positive Exponential Terms

For positive exponential terms, their impact on the sampling interval is not considered since it is assumed that u remains integrably bound in L-2 after the application of these terms. Therefore, u will still decay, albeit more slowly. The envelope of u would be even more slowly varying compared to the phase function and thus if the system is being sampled already at a maximum interval corresponding to the maximal phase frequency the system is automatically not under sampled.

The same is true for positive exponential terms in the frequency space, since the spectral representation is integrably bound in L-2 for this problem. However, in the WLG simulation it is found that the real exponential terms in frequency space corresponds to a gain at higher frequencies and attenuation at lower frequencies. Though, since the frequency interval remains fixed, this shift towards higher frequencies can cause instability for large crystal lengths.

To clarify: Eq. (104) is a non-unitary NLSE that naturally yields gain and absorption type terms. Thus, for its physical application, it is only valid in the regime where there is an overall absorption term per propagation increment. Otherwise, since there is no actual gain in the system, energy conservation would be violated even if solutions are integrably bound in L-2. This is thus, a stricter condition than the original assumptions outlined in section 4.2. Therefore, for a given input optical field, frequency range and material parameters, there is an upper bound propagation length where the equation is still valid, due to the effects of the positive exponential terms. Hence wise, once the total energy of u coming from an iteration starts to increase (and there is overall gain) the region of validity of the equation is violated. To overcome this problem, additional terms describing a clamping effect for the positive exponential terms have to be factored into Eq. (104).

C2.4 The Propagation Step-Size

As long as the above updated Nyquist conditions are valid for a propagation step size, the only additional source of error is the mean field approximation used in the two non-linear type operators. The magnitude of the envelope function should not vary considerably in the propagation step. Considering the effects of the real exponents as discussed in the previous sections of this appendix already can place some upper bounds on the propagation coordinate. However, the propagation coordinate is simply reduced until convergence of results as a function of propagation step size is achieved.

Appendix C3: Relevant Omissions, singularities and extensions to the NLSE

This appendix will cover certain omissions and errors in Eq.(104) as well as extensions to the equation. Eq. (104) is linearized in such a manner that higher order terms in the Taylor expansion about a given coordinate point $(\chi, \psi, \tau, \varsigma')$ are omitted. Therefore, the equation can be written in terms of the constants stated above, i.e. in terms of Ldf, Lds, etc. Also, it is assumed that the original pump peak contributes the most to the generated white light and thus, the constants are only calculated for the original pump signal. The slow-varying approximation of the envelope imposes the condition that the bandwidth is equal to the central frequency of the pump [chapter 4, 34]. In fact, mathematically, the equation can be extended past this bandlimited requirement. For example, this was done to simulate the experimental results in section 4.6.2. Mathematically, the only constraint is that the frequency bandwidth cannot violate the series convergence to the functional form of $\widehat{A}$ in its inverse space. Otherwise, the full divergent series will have to be considered, yielding un-physical solutions. This can be seen as the mathematical limits of the approximate NLSE for the system represented in Eq. (104). The series will be divergent if:

$$\frac{1}{\omega_o \tau_p} w \geq 1$$

And if:

$$\frac{1}{\omega_o \tau_p} w = 0$$

The series can be recast in an equivalent form that is convergent for $\frac{1}{\omega_o \tau_p} w \geq 1$ by algebraic manipulation (i.e., finding the equivalent Laurent series). Therefore, the functional form of the $\widehat{A}$ operator can still be used. However, the series will always be divergent for $\frac{1}{\omega_o \tau_p} w = 1$ and $\frac{1}{\omega_o \tau_p} w = 0$. The frequency representation of u has to be bandlimited, i.e., go to zero at these endpoints, to insure that when the series becomes invalid, the overall product between the series and u is zero.

$\frac{1}{\omega_o \tau_p} w = 1$, represents a point discontinuity, while $\frac{1}{\omega_o \tau_p} w = 0$ represents an asymptotic discontinuity. Thus, due to the integral nature of the Fourier transform, the point discontinuity can be ignored and the limiting value can be used (corresponding to the functional value in frequency space). However, sampling at this endpoint value can result in physically unsounds solutions, and this situation is avoided by limiting the bandwidth below this endpoint.

Therefore, the bandwidth can at-most be extended to:

$$-\omega_o \tau_p < w < \omega_o \tau_p$$

The other errors are more subtle. For example, as more frequencies are generated, the Lpl, Lmp,Lds,Ldf,etc. change and do not necessarily approximately equal the original. This is because they are all functions of χ, ψ, τ indirectly through the instantaneous frequency $\omega(\chi, \psi, \tau)$.

Also, the coefficient of multi-photon ionization (β^m) changes since different generated frequencies are at different photon orders relative to the band gap of the material. Therefore, at higher frequencies

away from the central frequencies, the equation underestimates the scattering and absorption due to the plasma since the multi-photon absorption length (Lmp) is higher than what it should be. If the intensity of these components are equivalent to the original peak pump intensity than numerically these components should have lower intensity distributions than what is given by the equation and in turn should generate less frequencies in the white light spectrum than their contributions in Eq. (104). However, the intensity of these components, especially near the end of the spectral bandwidth are much lower than the pump. Thus, this justifies the approximation that L_{mp} remains constant; the product of the increased β with the decreased intensity stays relatively constant within a certain range.

To minimize such errors if they do arise at the beginning of each slice along the propagation direction, I calculate, using u coming from the end of the previous slice:

$$L_{mp}(\chi, \psi, \delta\tau_n) = \frac{1}{\beta(\omega(\chi, \psi, \tau))^m I_o{}^{m-1}} \tag{154}$$

$$\delta\tau_n = \tau_n - 1 < \tau \leq \tau_n \tag{155}$$

$$\omega(\chi, \psi, \tau) = \omega_o + \frac{2\pi}{\tau_n}\frac{\delta\emptyset(\chi, \psi, \tau)}{\delta\tau} \tag{156}$$

I_o is the original peak intensity of the input pump pulse. $\omega(\chi, \psi, \tau)$ is the instantaneous frequency of the chirped pulse, m is the order corresponding to $\omega(\chi, \psi, \tau)$ (thus, m is as well a function of χ, ψ, τ). For the nth interval of reduced time and at the given reduced spatial coordinates the value of L_{mp} is calculated in the above manner.

$\emptyset$ is the phase of u, coming from the end of the previous slice and $\delta\tau$ is the τ step size (it is assumed that the instantaneous frequency values are slowly varying compared to the reduced time step size). Here it is considered that only the instantaneous phase of the pulse would register as a frequency change for the β^mcoefficient.

It is also assumed that within the interval $\delta\tau_n$ the change in L_{mp} is negligible and overall L_{mp} is a slowly varying function such that its τ derivative is negligible. Therefore, one can omit the derivative of L_{mp} when setting up the operators. If this assumption is violated it would be needed that the B operator would have to be changed to account for the additional derivative term; this also holds true for Lnl, lpl and Ldf.

For the differential equation in τ for normalized ρ it can be updated to:

$$\frac{\partial \rho}{\partial \tau} = \alpha \rho |u|^2 + \frac{\beta(\omega(\chi,\psi,\tau))^m I_o{}^m \tau_p}{\rho_o m \hbar \omega} |u|^{2m} \tag{157}$$

Where, the coefficient of inverse Bremsstrahlung is a weak function of the optical values of the pulse and can be treated as constant.

The plasma term in the NLSE is defined and scaled relative to ρ_o which is a constant parameter defined only for the input pulse. If there is an initial chirp in the pump pulse going into the crystal,

$$\rho_o(\chi,\psi) = \sum_{c=0}^{c=n} \frac{\beta(\omega(\chi,\psi,\tau))^m I_o{}^m \delta\tau}{m\hbar\omega(\chi,\psi,\tau)} \tag{158}$$

where,

$$\tau_{max} = n\delta\tau \tag{159}$$

and,

$$\frac{\partial \rho}{\partial \tau} = \alpha \rho |u|^2 + \frac{\beta(\omega(\chi,\psi,\tau))^m I_o{}^m \tau_p}{\rho_o(\chi,\psi) m \hbar \omega} |u|^{2m} \tag{160}$$

If the right hand term in (160) is close to unity than:

$$L_{pl}(\chi,\psi,\tau) = \frac{2}{\rho_o \sigma \omega(\chi,\psi,\tau)\tau_c} \tag{161}$$

If not:

$$L_{pl}(\chi,\psi,\tau) = \frac{2}{\frac{\beta(\omega(\chi,\psi,\tau))^m I_o{}^m \tau_p}{m\hbar\omega} \sigma\omega(\chi,\psi,\tau)\tau_c} \tag{162}$$

Any point discontinuities in the instantaneous phase can be omitted since the material cannot respond in a differential time scale. The response function of the material is limited to a finite time. As well, if the sampling points in reduced time lie on point discontinuities, than it is required to sample within the reduced time step and update the parameters accordingly.

When the instantaneous frequency is zero than it is imposed that the expression for ρ_o goes to zero at that interval in the summation. As well, the term on the right of the $\frac{\partial \rho}{\partial \tau}$ differential equation is zero for zero instantaneous frequency. L_{mp} would approach ∞ thus, in the NLSE, the expression where L_{mp} is used in the equation goes to zero.

Lds should be updated in a similar manner for the interval $\delta\tau_n$ whereby its values are taken at the instantaneous frequency. Ldf is taken at the instantaneous momentum corresponding to the instantaneous frequency for the interval $\delta\tau_n$ and the assumption is used that the spot size used in the calculation is the same as the original pump signal. Lnl can be updated in a similar manner.

Another point of interest is that the propagation coordinate step size is dependent on Ldf. Thus, the step length depends on the instantaneous frequency as well and changes for different intervals of time. However, the overall amount of iterations is fixed, since the total reduced length has the same scaling with Ldf.

Raman scattering is another effect that has been omitted and is out of the scope of the above results. It is assumed that the Raman response function timescale is longer than the optical pulse. Appendix C4 lists the modification necessary to factor in Raman type terms into the method.

Finally, the equation is a scalar equation valid for isotropic material where the white light is totally depolarized or linearly polarized [chapter 4, 49]. Under the circumstance that it is depolarized, one can make the assumption that the individual polarization states see the same $u_{average}$ and thus, this equation models the propagation of $u_{average}$.

The simulation can easily be extended for considering polarization. There will be two scalar coupled equations. The method is applied to each of those equations.

Appendix C4: Extension of the Model: Raman Terms (Convolution Terms), Proof of steps 1-7 and Higher Order Update to C Operator

C4.1 Operator for Raman Convolution Terms and Proof of steps 1-7

In this section, I will derive the exponential operator representation in the domain and inverse domains of convolution terms such as Raman terms. Also, since the derivation mirrors the proof of the solutions to the differential equations in steps 1-7, while deriving the Raman exponential operator, I will show the proof that can be applied for all differential equations in steps 1-7.

Convolution terms such as:

$$\int_{-\infty}^{\infty} f(\mathrm{t}')\mathrm{u}(\mathrm{t}'-\mathrm{t})\mathrm{d}\mathrm{t}' \equiv f(\mathrm{t}) \circ \mathrm{u}(\mathrm{t}) \tag{163}$$

Can still be analytically integrated like in steps 1-7. If f depends on z than the mean field approximation can be used in the same manner as demonstrated with those steps. The rest of the arguments of both functions above (x,y,z) is not shown, for the purposes of clarity, but are there. The Maclaurin series expansion of the exponential operator w.r.t the propagation coordinate of the above is:

$$\mathrm{e}^{\Delta z f(\mathrm{t})\circ} = 1 + \Delta z f(\mathrm{t}) \circ + \frac{1}{2!}(\Delta z f(\mathrm{t}) \circ)^2 + \frac{1}{3!}(\Delta z f(\mathrm{t}) \circ)^3 \ldots \tag{164}$$

It can be verified that this is a solution to the differential equation shown in steps 1-7, as follows:

If $u = \mathrm{e}^{zf(\mathrm{t})\circ} g(t)$, and using the identity of Eq. (164) in the differentiation (now with the free variable z), the following is obtained:

$$\frac{\partial \mathrm{e}^{zf(\mathrm{t})\circ} g(t)}{\partial z} = [f(\mathrm{t}) \circ + \frac{1}{1!}(zf(\mathrm{t}) \circ) f(\mathrm{t}) \circ + \frac{1}{2!}(zf(\mathrm{t}) \circ)^2 f(\mathrm{t}) \circ \ldots \frac{1}{3!}(zf(\mathrm{t}) \circ)^3 f(\mathrm{t}) \circ] g(t) \tag{165}$$

The above was obtained by differentiating Eq. (164) w.r.t to the propagation coordinate variable. Since $f(\mathrm{t})$ is assumed to be only a function of t, it can be treated as a constant in the differentiation. Eq. (165) uses the fact that differentiating a term w.r.t the propagation coordinate yields:

$$\frac{\partial \frac{1}{\mathrm{n}!}(zf(\mathrm{t}) \circ)^{\mathrm{n}}}{\partial z} = \frac{1}{(\mathrm{n}-1)!}(z)^{\mathrm{n}-1}(f(\mathrm{t}) \circ)^{\mathrm{n}} = \frac{1}{(\mathrm{n}-1)!}(zf(\mathrm{t}) \circ)^{\mathrm{n}-1} f(\mathrm{t}) \circ \tag{166}$$

Which is the result using the normal chain rule of differentiation. Also since,

$$\frac{1}{(\mathrm{n}-1)!}(zf(\mathrm{t}) \circ)^{\mathrm{n}-1} f(\mathrm{t}) \circ = f(\mathrm{t}) \circ \frac{1}{(\mathrm{n}-1)!}(zf(\mathrm{t}) \circ)^{\mathrm{n}-1} \tag{167}$$

Since the convolution is over the t variable and z can be treated as a constant w.r.t convolution. Also, convolutions of functions commute by property of convolution [chapter 4, 50].

Therefore, using Eq. (167) and factoring out the convolution (which can be done due to the multiplicative commutation property of convolution with the summation) term Eq. (165) becomes:

$$\begin{aligned}\frac{\partial \mathrm{e}^{zf(\mathrm{t})\circ}g(t)}{\partial z} &= f(\mathrm{t})\circ\left[1+\frac{1}{1!}(zf(\mathrm{t})\circ)+\frac{1}{2!}(zf(\mathrm{t})\circ)^2\ldots\frac{1}{3!}(zf(\mathrm{t})\circ)^3\right]g(t)\\ &= f(\mathrm{t})\circ(\mathrm{e}^{zf(\mathrm{t})\circ}g(t)) = f(\mathrm{t})\circ u(t,z)\end{aligned} \tag{168}$$

Where the last equality follows from the definition of u. If $u=\mathrm{e}^{zf(\mathrm{t})\circ}g(t)$, $\frac{\partial u}{\partial z}=f(\mathrm{t})\circ u(t,z)$ which is the differential equation that needs to be satisfied for the convolution term.

At $z=0$, $u=u(t,0)$, substituting $z=0$ above yields:

$$g(t)=u(t,0) \tag{169}$$

Giving, for a general coordinate step the integrated solution at $\mathrm{z}=\mathrm{z_o}+\Delta z$ (step-size, Δz, is weighted by a symmetrisation constant from the global step-size as shown in steps 1-7):

$$u(t,(n+1)\Delta z)=\mathrm{e}^{\Delta z f(\mathrm{t})\circ}u(t,n\Delta z) \tag{170}$$

Where n is some integer number relating to the slice number. Therefore, the exponential operator for the convolution term is verified to be $\mathrm{e}^{\Delta z f(\mathrm{t})\circ}$. If $f(\mathrm{t})$ is truly independent from z then the above is an exact solution. The above proof is the same for the $\wp$ operator (given the discussion in appendix C0.3 that ordering of operations in $\wp$ do not need to be considered and the propagation coordinate can be treated the same as a constant w.r.t to $\wp$, I.e, $\wp$ does not act on z). This Means that $\wp$ can be symbolically substituted for $f(\mathrm{t})\circ$ symbol in the proof above and the $\wp$ differential equation is proved.

If, like the α_1 and α_2 operators, $f(\mathrm{t})$ is not independent of z (here $f(\mathrm{t})$ can be a convolution coefficient function, like $f(\mathrm{t})\circ$ or a multiplicative coefficient function like for α_1 and α_2), than the above proof is valid, however, the mean-value approximation will have to be substituted in the proof. $u=\mathrm{e}^{zf(\mathrm{t},\mathrm{z_o})\circ}g(t)$ would have to be used. Then, the series expansion can be used, as outlined above. Using the expansion of the exponential operator w.r.t z shown in u about $\mathrm{z_o}$, the following is obtained:

$$\mathrm{e}^{zf(\mathrm{t},\mathrm{z_o})\circ}=1+(z-\mathrm{z_o})f(\mathrm{t},\mathrm{z_o})+\frac{1}{2!}(z-\mathrm{z_o})^2f(\mathrm{t},\mathrm{z_o})^2+\frac{1}{3!}(z-\mathrm{z_o})^3f(\mathrm{t},\mathrm{z_o})^3\ldots \tag{171}$$

The rest follows the same as the proof above. $f(\mathrm{t},\mathrm{z_o})$ is not a function of z so the derivative w.r.t z acts only on the powers of z. $f(\mathrm{t},\mathrm{z_o})$ can be factored out of the summation as in the above procedure since multiplicative ordering is non-specific and does not matter ($f(\mathrm{t},\mathrm{z_o})$ commutes with the summation and itself).

see appendix C4.3 for a relevant note on the α_2 operator.

C4.2 Raman/Convolution Term Frequency Representation

Since,

$$\mathrm{e}^{f(\mathrm{t})\circ}u=[1-f(\mathrm{t})\circ+\frac{1}{2!}(f(\mathrm{t})\circ)^2-\frac{1}{3!}(f(\mathrm{t})\circ)^3\ldots]\mathrm{u} \tag{172}$$

For clarity, the symmetrisation specific step-size increment is factored into *f*. The convolution raised to a power is defined as iterative convolutions of function *f*. As well, the ordering of these convolutions does not matter. Convolution in the time domain is equivalent to the Fourier transform of the product of the Fourier frequency representation of functions in the convolution For iterative convolutions, it can be shown as a Fourier identity that this is equivalent, in the time domain, to the Fourier transform of the product of the Fourier frequency representation of all functions in the convolution [chapter 4, 50]. Therefore, the following is true:

$$\mathrm{e}^{f(\mathrm{t})\circ}u = f_W\left[1 - \mathrm{f(w)} + \frac{1}{2!}\big(\mathrm{f(w)}\big)^2 - \frac{1}{3!}\big(\mathrm{f(w)}\big)^3 \ldots\right]\mathrm{u(w)|_t} \tag{173}$$

Which is equivalent to:

$$\mathrm{e}^{f(\mathrm{t})\circ}u = f_W\big[\mathrm{e}^{f(\mathrm{w})}\big]\mathrm{u(w)|_t} \tag{174}$$

The operator in the frequency space is simply: $\mathrm{e}^{f(\mathrm{w})}$ and can be applied in the manner shown in section 4.2.

Raman terms are essentially convolutions of the type shown here. The operator representation can thus, straightforwardly be derived in this numerical technique.

C4.3 Approximation Used in Justifying the Series Expansion of the Exponential C Operator and Higher Order Update to the C Operator

In section 4.2, the Maclaurin series expansion for the α_2 operator was shown using the Mean-value approximation outlined in steps 1-7, for $\mathbb{N}$, as:

$$e^{\alpha_2} = 1 + c_2\mathbb{N}\frac{\partial}{\partial\tau} + \frac{1}{2!}(c_2\mathbb{N})^2\frac{\partial}{\partial\tau}^2 + \frac{1}{3!}(c_2\mathbb{N})^3\frac{\partial}{\partial\tau}^3 \ldots \tag{175}$$

Where the step size is factored into $\mathbb{N}$. Strictly speaking however, the series expansion of α_2 is:

$$e^{\alpha_2} = 1 + c_2\mathbb{N}\frac{\partial}{\partial\tau} + \frac{1}{2!}\left(c_2\mathbb{N}\frac{\partial}{\partial\tau}\right)\left(c_2\mathbb{N}\frac{\partial}{\partial\tau}\right) + \frac{1}{3!}\left(c_2\mathbb{N}\frac{\partial}{\partial\tau}\right)\left(c_2\mathbb{N}\frac{\partial}{\partial\tau}\right)\left(c_2\mathbb{N}\frac{\partial}{\partial\tau}\right)\ldots \tag{176}$$

Since $\mathbb{N}$ is a function of τ the product of the derivatives and $c_2\mathbb{N}$'s cannot be re-arranged. They do not commute. However, if the approximation is used that $\mathbb{N}$ is a slow-varying function w.r.t to u, its derivative w.r.t τ can be assumed to be negligible (I.e., zero). In that case both of the above equations are equivalent and Eq.(175) can be used. Using, Eq.(175) in the WLG bulk simulation reproduces exactly what physically happens to the optical field when factoring in self-steepening (see discussion in section 4.2, section 4.3 and appendix C2). This is additional justification in using Eq.(175).

Given the fact that the α_2 incorporates the pertinent physics in a clear way in its application to the WLG problem, it is prudent to derive error estimations and to update the application of the operator in such a way that the error truncation is at least at the same level as general split-step operator methods: $\mathcal{O}(\Delta z^3)$ (or higher) as stated in section 4.2. This is accomplished as follows:

Eq. (176) can be expanded as follows (here to illustrate the step-size exponent, the step size is factored out of $\mathbb{N}$):

$$\begin{aligned} e^{\alpha_2} = \left[1 + \Delta z c_2\mathbb{N}\frac{\partial}{\partial\tau} + \frac{1}{2!}(\Delta z c_2\mathbb{N})^2\frac{\partial}{\partial\tau}^2 + \frac{1}{3!}(\Delta z c_2\mathbb{N})^3\frac{\partial}{\partial\tau}^3 \ldots\right] + \frac{\Delta z^2}{2!}\left[(c_2\mathbb{N})\frac{\partial}{\partial\tau}(c_2\mathbb{N})\frac{\partial}{\partial\tau}\right] \\ + \frac{\Delta z^3}{3!}\left[\left[(c_2\mathbb{N})^2\frac{\partial}{\partial\tau}^2(c_2\mathbb{N}) + (c_2\mathbb{N})\left[\frac{\partial}{\partial\tau}(c_2\mathbb{N})\right]^2\right]\frac{\partial}{\partial\tau}\right. \\ \left. + 3(c_2\mathbb{N})^2\frac{\partial}{\partial\tau}(c_2\mathbb{N})\frac{\partial}{\partial\tau}^2\right] \end{aligned} \tag{177}$$

The term is corrected up to $\mathcal{O}(\Delta z^4)$. If only $\mathcal{O}(\Delta z^3)$ is desired than the Δz^3 term on the RHS of Eq. (177) can be omitted. As described in section 4.2 since the first term of Eq. 174 is applied in (x,y,τ,w') space, I apply all corrections in that space as well. Derivatives of $c_2\mathbb{N}$ are numerically evaluated using the Fourier derivative identity. In the appropriate space this yields:

$$
\begin{aligned}
&e^{\alpha_2(\tau,\dots)}u(\tau,\dots) = \\
&\quad = f_{w'}\left\{\left[e^{-c_2\mathbb{N}iw'} + \frac{\Delta z^2}{2!}\left[(c_2\mathbb{N})\frac{\partial}{\partial\tau}(c_2\mathbb{N})(-iw')\right]\right.\right. \\
&\quad + \frac{\Delta z^3}{3!}\left[\left[(c_2\mathbb{N})^2\frac{\partial}{\partial\tau}^2(c_2\mathbb{N}) + (c_2\mathbb{N})\left[\frac{\partial}{\partial\tau}(c_2\mathbb{N})\right]^2\right](-iw')\right. \\
&\quad \left.\left.\left. + 3(c_2\mathbb{N})^2\frac{\partial}{\partial\tau}(c_2\mathbb{N})(-iw')^2\right]\right]u(w',\dots)\right\}|_\tau
\end{aligned}
\tag{178}
$$

The $e^{-c_2\mathbb{N}iw'}$ is the series convergence of the first term of Eq. (177) in the (x,y, τ, w') space and was derived in detail in section 4.2. The identity from this derivation is used here. Application of the exponential α_2 operator in this way can yield a $\sigma(\Delta z^4)$ error truncation. If additional error truncation is necessary then additional terms of the expansion of Eq. (176) can be obtained and the summation in Eq. (178) updated accordingly. The $\hat{C}$ operator, being the α_2 operator in the WLG simulation is updated according to Eq. (178) for $\sigma(\Delta z^4)$ error.

C4.4 Relevant Note on Terminology

In the above analysis the Maclaurin series is used when the coordinate value z_o can be regarded as zero (the origin) for the local coordinate system of the operator without any loss of generality. For example, the Taylor series was used in Eq. (171). When using the mean-value approximation, the Maclaurin series can be used with z_o being regarded as the origin without any loss of generality but the reader must keep in mind that the functions of z in the operators are at z_o in the calculation and for that step can be regarded as constant over the propagation coordinate.

Chapter 5: Thesis Outlook

In chapter 2 a novel fiber oscillator was constructed to be used for electron diffraction experiments. Two oscillators outputting a compressible pulse to sub 90fs with a central wavelength of 1.03 μm was constructed based on the non-linear polarization mode-locking scheme. Average power was 250mW to 300mW, at rep.rates of 41MHz and 31 MHz. The Oscillators had an amplitude stability of 0.2% fluctuations which out-competes traditional Ti:Sapphire systems. This demonstrates a new oscillator that is very compatible with downstream electron diffraction experiments and meets the design criteria for these experiments both in average power, pulse duration and stability.

In chapter 3, a solid-state regenerative amplifier was constructed that amplified pulses to 0.4mJ at a repetition rate of 1 kHz. The novel simulation scheme outlined in the chapter matches with experimental data and thus a robust simulation model was derived for such systems. The next step is to increase the amplification by changing the crystal doping in the cavity and by tuning the pump beam to match the signal spot-size, thereby increasing the amount of stored energy the signal has access to.

The new fiber oscillator and regenerative amplifier scheme will be fed into a pulse compression stage and then used for electron diffraction experiments, replacing conventional laser sources employed in these labs.

In chapter 4, I derived a new and fast numerical theory to simulate, in all three spatial dimensions and time, a wide class of generalized non-linear Schrodinger equations. I then performed simulations on white-light generation in bulk in all spatial dimensions and time and various hard to simulate non-linear effects such as plasma effects and self-steepening were included in the simulations. Simulations were done on a YAG system and matches published experimental results well. This technique and simulation tool can be used in the design process to generate a wide-band coherent spectrum for molecular coherent control experiments. Fundamental physical effects in the generation of white-light are explored and described in detail in this chapter. Finally, an adaptive algorithm for the simulation is described in this chapter along with extensions and future steps.

The simulation will be extended to incorporate Raman contributions to the white-light spectrum. A beam shaping transmission-phase mask design tool was also developed to shape the beam for various downstream applications (such as seeding OPA's).

The robust femtosecond source and the method and simulations developed in this thesis unlock new experimental possibilities in pump-probe experiments. The laser source can be tuned to output a large number of different possible optical pulses to drive photoelectron generation at the photocathode. New advances in electron source technology for imaging atomic motions in real time then can be more effectively explored. The method and simulation technique developed to explore white light generation in bulk material will enable experimentalists to design accurate optical pulses for driving the sought after optically induced chemical changes in materials. The intended goal of this thesis is then accomplished: An optical toolkit has been developed for high end electron diffraction pump probe experiments for both the electron probe and optical pump at the sample.